AD-A170 692 CLOUD CAVITATION AND COLLECTIVE BUBBLE DYNAMICS(U) 1/3
TRACOR HYDRONAUTICS INC LAUREL MD G L CHAHINE ET AL.
15 MAR 86 TR-83017-1 N00014-83-C-0244

UNCLASSIFIED F/G 20/4 NL

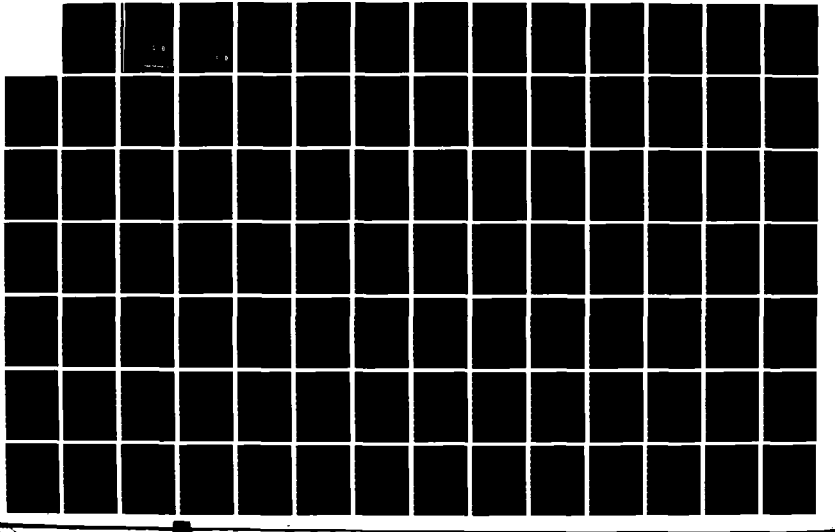

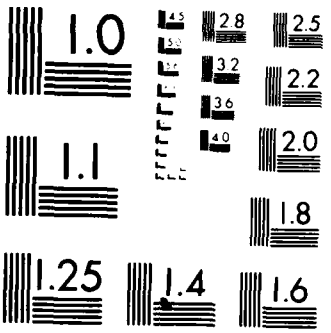

CLOUD CAVITATION AND COLLECTIVE BUBBLE DYNAMICS

by

Georges L. Chahine,
Kenneth M. Kalumuck,
and
Thomas O. Perdue

March 1986

Tracor Hydronautics, Inc.
7210 Pindell School Road Laurel, Maryland 20707

Tracor Hydronautics

TECHNICAL REPORT
83017-1

CLOUD CAVITATION AND COLLECTIVE BUBBLE DYNAMICS

by

Georges L. Chahine,
Kenneth M. Kalumuck,
and
Thomas O. Perdue

March 1986

The information in this report is based upon
work supported by:
Naval Sea Systems Command
General Hydrodynamics Research Program
Administered by
David Taylor Naval Ship Research and Development Center
Under
Contract No. N00014-83-C-0244

UNCLASSIFIED

SECURITY CLASSIFICATION OF THIS PAGE

AD-A170 692

REPORT DOCUMENTATION PAGE

1a REPORT SECURITY CLASSIFICATION: UNCLASSIFIED	1b. RESTRICTIVE MARKINGS: N/A
2a SECURITY CLASSIFICATION AUTHORITY: N/A	3 DISTRIBUTION/AVAILABILITY OF REPORT: APPROVED FOR PUBLIC RELEASE; DISTRIBUTION UNLIMITED
2b DECLASSIFICATION/DOWNGRADING SCHEDULE: N/A	
4 PERFORMING ORGANIZATION REPORT NUMBER(S): Technical Report 83017-1	5 MONITORING ORGANIZATION REPORT NUMBER(S)
6a NAME OF PERFORMING ORGANIZATION: Tracor Hydronautics, Inc. / 6b OFFICE SYMBOL (If applicable)	7a NAME OF MONITORING ORGANIZATION: DAVID W. TAYLOR NAVAL SHIP RESEARCH AND DEVELOPMENT CENTER, Code 1504 (1505)
6c ADDRESS (City, State, and ZIP Code): 7210 Pindell School Road, Laurel, MD 20707	7b. ADDRESS (City, State, and ZIP Code): BETHESDA, MARYLAND 20084-5000
8a NAME OF FUNDING/SPONSORING ORGANIZATION: Naval Sea Systems Command / 8b OFFICE SYMBOL (If applicable): SEA 05R24	9 PROCUREMENT INSTRUMENT IDENTIFICATION NUMBER: Contract Number - N00014-83-C0244
8c ADDRESS (City, State, and ZIP Code): Washington, D. C. 20360	10 SOURCE OF FUNDING NUMBERS

PROGRAM ELEMENT NO	PROJECT NO	TASK NO	WORK UNIT ACCESSION NO
61153N	SR 023 01	23454	N/A

11 TITLE (Include Security Classification): Cloud Cavitation and Collective Bubble Dynamics

12 PERSONAL AUTHOR(S): Chahine, Georges L., Kalumuck, Kenneth M., and Perdue, Thomas O.

13a TYPE OF REPORT	13b TIME COVERED	14 DATE OF REPORT (Year, Month, Day)	15 PAGE COUNT
Technical	FROM 11/83 TO 3/15/86	86 3 15	151 + Figures

16 SUPPLEMENTARY NOTATION: Sponsored under the Naval Sea Systems Command General Hydromechanics Research (GHR) Program administered by the David W. Taylor Naval Ship R&D Center, Code 1504(1505), Bethesda, Maryland 20084-5000

17 COSATI CODES			18 SUBJECT TERMS (Continue on reverse if necessary and identify by block number)
FIELD	GROUP	SUB-GROUP	(U) GHR Program, Cavitation, Cloud, Bubble Dynamics, Gas Diffusion, Heat Transfer, Collapse, Noise
20	04		

19 ABSTRACT (Continue on reverse if necessary and identify by block number)

The study described in this report extends our knowledge of single bubble dynamics to multibubble dynamics. Within the restriction of characteristic bubble size small compared to interbubble distance, the dynamics of a bubble cloud is investigated. Dynamic effects in absence as well as in presence of heat and mass transfer at the bubble wall are considered. The matched asymptotic expansion method is used and enables derivation of differential equations for the bubble shape components at the various orders of approximation. These were solved numerically and the pressure field was deduced. When, during a significant portion of the imposed pressure field history, the liquid is superheated or gas supersaturated, heat and mass transfer at the interface interfere with the dynamics of the bubble growth or oscillations. In that case, the dynamic equation of a bubble in the cloud is coupled to the heat or mass transfer equation by the value of the partial pressures of the liquid vapor and noncondensible gas inside the bubble which are then transfer dependent. This problem is solved when the liquid properties or conditions are such that the variation of the liquid temperature of the gas concentration in the liquid occurs primarily in a thin boundary layer at the bubble wall. In that case an integral equation relates bubble dynamics and heat or mass transfer at the bubble interface.

over --

20 DISTRIBUTION/AVAILABILITY OF ABSTRACT	21 ABSTRACT SECURITY CLASSIFICATION
☒ UNCLASSIFIED/UNLIMITED ☐ SAME AS RPT ☐ DTIC USERS	UNCLASSIFIED

22a NAME OF RESPONSIBLE INDIVIDUAL	22b TELEPHONE (Include Area Code)	22c. OFFICE SYMBOL
Mr. V. J. Monacella	202-227-1503	Code 1504/1505

DD FORM 1473, 84 MAR — 83 APR edition may be used until exhausted. All other editions are obsolete.

SECURITY CLASSIFICATION OF THIS PAGE

UNCLASSIFIED

19. ABSTRACT - (Continued)

A fundamental experimental program was conducted in parallel with the theoretical effort described here. Systematic observations of bubble dynamics using high speed photography and measurements of acoustical pressures were conducted. Spark-generated bubbles were produced at precise locations near complex solid wall geometries. By application of the method of images, the bubble behavior near the solid boundaries is similar to that in the presence of a set of bubble images in the wall. Observations confirmed and complemented the theory since cases of both low and high void fractions could be studied. A set of experiments of a more preliminary nature concerned sound wave propagation through a sheet of bubbles. By varying the frequency of the emitted signals and the characteristics of the bubble generator, correlations could be made between the attenuation of the acoustic wave through the bubble screen and the size distribution of the bubbles.

Several numerical codes were implemented as a result of the multibubble cloud theory developed in this program. These codes have been exercised to investigate bubble cloud behavior. A cumulative effect is observed which tends to reinforce any pressure deviations from the ambient value due to bubble dynamics. The most dramatic effect is observed during bubble collapse. The cumulative effect is mainly due to the fact that each bubble ends its collapse under the influence of pressures generated by the collapse of the other bubbles orders of magnitude higher than the imposed ambient pressure. This would tend to explain the observed high erosion intensities and the bending of some propeller trailing edges. Mass and heat transfer are both seen to reduce bubble growth rate. Bubble interactions also play a significant role in bubble growth -- mainly by the modification of the pressure field. This interaction results in a reduced growth rate which makes the bubble radius at any given time smaller than would be found for an isolated bubble. The dissolved gas concentration in the liquid exhibits similar behavior. The effective gas compression law is seen then to vary rapidly from an adiabatic behavior at the beginning of the growth to an isothermal behavior.

TABLE OF CONTENTS

TABLE OF CONTENTS

FOREWORD AND ACKNOWLEDGEMENTS

The study described in this report was conducted at Tracor Hydronautics, Inc., Howard County, Laurel, Maryland. This program was supported by the Naval Sea Systems Command, General Hydrodynamics Research Program administered by the David Taylor Naval Ship Research and Development Center under Contract No: N00014-83-C-0244.

We would like to express our gratitude to Mr. Justin McCarthy from DTNSRDC for his guidance and support during the conduct of this work. We also thank Dr. Young Shen from DTNSRDC for very useful discussions and suggestions. Also we extend our sincere appreciation to the many present and previous colleagues at Tracor Hydronautics for their encouragement and direct support. We particularly thank Gary S. Frederick, Ron Watson, and Charles Sirian for their direct contribution to the experimental study; and Dr. Han Lieh Liu for his contributions to the heat transfer problem.

1.0 INTRODUCTION

The design criteria for high-speed ship propellers involve tradeoffs between efficiency and cavitation, and strength and vibration of the propeller. Operating in ship wakes at relatively low cavitation numbers, the propeller will, at least intermittently, cavitate, inducing erosion of the blades, loss of efficiency, noise, vibration, and occasionally structural failure of nearby plating. These harmful effects are mainly due to the collapse of unsteady cavities. These include individual bubbles as well as sheet cavities and "clouds" (Figure 1.1).

Adequate and increasingly sophisticated theories for individual bubble growth and collapse exist (see the reviews by Plesset and Prosperetti, 1977, and Hammitt, 1980). While the transition to sheet cavity is not well understood, a large number of experimental observations of sheet cavitation are available (Shen and Peterson, 1979, Bark and Barlekom, 1979, and Bark, 1985). A steady, then unsteady, theory for sheet cavitation was recently developed (Tulin, 1980, and Tulin and Hsu, 1980). Downstream of a "steady" sheet cavity a region of high population of tiny bubbles can be observed and is especially known to be associated with erosion. However, as concluded from observations by Tanabayachi and Chiba (1977), an unsteady sheet cavity is required for the formation of coherent clouds of very fine bubbles. These clouds are either detached from the frothy mixture at the trailing end of the unsteady sheet, or generated in a finite region of the liquid downstream of the unsteady sheet where significant fluctuating pressures exist.

As the pressures generated by single bubble collapse are not strong enough to explain the intense erosion in the subject region and the high forces needed, for example, to bend the trailing edge, cloud cavitation has been held responsible since Van Manen's (1963) work. This is supported experimentally by a very close correlation between the dynamics of these clouds and the sharpest and highest pressure pulses detected on an oscillating hydrofoil (Bark and Barlekom, 1979). Similar phenomena have been observed with ultrasonic cavitation (Hanson and Mørch, 1980).

Apart from some information on the frequency of generation of cloud cavitation, the experimental observations and measurements are very qualitative and do not allow at the present time any quantitative predictions. In addition, the lack of understanding of the dynamics of such cavities makes it impossible to explain any scaling effects and to correct for them. Theoretical and fundamental studies are thus needed as guidance for future design and experimentation.

To our knowledge, since the early work of Van Wijngaarden (1964) only a few publications by Mørch (1977, 1980, and 1982) and Hanson and Mørch (1980) have dealt theoretically with the problem of "collective bubbles collapse" or "cavity cluster collapse." However, a large amount of literature has been devoted to the modeling of bubble-liquid mixture behavior using either a continuum medium approach or a "two-fluid" approach (Zwick, 1959; Van Wijngaarden, 1972, 1976, 1980, and 1982; Zuber, 1964; Ishii, 1975). This subject has recently regained a lot of interest as is shown by several very recent publications (D'Agostino and Brennen; 1983, Rubinstein, 1985; Caflish, et. al, 1985a-b; Ng and Ting, 1986; Miksis and Ting, 1986;...etc.)

In order to explain the phenomenon of propeller blades bent at the trailing edge, Van Wijngaarden (1964) considered the case of a uniform layer of cavities on a solid wall. He studied its unidimensional collective collapse when the surrounding fluid is suddenly exposed to a pressure increase. He derived the continuity and momentum equations for the layer, neglecting the convective and dissipative terms and assuming that the volume fraction of gas is small enough to warrant such approximations. However, he did take into account the individual bubble radial motion and translation, neglecting viscous effects. Solving the derived system of equations, Van Wijngaarden found a considerable increase of the pressure along the wall due to collective effects.

Recently d'Agostino and Brennen (1983), using an approach similar to that of Van Wijngaarden, considered the unidimensional problem of a spherically symmetric cloud. Considering small harmonic fluctuations of the far field pressure, they investigated the cloud response for various oscillating frequencies. Neglecting bubble-liquid relative motion and bubble interactions, they obtained very interesting results on the oscillations of the whole cloud comprised of equal sized bubbles. Cases for which the natural frequency of the cloud is much smaller than the bubble frequency were found. A shielding of the cloud core by the outer layer was obtained when the forcing frequency was higher than the individual bubble frequency. The neglect of the bubble translation velocity and of bubble interactions are, however, major assumptions which require further analysis.

Mørch (1977, 1980), concerned with ultrasonic cavitation fields, considered the collapse of a hemispherical "cluster"

near a wall, which he extended by symmetry to the case of a spherical cloud. He characterized the cloud only by its radius and a uniform void fraction, α, constant in time, and developed the following model. A pressure rise in the liquid leads to the formation of a shock wave on the "cloud boundary." The shock moves toward the cloud center leaving no bubbles behind it and thus constitutes the cloud boundary at each time. The collapse time of a spherical cloud was found to be α times the Rayleigh collapse time of a spherical bubble of the same initial radius. Although a very interesting approach, especially for the calculation of the collapse time, this model (like Rayleigh's model for spherical bubble collapse) is incapable of adequately calculating the pressure field. At the end of the collapse the cloud radius is zero, and the velocities and pressures are infinite since the model does not allow the bubbles to contain noncondensibles. The main physical assumption (presence of a shock wave dividing the space in two regions, one containing bubbles which do not sense the pressure variations until a later time stage, and another one where all bubbles have collapsed) is valid only for relatively high void fractions. The case of a spherical single cavity of the same size as the whole cloud is the perfect extreme example of the domain of validity of this approach. Hanson and Mørch (1980) and Mørch (1982) extended the same model to a cylindrical cloud and a layer of bubbles on a solid plate.

In this report we extend the singular perturbation theory earlier developed to study the interaction between collapsing bubbles (Chahine and Bovis, 1981) to an asymptotic theory for the collective behavior of a multibubble system. A general theory including mass and heat transfer is first presented, then within the constraints of simplifying assumptions, particular

studies are developed. The study of the purely dynamical behavior of the bubble cloud is the most advanced, and codes for a system of N equi-sized symmetrically distributed bubbles (Chahine 1982 a,b,c; Chahine and Shen, 1985) as well as a code for any given distribution of bubbles were developed and extensively used. For instance, the symetrical program was applied to the study of the use of a venturi as a cavitation susceptibility meter and has been recently improved to include gravity effects and the corresponding bubble liquid relative velocity. Heat (Chahine and Liu, 1983, 1984, and 1985) and mass transfer across the bubble-liquid interface are the subjects of two separate studies. In both cases we have considered the simplifying assumptions of a symmetrical bubble configuration and of a thin boundary layer in which either temperature or gas concentration varies. Two separate codes were developed, based on these two studies, and some illustrative examples are presented here. Liquid compressibility is modeled in an additional code by use of an artificially input finite sound speed and time duration for propagation from one bubble to another. Systematic experimental observations of spark generated bubbles near complex wall geometries simulating a multibubble system were made in order to validate the theory. Simultaneously, pressuresgenerated by the simulated cloud were measured and analyzed (Chahine and Sirian, 1985). Acoustic transmission through a sheet of bubbles was investigated using bubbles generated by air injection and emitting and receiving hydrophones.

2.0 GENERAL FORMULATION OF THE PROBLEM

As a first step to study the general problem of a bubble cloud in a flow field and near solid boundaries, let us consider a cloud of bubbles in an unbounded medium of uniform pressure, P_∞, concentration of dissolved gas, C_∞, and temperature, T_∞. This corresponds to the case where the size of the cloud is small compared to the flow field characteristic length scale. P_∞, C_∞, and T_∞ are then the local values of the pressure, the concentration, and the temperature in the flow field in the absence of the cloud. We further assume the liquid to be inviscid and incompressible and the flow irrotational. These assumptions are commonly accepted and are justified in cavitation and boiling heat transfer studies except in the last phases of bubble collapse. The neglect of finite sound speed effects can also be unacceptable in the very early phases of bubble growth (Baumeister and Hamill, 1969). However, we will not be concerned with these early times ($t<10^{-8}$s), especially since numerical experiments have shown that the later history is influenced very little by the value of the initial time at which the computation is started. The bubble cloud behavior is sought when the ambient pressure, $P_\infty(t)$, is time dependent.

In order to determine the flow field in the bubble liquid medium and to obtain the motion and deformation of any bubble in the cloud, one must solve the Laplace equation for the velocity potential, Φ

$$\Delta\Phi = 0 \ , \qquad (2.1)$$

subjected to kinematic and dynamic conditions on the bubbles' surfaces.

The equation of a bubble surface in a coordinate system moving with velocity $\dot{b}^i$ in the direction $\underline{e}_z$, is $r = R^i(\theta,\phi,t)$. $\mathscr{C}^i$ and $\underline{n}^i$ are respectively the local curvature of the surface of bubble B^i and its unit normal vector at the point $M(r,\theta,\phi)$. γ and T_R are respectively the surface tension of the liquid and its temperature at the bubble wall. P_g and P_v are the partial pressures of the noncondensible gas and the vapor inside the bubble. The boundary conditions can then be written:

$$\underline{\nabla}\Phi \cdot \underline{n}^i \Big|_{r=R^i(\theta,\phi,t)} = [\dot{R}^i \underline{e}_r + \dot{b}^i \underline{e}_z]\, \underline{n}^i \quad , \qquad (2.2)$$

$$\rho\left[\dot{\Phi} - \dot{b}^i \underline{e}_z + \frac{1}{2} \left|\underline{\nabla}\Phi\right|^2_{r=R^i(\theta,\phi,t)}\right] = P_\infty(t) - P_v^i(T_R) - P_g^i(t) + 2\,\gamma^i(T_R)\mathscr{C}^i(\theta,\phi,t) \quad , \qquad (2.3)$$

where Φ and the operator ∇ are expressed in the moving coordinate system. Due to the low value of the vapor density, ρ_v, the pressure of the gas and the vapor inside the bubble can be assumed to be uniform as long as the spherical symmetry is preserved.

Due to the relatively very short time of vaporization compared to bubble dynamics and gas diffusion characteristic times, the vapor is considered to instantaneously flow in and out of the bubble, and P_v^i is taken equal to the value of the equilibrium vapor pressure of the liquid at the bubble wall temperature. When the bubble shape deviates moderately from a sphere we will assume that both the temperature along the bubble wall and the value of the vapor pressure vary accordingly. Under this assumption, the pressure, P_v^i, may be uniform inside the bubble far from the bubble surface but accomodates itself to

the temperature controlled value in the vicinity of the interface. More details of the way this happens inside the bubble are not needed here since the flow field of the vapor is of no relevance as long as the velocities are subsonic. The gas and the vapor are taken to comprise an ideal gas mixture and possess the same temperature. The partial pressure of the gas, P_g, is determined using the ideal gas law as well as an energy balance of the bubble content. The concentration of dissolved gas at the bubble surface is related to the partial pressure of the gas within the bubble by Henry's Law,

$$P_g^i = H\, C^i(R^i) \,, \tag{2.4}$$

where H is Henry's constant.

The values of the equilibrium vapor pressure $P_v(T_R)$ and of the surface tension $\gamma(T_R)$ constitute the coupling between the dynamic and the heat problems.

Similarily the value of $P_g^i(t)$ constitutes the coupling between the dynamic and the mass transfer (gas diffusion) problem. To determine the temperature at the bubble wall, $T_R(\theta, \phi, t)$, one needs to solve the energy equation in the liquid,

$$\dot{T} + \underline{\nabla}\phi \cdot \underline{\nabla}T = D \cdot \Delta T, \tag{2.5}$$

where D is the thermal diffusivity of the liquid. Equation (2.5) is subjected to a boundary condition on the bubble wall stating that the heat locally lost at any point of the interface is used to vaporize an amount of liquid determined by the local bubble volume expansion rate. If ρ_v is the vapor density, L

the latent heat of the liquid, and K its thermal conductivity, the heat balance equation over the bubble surface can be written in spherical coordinates:

$$K \iint \frac{dT}{dn^i}\bigg|_{r=R^i(\theta,\phi,t)} R^{i^2}(\theta,\phi,t)\ \sin\theta\ d\theta d\phi = \rho_v L \frac{d}{dt}\left[\iint \frac{R^{i^3}(\theta,\phi,t)}{3}\ \sin\theta\ d\theta\ d\phi\right] \quad . \tag{2.6}$$

This equation is satisfied if the following elementary equilibrium equation applies locally at the bubble surface:

$$\frac{\partial T}{\partial n^i}\bigg|_{r=R^i(\theta,\phi,t)} = \frac{\rho_v L}{K}\ \dot{R}^i \quad . \tag{2.7}$$

The concentration of gas in the liquid, $C(r,\theta,\phi,t)$, is determined by the diffusion equation

$$\dot{C} + \underline{\nabla}\phi \cdot \underline{\nabla}C = D_g \cdot \Delta C \quad , \tag{2.8}$$

where D_g is the molar diffusivity of the gas in the liquid. This equation is subjected at the bubble wall to the condition that the concentration at the interface is equal to the saturation concentration at the partial pressure of the gas in the bubble

$$C(R^i) = C_{sat} \quad . \tag{2.9}$$

C_{sat} is related to P_g by Henry's law, (2.4). The molar rate of transport of gas across the interface, $\dot{n}_g$, is related to

the gradient of gas concentration in the liquid at the bubble wall by the relation

$$\dot{n}_g = D_g \iint \left. \frac{\partial C}{\partial n^i} \right|_{r=R^i(\theta,\phi,t)} R^{i\,2}(\theta,\phi,t) \sin\theta \, d\theta \, d\phi \qquad (2.10)$$

Time integration of (2.10) determines at every instant the total number of moles of gas, n_g, in the bubble. The partial gas pressure inside the bubble is then related to its volume and to n_g by a perfect gas equation of state. The only remaining variable needed to apply this perfect gas law is the gas temperature inside the bubble. The application of the first law energy balance for the bubble interior relates this temperature to the boundary work due to volume change, the enthalpy transfer due to transport of gas and vapor across the bubble wall, and change in internal energy of the bubble contents. This is expressed in detail in Section 6.

Equations (2.1) to (2.10) form, with the bubble energy equation and the initial and at-infinity conditions (known T_∞ and $P_\infty(t)$), a complete set of equations which must be solved to determine the flow, concentration, and temperature fields.

3.0 DYNAMICS PROBLEM: SINGULAR-PERTURBATION THEORY

3.1 Method

The following approach is applicable to a cloud of bubbles of low void fraction. Provided that the characteristic size of a bubble in the cloud, r_{b_o}, is small compared to the characteristic distance between bubbles, ℓ_o, we can assume, in the absence of an initial relative velocity between the bubble and the surrounding fluid, that each of the individual bubbles reacts, in first approximation, to the local pressure variations spherically as if isolated. To the following order of approximation, interactions between bubbles induce bubble motion and deformation and are taken into account. This approach is an extension of the earlier studies by Chahine and Bovis (1981) and Bovis and Chahine (1981) on the collapse of a bubble near a solid wall and a free surface (later presented more generally for nonspherical bubbles by Chahine, 1982).

Since the problem possesses two different length scales, ℓ_o and r_{b_o}, we can consider two subproblems: one concerned with the macroscale and the other one with the microscale. The "outer problem" is that considered when the reference length is set to be ℓ_o. This problem addresses the macrobehavior of the cloud, and the bubbles appear in it only as singularities. The "inner problem" is that considered when the lengths are normalized by r_{b_o} and its solution applies to the vicinity of the considered individual bubble of center B^i. The presence of the other bubbles, all located at infinity in the "inner problem", is sensed only by means of the matching condition with the "outer problem". That is to say, physically the boundary conditions at infinity for the "inner

problem" are obtained, at each order of approximation, by the asymptotic behavior of the outer solution in the vicinity of B^i. Mathematically, one has to match term by term the inner expansion of the outer solution with the outer expansion of the inner solution using the same asymptotic sequence in the two expansions.

3.2 First Order Approximation

The determination of the flow field and the dynamics of any of the individual bubbles, B^i, is accessible once the boundary conditions at infinity in the corresponding "inner region" are known. Here we impose the restrictive assumption that the void fraction is low enough so that the information about the variation of the ambient pressure around the cloud, $P_\infty(t)$, is transmitted to the microscale in a time scale much shorter than the bubble collapse time. Therefore, in the absence of a slip velocity between the considered bubble and the surrounding fluid and when interactions are neglected, the only boundary condition at infinity is the imposed pressure variation $P_\infty(t)$.

When a finite value of the sound speed in the cloud medium must be accounted for, $P_\infty(t)$ can be approximated by $P_\infty(t')$ where $t' = t - x/c$ and x represents the minimum thickness of the cloud shell at the bubble location. To address the problem more rigourously one must solve the two-phase medium flow equation using, for example, a method similar to that proposed in Section 7.0. The "inner problem" is therefore spherically symmetric and its solution is given by the well known Rayleigh-Plesset equation. With the assumption that the liquid is inviscid and incompressible, this equation can be written as follows when mass and heat transfer are neglected

$$a_o \ddot{a}_o + \frac{3}{2} \dot{a}_o^2 = -\bar{P}_\infty(t) + \bar{P}_{g_o} (a_o^{-3k} - 1) + W_e^{-1} (1 - a_o^{-1}) \quad . \quad (3.1)$$

This equation is slightly modified when P_v and P_g are dependent on the transfer of heat or mass across the surface. It is rewritten in those cases in the corresponding sections. In this equation, where the superscript i is omitted for convenience, $a_o(t)$ is the radius of bubble B^i normalized by r_{b_o}. The times are normalized by the Rayleigh time, T_o, based on r_{b_o} and a characteristic value of the pressure variations, ΔP. All pressures are normalized by ΔP. $\bar{P}_{g_o}$ is the initial normalized gas pressure in the bubble. Thus,

$$T_o = r_{b_o} \rho^{1/2} / (\Delta P)^{1/2} \quad , \quad (3.2)$$

$$\bar{P}_{g_o} = P_{g_o} / (\Delta P) \quad , \quad (3.3)$$

$$\bar{P}_\infty(t) = (P_\infty(t) - P_o) / (\Delta P) \quad . \quad (3.4)$$

The Weber number is related to the surface tension, γ, ΔP, and r_{b_o} by:

$$W_e = r_{b_o} \cdot (\Delta P) / 2\gamma \quad . \quad (3.5)$$

The noncondensible gas pressure inside the bubble, P_g, is assumed to have a polytropic behavior, $P_g \, a_o^{3k} =$ constant, where k is the polytropic coefficient ($1 < k < c_p/c_v$).

For a given $P_\infty(t)$, Equation (3.1) can be solved for the variation of the bubble radius, $a_o(t)$. This allows the subsequent determination of the pressure field around the bubble of center B^i, by the use of

$$P_o(B^i, r, t) = \bar{P}_\infty(t) + r^{-1} (2 a_o \dot{a}_o^2 + a_o^2 \ddot{a}_o) - a_o^4 \dot{a}_o^2/2r^4, \quad (3.6)$$

where r is the distance between B^i and a given point M in the fluid.

3.3 Interactions

When interactions cannot be neglected, but an "inner region" enclosing the bubble B^i can still be defined, the boundary conditions at infinity can be much more complex. First, the macroscale pressure in the cloud at B^i, $P(B^i, t)$, can be very different from the imposed far field pressure $P_\infty(t)$. Second, a relative velocity between the bubble and the surrounding fluid, $U(B^i, r, t)$ can exist causing the bubble to be nonspherical. Both P and U can be determined only by solving the equations of motion of the two-phase medium (see Section 7.0). In this section we will limit ourselves to a small perturbation theory whose interest will be to give the behavior of the solution when the perturbation grows continuously. In that case $P(B^i, t)$, which is the driving pressure for the collapse of the bubble B^i, is only a perturbation of the imposed far field pressure, $P_\infty(t)$, and $U(B^i, r, t)$ is a perturbation of the spherical velocity due to the bubble volume variation.

If we assume that the liquid flow is irrotational, we can define a velocity potential for the macroscale ("outer problem"), $\phi(B^i, t)$, and a velocity potential for the microscale ("inner problem"), $\phi^i(B^iM, t)$ such as:

$$\Delta\phi = \Delta\phi^i = 0 \quad (3.7)$$

The matching condition between these two potentials expresses the at-infinity conditions for ϕ^i, and replaces the conditions on $P(B^i, t)$ and $U(B^i, r, t)$. This is written:

$$\lim_{\substack{\vec{B^iM} \to \infty}} \phi^i(\vec{B^iM}, t) = 0 + \varepsilon\, \phi_1(B^i, t) + \varepsilon^2 \phi_2(B^t, t) + \ldots \tag{3.8}$$

Since bubble interactions vanish when ε goes to zero, in the absence of relative velocity between the surrounding fluid and the bubbles in the cloud, $\Phi_o \equiv 0$. Φ_1, Φ_2, ... are the contributions of the whole cloud to the boundary condition at infinity for the inner problem (i). Using the results obtained with the interaction of two bubbles (Chahine and Bovis, 1981) and the property of addition of potential flows, this condition can be written:

$$-\lim_{r \to \infty} \phi^i(B^iM, t) = \sum_{j=1}^{N} \left[\left(\frac{\ell_o}{\ell_o^{ij}} \right) \left(\varepsilon\, q_o^j + \varepsilon^2\, q_1^j + \varepsilon^3\, q_2^j + \ldots \right) + \right.$$

$$+ \left(\frac{\ell_o}{\ell_o^{ij}} \right)^2 \left(\varepsilon^2\, q_o^j + \varepsilon^3\, q_1^j + \ldots \right) \quad r \cos\theta^{ij} +$$

$$\left. + \left(\frac{\ell_o}{\ell_o^{ij}} \right)^3 \left(\varepsilon^3\, q_o^j + \ldots \right) \quad r^2\, \mathcal{P}_2\, (\cos\theta^{ij}) + \ldots \right] \quad . \tag{3.9}$$

where the superscript (j) denotes quantities corresponding to the other bubbles, B^j. ℓ^{ij} is the initial distance between the bubble centers B^i and B^j. θ^{ij} is the angle MB^iB^j, and r the distance B^iM, where M is a field point in the fluid (see Figure 3-1). $\mathcal{P}_n(\cos\theta)$ is the Legendre polynomial of order n and argument $\cos\theta$. q_n^j is the correction of order ε^n of the strength, $q_o^j = \dot{a}_o^j\, (a_o^j)^2$, of the source representing

the first-approximation spherical oscillations of the bubble B^j.

Expressed in physical terms (velocities, pressures), the boundary condition (3.9) states that the first order correction, (ε), to the nonperturbed spherical behavior, $a_o(t)$, of the bubble B^i is a spherical modification of the collapse driving pressure. This would introduce, as for two bubbles, a spherical correction $a_1(t)$ of the variations $a_o(t)$. At the following order, (ε^2), a second correction of the uniform pressure appears, as well as a uniform velocity field accounting for a slip velocity between the bubble and the surrounding fluid. Again, as in the two-bubble case, this induces a spherical correction, $a_2(t)$, of $a_o(t)$, and a nonspherical correction $f_2^i(t) \cos\theta^{ig}$, where θ^{ig} is a direction to be determined from all the θ^{ij}. Things become more complex at the order of expansion ε^3, where in addition to the uniform pressure and velocity corrections, $a_3^i(t)$ and $f_3^i(t) \cos\theta^{ig}$, a velocity gradient is to be accounted for, to generate a nonspherical correction, $g_3^i(t)\ (3\cos^2\theta^{ig}-1)/2$.

As a result, the equation of the surface of the bubble B^i can be written in the form:

$$R\ \theta^{ij},\ t) = a_o^i(t) + \varepsilon\, a_1^i(t) + \varepsilon^2\ [a_2^i(t) + f_2^i(t) \cdot \cos\theta^{ij}] +$$

$$+ \varepsilon^3\ [a_3^i(t) + f_3^i(t)\ \cos\theta^{ij} + g_3^i(t)\ \mathcal{P}_2\ (\cos\theta^{ij})\ ] + \ldots, \quad (3.10)$$

where $a_o(t)$ is given by the Rayleigh-Plesset Equation (3.1), while the other corrections are obtained by solving the following differential equations in which the superscripts (i) are omitted for convenience:

$$a_o\ddot{a}_1 + 3\dot{a}_o\dot{a}_1 + a_1F_o(a_o, W_e, P_{g_o}, K) = \Sigma_j - \left(\frac{\ell_o}{\ell_o^{ij}}\right) \dot{q}_o^j \quad ,$$

$$a_o\ddot{a}_2 + 3\dot{a}_o\dot{a}_2 + a_2F_o + F_1(a_o, a_1, W_e, P_{g_o}, K) = \Sigma_j - \left(\frac{\ell_o}{\ell_o^{ij}}\right) \dot{q}_1^j \quad ,$$

$$a_o\ddot{a}_3 + 3\dot{a}_o\dot{a}_3 + a_3F_o + F_2(a_o,a_1,a_2,W_e,P_{g_o},K) = \Sigma_j - \left(\frac{\ell_o}{\ell_o^{ij}}\right) \dot{q}_2^j \quad ,$$

$$a_o\ddot{d}_2 + 3\dot{a}_o\dot{d}_2 = \Sigma_j - 3\left(\frac{\ell_o}{\ell_o^{ij}}\right)^2 (\dot{a}_oq_o^j + a_o\dot{q}_o^j) \quad , \qquad (3.11)$$

$$a_o\ddot{d}_3 + 3\dot{a}_o\dot{d}_3 + 3F_3(a_o, a_1)\, d_2 = \Sigma_j - 3\left(\frac{\ell_o}{\ell_o^{ij}}\right)^2 (a_oq_1 + a_o\dot{q}_1 + Fq_o^j) \quad ,$$

$$a_o\ddot{g}_3 + 3\dot{a}_o\dot{g}_3 - (\ddot{a}_o - 6/W_ea_o^2)\, g_3 = \Sigma_j - 5\left(\frac{\ell_o}{\ell_o^{ij}}\right)^3 (a_o^2\dot{q}_o^j + 2a_o\dot{a}_oq_o^j) \quad .$$

In these equations F_o, F_1, F_2, F_3 are known functions depending on the physical constants, W_e and P_{g_o}, and on the calculated preceding orders of approximation. The deformations f_2, f_3 of the bubble B^i and the motion of its center toward B^j, ℓ_2, ℓ_3, have been replaced by d_2, d_3 which indicate the total motion of the point E_i (Figure 3.1).

$$\dot{d}_2 = \dot{f}_2 - \dot{\ell}_2; \quad \dot{d}_3 = \dot{f}_3 - \dot{\ell}_3 \qquad (3.12)$$

When all the initial radii of the bubbles in the cloud are identical, these right-hand sides are obtained by multiplying the two-bubble case right-hand sides by one of the geometrical constants c_1, c_2, c_3:

$$c_1 = \Sigma_j \, (\ell_o / \ell_o^{ij}) \quad ,$$

$$c_2 = \Sigma_j \, (\ell_o / \ell_o^{ij})^2 \cdot \cos\theta^{ij} \quad , \qquad (3.13)$$

$$c_3 = \Sigma_j \, (\ell_o / \ell_o^{ij})^3 \cdot \mathcal{P}_2 \, (\cos\theta^{ij}) \quad .$$

We can now compute the behavior of B^i by solving the obtained differential equation using a multi-Runge-Kutta procedure. The behavior of the whole cloud can then be obtained.

Comparison of Equations (3.11) with those obtained in the case of two-bubbles shows that the N-bubbles in the cloud other than B^i can be replaced by a unique bubble of strength, q_n^{ig}, located at G^i, a distance ℓ_o^{ig} from B^i in the direction defined by the angle $MB^iG^i = \theta^{ij}$. As this equivalent bubble should induce the same pressure and velocities as defined by (3.9), its characteristics are obtained by the equations:

$$q_n^{ig} / \ell_o^{ig} = \sum_{j=1}^{N} q_n^j / \ell_o^{ij} \quad , \qquad (3.14)$$

$$\vec{e}_{ig} \cdot q_n^{ig} / (\ell_o^{ig})^2 = \sum_{j=1}^{N} \vec{e}_{ij} \cdot q_n^j / (\ell_o^{ij})^2 \quad , \qquad (3.15)$$

where $\vec{e}_{ig}$ and $\vec{e}_{ij}$ are unit vectors of the directions B^iG^i and B^iB^j respectively (Figure 3.1), and n is the order of approximation. These equations define the angle θ^{ig}, and the direction in which $d_n^i(t)$ is measured (Equations (3.10) and (3.12)).

3.4 Pressure Field

Once the "inner problems" are solved, the nondimensional outer potential, Φ, can be written:

$$\bar{\phi}(M,t) = -\Sigma_i \left[\frac{\tilde{q}_o^i}{\bar{r}^i} + \varepsilon \frac{\tilde{q}_1^i}{\bar{r}^i} + \varepsilon^2 \frac{\tilde{q}_2^i}{\bar{r}^i} + \varepsilon^3 \left(\frac{\tilde{q}_3^i}{\bar{r}^i} - \frac{\tilde{h}_2^i}{r^{i\,2}} \cos\theta^{ig} \right) + 0(\varepsilon^3), \right] \tag{3.16}$$

where bars denote nondimensional "outer" quantities, and tildes nondimensional "inner" quantities.

$$\bar{\phi} = \phi \cdot \varepsilon T_o / r_{b_o}^2, \quad \tilde{q}_n^i = q_n^i \cdot T_o / r_{b_o}^3, \quad \bar{r}^i = r^i / \ell_o \tag{3.17}$$

T_o is the characteristic time of the bubble collapse and r^i is the distance between a field point M and B^i. The Bernoulli equation enables one to calculate the pressure, P, using Equation (3.16). In the nondimensional form we have:

$$\bar{p}(M,t) = \frac{p(M,t) - P\infty(t)}{\Delta P} = -\varepsilon \frac{\partial \phi}{\partial t} - \frac{1}{2} \varepsilon^4 \left| \nabla \phi \right|^2 . \tag{3.18}$$

ΔP is the amplitude of the pressure driving the collapse and $t = t/T_o$, where

$$T_o = r_{b_o} \sqrt{\rho / \Delta p} \quad . \tag{3.19}$$

As an illustration, in a uniform field of bubbles any bubble has the same geometrical position relative to the others, and thus the same behavior. The general expression (3.8) simplifies considerably to become:

$$p(M,t) = (\varepsilon \dot{\tilde{q}}_o + \varepsilon^2 \dot{\tilde{q}}_1 + \varepsilon^3 \dot{\tilde{q}}_2 + \varepsilon^4 \dot{\tilde{q}}_3) \sum_i \frac{1}{\bar{r}^i} +$$

$$-\varepsilon^4 \dot{\tilde{h}}_2 \sum_i \frac{\cos\theta^{ig}}{\bar{r}^{i\,2}} - \varepsilon^4 \frac{\tilde{q}_o^2}{2} \cdot \left| \nabla \sum_i \frac{1}{\bar{r}^i} \right|^2 + O(\varepsilon^4) \,. \quad (3.20)$$

In this expression, the two first summations are geometrical constants similiar to c_1, c_2 (3.4). The last one is more complex, but is more easily calculated when written as follows:

$$\left[\bar{\nabla} \sum_i \frac{1}{\bar{r}^i}\right]^2 = \left[\sum_i \left(\frac{-1}{\bar{r}^{i\,2}}\right) \vec{e}^{im}\right]^2 , \quad (3.21)$$

where $\vec{e}^{im}$ is the unit vector of the direction $\vec{B^i M}$. If one knows the direction, MV_o, of the velocity at M, at the first order of approximation, and if α^{iv} is the angle $B^i M V_o$ (Figure 3.1), then:

$$\left[\bar{\nabla} \sum_i \left(\frac{1}{\bar{r}^i}\right)\right]^2 = \left[\sum_i \left(\frac{\cos\theta^{iv}}{\bar{r}^{i\,2}}\right)\right]^2 \quad (3.22)$$

In the general case when the bubbles do not all behave identically an expression similar to (3.20) applies in which the summation sign concerns not only the geometry but also the source and dipole intensities, q^i and h^i.

4.0 DYNAMICS PROBLEM: NUMERICAL STUDY AND RESULTS

4.1 Numerical Codes Developed

Several numerical codes have been developed during this study. For treating only dynamics (mass and heat transfer neglected), two main numerical programs can be distinguished: CLDSYM and MULTIBBL. Other programs were also implemented that are improvements or modifications of these two codes. The two main programs are distinguished by the cloud geometry: either symmetrical or arbitrarily described.

When all the bubbles have the same initial size, and when their initial geometrical configuration is symmetrical, they all behave identically by reason of symmetry. At a given order, all the functions q_n^j, which appear in Equation (3.9) are the same. Therefore, the summation applies only to geometrical constants which are known at the beginning of the computation and depend only on the bubbles' distribution. The three constants, c_1, c_2, and c_3, defined in (3.13) are then needed to compute the seven components of $R(\theta,t)$ up to the order ϵ^3 included. They are used as input to the numerical program dubbed CLDSYM, which uses a multi-Runge-Kutta procedure to compute the bubble motion as well as the generated flow and pressure field. Figure 4.1 shows a simplified flow chart of the numerical procedure.

When the bubbles have different initial radii, and when their distribution in the liquid does not correspond to any particular symmetrical configuration, the simplification described above does not apply. A second numerical program dubbed MULTIBBL has been developed for this more general case.

The flow chart in Figure 4.2 describes this program. In this flow chart Q_m represents the right-hand side of Equation (2), while q_m represents the strength of the flow sources obtained at the order of approximation m. This program allows the computation of more realistic cases where the bubble sizes and distribution are input and do not correspond to any idealized perfect configuration as with CLDSYM. More realistic pressures in the far field as well as on nearby walls are then obtained since the different bubble collapses are not in phase as for the case of a symmetrical configuration of equal sized bubbles.

A third program dubbed CLDMAIN2 was implemented for the cases where the computation spans over several thousand times the bubble characteristic time. This program adapts a variable time step scheme to the symmetrical bubble cloud case. An England Runge-Kutta procedure is used. This method computes the numerical errors introduced at each time step and determines the time increment needed to both minimize computation time and to not exceed an imposed acceptable margin of error. A major advantage of this code is its capacity to describe very rapid bubble radius variations such as occurs during strong explosive growth or collapse. This code was used for the analysis of bubble dynamics in a venturi cavitation susceptibility meter and about a hydrofoil.

A fourth program dubbed MULTICOMP was derived from MULTIBBL and employs a finite sound speed input. The information propagation from one bubble to another is retarded by an amount equal to the ratio between the interdistance and this finite sound speed. This program was used to study the influence of time lags creating phase differences between bubble oscillations.

These four programs were used to analyze several variables. The objectives of exercising these programs were to debug them, demonstrate their performance, and obtain trends of behavior. Below we illustrate some of the results obtained in order to gain some understanding of the behavior of a bubble cloud and how it differs from the behavior of isolated bubbles. The influence of the main parameters will be stressed.

4.2 Preliminary Discussion on Bubble Interaction

It is helpful, in order to understand the various numerical results, to consider the pressure field generated by the collapse of an individual bubble. Let us consider the pressure history at a point M at a distance ℓ_0 from an isolated bubble when the ambient pressure is submitted to a sudden pressure jump. As we can see from Figure 4.3, the resulting perturbation pressure, i.e., the difference between the pressure at ℓ_0 and the far field pressure, is negative for $t<0.75$ for the considered case. Later, for $t>0.75$, the pressure at ℓ_0 increases rapidly to 2.3 times the imposed pressure at the end of the bubble collapse. This observation is a key to the understanding of multibubble behavior in a sudden pressure increase. Indeed, if a fictitious bubble which does not influence the process is centered in B_1, it will first sense a less important and more gradual increase in the surrounding pressure at the beginning of the collapse. In the case considered (Figure 4.3), instead of a nondimensional surge of the pressure from 0 to 1, P jumps only to 0.84 then rises slowly, not attaining 1 until $t=0.75$. This induces a relative decrease in the intensity of the first phase of the bubble collapse and affects the bubble radius variation with time

exactly as seen later in Figure 4-6. Later, the sharp rise in the pressure field makes the subsequent end of the collapse much more violent.

Figure 4-4 illustrates the case where the ambient pressure field is modified by the collapse of more than one bubble. This figure is intended to explain both cumulative effects due to a multibubble system and modification due to different bubble size, bubble interdistance, and delay times (compressibility) effects. The figure illustrates these effects by considering two bubbles. Had the two bubbles, A and B, been of the same size and at equal distance from M, the two corresponding pressure time profiles would have superimposed.
In this case, both effects described above (initial relative pressure reduction and subsequent dramatic pressure increase) will be doubled (without any additional consideration of the interaction such as modification of the pressure histories). The interaction between bubbles A and B would amplify the phenomena described above. Now, if bubbles A and B are either at a different distance from M or are not of equal size, the pressure profiles will not overlap. If they are of equal size but at different distances from M, the pressure peaks would occur simultaneously unless compressibility effects are included. A delay time corresponding to the difference in the travel paths will then occur between the two peaks.

From the above discussion it is evident that the behavior of a fictitious bubble located at M will strongly depend on both the sizes of the other interacting bubbles and their space distribution. Compressibility would have the same effect as a nonsymmetric bubble distribution in addition to its influence on

the collapse intensity and amplitude of the generated pressures. It would therefore tend to reduce the collective effect expected from the incompressible symmetrical case.

4.3 Simple Case of a Step Function for the Ambient Pressure Field

We consider a distribution of bubbles centered on the surface of a sphere, and we admit that each of the bubbles has the same position relative to the others. In this case the numerical computation time is reduced. As examples, we will consider the bubble behavior and the pressures generated for two types of ambient pressure time functions. In both cases the bubbles are at equilibrium with the ambient pressure, P_o, at $t = 0$. Then, in case A, the ambient pressure jumps to a new constant value, $P_o + \Delta P$, at the following instant. In the second case B, the imposed pressure drops first to a constant value, $P_o - \Delta P$, keeps this value until $t = \Delta T$, and then comes up again to the initial value P_o (Figure 4.5). As an illustration we will consider the pressures generated a) in the center of the sphere; b) at the location of the bubble B^i if it were removed and c) at a point outside the cloud at a distance r_{b_o} from B^i. We will compare the results with the isolated bubble case.

Knowing the initial bubble configuration and thus c_1, c_2, and c_3 the relation between the cloud radius, R, and ℓ_o is: $R = 1/2\ \ell_o\ c_1/c_2$. In the cloud center, position (a), the three summations in (3.20) have, respectively, the values N/R, N/R, and 0. In position (b) these values are c_1, c_2, and c_3, and at a distance r_{b_o} from B^i the values are approximated by $c_1 + \varepsilon^{-1}$, $c_2 - \varepsilon^{-2}$, and $(c_2 + \varepsilon^{-2})^2$.

Various spherically symmetrical cloud configurations were investigated numerically. In Figure 4.6 the results of five different computations for a sudden jump in the imposed ambient pressure are compared, expansions being conducted up to ϵ^3. The ratio, $\epsilon = r_{b_o}/\ell_o$, was kept constant and at a value of 0.05. The cases of two, three, and twelve bubbles are presented together with that of an isolated bubble. The fifth case is an intermediate situation between the configurations of three and twelve bubbles. This case is arbitrary and is only determined by the choice of c_1, c_2, and c_3. In each case the variation with time of the distance, B^iE^i, between the extreme point on a bubble E^i, and its initial center, B^i, is chosen to represent the bubble dynamics. Taking the bubble collapse in an unbounded fluid as reference, it is easy to see from Figure 4.6 how increasing the number of bubbles changes the dynamics of the one studied. We can observe first that, during the early slow phase of the implosion process, the collapse is significantly delayed. At any given nondimensionsal time the distance between B^i and E^i (and simultaneously the bubble characteristic size) is greater when the number, N, of interacting bubbles increases. Then, in the final phase of the implosion the tendency is reversed: the phenomenon speeds up and, in a shorter total implosion time, the final velocities of the motion are higher when N increases. The effect is explained by accounting for the modification of the driving pressure of the collapse of any bubble due to the dynamics of the other bubbles as described in Section 4.2.

Figure 4.7 shows the behavior of the bubbles in the case of a pressure variation of type B (Figure 4.5). The cases of an isolated bubble and two, three, five, and twelve bubbles are investigated again, and the variations of B^iE^i with time are

represented. The ratio ε and the duration ΔT of the pressure drop are kept constant and at the particular values of 0.1 and 0.8 respectively. Here, as in the preceding figure, noticeable changes can be observed when the degree of interaction increases. First, the growth is slowed down and retarded in comparison with the isolated case. Then, the collapse is accelerated and as a result the total implosion time decreases with an increase in the number of bubbles, N. While for N = 2, the total implosion time is greater than that of an isolated bubble, for N = 12 the time is significantly smaller. As we will see below this acceleration of the collapse makes the generated pressures at the end of the collapse higher than for the single bubble case.

Figure 4.8 compares for the same cloud configuration (twelve bubble, $\varepsilon = 0.1$) the bubble behavior for three values of the duration, ΔT, of the pressure drop. The greater ΔT is, the longer the bubble is allowed to grow. As a result the maximum size it attains is bigger, but its lifetime is smaller. Thus, the resulting collapse is much stronger.

As explained in Section 4.2, using Figure 4.3, the observations made above for a sudden pressure jump can be explained by considering how the presence of a reacting bubble modifies the local pressure field from that imposed at infinity. The same type of reasoning can be applied to the case of a finite-time pressure drop. As we can see in Figure 4.9, in the first time period, ΔT, the pressure sensed at a distance ℓ_o from the bubble center, B_o, is higher than the imposed one. As a result, a second fictitious bubble placed at this distance from B_o would have a slower growth during this first period, ΔT. This phenomena is however reversed in the second

phase as an expansion wave is generated by the growing bubble B_o. In the third and last phase a compression wave increases the driving pressure for collapse making this one more intense.

In Figure 4.10, we see an example of the pressures generated during the bubble history at two locations: a) the center of the cloud and b) the center of one bubble, B^i, in its absense. These pressures are compared with those generated during the growth and collapse of an isolated bubble at a distance equal to the spherical cloud radius. We have selected the case of a finite time, $\Delta T = 0.6$, pressure drop. The same observations made while interpreting Figure 4.9, can be repeated here but with much more accentuated values of the pressure rises. After the imposed ambient pressure increases, the nondimensional pressures generated by the twelve bubble cloud are first positive, then a pressure expansion period is observed for $1.9 < t < 3.4$, followed by a high pressure surge at the end of the collapse. The corresponding bubble radius variation with time is that represented in Figure 4.8 (12 bubbles $\Delta T = 0.6$).

Figure 4.11 is a collection of the results obtained from several cases studied. The maximum nondimensional pressures generated during the cloud collapse are represented versus the number of bubbles in the cloud. The cumulative effect is obvious since the values obtained vary over a range of several orders of magnitude. The numbers presented should not be considered accurate since other scales for times, pressure, and lengths are needed at the end of the collapse. Instead, they are presented here to give an indication of how tremendous pressures can be generated with an increasing number of interacting bubbles, and to give an idea of the trend of this increase. In this figure, the maximum pressures are presented

at the cloud center, C, at B^i when it is removed and at a distance r_{b_o} from the center of one of the bubbles in the cloud.

These results show the important role played by the gas content of the bubbles which was neglected in Mørch's contributions. Increasing P_{g_o} from 0.1 to 0.2 has dramatically reduced the generated pressures. This is mainly due to the cushioning effect of the gas which significantly reduces the velocities attained at the end of the implosion.

Another very interesting observation from Figure 4.11 is that the imposed pressure variation B (pressure drop of finite duration followed by a recompression) moves the maximum pressures generated at the end of the collapse toward much lower values than for pressure jump case A. This effect is not due to the apparent higher gas content in this case. Indeed, the value of P_g to consider for comparison purposes should be for all cases that at the start of the collapse -- when the bubble has its maximum volume. For example, for the case of twelve bubbles and a pressure drop ($\Delta T = 0.8$, $P_{g_o} = 0.53$) the value of R_{max}/R_o is 1.63 (Figure 4.7). Then, accounting for the gas expansion, the gas pressure at the beginning of the collapse is $P_g = P_{g_o} (1.63)^{-4.2} \simeq 0.07$. The effective gas content is thus smaller, and since the value of ε is bigger (0.2 instead of 0.1), the observed pressure drop is intrinsically related to the imposed pressure function. The pressure attenuation observed is explained by the initial influence of the cumulative effect on the bubble behavior in the cloud which is not the same at the start of the growth or at the collapse (Figures 4.3 and 4.9). In the classical pressure jump case the initial cumulative effect is to prevent the bubble size

from being small when the collapse pressure surge starts. Conversely, the initial cumulative effect in the second type of imposed ambient pressure (case B) is to reduce the size of the bubble when the collapse pressure surge occurs. As a result the potential energy for collapse in case B is relatively smaller.

Finally, Figure 4.12 shows the influence of the duration of the pressure drop on the maximum pressures generated. By applying the same reasoning as above to the initial gas pressures one can conclude that the increase of the maximum pressure with ΔT is mainly due to a decrease in the effective initial gas content at the start of the collapse since the maximum bubble radius increases with ΔT.

The above results show that even for very low void fractions, collective bubble collapse can generate pressures orders of magnitude higher than those produced by single bubble collapse. This would tend to explain the observed high erosion intensities and the bending of trailing edges. The cumulative effect comes from the fact that the interaction increases the driving pressure of collapse of each individual bubble. This augments the violence of its implosion and thus the interaction with the other bubbles. Thus, each bubble ends its collapse not under the effect of a pressure of the same order as the ambient, but orders of magnitude higher. This cumulative effect would not exist if the void fraction is high enough for the cloud to behave as a single bubble. This leads us to believe that there exists a critical value for the void fraction for maximum erosion.

4.4 Comparison to Spark Generated Simulated Multibubble Configurations

We describe in Section 8.0 some experimental tests conducted to simulate symmetrical bubble cloud configurations. A spark-generated bubble method is used in combination with high-speed photography and sound measurements. Bubbles were generated in the vicinity of complex wall configurations such that the generated bubble and its images in the walls comprise a symmetrical multibubble set. The ratio ε of bubble characteristic size to interbubble distance was varied by changing the distance between the electrodes and the walls. This parameter was one of the main measurable quantities in the experiments. The other parameters were bubble size history and pressure histories at selected points in the experimental tank. However, one key parameter which is not readily measurable is the gas pressure inside the generated bubble. Since knowledge of $\bar{P}_{g_o}$ is essential for any quantitative comparison with experiment, we have selected to use it as a free parameter and see if it is possible to match the experimental results by selecting a particular value of $\bar{P}_{g_o}$.

Figure 4.13 shows an example of the influence of $\bar{P}_{g_o}$ on the collapse of 4 bubbles (or a bubble in a two-dimensional corner). As mentioned earlier, the collapse is significantly softened when the initial gas pressure (or the initial amount of gas) in the bubble is increased (behavior similar to the isolated bubble case). The bubble oscillates smoothly for $\bar{P}_{g_o} \geq 0.15$, while a significant violent implosion is observed for $\bar{P}_{g_o} < 0.10$. This behavior is further enhanced for larger values of ε. This can be seen in Figure 4.14 for the same case of a four-bubble cloud ($\bar{P}_{g_o} = 0.1$), and in more

detail in Figures 4.15 and 4.16 for a twelve bubble configuration. These three figures show the behavior of a bubble in the cloud when either the bubble sizes are increased with the same spacing or the spacing is decreased for the same bubble size. First, the classical lenghtening effect of the bubble period is observed (Figure 4.15, $\varepsilon = 0.01$ and Figure 4.16, $\varepsilon = 0.02$). For larger values of ε, however, the same effect as an increase in the number of bubbles (Figure 4.6) is observed -- namely an initial slowing down of the collapse process followed by a very significant enhancement. As a result, the collapse time is shortened. For larger values of ε, $\varepsilon > 0.07b$ in Figure 4.15 and $\varepsilon > 0.14$ in Figure 4.16, the asymptotic method obviously fails. A reversal of the collapse process is observed and cannot be easily explained. There might be, however, some correspondance between these trends and the experiments which indicate the presence of an optimum value of ε for maximum collapse intensity (see Section 8.0).

Figures 4.17 to 4.19 attempt to quantitatively compare the theoretical model and the spark-generated bubble experiments. As mentioned earlier, the difficulty with the experiment is the inability to control, or even to simply measure, the initial gas pressure in the bubble. This raises some questions about the accuracy of the results obtained. With this in mind we ran several sets of numerical cases in which $\bar{P}_{g_o}$ and the number of bubbles was maintained constant and ε varied. In each case, the value of the normalized time at which the bubble radius achieved its first minimum was noted, and the values compared with the experimental observations. Figures 4.17 to 4.19 show plots of these values of the bubble "first period of oscillation" as function of ε. Even if the comparison does not seem to be very encouraging at first, a closer look enables one to make

several interesting observations. Oscillations in the theoretical curves indicating strong nonlinearities appear as for the experimental curves. This is particularily visible in Figure 4.17 for the case of a four-bubble cloud. These oscillations are particularily important when the initial normalized gas pressure $\bar{P}_{g_o}$ is high. The combination of the experimental points and the theoretical curves seem to indicate that for the four-bubble case $\bar{P}_{g_o}$ was in the range 0.1 to 0.2. Examination of Figures 4.18 and 4.19 indicate lower values for the two other series of experiments -- simulated eight-bubble case (bubble in a three-dimensional corner) or twelve-bubble case (bubble in a pyramidal corner). A value lower than 0.1 seems to apply for Figure 4.19, and $\bar{P}_{g_o} \simeq$ 0.05 seems to apply to Figure 4.18. These differences with the same spark generation system in the same work conditions can be related to different degrees of water degasing, or to the rearrangement of the electrodes between one set of experiments and another. Scatter and/or oscillations of the results seem to be reduced with $\bar{P}_{g_o}$. However, the general trend of the existence of minimum values of bubble oscillation period or higher collapse pressure (see Section 8.0) seems to be confirmed by both theory and experiment. Shima, et al. (1983) have made similar observations for another range of values of ε, $\varepsilon \geq 1$.

4.5 Study of Multibubble Dynamics in a Venturi Cavitation Susceptibility Meter

4.5.1 Introduction

The development of techniques to measure cavitation nuclei distribution in laboratories and oceans has been intensified in recent years. Review studies on the subject have been presented

recently by Shen and Peterson (1983) and Billet (1984). One of the devices being developed and to which the multibubble study will be applied here is the Cavitation Susceptiblity Meter (CSM). This is a venturi system with a specially tailored geometry for cavitation nuclei measurements (Oldenziel, 1982 and Lecoffre and Bonnin, 1979). Microbubbles entering the venturi grow at the throat and are detected either optically or acoustically. In the first case they have to exceed a certain size to be perceived, while in the second case the noise generated during the implosion of these bubbles has to exceed a certain acoustical level. Therefore in this method a "critical pressure", P_{cr}, at the venturi throat, below which cavitation events are detected by the CSM, is measured.

The classical cavitation number, σ, (Thomas number) has been widely used in scaling cavitation inception between model and prototype:

$$\sigma = \frac{P_\infty - P_v}{\frac{1}{2} \rho V_\infty^2} \quad . \qquad (4.1)$$

In this expression P_∞ and V_∞ are the characteristic pressure and velocity, ρ the liquid density, and P_v the liquid vapor pressure. This definition assumes that cavitation inception occurs when the liquid pressure drops below vapor pressure. However, it has been recognized for a long time, using static equilibrium theory, that there exists for each initial nuclei size a critical pressure, usually much lower than p_v, below which unstable bubble growth occurs. Since in a liquid, nuclei are distributed in a relatively wide range of sizes, the definition of a "liquid critical pressure" can only be done by introducing an inception criterion such as a threshold amplitude

and rate of the detected cavitation "events." It has been demonstrated experimentally that if p_v is replaced by such a "critical pressure" of the liquid, the correlation of cavitation inception observed experimentally between different model sizes is greatly improved (Keller, 1984). It is implied that by doing so one accounts for differences in the nuclei population without having to determine the actual bubble size distribution. With the CSM a "critical pressure" at the venturi throat is determined by varying the throat velocity and counting the occurrence of cavitation bursting optically or acoustically. If, in addition, there exists a thorough theoretical knowledge of the relationship between fluid flow characteristics, nuclei initial size and needed critical pressures to initiate cavitation events, the CSM might be useful as a bubble nuclei size detector. Thi section attempts to improve on this knowledge by considering bubble dynamics and interactions between bubbles and with the main flow into the venturi. This investigation is to be added to earlier studies by d'Agostino and Acosta (1983) and Shen and Gowing (1984).

Cavitation susceptibility meters are designed in such a way that when in operation there is only one bubble in the venturi throat at a given time (See, for instance, the paper of d'Agostino and Acosta, 1983). However, in practice multibubbles appear occasionally in the venturi and invalidate the method of detection. In this section multibubble interaction is included in the study of cavitation inception in the CSM venturi system, and its influence on the inception criterion is investigated.

Due to the restriction of the pipe wall, the velocity field and the pressure field in a venturi system are altered when the microbubbles begin to grow. This subject has been studied by

d'Agostino and Acosta (1983) for a single spherical bubble entering from a reservoir into a semi-infinite pipe of constant cross-section. In the present paper we consider the case where multiple bubbles are present in a venturi and we derive an expression for the pressure correction due to the wall restriction. This correction is included as an option in the symmetrical multibubble code, CLDMAIN1, when the bubbles are grouped together as a cloud. The growth and collapse of a single bubble and multibubbles in a venturi system with contraction, throat, and diffuser zones of various diameters are computed considering the venturi wall restriction.

4.5.2 Single Bubble Static Equilibrium and Dynamics

We have earlier defined the critical pressure of a liquid as the pressure (or tension) below which significant bubble growth or activity is detectable. In fact, as can be deduced from the dynamic stability analysis of the static equilibrium of isolated spherical bubbles, there is a different critical pressure for each initial bubble size considered. The balance of pressure across the bubble interface can be written:

$$P = P_v + P_g - 2\,\gamma/R \quad , \qquad (4.2)$$

where P is the ambient pressure, P_v and γ are the liquid vapor pressure and surface tension and R is the equilibrium bubble radius. P_g is the pressure of noncondensible gas inside the bubble. If we neglect gas diffusion (see Section 6) we can assume that the gas behaves ideally with the law of compression:

$$P_g\, R^{3K} = \text{Constant} \quad , \qquad (4.3)$$

the polytropic constant K lies between 1 (isothermal case) and c_p/c_v (adiabatic case). The relationship between the ambient pressure, P, and the equilibrium radius, R, is therefore univocally defined for a given reference value R_o, or P_{g_o},corresponding to a reference pressure P_o:

$$P = P_v + P_{g_o} \left(\frac{R_o}{R}\right)^{3K} - \frac{2\gamma}{R} \quad , \qquad (4.4)$$

with

$$P_{g_o} = P_o - P_v + \frac{2\gamma}{R_o} \quad . \qquad (4.5)$$

Figure 4.20 shows an example of the static equilibrium curves P(R) for the isothermal case, K = 1.

The unstable portions of these curves correspond to $dP/dR > 0$, while the critical pressure, P_{cr} and radius, R_{cr}, are given by $dP/dR = 0$. These critical values are related to each other and to the initial conditions by the relations:

$$R_{cr}^{3K-1} = \frac{3K\ P_{g_o}\ R_o^{3K}}{2\gamma} \quad , \qquad (4.6)$$

$$P_v - P_{cr} = \frac{3K-1}{3K} \cdot \frac{2\gamma}{R_{cr}} \quad . \qquad (4.7)$$

Therefore a bubble of initial size R_o at the ambient pressure P_o would explosively grow (no static equilibrim) if the pressure around it drops below P_{cr}. One should note that P_{cr} is always lower than P_v and tends toward it when R_o is very large.

A question of great interest to the venturi CSM as an eventual bubble size detector is, for a given reference pressure P_o (depth of submergence) and throat velocity V_t, what is the initial radius of the bubble or nucleus which would reach the critical size at the throat pressure, P_{th}? All bubbles of larger radius would then be unstable, while smaller bubbles would remain undetectable. In terms of the maximum throat velocity (accounting for pressure loss by viscous effects) P_{th} can be written

$$P_{th} = P_o + \frac{1}{2} C_{pmin} \rho V_t^2 \quad , \qquad (4.8)$$

and the relation between R_o and the critical throat velocity, V_{tc}, is

$$P_{th} - p_v = P_o + \frac{1}{2} \rho C_{pmin} V_{tc}^2 - P_v$$

$$= \frac{2\gamma(1-3K)}{3KR_o} \; 3K + \left[\frac{3KR_o (P_o-P_v)}{2\gamma}\right]^{\frac{-1}{3k-1}} . \qquad (4.9)$$

For a given critical throat velocity, V_{tc}, any bubble larger than R_o would grow explosively. Conversely for a given bubble size any V_t larger than the critical velocity would render the pressure at the throat below the bubble critical pressure. Figure 4.21 shows the relationship between R_o and V_t for various ambient pressures and for K = 1.4. Note the sensitivity to the critical velocity for relatively "large" radii (e.g., $R_o > 1$ μm). Very small changes in V_t induce large changes in R_o. This underlines the major practical problem in the use of the CSM as a bubble size detector. Much less sensitivity would be obtained if P_{th} were the variable controlled in the experiments (see Figure 4.20).

The original concept for the use of the venturi cavitation susceptibility meter was based on the above static equilibrium approach. Actually, the above reasoning can be invalidated when bubble dynamics is taken into account in the two following configurations (Darrozes and Chahine, 1983):

a. The pressure in the throat drops below the critical pressure but the considered bubble does not remain long enough in this region to grow explosively.

b. The imposed pressure is always above the critical pressure but pressure variations are great enough for an intense collapse and therefore a strong acoustical signal to be generated.

In order to account for the above phenomena, the complete bubble dynamical equation must be solved for the particular venturi CSM pressure field. In the case of a single bubble of negligible size compared to the throat diameter, the classical Rayleigh-Plesset equation adequately describes the bubble radius variations. The external pressure in this equation, P(t), is the pressure "felt" by the bubble during its traverse of the venturi. It is the pressure in the liquid in the absence of the bubble at the location of its center. The bubble position x(t) is obtained from the bubble translation velocity $V_b(t)$

$$x(t) = \int_o^t V_b(t)\, dt \quad . \qquad (4.10)$$

If we neglect relative velocity between the bubble and the liquid, V_b is the fluid velocity which varies along the venturi. Actually the slip velocity could be important and should be included in future developments of this study (see Section 4.5.5).

When the bubble growth rate is large enough to significantly modify the liquid flow rate into the venturi, the pressure field in the venturi has to be modified to account for the resulting pressure variations. Similarly, the Rayleigh Plesset equation alone is not adequate to describe the case where interaction between several bubbles crossing simultaneously the venturi is considered.

4.5.3 Multibubble Interaction with Venturi Mean Flow

Under the basic assumption of small bubble radius size relative to bubble spacing and to flow characteristic length (for instance throat radius), in first approximation each bubble behaves independently and the basic flow is undisturbed by the presence of the cloud. With this approach and at this order of approximation, the pressure field to which each bubble in the cloud reacts is that existing at the location of its center in its absence. At higher orders bubbles interact with each other, and due to the restricted nature of the flow in the venturi they modify the main flow into the venturi. The influence of the cloud dynamics on the basic flow becomes important when the cloud volume rate attains a significant fraction of the mean volume flow rate. We will try here to account for this correction since its implementation is rather simple.

Let $\mathcal{V}(t)$ be the total volume of bubbles present at time t in the venturi (these bubbles could be either a certain number of isolated separated bubbles or a bubble cloud). The difference between the upstream and downstream flow rates into the venturi is equal to $\dot{\mathcal{V}}$. With a unidimensional approach to the venturi flow it is reasonable to write that the mean flow entering the venturi is then modulated as follows:

$$V_o = U_o - \alpha \dot{\mathcal{V}}/A_o \quad , \qquad (4.11)$$

where A_o is the area of the venturi at its entrance and U_o the undisturbed velocity at this location. α is the fraction of the displaced liquid volume rate due to the bubble which propagates upstream during the bubble growth. α needs to be determined with an additional equation not available presently. We will assume from here on that $\alpha = 0.5$. If all bubbles were concentrated at $x = X$ then, between the venturi entrance ($x = 0$) and X, the velocity in the venturi can be related to the undisturbed velocity U(x) by an relation equivalent to (4.11), valid in the small perturbation approach:

$$V(x) = U(x) - \frac{\dot{\mathcal{V}}}{2A(x)} \quad ; \qquad x \leq X \quad . \qquad (4.12)$$

If in addition the flow is assumed to be potential, then the velocity potential can be written:

$$\phi(x) = \phi_o(x) - \int_{-\infty}^{x} \frac{\dot{\mathcal{V}}}{2A(s)}\, ds \qquad (4.13)$$

Bernoulli's theorem between x and a field point upstream where the pressure is P_a and the fluid is at rest can be written:

$$\frac{P_a}{\rho} = \frac{P(x)}{\rho} + \frac{\partial \phi(x)}{\partial t} + \frac{1}{2}\left[\frac{\partial \phi(x)}{\partial x}\right]^2 \qquad (4.14)$$

We can now define a perturbation pressure p'(x) such that

$$P(x) = P_{st}(x) + p'(x) \quad , \qquad (4.15)$$

where P_{st} is the steady state pressure in absence of bubbles. Combining (4.13), (4.14), and (4.15) one obtains the following expression for p'(x) where a higher order term in $(\dot{\mathcal{V}}/A)^2$ has been neglected.

$$\frac{p'(x)}{\rho} = \int_{-\infty}^{x} \frac{\ddot{\mathcal{V}}}{2A(\alpha)}\, d\alpha + U(x)\, \frac{\dot{\mathcal{V}}}{2A(x)} \quad . \qquad (4.16)$$

In a matched asymptotic approach the imposed pressure field around any bubble or cloud at location X is given by (4.15), and for the corresponding first order bubble the imposed pressure term combines the undisturbed pressure in the venturi at the bubble location and the correction p'(x) given by (4.16).

If the bubble cloud is composed of N bubbles of equal size then

$$\mathcal{V} = 4\ \pi\ NR^3/3 \quad , \qquad (4.17)$$

and the Rayleigh Plesset equation becomes:

$$\rho\ [R\ddot{R} + \frac{3}{2}\ \dot{R}^2] + 4\mu\ \frac{\dot{R}}{R} = P_{g_o}\left(\frac{R_o}{R}\right)^{-3K} + P_v - \frac{2\gamma}{R} +$$

$$- \left[P(X(t)) + 2\pi\rho N \left(\frac{\bar{R}^2\dot{R}U(X)}{A(X)} + \int_{-\infty}^{X} \frac{2R\dot{R}^2+R^2\ddot{R}}{A(x)}\, dx\right)\right]. \qquad (4.18)$$

D'Agostino and Acosta (1983) derived a similar equation for a semi-infinite pipe of constant cross section A_o. Equation (4.18) combined with the system of Equations (3.11) can be solved numerically using a multi-Runge-Kutta procedure, to investigate interaction of bubbles with the venturi main flow and with each other.

4.5.4 Numerical Results and Interpretation

A series of computer runs were made using the above described method. The objective of this investigation was to

compare the behavior of an isolated spherical bubble with that of a bubble in a cloud. Both sets of cases were considered for the NSRDC venturi shown in Figure 4.22 with and without pressure correction due to the modification of the mean flow by the presence of the bubbles. The results obtained are illustrated in the following examples and figures. Due to viscous effects a C_{pmin} of -1.22 was measured at NSRDC for this venturi (see Shen, et al., 1984) and was accounted for in the following computations.

The bubble wall motion during its traverse through the venturi is illustrated in Figure 4.23 for a bubble of 10 μm initial radius. In most cases computations were started at the throat entrance (X = 0.825 cm) in order to reduce computation time. This is acceptable since comparative tests have shown that no significant error is then introduced. A typical bubble radius history can be described as follows. Near the throat entrance the bubble radius oscillates for a certain number of cycles which decreases with increasing flow velocity. Then, if this velocity is large enough a continual growth is observed until the bubble reaches the venturi expansion area. This is followed by a more or less violent bubble implosion which may be detected acoustically. Since this behavior is primarily controlled by a balance between gas pressure inside the bubble and the imposed ambient pressure, a key factor is the polytropic constant, K. The isothermal case (K = 1) is the most easily manageable mathematically and has therefore been studied by many investigators. Its use is justified when the bubble wall motion is slow enough so that the gas temperature remains constant. However; the value of K can vary widely during the bubble history (see Plesset and Prosperetti, 1977 and Section 6). Figure 4.23 shows the importance of K by comparing

the results for the two classical values of K: 1 and 1.4. Larger maximum radii are obtained with K = 1. Two velocities at the throat are also considered in Figure 4.23. Here we see that for a slight variation of V_t the maximum bubble radius can be doubled. Therefore, if the criterion of cavitation inception is thatbubble radius exceeds, let us say, 150 μm then V_t = 25.0 m/s would be below inception and V_t = 25.2 m/s would be slightly above it. The static equilibrium curves (Figure 4.21) derived from Equation (4.9) give, however, a lower value for the critical throat velocity, V_t = 24.95 m/s. This relatively small difference of about 0.8 percent is significant for the precision needed in the measurement of V_t in order to use the CSM venturi effectively. Note that if the throat velocity at inception was 24.95 m/s the critical pressure would be -500 pascals while one obtains -8000 pascals with 25.2 m/s. The difference in P_{cr} is therefore very significant between the static and dynamic approaches.

Figures 4.24 and 4.25 show the maximum size attained by a bubble crossing the venturi CSM as a function of the velocity at the throat. Bubbles of different initial sizes at the same initial reference pressure are considered. Single bubble results are compared with symmetrical multibubble configurations. Several very interesting observations can be made from studying these figures and the corresponding numerical results. Bubble size scaling effects are observed as follows. At the lower velocities bubbles exhibit an oscillatory behavior all the way through the venturi (e.g., V_t < 25.1 m/s for R_o = 5 μm; V_t < 24.8 m/s for R_o= 20 μm). Their radius oscillates between a fraction of R_o and a maximum radius of a few times R_o. At the higher velocities the bubbles experience an explosive growth followed by a strong implosion. Bubble size

scaling effects are expressed by the fact that while initially larger bubbles have a larger growth rate at the low venturi throat velocities, the trend is reversed at higher velocities (Figure 4.24). The result of this scaling effect is that at large velocities (e.g., $V_t \simeq 25.8$ m/s for the cases considered) single isolated bubbles of 5, 20, and 50 μm initial size attain the same maximum size. This could be seen on Figure 4.24 where the dimensional variables are represented for the same data points as in Figure 4.25. This result is also related to the fact that the considered venturi has a long enough throat to allow the above bubbles to grow to significant sizes.

The effects of bubble interactions and restricted mean flow correction show up in a similar way when single bubble and multibubble results are compared. At lower velocities bubble oscillations in the throat area close to the entrance are amplified when the collective behavior of the bubble cloud is considered (see Figure 4.27 for details). As a result larger maximum sizes are obtained with multibubbles but also very early collapses are achieved in the throat section before reaching the expansion. At higher velocities the opposite phenomenon is observed. An explosive bubble growth is then achieved, and the multibubble effect is to inhibit the growth rate of each bubble in the cloud. This is mainly due to a reduction of the pressure drop around each bubble induced by the motion of the other bubbles. One can notice in both Figures 4.24 and 4.25 that while multibubble effects weakly modify the 5 micron bubble curves, a dramatic change is seen for the 20 micron bubble. In the latter case bubble interactions are much stronger and shift the behavior of the bubble from an explosive growth to strong oscillations which induce an early collapse even for velocities as high as 25.6 m/s. At higher values of ε (bubbles closer to

each other) this effect can be seen even for the 5 μm bubble at V_t = 25.8 m/s (case ε = 0.05 on Figures 4.24 and 4.25).

Figures 4.24 and 4.25 could also be used to determine dynamic cavitation inception. This could be done by using either an "acoustical" criterion, R_{max}/R_o greater than a certain value, or an "optical" criterion, the actual bubble size exceeding a given value. If we adopt criteria used earlier in the literature we have the following value for V_t at inception as compared to static equilibrium values.

Criterium	R_o μm	V_t Static m/s	V_t Single Bubble m/s	V_t 5-Bubble m/s
$R/R_o > 10$	5	25.08	25.17	25.13
$R > 150\,\mu m$	5	25.08	25.24	25.22
$R/R_o > 10$	20	24.89	25.13	25.70
$R > 150\,\mu m$	20	24.89	25.08	25.62

From the above table one can notice that predictions with static theory are conservative. For a given bubble size they show earlier inception. Similarly, for a given velocity, static theory predicts the activation of a broader range of nuclei. For instance, at 25.08 m/s all bubbles larger than 5 μm are predicted to be unstable while dynamics show that only those above 20 μm will be observed with the optical criterion. Larger differences between statics and dynamics result for the case of a multibubble system. One should however recognize that differences in V_t are relatively small especially when considering present practical considerations in the control of this velocity. On the other hand, note that the resulting critical pressure varies in a very wide range between the various approaches. The difference between these values is very

important to account for in cavitation tunnel tests where the ambient pressure is low. This encourages effort toward a better control of V_t or P_{cr}. This, as well as additional information given below, might explain the discrepencies between optical and CSM measurements of bubble distributions. Large size bubbles in a cloud formation are not excited at the velocities expected from static theory and are therefore not counted when interpreting experimental CSM results.

Figures 4.26 and 4.27 illustrate some details of the results presented in Figures 4.24 and 4.25. The influence of the velocity at the venturi throat on the dynamics of a bubble of initial radius 5 μm can be seen in Figure 4.26. One can observe an earlier explosive growth of the bubble at the higher velocity as well as the achievement of a greater maximum bubble radius. The bubble reaches its maximum size in the venturi diffuser zone after leaving the throat. This is due to its response time to a change in the ambient pressure. At higher velocities the maximum is achieved farther downstream. The influence of multibubble interaction and of restricted mean flow modification on the bubble dynamics can also be seen in Figure 4.26. The explosive growth, as observed in Figures 4.24 and 4.25, is inhibited by multibubble interaction more significantly at the higher velocities. The location, x, of maximum radius and the location of the collapse are then closer to the throat exit. This effect increases with the ratio between bubble size and distance, ε. For a larger ε the influence of oscillations is very much increased and the bubble collapses much earlier in the venturi throat (e.g., for $\varepsilon = 0.05$, the collapse is $x = 1.30$ cm instead of $x = 2.8$ cm).

Figure 4.27 shows the influence of the initial size of a bubble on its dynamics and the modification of the behavior by interbubble and mean flow interactions. All cases are considered for the same ambient pressure and throat velocity. The larger bubbles achieve their maximum size further downstream inside the venturi diffusion section. When interactions are considered the bubble of initial radius R_o = 5 μm has its behavior moderately modified, similar to what is shown in Figure 4.26. However, for the 20 μm bubble the modification of the behavior is dramatic. Large oscillations are induced through interactions and an early collapse at X ≈ 1.35 cm occurs inside the venturi throat. Such a bubble cloud would not be detected optically and probably not acoustically if the intensity of the collapse is not strong enough.

For the present user of the Venturi Cavitation Susceptibility Meter, the curves relating the initial radius of a detectable bubble to the critical velocity at the throat are the most useful. Figure 4.21 showed those curves based on static equilibrium considerations. Any bubble of initial radius larger than that given by these static predictions would grow explosively at the corresponding velocity. The discussions above pertaining to Figures 4.24 to 4.27 have shown that the problem is more complex when dynamics and interactions are taken into account. This fact can be illustrated, as in Figure 4.28, by comparing R_o versus V_t obtained by both static and dynamic considerations. Here one can observe significant discrepencies at the larger bubble radii and also at the higher velocities. Again these theoretical differences are relatively small when expressed in terms of V_t but reflect very large differences in the critical pressures. The most interesting results seems to be the presence of a minimum in the dynamic

curve. This implies that at a given velocity above a minimal value (25.1 m/s in the case of Figure 4.28) only a finite range of bubble radii are excited. Compare this prediction with the conclusion from statics that all bubbles above a critical radius become active. This may also explain the experimentally observed lower number of detected bubbles in the venturi CSM as opposed to the scattering method.

The information obtained in this work on bubble size history in the venturi as a function of the imposed flow conditions and initial bubble radii should be complemented and could be used to determine nuclei population. This could be implemented if the venturi CSM is instrumented to measure bubble sizes in the venturi at several locations. This could be done by simple optical sensors.

The analyses should be refined and extended to include bubble-liquid slip velocity and a fine description of bubble collapse. Slip velocity could modify the bubble time response and quantitatively change the results obtained. A precise description of the implosion would allow us to accurately compute the pressures generated and therefore would be very helpful for acoustic detection.

4.5.5 Extension of Study to the Flow Around a Hydrofoil

The program developed to study bubble behavior in a "slowly-varying" pressure field (relative to the bubble period of oscillation) has been extended from the venturi case to that of a hydrofoil. The program is CLDMAIN2. The user inputs the pressure profile in terms of coefficients of a polynomial. The study differs from that of the venturi by the fact that gravity

forces have been included. Therefore, slip velocity between the bubble and the surrounding liquid had to be included. This is obviously necessary if the bubble dynamics in the wake are to be monitored. The presence of gravity introduces also a modification of the input pressure field. The pressure driving the bubble behavior is now dependent on the position of the bubble relative not only to the foil but also to a free surface.

The balance of forces on the bubble is at each instant between buoyancy, drag, and acceleration forces. This can be written for a bubble of center B(t), radius a(t) and velocity $V_B(t)$:

$$\frac{2}{3}\ \pi\ a^3\ (\rho_\ell + 2\rho_g)\ \frac{dV_B}{dt} = 4\ \pi\ \mu\ a\ (V_B - V_\ell) - 2\pi\ a^3\ \nabla p + 2\ \pi\ \rho_\ell\ a^2\ \dot{a}\ (V_\ell - V_B) \quad . \qquad (4\text{-}19)$$

Here μ is the liquid viscosity, ρ_ℓ and ρ_g are the liquid and gas densities, ∇p is the pressure gradient and V_ℓ is the liquid velocity. These two are related by the approximate relation

$$\nabla p = dV_\ell/dt \quad , \qquad (4\text{-}20)$$

and for the present case (bubble behind foil)

$$\nabla p = -\ \rho g \ . \qquad (4\text{-}21)$$

Therefore, Equation (4.19) can be written in terms of the relative velocity, V_t.

$$\dot{V}_t = - \left[6 \frac{\nu}{a^2} + 3 \frac{\dot{a}}{a}\right] V_t + 2 g \quad , \qquad (4\text{-}22)$$

where ν is the liquid kinematic viscosity and

$$V_t = V_B - V_\ell \quad . \qquad (4\text{-}23)$$

Equation (4.22) was solved using a Runge-Kutta procedure similar to those used for the various bubble radius components and was implemented in CLDMAIN2. This implementation is in fact very similar to that needed for the general case of a slip velocity (due to inertial and drag effects) between the bubble and the surrounding liquid.

4.6 Asymmetric Bubble Cloud Configurations

In this section we present a few illustrations of multibubble dynamics when all bubbles in the cloud do not behave identically due to symmetry. To do so we have used the developed code MULTIBBL (see flow chart, Figure 4.2) in which the position and size of the bubbles are entered using cartesian or spherical coordinates. Figures 4.29 and 4.30 show the results for the simple example of a configuration of three bubbles of different sizes. The comparison between the bubble behavior when isolated and in the presence of the two other bubbles shows interesting results. When two large bubbles collapse in the presence of a smaller one, the rate at which their radii decrease with time is slightly reduced (Figure 4.29) and the oscillation period is increased. However, the behavior of the smaller bubble is dramatically modified. Following the end of the first collapse, the rebound of the bubble (due to the presence of noncondensibles) is much stronger and is presumably

intensified by the perturbation pressure field due to the two other bubbles' implosion (see Figure 4.4). Later the small bubble has a weak growth and implodes strongly for t~0.93 when the local pressure field attains a peak.

The case of two small bubbles and one large one (Figure 4.30) shows the same trends. However, in this case the large bubble is much less influenced by the presence of two smaller ones than by the presence of one smaller and one identical bubble as in Figure 4.29. The deviation of the small bubbles' radii from the isolated case is also much less dramatic.

Figures 4.31 and 4.32 address the question of the influence of cloud geometry (bubble space distribution) on cloud dynamics. Three multibubble configurations, all having the same global void fraction (total bubble volume over volume in which they are distributed), are compared. In the three cases, twelve bubbles of equal initial sizes (R_0=1) are located on or inside a sphere of nondimensional radius 15. In the first case, the centers of all twelve bubbles are located on the sphere of radius 15. In the second case, six are centered on the same sphere while the six others are on a concentric sphere of radius 7.5. The third configuration is composed of four bubbles centered on the outer sphere of radius 15, four others are centered on a sphere of radius 10, and the innermost layer of four bubbles is on a sphere of radius 5. Figures 4.31 and 4.32 show that the cumulative effect is greatly enhanced for the inner layer of bubbles. The initial weakening of the implosion as well as its later amplification are more pronounced (even for the outer shell of bubbles) when, for the same global void fraction, the number of shells is increased. Similarly in the

same cloud the effects are more pronounced for the inner-most layer of bubbles. Apparently, the predominant factor is the relative bubble size and spacing (parameter $\varepsilon = r_{b_0}/\ell_0$ in the theory). In both figures the formation of a reentering jet at each bubble's wall occurs when the radius becomes zero. The negative values seen in the figure are meaningless, and the computation should be stopped at that point. One can notice that this occurs much earlier for the shell closest to the cloud center (Figure 4.32).

Figure 4.33 is intended to show the capabilities of the program MULTIBBL as well as the complexity of the bubble behavior for a random bubble configuration. Here, twelve bubbles have been located randomly in a space enclosed within a sphere of radius 7. Similarly, the initial bubble radii were chosen in a random fashion between 0 and 1. Both these are shown via the table in Figure 4.34. We will not try to dwell too much on the interpretation of this figure since the randomness makes any rapid analysis empirical. As a general statement, we can say that while each bubble has the tendency to collapse at its own period of oscillation, the interactions make the behaviors at the rebounds, and the following collapses quite independent of the initial radius. In addition, the smaller the initial bubble size, the more influence of the interaction can be seen.

Figures 4.35-4.37 consider the case of the growth and collapse of a symmetrical configuration of six bubbles near a solid wall. A pressure drop of finite duration, $\Delta T = 0.8$, has been imposed on the six-bubble cloud. Four of the bubbles are in a plane parallel to the wall and at a normalized distance of 12.5 from this wall. The two last bubbles are on a line

perpendicular to the wall and are centered respectively at 5 and 20 bubble radii from the wall. The presence of the wall creates the asymmetry and shows three different behaviors of the initially identical bubbles. The geometrical configuration being such as described above, the four bubbles in the plane parallel to the solid wall behave identically (bubble 3 in the figure). The two remaining bubbles on the axis perpendicular to the solid wall have different behaviors. The bubble closest to the wall is bubble No. 1 in the figures and the farthest away is bubble No. 6 in the figures. Figures 4.35 and 4.36 indicate that the four bubbles in the midplane seem to be the most influenced by bubble interactions. They are followed by the bubble closest to the wall. This result is probably due to the fact that the distance to the wall is not small enough from the image cloud to influence the closest bubble in the analyzed case (bubble radii=1, location of centers on sphere of radius=7.5, and distance from wall=5).

The comparison between Figures 4.35 and 4.36 shows the influence of a finite sound speed in the liquid on the bubble radius history. For a normalized sound speed of 30 (actual speed = $30\ell_0/(r_{b_0}\sqrt{\rho/\Delta P})$), Figure 4.36 shows a weakened interaction compared to the infinite sound speed case. As discussed in Section 4.2, this is due to the fact that a finite sound speed induces a time delay between the emission of the pressure oscillations from one bubble and its arrival to another. The flow due to a point source of intensity q(t), for instance, at a distance r is $r^{-2}q(t-r/c)$ instead of $r^{-2}q(t)$. The result shown in Figures 4.35 and 4.36 is, however, not general since a time delay could, depending on its amount and the shape of the various bubble pressure functions,

act in such a way as either to intensify or dampen the implosion.

Figure 4.37 shows the shape of the bubbles at different times during the implosion process. The three bubble behavior types described above (four bubbles in the middle plane, farthest, and closest bubble to the wall) are shown side by side. These profiles give a better idea of the behavior and deformation of the three bubble types.

5.0 INCLUSION OF HEAT TRANSFER AT THE BUBBLE WALL: SUPERHEATED LIQUIDS

5.1 Introduction

Many modern processes deal with various fluids in conditions where both heat transfer effects and inertia contribute in controlling the bubble behavior. Examples of such fluids are hydrocarbons, liquid metals, cryogenic fluids,and demineralized hot water at temperatures as high as 300°C. Heat transfer boiling or cavitation appears with these liquids in such applications as high speed flows of sodium-cooled fast-breeder reactors in nuclear power engineering, circulation of cryogenic liquid in pumps in aerospace engineering, and flow of hot water in nozzles and tubes in steam power plants. Accidents, such as loss of vacuum insulation in cryogenic storage tanks and loss of coolant in nuclear power plants, are sources of boiling nucleation and of major safety concern (Plesset, 1980).

In the previous sections, we investigated analytically and numerically the collapse of a bubble cloud due to an increase of the ambient pressure neglecting heat transfer. A cumulative effect was shown leading to pressures generated during the collapse significantly larger than would be computed by adding the effects of individual bubbles. This explained the observations of the bent trailing edge of propellers subjected to cloud cavitation. In this section, we extend the singular perturbation approach earlier developed to study the cases where heat transfer effects cannot be neglected. We then investigate numerically the growth of a bubble cloud in a superheated fluid following a sudden depressurization. Both a general approach

and a thermal boundary layer approximation are studied analytically, and methods of numerical solution are described. Numerical computations are then conducted only for a symmetrical cloud bubble configuration with the boundary layer approximation and when deviations from sphericity are very moderate.

The general equations of the problem have been presented in Section 2.0 and will not be rewritten here. Similarly, we consider a singular perturbation theory as in Section 3.0 assuming a small ratio of bubble size to bubble interdistance.

5.2 Singular Perturbaton Approach

5.2.1 Normalizations

In order to make asymptotic expansions (and thus to compare orders of magnitudes) an accurate choice of characteristic scale variables is fundamental. For the length scales, we chose as in Section 3.0 the bubble characteristic radius r_{b_o} in the inner problem, and the interbubble distance ℓ_o in the outer. However, the relationship between r_{b_o} and the characteristic initial bubble radius, R_o, is not obvious. Indeed, while in the case of bubble collapse, the bubble radius stays of order R_o in the mathematical sense, ($R(\varepsilon) = O(R_o)$ if there exists a constant λ independent of ε such that $|R| < \lambda|R_o|$); such is not the case for the bubble cloud growth studied here. Therefore r_{b_o} is chosen arbitrarily much larger than R_o but such that the inequality

$$r_{b_o}/\ell_o = \varepsilon << 1 \qquad (5.1)$$

is valid. Consequently, the results of the computations will be valid only as long as the radius of any bubble in the cloud does not greatly exceed r_{b_o}.

The time scale choice is simple once r_{b_o} is known. In the case of a significant pressure drop, as for the problem of sudden depressurization of a superheated system, this time scale is related to the pressure drop ΔP, through

$$\tau_o = r_{b_o} \sqrt{\rho/\Delta P} \quad . \tag{5.2}$$

ΔP could also be the order of magnitude of the imposed pressure fluctuations when $P_\infty(t)$ is a prescribed function of time.

As mentioned earlier, in both the "inner" and the "outer" regions, the flow in the first approximation is that due to a distribution of dynamic sources and heat sinks. The characteristic strength of the dynamic sources is $q_o = r_{b_o}{}^3/\tau_o$, and depending on whether one considers the "inner" or the "outer" problem, the resulting velocity potential, Φ, has the scales:

$$\Phi_o^{in} = r_{b_o}{}^2/\tau_o \quad , \quad \Phi_o^{out} = r_{b_o}{}^3/\ell_o \tau_o \; . \tag{5.3}$$

Since the maximum temperature drop occurs near the bubble wall,and since a lower bound for this temperature is the boiling temperature of the liquid, T_b, at the imposed ambient pressure, P_∞, the temperature departure from T_∞ is scaled with the amount of superheat, $(T_\infty - T_b)$.

With these characteristic scales, nondimensional variables all of order unity are introduced through the following definitions, where bars denote outer nondimensional variables and tildes inner ones:

$$\tilde{r} = r/r_{b_o} \quad ; \quad \bar{r} = r/\ell_o \quad ;$$

$$\bar{\ell}^{ij}(t) = \ell^{ij}(t)/\ell_0; \quad \tilde{\dot{b}}(t) = \dot{b}\tau_0/r_{b_0};$$

$$\tilde{t} = \bar{t} = t/\tau_0; \quad \tilde{T} = \bar{T} = T/(T_\infty - T_b); \tag{5.4}$$

$$\tilde{p}(t) = \bar{p}(t) = p(t)/\Delta P \quad ;$$

$$\tilde{\Phi}(t) = \Phi^{in}(t)/\Phi_0^{in} \; ; \; \bar{\Phi}(t) = \Phi^{out}(t)/\Phi_0^{out}.$$

Each of the unknowns, X, is then expanded in a power series of ε as follows:

$$X = X_0 + \varepsilon X_1 + \varepsilon^2 X_2 + \varepsilon^3 X_3 + 0(\varepsilon^3). \tag{5.6}$$

5.2.2 First Order of Approximations (ε^0)

When ε goes to zero, the distance between bubbles goes to infinity, interactions vanish, and in the absence of a slip velocity between the test bubble and the surrounding fluid, the only boundary condition at infinity is the imposed ambient pressure variation $P_\infty(t)$. The "inner problem" is therefore spherically symmetrical and its solution is given by the well-known Rayleigh-Plesset equation. This can be written with the superscript (i) omitted for convenience:

$$\bar{a}_o \ddot{\bar{a}}_o + \frac{3}{2} \dot{\bar{a}}_o^2 = -\bar{P}_\infty(t) + \pi_o(t) - \frac{2\bar{W}_e}{a_0} \bar{\gamma}(t) - \mathscr{P} \quad . \qquad (5.7)$$

The nondimensional parameters are defined by the relations:

$$\bar{P}_\infty(t) = \frac{P_\infty(t) - P_\infty(o)}{\Delta P} \quad , \quad \mathscr{P} = \frac{P_\infty(o) - P_v(o)}{\Delta P} \quad ,$$

$$\pi_o(t) = \frac{p_v(t) - p_v(o)}{\Delta P} \quad , \quad W_e^{-1} = \frac{\gamma(o)}{r_{b_o} \Delta P} \quad , \qquad (5.8)$$

$$\bar{\gamma}(t) = \gamma(t)/\gamma(o).$$

Here $\gamma(t)$ and $p_v(t)$ are, respectively, the surface tension coefficient and the liquid vapor pressure at the bubble wall temperature at time t. The initial equilibrium condition at the bubble interface is

$$\mathscr{P} + 2W_e^{-1}/R_o = 0 \quad . \qquad (5.9)$$

For a given $P_\infty(t)$, equation (5.7) can be solved for the variations of the bubble radius, $a_0{}^i(t)$. This allows the subsequent determination of the higher order approximations of the bubble radius.

When the temperature at the surface of the bubble departs significantly from the ambient temperature, it is necessary to couple equation (5.7) with the energy equation to account for the dependence of p_v and γ on temperature. At this order, the problem is spherically symmetrical, and the energy equation, (2.5), reduces to the following nondimensional equation:

$$\frac{\partial \tilde{T}_o}{\partial \tilde{t}} - \frac{\tilde{a}_o^2 \dot{\tilde{a}}_o}{\tilde{r}^2} \frac{\partial T_o}{\partial \tilde{r}} = P_e^{-1} \frac{1}{\tilde{r}^2} \frac{\partial}{\partial \tilde{r}} \left(\bar{r}^2 \frac{\partial \tilde{T}_o}{\partial \tilde{r}} \right) \quad , \qquad (5.10)$$

where the Peclet number, P_e, is the ratio of the thermal diffusion time, $r_{b_o}^2/D$, to the bubble characteristic time τ_o,

$$P_e = r_{b_o}^2/(D\ \tau_o) \quad . \qquad (5.11)$$

The heat balance on the bubble-liquid interface reduces at this order of approximation to the following normalized equation

$$\frac{\partial \bar{T}_o}{\partial \tilde{r}} = \frac{\rho_v\ L\ r_{b_o}^2}{K\ \tau_o (T_\infty - T_b)} \cdot \dot{\tilde{a}}_o = \mathscr{A}\, \dot{\tilde{a}}_o \quad . \qquad (5.12)$$

5.2.3 Interactions

a. Order ε

In the asymptotic theory presented here, the local pressures and temperatures driving the growth of any bubble $B^{(i)}$ are a perturbation of the imposed far field pressure, $P_\infty(t)$, and temperature, T_∞. Since these perturbations are due to the presence of the other bubbles in the flow field, the leading terms can be obtained directly once the first order behavior of all the bubbles in the cloud is determined. For instance, once equations (5.7), (5.10), and (5.12) are solved, the variations with time of the radius, $a_0^j(t)$, of any cavity in the cloud are determined. This allows the determination of the intensity of all sources $q_0^j(t)$:

$$\tilde{q}_o^j(t) = \tilde{a}_o^{j\ 2}\ \dot{\tilde{a}}_o^j \quad . \qquad (5.13)$$

Consequently, the resultant "outer" potential flow is determined to this order by:

$$\bar{\Phi}_o(M, t) = \sum_{j=1}^{N} \frac{\tilde{q}_o^j(t)}{|\underline{MB}^j|} \quad , \tag{5.14}$$

where M is a field point, and B^j the center of the bubble $B^{(j)}$, and also the location of the source (j). The asymptotic expansions of $\Phi_0(M,t)$, when the normalized distance $|\underline{MB}^i| = \varepsilon r^i$ goes to zero, contain additional terms other than the leading source term, $q_0{}^i/r^i$, corresponding to the order zero "inner" potential flow,

$$\tilde{\Phi}_o^i = \tilde{q}_o^i(t)/\tilde{r}^i \quad . \tag{5.15}$$

These terms express the interactions and are responsible for the flow and bubble shape corrections. For instance, by application of the matching principle (n - m rule, Van Dyke, 1964), the order ε term will determine the boundary condition at infinity for the order ε "inner" velocity potential, i.e.,

$$\lim_{\tilde{r}^i \to \infty} \tilde{\Phi}_1^i = \sum_{j \neq i} \left(\frac{\ell_o}{\ell_o^{ij}} \right) \tilde{q}_o^j \quad , \tag{5.16}$$

where $\ell_0{}^{ij}$ is the initial distance between the two cavities' centers B^i and B^j.

In addition to the at-infinity boundary condition (5.16) the first correction, $\Phi_1{}^i$, of the undisturbed potential flow, $\Phi_0{}^i$, has to satisfy the Laplace equation, (2.1), as well as boundary conditions on the surface of the bubble $B^{(i)}$. These are the contributions to order ε of the expansions in powers of

ε of Conditions (2.2) and (2.3) made dimensionless. Similarly, the first correction, T_1, of T_o has to satisfy the equations derived from (2.5) and (2.7).

Due to Condition (5.16) the dynamic problem remains spherical. To this order the effect of the other bubbles does not introduce any asymmetries, and only changes the level of the velocity potential. Therefore, the correction at this order stems from a modification in the "inner" problem of the pressure imposed at infinity by the time derivative of the added at-infinity velocity potential, (5.16). As a result, the solution of the dynamic problem at order ε is given again by a source term which corrects the leading term $\Phi_0{}^i$. This solution can be written:

$$\tilde{\Phi}_1^i = \frac{\tilde{q}_1^i(t)}{\tilde{r}} + \sum_{j\neq i} \left(\frac{\ell_o}{\ell_o^{ij}}\right) \tilde{q}_o^j(t), \qquad (5.17)$$

where the source intensity, $q_1{}^i$, is given by:

$$\tilde{q}_1^i = \tilde{a}_o^{i\,2}\,\dot{\tilde{a}}_1^i + 2\tilde{a}_o^i\,\dot{\tilde{a}}_o^i\,\tilde{a}_1^i \quad . \qquad (5.18)$$

In order to satisfy the boundary conditions at the bubble surface, the first correction, $a_1{}^i$, of the bubble radius has to satisfy the following differential equation, where the superscript i has been omitted:

$$\tilde{a}_o\ddot{\tilde{a}}_1 + 3\dot{\tilde{a}}_o\dot{\tilde{a}}_1 + \tilde{a}_1(\ddot{\tilde{a}}_o - 2W_e^{-1}\tilde{a}_o^{-2}) = -\sum_{j\neq i}\left(\frac{\ell_o}{\ell_o^{ij}}\right)\dot{\tilde{q}}_o^j + \Pi_1(t). \qquad (5.19)$$

Here $\pi_1(t)$ is a correction of $\pi_o(t)$ and expresses the second approximation of the value of the vapor pressure at the bubble

wall. Using the expansions of the temperature in powers of ε as in (5.6), $\pi_o(t)$ and $\pi_1(t)$ can be expressed as

$$\pi_o(t) = \left[p_v(T_o(a_o,t)) - p_v(T_\infty) \right] / \Delta P \quad , \qquad (5.20)$$

$$\pi_1(t) = \left[p_v(T_1(a_o,t)) + a_1 \frac{\partial T_o}{\partial r}(a_o,t) \frac{dp_v}{dT}(T_o(a_o,t)) \right] / \Delta P . \qquad (5.21)$$

For the study of the heat problem it is useful to introduce the following variable (again omitting the superscripts i):

$$y = \frac{1}{3} \left[\tilde{r}^3 - \tilde{R}^3(\theta,t) \right] \quad , \qquad (5.22)$$

by analogy with the spherical bubble case (Prosperetti and Plesset, 1978). With this variable change, the normalized energy equation can be written:

$$\dot{\tilde{T}} + \frac{\partial \tilde{T}}{\partial y} \left[\tilde{r}^2 \frac{\partial \tilde{\Phi}}{\partial r} - \tilde{R}^2 \dot{\tilde{R}} \right] = P_e^{-1} \left\{ \frac{\partial}{\partial y} \left(\tilde{r}^4 \frac{\partial \tilde{T}}{\partial y} \right) + \right.$$

$$\left. + \frac{1}{\tilde{r}^2 \sin\theta} \left[\frac{\partial}{\partial \theta} \left(\sin\theta \frac{\partial \tilde{T}}{\partial \theta} \right) - \frac{\partial}{\partial \theta} \left(\tilde{R}^2 \frac{\partial \tilde{R}}{\partial \theta} \sin\theta \frac{\partial \tilde{T}}{\partial y} \right) \right] \right\} + o(\varepsilon^3) . \qquad (5.23)$$

After replacing $\tilde{r}$ by its value derived from (5.22), and accounting for the expansions of $R(\theta,t)$, we obtain at the orders ε° and ε, the relations:

$$\dot{\tilde{T}}_o - P_e^{-1} \frac{\partial}{\partial y} \left(\eta^4 \frac{\partial \tilde{T}_o}{\partial y} \right) = 0 \quad , \qquad (5.24)$$

and

$$\dot{\tilde{T}}_1 - P_e^{-1} \frac{\partial}{\partial y} \left(\eta^4 \frac{\partial \tilde{T}_1}{\partial y} \right) = P_e^{-1} \frac{\partial}{\partial y} \left(4 \eta \tilde{a}_1 \tilde{a}_o^2 \frac{\partial \tilde{T}_o}{\partial y} \right) , \qquad (5.25)$$

where

$$\eta = (\tilde{a}_o^3 + 3y)^{1/3} \quad . \tag{5.26}$$

Similarly, the heat balance condition on the bubble wall becomes at order ε° and ε:

$$\tilde{a}_o^2 \left.\frac{\partial \tilde{T}_o}{\partial y}\right|_{y=0} = \mathcal{A}\, \dot{\tilde{a}}_o \quad , \tag{5.27}$$

and

$$\tilde{a}_o^2 \left(\frac{\partial \tilde{T}_1}{\partial y} + 2 \frac{\tilde{a}_1}{\tilde{a}_0} \frac{\partial \tilde{T}_o}{\partial y} \right)_{y=0} = \mathcal{A}\, \dot{\tilde{a}}_1 \quad . \tag{5.28}$$

b. Higher Orders

Continuing the same procedure as in the preceding section, one can derive the successive equations for the flow field, the temperature field and the bubble motion. The solution of the problem is made easier by the use of series expansions of the velocity potential in spherical harmonics, and of the bubble surface equation and the temperature field in Legendre polynomials, $P_n(\cos\theta)$. The boundary condition at infinity for any particular "inner" problem (i), obtained by expanding the expression of Φ near B^i (Chahine and Bovis, 1983; Chahine, 1982) can then be shown to be up to order ε^3:

$$\lim_{\tilde{r} \to \infty} \tilde{\Phi}^i(M,t) = \sum_{i \neq j} \{-\varepsilon\, \lambda_{ij} \tilde{q}_o^j - \varepsilon^2 (\lambda_{ij}^2 \tilde{q}_o^j \tilde{r} \cos\theta^{ij} + \lambda_{ij} \tilde{q}_1^j) +$$

$$-\varepsilon^3 [\lambda_{ij}^3 \tilde{q}_o^j \tilde{r}^2 P_2(\cos\theta^{ij}) + \lambda_{ij}^2 \tilde{q}_1^j \tilde{r} \cos\theta^{ij} + \lambda_{ij} \tilde{q}_2^j] + \ldots\}. \tag{5.29}$$

Here q_n^j is the correction at order ε^n of q_0^j, the strength of the source representing the first-approximation spherical volume change of the bubble $B^{(j)}$, and

$$\lambda_{ij} = (\ell_o / \ell_o^{ij}) \quad . \tag{5.30}$$

The superscript j denotes quantities corresponding to the other bubbles, $B^{(j)}$, and θ^{ij} is the angle MB^iB^j between B^i, B^j, and a field point in the fluid, M, (see Figure 1).

Expressed in physical terms (velocities, pressures), the boundary condition (5.29) indicates that the order ε correction to the nonperturbed spherical flow field around the test bubble is a spherical modification of the collapse driving pressure. This introduces, as we have seen in the preceding section, a spherical correction $a_1^i(t)$ to the radius variations $a_0^i(t)$. At the following order, ε^2, a second correction of the at-infinity uniform pressure appears, and a uniform velocity field expressing a slip velocity between the bubble and the surrounding fluid is to be added. Going through the expansions of the boundary conditions at the bubble surface, one can show that this induces a spherical correction, $a_2^i(t)$, of $a_0^i(t)$, and a nonspherical correction $f_2^i(t) \cdot \cos\theta^{ig}$ (Chahine and Bovis, 1983, Chahine, 1982). θ^{ig} is an angle which can be compounded from all the θ^{ij}'s (see Figure 3.1). Things become more complex at the order of expansion ε^3, where in addition to the uniform pressure and velocity corrections, a velocity gradient generated by the flow field associated with the motion of all the other bubbles, is to be accounted for to generate a nonspherical correction of form $P_2(\cos\theta^{ig})$.

Resulting from the above remarks on the at-infinity boundary condition, one can show that the equation of the surface of the bubble $B^{(i)}$ and the temperature can be written as:

$$\tilde{R}^i(\theta^{ig},t) = \tilde{a}_o^i(t) + \varepsilon\,\tilde{a}_1^i(t) + \varepsilon^2\,[\tilde{a}_2^i(t) + \tilde{f}_2^i(t)\cdot\cos\theta^{ig}] +$$

$$+ \varepsilon^3\,[\tilde{a}_3^i(t) + \tilde{f}_3^i(t)\cdot\cos\theta^{ig} + \tilde{g}_3^i(t)\cdot P_2(\cos\theta^{ig})] + o(\varepsilon^3), \tag{5.31}$$

$$T(r,\theta^{ig},t) = T_o(r,t) + \varepsilon\,T_1(r,t) + \varepsilon^2[T_{20}(r,t) + T_{21}(r,t)\cdot\cos\theta^{ig}] +$$

$$+ \varepsilon^3[T_{30}(r,t) + T_{31}(r,t)\cdot\cos\theta^{ig} + T_{32}(r,t)\cdot P_2(\cos\theta^{ig})] + o(\varepsilon^3), \tag{5.32}$$

provided that the initial bubble shape is spherical. Therefore, up to the order ε^3 each inner problem is axisymmetric, and the axis of symmetry for every bubble is in the direction, B^iG, of its motion towards the bubble cloud "center".

We introduce $\dot{d}_n$ defined as the sum of the deformation rate, $\dot{f}_n$, and of the origin of axis translation velocity, $\dot{b}_n$, both of form $\cos\theta$:

$$\dot{\tilde{d}}_n = \dot{\tilde{f}}_n + \dot{\tilde{b}}_n \quad . \tag{5.33}$$

One then obtains the following differential equations for the order ε^2 radius components, and d_2, similar to (3.11).

$$\tilde{a}_o\ddot{\tilde{a}}_2 + 3\,\dot{\tilde{a}}_o\dot{\tilde{a}}_2 + \tilde{a}_2\,(\ddot{a}_o - 2W_e^{-1}\,\tilde{a}_o^{-2}) =$$

$$-\frac{3}{2}\,\dot{\tilde{a}}_1^2 - \tilde{a}_1\,\ddot{\tilde{a}}_1 - 2W_e^{-1}\,\tilde{a}_1^2\,\tilde{a}_o^{-3} + \Pi_2(t) - \sum_{i\neq j}\lambda_{ij}\,\dot{\tilde{q}}_1^j\,, \tag{5.34}$$

$$\tilde{a}_o\ddot{\tilde{d}}_2 + 3\,\dot{\tilde{a}}_o\dot{\tilde{d}}_2 = \Pi_{21}(t) - 3\sum_{i\neq j}\lambda_{ij}^2\,(\dot{\tilde{a}}_o\tilde{q}_o^j + \tilde{a}_o\dot{\tilde{q}}_o^j)\,\frac{\cos\theta^{ij}}{\cos\theta^{ig}}. \tag{5.35}$$

In the above equations, the superscript i has been omitted, and $a_o(t)$ and $a_1(t)$ are obtained at the preceding orders by solving the differential equations (5.7) and (5.19). $\Pi_{nm}(t)$ are higher order approximations of the nondimensional difference between the vapor pressure at any time and its initial value. The indexes n,m correspond to those used in the expansions of the temperature, Equation (5.32).

The energy equations at order ε^2 can be written using

$$\eta = (\tilde{a}_0^3 + 3y)^{1/3} , \tag{5.36}$$

$$\dot{\tilde{T}}_{20} - P_e^{-1} \left(\eta^4 \frac{\partial \tilde{T}_o}{\partial y}\right) =$$

$$P_e^{-1} \frac{\partial}{\partial y} \left[(4\tilde{a}_o\tilde{a}_1^2\eta + 4\tilde{a}_o^2\tilde{a}_2\eta + 2\tilde{a}_o^4\tilde{a}_1^2\eta^{-2}) \frac{\partial \tilde{T}_o}{\partial y} + 4\tilde{a}_o^2\tilde{a}_1\eta \frac{\partial \tilde{T}_1}{\partial y}\right], \tag{5.37}$$

$$\dot{\tilde{T}}_{21} - P_e^{-1} \left[\frac{\partial}{\partial y} \left(\eta^4 \frac{\partial \tilde{T}_{21}}{\partial y}\right) - 2\eta^{-2} \tilde{T}_{21}\right] =$$

$$\left(\frac{2h_2}{\eta} + 2\tilde{a}_o\tilde{a}_o\tilde{f}_2 + \tilde{a}_o^2\dot{\tilde{f}}_2 + \sum_{i\neq j} \lambda_{ij}^2 \tilde{q}_o^j \frac{\cos\theta^{ij}}{\cos\theta^{ig}} \eta^2\right) \frac{\partial \tilde{T}_o}{\partial y} +$$

$$P_e^{-1} \left[2\eta^{-2} \tilde{a}_o^2 \tilde{f}_2 \frac{\partial \tilde{T}_o}{\partial y} + \frac{\partial}{\partial y} \left(4\eta \tilde{f}_2 \tilde{a}_o^2 \frac{\partial T_o}{\partial y}\right)\right] . \tag{5.38}$$

The corresponding conditions of heat balance on the bubble wall are

$$\tilde{a}_o^2 \left[\frac{\partial \tilde{T}_{20}}{\partial y} + \frac{2\tilde{a}_1}{\tilde{a}_0} \frac{\partial \tilde{T}_1}{\partial y} + 2 \left(\frac{\tilde{a}_2}{\tilde{a}_0} + \frac{\tilde{a}_1^2}{\tilde{a}_o^2}\right) \frac{\partial \tilde{T}_o}{\partial y}\right]_{y=0} = \mathcal{A} \dot{\tilde{a}}_2 , \tag{5.39}$$

$$\tilde{a}_o^2 \left[\frac{\partial \tilde{T}_{21}}{\partial y} + 2 \frac{\tilde{f}_2}{\tilde{a}_0} + \frac{\partial \tilde{T}_o}{\partial y} \right]_{y=0} = \mathcal{A} \dot{\tilde{f}}_2 \quad . \qquad (5.40)$$

Similar equations can be derived for order ε^3 (Chahine and Liu, 1983) and are not presented here for conciseness.

5.3 Numerical Solution

5.3.1 General Solution

The system of equations derived up to order ε^3 constitutes a set of 14 equations for the 14 unknown components of $R^i(\theta,t)$, and $T^i(\theta,t)$ (expansions (5.31) and (5.32)). By solving this system one determines completely the flow and temperature fields as well as the bubble motion and deformation. A numerical solution of these equations is feasible and could be performed using the same procedure as Dalle Donne and Ferranti (1975). Their study dealt with a single bubble growth and thus solved only equations (5.7), (5.10), and (5.12). Here the same approach would have to be performed for all seven components of the bubble radius (up to ε^3).

Since the equations are not independent, the procedure would start by determining at a given time step the temperature at the lowest order of approximation (ε°) and the corresponding radius approximation. Knowing this, one can compute the successive temperature corrections, and the successive radius corrections. At each time step an iteration process would be used to insure a good correspondence between the obtained temperature and radius values. Stepping in time of

the computation could be obtained with a Runge-Kutta procedure which solves each differential equation yielding the bubble radius values. The determination of the temperature field is more elaborate and requires a stepping in both time and in space. This latter involves writing a finite difference scheme and replacing the integration field with a grid of mesh points. This general solution is not developed here. We considered instead the cases where large initial superheats make a thermal boundary layer approximation valid.

5.3.2 Thermal Boundary Layer Approximation

If the distance δ in which the temperature rises from its value at the bubble wall to approximately the imposed ambient temperature, T_∞, is small compared with the bubble radius, R, an approximate solution can be obtained more easily than with the method described in the preceding paragraph. By considering heat diffusion in the liquid, spherical bubble growth rate, and a heat balance at the bubble-liquid interface, Plesset and Prosperetti (1977) estimate δ/R by:

$$\frac{\delta}{R} \simeq \frac{D\, L\, \rho_v}{K\,(T_\infty - T_b)} = \frac{\rho_v}{\rho}\,\frac{L}{C(T_\infty - T_b)} = J^{-1} . \quad (5.41)$$

Thus, a boundary layer approximation is valid as long as the Jacob number, J, is much larger than one. For a spherical bubble, comparisons between numerical computations obtained using this approximation and those obtained by solving the exact equations gave very close agreement for $J \geq 3$, (Prosperetti and Plesset 1978 and Plesset, 1980).

When the boundary layer approximation is used, the system of heat equations, presented above, simplifies considerably. Indeed, in that case the temperature departs from T_∞ only in the liquid region close to the bubble-liquid interface, and the values of r which are of interest are close to $R(\theta,t)$. The variable, y, defined in (5.22), is then small compared to a^3, and we can write

$$y = \xi \tilde{y} \tilde{a}_o^3 \quad , \tag{5.42}$$

where y and a_o are of order 1, and ξ is a small parameter $[\xi=O(J^{-1})]$. The problem considered then contains two small parameters ε and ξ, and an asymptotic solution uniformly valid when both ε and ξ go to zero can be obtained when a relationship between the two parameters is defined through the use of the principle of least degeneracy (Darrozes, 1971).

Considering the heat equation, (5.23), one can determine the relation needed between ε and ξ to conserve the maximum number of terms in the leading orders of approximation. In order to prevent the order ε^0 expansion, (5.24), from degenerating when ξ goes to zero, the Peclet number has to be large enough to satisfy

$$P_e = O(\xi^{-2}) \quad , \tag{5.43}$$

in which case both terms of the equation are conserved. Similarly, to conserve the maximum terms at the following order, ε, one needs to keep together the leading terms coming from the expansions in powers of ε and those from expansions in power of ξ (e.g., in the expansions of η^4). This "least degeneracy" is obtained when

$$\xi = O(\varepsilon) \quad . \tag{5.44}$$

Using the relationships (5.43) and (5.44) between P_e, ξ, and ε, the expansions become straightforward.

The equations obtained at the first order expansion in both parameters (orders ε° and ξ°) are those for the case of an isolated bubble. These equations are the Rayleigh-Plesset equation (5.7) and the heat equation (5.24) in which η^4 takes the value a_o and which becomes:

$$\dot{T}_o + P_e^{-1} \frac{\partial}{\partial y}\left(a_o^4 \frac{\partial T_o}{\partial y}\right) = 0 \qquad (5.45)$$

A solution is readily available for this case and was derived by Plesset and Zwick (1952) and Forster and Zuber (1954) using Laplace transform methods. The nondimensional temperature at the bubble wall is given by:

$$\tilde{T}_o(\tilde{a}_o,\tilde{t}) = \tilde{T}_\infty - \left(\frac{D}{\pi\tau_o}\right)^{1/2} \cdot \frac{r_{b_o}}{K(T_\infty - T_b)} \cdot \int_o^{\tilde{t}} L(x)\,\rho_v(x) \frac{\tilde{a}_o^2(x)\,\dot{\tilde{a}}_o(x)}{\left[\int_x^{\tilde{t}} \tilde{a}_o^4(y)\,dy\right]^{1/2}} dx, \qquad (5.46)$$

where, to be consistent with the assumptions made in deriving this solution, D and K are constant and evaluated at T_b while L and ρ_v are functions of time. The numerical procedure is greatly simplified now that an analytical expression for the temperature at the bubble wall is known. The finite difference method which would have been used in the general case is here replaced by a numerical computation of the integral equation (5.46). An iteration procedure is required to insure that the computed value of $T_o(a_o,t)$ does not differ significantly from the value presumed in the computation of the integrand.

Plesset and Zwick (1952) also gave the solution of the problem when equation (5.46) contains a right hand side which is a known function of time (heat source term). Using a matched asymptotic procedure they also computed the following order of approximation, $0(\xi)$. These solutions correspond to the following order equations in powers of ε and ξ for the multibubble problem. For simplicity these equations will not be listed here.

5.4 Numerical Examples for Symmetrical Clouds

In order to illustrate the method presented above we consider numerical solutions for a cloud of simple geometry. The bubbles are distributed in a symmetrical configuration and are initially of equal size. With this configuration all bubbles have the same radius history. All summations in the dynamic equations (5.19, 5.34, 5.35) reduce to multiplications of the characteristics of a single bubble by one of the three geometrical constants c_1, c_2, c_3 defined earlier in (3.13).

An additional simplification of the numerical solution can be introduced if one notices that during the bubble growth the departure from the initial spherical shape happens very late in the bubble history and only when the asymptotic approach starts losing its validity. This is not true for the cloud collapse (see preceding section). Figure 5.1 shows the variation with time of the major radius of an individual bubble in a cloud configuration of N bubbles symmetrically located on a sphere. For this figure, heat transfer has been neglected. We observe, for the isolated bubble, the well known asymptotic linear growth behavior. However, when the number of interacting bubbles increases, the pressure field associated with the dynamics of

the other bubbles in the cloud reduces the growth rate of the test bubble. This deviation increases with the number of bubbles, N, until for N = 12 for the case studied, the method apparently fails for $t > 0.1$. The radius corrections (illustrated in the figure by the amount of deviation of the radius in an N-bubble case from the isolated bubble case) become large compared with the order zero radius. Figure 5.2 shows, for the same bubble configuration, the ratio of the nonspherical to the spherical part of $R(\theta,t)$ in the expansion (5.31). In all cases but the obvious one where the method breaks down, the relative deformations remain less than 4 percent while the bubble radius is 2,000 times its initial value. Based on this observation and as a first step towards a more precise solution, we have neglected in the numerical program developed the contribution of nonsphericity to the heat transfer problem. Therefore, the temperature field was approximated by a spherically symmetrical field. However, this field accounts for interactions and differs from that of the isolated bubble case because of the contributions of the higher order spherical terms of the bubble equation. Indeed, Equation (5.46), relating the bubble wall temperature to a spherical bubble radius history, was applied to the spherical part of the bubble radius, i.e., to

$$\bar{A}(t)=\bar{a}_0(t)+\epsilon\,\bar{a}_1(t) + \epsilon^2\,\bar{a}_2(t) + \epsilon^3\,\bar{a}_3(t) \quad . \qquad (5.47)$$

With this simplification, at any time step all dynamical equations are solved using the value of the vapor pressure corresponding to the liquid temperature at the radial distance $A(t)$. This temperature is computed at the preceding time step using equation (5.46). The nonspherical part of the bubble shape is not disregarded and is computed neglecting variations

of the liquid temperature along the bubble surface. This is valid as long as the bubble deformation is negligible. Since we restrict this study to that case, the validity of the results is checked by monitoring the relative value of the computed nonspherical to the spherical components of the bubble surface equation. The computation is stopped when an imposed limit is exceeded. Figure 5.3 presents a flow chart of the developed code HOTCLD.

A series of numerical cases was studied using a VAX 11/750 computer. We have considered different variations of the number of bubbles and configuration, the ambient pressures, the initial bubble radius, and the amount of superheat. The duration of a typical run was about 10 minutes of CPU time (for 2,000 time steps). The computation involves the solution of the heat and dynamical equations for an N bubble configuration, the study of the corresponding case of an isolated bubble with and without heat transfer, and the computation of pressure histories at three locations in the flow field.

In all the presented figures, the curves are stopped when the computations become invalid due to large bubble interactions. Figure 5.4 shows clearly the influence of interactions on the bubble radius history. Since the bubble does not remain spherical, the value of $R(\theta^{ig})$ represented in this figure corresponds to the point on the bubble closest to the cloud center, the "lower-minor radius." (See Figure 3.1.) The classical results of asymptotic growth in t for the inertia-controlled bubble expansion and in t^{α} for the heat-controlled bubble expansion can be seen. If there was no pressure drop α would be 1/2. However, here α is much closer to 1, as obtained by earlier studies on single bubbles (Jones

and Zuber, 1978; Theofanous et al., 1969; and Cha and Henry, 1981). The most important result obtained here is that bubble growth is inhibited by bubble interactions. Very clearly at a given time the bubble size decreases with the number of interacting bubbles. This decrease exceeds 20 percent for a 5 bubble system for nondimensional times larger than 10, or one millisecond after the start of the growth (case of Figure 5.4).

Figure 5.5 shows the effect of bubble interactions on the liquid temperature at the bubble wall. The presence of other growing bubbles in the field is seen to reduce the heat transfer at the bubble wall and thus the temperature drop in its vicinity. For example, for a five-bubble system the deviation from the isolated bubble case of the temperature drop is more than 30 degrees one millisecond after the initial pressure drop. This result, coupled with that obtained for the variations of the bubble radius, is important for any practical computation of heat transfer in a two-phase medium.

Figure 5.6 shows the modification of the bubble shape during its growth for the same N-bubble systems shown in Figures 5.4 and 5.5. Represented are the bubble shapes at two instants during the growth process. As expected, in the presence of an N-bubble cloud, the side of the bubble facing the cloud center is seen to be slightly "pushed away" from the cloud center and the bubble is seen to elongate in a direction tangential to the sphere. However, any point on its surface always remains inside the corresponding fictitious isolated bubble growing under the same conditions. The deformation decreases as the number of interacting bubbles increases.

Figures 5.7 and 5.8 show the influence of the amount of pressure drop and initial superheat on the bubble growth. These figures consider an isolated bubble as well as a five-bubble system. The same remarks made in the preceding paragraphs apply here when the influence of the number of bubbles is considered. In all cases the initial bubble radius is the same, and the pressure drops to the same value. However, since the initial pressures vary from one case to another and since all bubbles are considered to be initially at equilibrium, the initial temperature and thus the initial amount of superheat varies from one case to another. To isolate the two effects one has to consider the case where the bubbles are not initially at equilibrium. Another option would be to have the same initial pressure, radius and temperature and to vary the value of P_{inf}. We consider this case below. Figures 5.7 and 5.8 show that the normalized bubble radii and growth rates are larger at any given time when the amounts of pressure drop and superheat are greater. In the absence of heat transfer, scaling effects are mainly due to the differences in the Weber number, W_e and the initial pressure parameter . When heat transfer effects are included, there is an additional parameter, the Jacob number. These effects counterbalance each other in real time, and one observes a minor influence of the initial value of the pressure (for the same initial radius) when the radius variations are plotted with dimensional variables (Chahine and Liu, 1983).

A similar result is seen when, for the same initial bubble radius and liquid temperature, the ambient pressure drops from the same initial pressure to different subsequent values. In this case the initial amount of superheat is the same for all the cases of pressure drop studied. However, the subsequent

amounts of superheat differ from one case to another. The use of nondimensional variables decreases (but does not cancel, because of nonlinearities) the influence of dynamic factors, however it does not alter thermal effects. The results (Figure 5.9) show again a larger bubble radius during the growth period for higher pressure drops. The comparison with the five-bubble case can also be observed and shows again the retarding effect on bubble growth due to collective bubble behavior. Figure 5.10 completes the picture by showing the temperature drop at the bubble wall for the different cases studied. The same observations as those made above are repeated, namely higher temperature drops for smaller pressure drops or higher number of interacting bubbles.

The last series of results consider the influence of the initial bubble size for given fixed pressure conditions. With the assumption that the bubble is initially at equilibrium, the modification of the initial bubble size also corresponds to a change of the amount of superheat. Figure 5.11 shows the predominance of the effect of the amount of superheat factor on the bubble growth; initially smaller bubbles attain greater sizes because of larger amounts of superheat. This effect is, however, coupled with the nonlinearities of the dynamical equations which favor smaller initial bubble radii in the first phase of the growth. Figure 5.12 shows the same effect with nondimensional variables and compares a five-bubble system with the isolated bubble case. One can notice that the inhibition effect due to bubble interactions is larger for smaller initial bubbles or larger amounts of superheat. Finally, Figure 5.13 describes the temperature drop at the bubble wall for the same cases.

The results obtained show that a significant influence of bubble interactions on bubble growth and heat transfer exists. The effects of this influence can be summarized as follows:

a. The growth rate of the bubbles is reduced,

b. The radius of any bubble at a given time is smaller than would be found for an isolated bubble, and

c. The temperature drop at the bubble wall is smaller at any given time than would be found for an isolated bubble.

These effects increase with the number of interacting bubbles as well as with the amount of superheat and pressure drop. These results, which were obtained using small perturbations assumptions, are expected to remain valid and become more significant when the void fraction becomes larger. Accounting for these effects is important for increasing the accuracies of the existing transient two-phase flow codes.

The study presented here could be improved by introducing a finite speed wave propagation in the cloud and by accounting for the compressibility of the medium. The analytical equations derived for the general bubble configuration case (no symmetry and unequal bubble size) could be expanded to a numerical approach in a relatively simple manner. The resolution of the problem could also be extended to low superheat cases (small Jacob numbers) and to larger interactions and bubble deformations by numerically implementing the analytical approach presented above which was not used in the numerical examples.

6.0 INCLUSION OF GAS DIFFUSION AT THE BUBBLE WALL

6.1 Introduction

An analysis was developed for the inclusion of the effects of gas diffusion into and out of cavitation bubbles in clouds. The solution scheme is similar to that used by Chahine and Liu (1985) for heat transfer to a bubble in a superheated liquid (see Section 5). The equations governing mass diffusion have been coupled to those governing bubble dynamics and non-spherical deformations. The equations solved include the Rayleigh-Plesset equation for bubble dynamics, the transport equation for the dissolved gas in the liquid, and an energy equation for the bubble (first law of thermodynamics). An ideal gas equation of state is assumed for the bubble which is taken to contain a mixture of noncondensible gas and vapor. These two components are considered to form an ideal gas mixture. Due to the relatively very short characteristic time of vaporization compared to bubble dynamic and gas diffusion characteristic times, the quantity of vapor in the bubble is assumed to vary instantaneously such that the vapor pressure remains constant and at the equilibrium value for the liquid temperature. A boundary layer solution analogous to that of Plesset and Zwick (1952) is utilized for the gas transport equation. This provides an expression for the gas concentration at the bubble surface as a function of time. The concentration of dissolved gas at the bubble surface is related to the partial pressure of the gas within the bubble by Henry's law. The gas concentration varies from the ambient initial value in the liquid to the bubble wall value over a thin boundary layer.

6.2 Equations Governing Mass Diffusion

6.2.1 General Equations

The transport of noncondensible gas in the liquid medium is governed by

$$\frac{\partial C}{\partial t} + \underline{v} \cdot \underline{\nabla} C = D_g \nabla^2 C \qquad (6.1)$$

subject to the boundary and initial conditions:

$$\begin{aligned} &C \to C_\infty \quad \text{for} \quad r \to \infty \ , \\ &C = C_\infty \quad \text{for} \quad t \leq 0 \ \text{and} \ r \geq R \ , \\ &C = C_{sat}, \quad r = R, \quad t > 0 \ . \end{aligned} \qquad (6.2)$$

Here, C is the concentration of dissolved gas in the liquid in units of moles per unit volume, D_g is the molar diffusivity of the gas component in the liquid, and R is the radial location of the bubble wall. In general, $R = R(\theta, \phi, t)$. The gas concentration is taken to be saturated at the bubble wall: $C = C_{sat}$. With this assumption, the gas concentration at the bubble wall can be related to the partial pressure of that gas component in the bubble by Henry's Law:

$$P_g = H\, C_{sat} = H \cdot C(r=R) \ , \qquad (6.3)$$

where P_g is the partial pressure of noncondensible gas within the bubble (taken to be uniform throughout the bubble) and H is Henry's constant at the liquid temperature, a property of the gas-liquid combination.

As the bubble grows or shrinks, noncondensible gas will be transported across the bubble wall. The net transport of gas into the bubble can be related to the gradient of gas concentration in the liquid at the bubble wall:

$$D_g \int_S \frac{\partial C}{\partial n}\bigg|_{r=R} dS = \dot{n}_g \quad , \tag{6.4}$$

where S is the surface of the bubble, $\underline{n}$ is the direction normal to the bubble surface, and $\dot{n}_g$ is the time rate of change of the total number of moles of gas, n_g, within the bubble.

6.2.2 Boundary Layer Solution for Gas Concentration

A general, detailed solution of equations (6.1-6.3) would likely involve a time consuming numerical approach, such as a space and time dependent finite difference scheme, and is not necessary for many cases of interest. Plesset and Zwick (1952) and Forster and Zuber (1954) obtained a solution to (6.1-6.3) for the case of an isolated spherical bubble for which appreciable concentration gradients are confined to a boundary layer of thickness δ which is small compared to the bubble radius:

$$C = C_\infty - \left[\frac{D_g}{\pi}\right]^{1/2} \int_o^t \frac{R^2 \frac{\partial C}{\partial r}\Big|_{r=R}}{\left[\int_x^t R^4(y)\,dy\right]^{1/2}} dx. \tag{6.5}$$

This expression applies to the first order approximation of the bubble radius, $R = a_o(t)$. A similar relation is found applicable to $R = a_o(t)$ in the heat transfer study (see Section 5.0 and Equation 5.46). Equation (6.4) can then be expressed as

$$a_o^2 \left.\frac{\partial C}{\partial r}\right|_{r=a_o} = \frac{\dot{n}_g}{4\pi D_g} , \qquad (6.6)$$

and substituted into (6.5) to obtain

$$C = C_\infty - \frac{1}{4\pi} [\pi D_g]^{-1/2} \int_o^t \frac{\frac{\partial}{\partial x} n_g}{\left[\int_x^t a_o^4 (y)\, dy\right]^{1/2}} dx. \qquad (6.7)$$

We now nondimensionalize the variables in (6.7) and define

$$\bar{C} = C/C_\infty ,$$

$$\bar{n}_g = n_g/n_{g_o} ,$$

$$\bar{t}, \bar{x}, \bar{y} = t/\tau, x/\tau, y/\tau , \qquad (6.8)$$

$$\bar{a}_o = a_o/r_{b_o} ,$$

$$\bar{r} = r/r_{b_o} ,$$

where

C_∞ is the gas concentration for $r \to \infty$,

r_{b_o} is a reference characteristic bubble radius,

n_{g_o} is the number of moles of gas in a bubble of radius r_{b_o} at equilibrium at t=0, and

$\tau = r_{b_o}\sqrt{\rho/\Delta P}$ is the characteristic time for growth of a bubble of radius r_{b_o}.

Equation (6.7) becomes, in nondimensional form:

$$\bar{C} = 1 - \left[\frac{1}{\pi \tau\ D_g}\right]^{1/2} \frac{n_{g_o}}{4\pi r_{b_o}^2\ C_\infty} \int_o^{\bar{t}} \frac{\dot{\bar{n}}_g}{\left[\int_{\bar{x}}^{\bar{t}} \bar{a}_o^4\ (\bar{y})d\bar{y}\right]^{1/2}} d\bar{x} \quad .(6.9)$$

Let ρ_{g_o} be the initial density of the gas in the bubble. Then

$$n_{g_o} = m_{g_o} / M_g = \frac{4}{3}\ \pi\ r_{b_o}^3\ \rho_{g_o} / M_g \quad , \qquad (6.10)$$

where M_g is the gas molecular weight and m_{g_o} is the mass of gas in the reference bubble of radius r_{b_o}. Equation (6.9) can then be written as

$$\bar{C} = 1 - \frac{1}{3}\ \left[\frac{r_{b_o}^2}{\pi \tau\ D_g}\right]^{1/2} \frac{\rho_{g_o}}{M_g\ C_\infty} \int_o^{\bar{t}} \frac{\dot{\bar{n}}_g}{\left[\int_{\bar{x}}^{\bar{t}} \bar{a}_o^4\ (\bar{y})d\bar{y}\right]^{1/2}} d\bar{x}, \quad (6.11)$$

for C_∞ expressed in moles per unit volume, and ρ_{g_o} in mass per unit volume. If the dissolved gas concentration is expressed as a volume fraction (e.g., cm^3 of gas per cm^3 of water), we will let C_∞ be the concentration at infinity and

$$C_\infty^v = C_\infty\ M_g / \rho_{g_o} \quad . \qquad (6.12)$$

Then equation (6.11) becomes

$$\bar{C}^v = 1 - \frac{1}{3C_\infty^v} \left[\frac{r_{b_o}^2}{\pi \tau D_g} \right]^{1/2} \int_o^{\bar{t}} \frac{\dot{\bar{n}}_g}{\left[\int_{\bar{x}}^{\bar{t}} \bar{a}_o^4 (\bar{y}) d\bar{y} \right]^{1/2}} d\bar{x} \quad , \quad (6.13)$$

where $\bar{C}^v$ is now a volume fraction concentration nondimensionalized on C_∞^v. We will use expression (6.13) for the transport of noncondensible gas across the bubble wall.

6.2.3 Equation of State Within the Bubble

The gas and vapor within the bubble are taken to comprise an ideal gas mixture, and the equation of state for that mixture is given by

$$(P_g + P_v) \; V_b = (n_g + n_v) \; R_u \; T_g \quad , \qquad (6.14)$$

where

P_g, P_v = partial pressures of gas and vapor,

V_b = volume of bubble,

n_g, n_v = number of moles of gas and vapor within the bubble,

R_u = Universal gas constant, and

T_g = Absolute temperature of the gas and vapor mixture within the bubble.

The temperatures of the gas and vapor phases are taken to be the same, T_g. For an ideal gas mixture, each component also obeys the ideal gas law:

$$P_g V_b = n_g R_u T_g \quad ,$$

$$P_v V_b = n_v R_u T_g \quad . \qquad (6.15)$$

In this analysis, the partial pressure of the vapor is fixed (at the equilibrium value for the constant liquid temperature) while P_g is allowed to vary with bubble behavior, mass transfer, and the bubble energy balance.

We nondimensionalize with the characteristic value of pressure change, ΔP, and the equilibrium values at the characteristics bubble radius, r_{b_o}:

$$\bar{P}_g, \bar{P}_v = P_g/\Delta P, P_v/\Delta P \quad ,$$

$$\bar{n}_g, \bar{n}_v = n_g/n_{g_o}, n_v/n_{g_o} \quad ,$$

$$\bar{V}_b = V_b/(\tfrac{4}{3} \pi r_{b_o}^3) = \bar{a}_o^3 \quad , \qquad (6.16)$$

The temperature is normalized on the liquid temperature, T_l

$$\bar{T}_g = T_g/T_l, \qquad (6.17)$$

Equation (6.14) can then be written as

$$(\bar{P}_g + \bar{P}_v) \bar{V}_b = \beta (\bar{n}_g + \bar{n}_v) \bar{T}_g \quad , \qquad (6.18)$$

where

$$\beta \equiv \frac{R_u \, n_{g_o} \, T_l}{\frac{4}{3} \pi \, r_{b_o}^3 \, \Delta P} = \frac{P_{g_o}}{\Delta P} = \bar{P}_{g_o} , \qquad (6.19)$$

since

$$P_{g_o} = \frac{n_{g_o} \, R_u \, T_l}{\frac{4}{3} \pi \, r_{b_o}^3} , \qquad (6.20)$$

the partial pressure of gas in a reference bubble of radius r_{b_o} at equilibrium for the initial liquid pressure and temperature. Thus, the quantity β can be viewed both as a ratio of the reference bubble gas partial pressure to driving liquid pressure change or as a dimensionless universal gas constant. Similarly, we write

$$\bar{P}_g \, \bar{V}_b = \beta \, \bar{n}_g \, \bar{T}_g ,$$

$$\bar{P}_v \, \bar{V}_b = \beta \, \bar{n}_v \, \bar{T}_g . \qquad (6.21)$$

Use of the ideal gas equations of state has introduced another unknown, T_g, and thus necessitates use of another condition. This is provided by the first law energy balance of the ideal gas mixture within the bubble. Two cases are considered. In the first case, the approximation is made that the gas and vapor mixture temperature is constant and equal to that of the liquid. This approximation is valid when the bubble is initially at the liquid temperature, and changes in bubble size occur slowly enough such that heat transfer can equilibrate the bubble and liquid temperatures. The second, more complicated case, involves writing the first law energy balance for

the bubble with mass transfer across its surface. This formulation allows for T_g to differ from T_l without an arbitrary adoption of a polytropic constant. Its use actually enables determination of the effective polytropic constant.

In the first approach, the change in state of the isothermal ideal gas is given by

$$\frac{\bar{P}_g \bar{V}_b}{\bar{n}_g} = \text{constant} = \left.\frac{\bar{P}_g \bar{V}_b}{\bar{n}_g}\right|_{R = r_{b_o}} = \bar{P}_{g_o} ,$$

$$\bar{P}_g = \bar{P}_{g_o} \frac{\bar{n}_g}{\bar{V}_b} = \bar{P}_{g_o} \frac{\bar{n}_g}{\bar{a}_o^3} \qquad (6.22)$$

This provides a simple relation between the number of moles of gas, the gas partial pressure, and the bubble volume at different times.

6.2.4 Energy Balance

For the second approach, we consider the bubble wall to constitute a deformable and permeable control surface and write the first law energy balance for the control volume bounded by that surface:

$$d U = - d W + \sum_i \dot{n}_i h_i \, dt \quad ; \quad i = v, g , \qquad (6.23)$$

where

dU = Change in internal energy of the control volume in time dt,

dW = Work done by the control volume on its surroundings in time dt,

n_i = Net molar rate of mass transfer of component i into the control volume, and

h_i = Specific enthalpy of component i.

In (6.23), we have neglected changes in kinetic and potential energies of the bubble and any heat exchange between gas and liquid. We further assume that the bubble wall remains at the liquid temperature T_l, although the gas and vapor mixture within the bubble is free to assume any temperature dictated by (6.23). This is consistent with the neglect of heat transfer into the liquid. The partial pressure of the vapor, P_v, within the bubble is taken to be constant and equal to the equilibrium vapor pressure at T_l. Thus P_v remains constant due to the assumption that the bubble wall temperature remains at T_l. Although P_v is constant, n_v will change as the bubble volume changes and vapor will condense or liquid vaporize at the bubble wall. This results in a form of heat or energy exchange between the bubble and the liquid that is accounted for by the term $\dot{n}_v h_v$ of (6.23). The temperature of both gas and vapor components crossing the control surface in either direction is taken to be T_l, the temperature of the bubble wall.

With these assumptions and the previous assumption of ideal gas behavior for both the vapor and noncondensible gas components, we can write

$$dU = c^g_{v,v}\, d(n_v\, T_g) + c^g_{v,g}\, d(n_g\, T_g) \quad , \tag{6.24}$$

$$\sum_i \dot{n}_i\, h_i = (\dot{n}_v\, c^l_{p,v} + \dot{n}_g\, c^l_{p,g})\, T_l \quad . \tag{6.25}$$

AD-A170 692 CLOUD CAVITATION AND COLLECTIVE BUBBLE DYNAMICS(U) 2/3
TRACOR HYDRONAUTICS INC LAUREL MD G L CHAHINE ET AL.
15 MAR 86 TR-83017-1 N00014-83-C-0244

UNCLASSIFIED F/G 20/4 NL

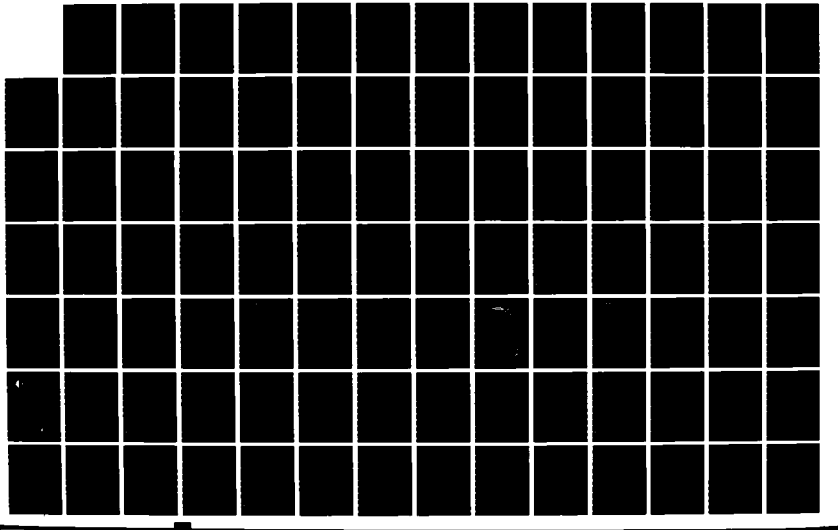

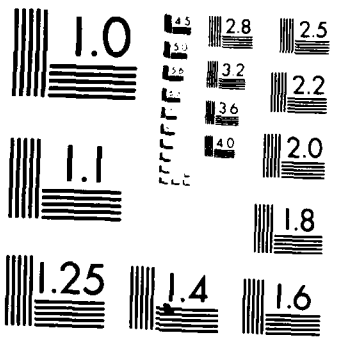

Here, $c^{m}_{i,j}$ is the molar specific heat of component j evaluated at temperature T_m. The notation can be summarized as:

i = p, specific heat at constant pressure,

i = v, specific heat at constant volume,

j = g, specific heat of the gas component,

j = v, specific heat of the vapor component,

m = g, evaluated at the gas-vapor mixture temperature, T_g, and

m = l, evaluated at the bubble wall or liquid temperature, T_l.

The work term in (6.23) can be expressed as the boundary work in moving the bubble surface

$$dW = (P_v + P_g)\, dV_b \quad . \tag{6.26}$$

Combining (6.23-6.26) and rearranging, we obtain

$$c^{g}_{v,v} \frac{d}{dt} (n_v T_g) + c^{g}_{v,g} \frac{d}{dt} (n_g T_g)$$

$$= - (P_v + P_g) \dot{V}_b + (\dot{n}_v c^{l}_{p,v} + \dot{n}_g c^{l}_{p,g}) T_l \quad . \tag{6.27}$$

We use the same nondimensionalizations as before and

$$\bar{c}^{m}_{ij} = c^{m}_{i,j} / R_u \tag{6.28}$$

We then write (6.27) in dimensionless form and obtain:

$$\bar{c}^{g}_{v,v} \frac{d}{d\bar{t}} (\bar{n}_v \bar{T}_g) + \bar{c}^{g}_{v,g} \frac{d}{d\bar{t}} (\bar{n}_g \bar{T}_g) =$$

$$- \frac{1}{\beta} (\bar{P}_v + \bar{P}_g) \dot{\bar{V}}_b + (\dot{\bar{n}}_v \bar{c}^{l}_{p,v} + \dot{\bar{n}}_g \bar{c}^{l}_{p,g}) \quad . \qquad (6.29)$$

Recall that β can be viewed as a dimensionless gas constant or as the ratio of P_{g_o} to ΔP.

Equation (6.29) together with the ideal gas equations of state (6.18, 6.21) are the equations which must be solved for the nonisothermal case in place of (6.22) for the isothermal case. The complete set of simultaneous equations to be solved consists of the bubble dynamics equations (3.11), the boundary layer approximation for gas diffusion subject to Henry's Law (6.3) and conditions (6.2, 6.3), and either the isothermal ideal gas change of state equation (6.22) or the ideal gas equations of state (6.18, 6.21) together with the first law energy balance (6.29). This set of equations accounts for both dynamic and gas diffusion effects on bubble behavior.

6.3 Solution of the Equations Due to Mass Diffusion

We now describe the schemes adopted for solution of the coupled sets of equations described above for including bubble dynamics and mass diffusion effects in bubble behavior. we first approach the solution of the energy balance (6.29) by choosing to allow it to determine the gas partial pressure P_g and its rate of change $\dot{\bar{P}}_g$. With this scheme, we then utilize (6.3, 6.13) to solve for $\dot{\bar{n}}_g$ and $\bar{n}_g$. This format is somewhat arbitrary. However, we have found this to be much better

behaved numerically then using (6.3, 6.13) to determine $\bar{P}_g$, differentiating to find $\dot{\bar{P}}_g$ and using (6.29) to determine $\dot{\bar{n}}_g$ and $\bar{n}_g$.

Combining (6.21) and (6.29) we obtain

$$\bar{c}^g_{v,v}\bar{P}_v\dot{\bar{V}}_b+\bar{c}^g_{v,g}(\bar{P}_g\dot{\bar{V}}_b+\bar{V}_b\dot{\bar{P}}_g)+(\bar{P}_v+\bar{P}_g)\dot{\bar{V}}_b-\beta(\dot{\bar{n}}_v\bar{c}^1_{p,v}+\dot{\bar{n}}_g\bar{c}^1_{p,g})=0 \quad ,(6.30)$$

where the condition that P_v is constant is employed. We eliminate $\dot{\bar{n}}_v$ as a variable by relating it to $\dot{\bar{n}}_g$ using (6.21)

$$\bar{n}_v = \bar{n}_g\ \bar{P}_v/\bar{P}_g \quad ,$$

$$\dot{\bar{n}}_v = \bar{P}_v\ (\dot{\bar{n}}_g/\bar{P}_g - \bar{n}_g\ \dot{\bar{P}}_g/\bar{P}_g^2) \quad . \qquad (6.31)$$

Thus (6.30) becomes

$$\frac{1}{\beta}\ [\bar{c}^g_{v,v}\ \bar{P}_v\ \dot{\bar{V}}_b + \bar{c}^g_{v,g}\ (\bar{P}_g\ \dot{\bar{V}}_b + \bar{V}_b\ \dot{\bar{P}}_g) + (\bar{P}_v + \bar{P}_g)\ \dot{\bar{V}}_b\ ]$$

$$- \bar{c}^1_{p,v}\ \frac{\bar{P}_v}{\bar{P}_g}\ \dot{\bar{n}}_g + \bar{c}^1_{p,v}\ \bar{n}_g\ \frac{\bar{P}_v\ \dot{\bar{P}}_g}{\bar{P}_g^2} - \bar{c}^1_{p,g}\ \dot{\bar{n}}_g = 0 \quad . \qquad (6.32)$$

The relation between specific heats for an ideal gas in dimensional form is given by

$$c_p - c_v = R_u \quad ,$$

or in dimensionless form

$$\bar{c}_v = \bar{c}_p - 1 \quad . \qquad (6.33)$$

We can thus express all values of $\bar{c}_v$ in terms of the corresponding $\bar{c}_p$ quantities.

Using these expressions, equation (6.32) can be arranged in the form of a differential equation for $\bar{P}_g$:

$$\dot{\bar{P}}_g \, (A + B/\bar{P}_g^2) + \bar{P}_g \, D - E/\bar{P}_g + F = 0 \quad , \tag{6.34}$$

where A,...,F are defined as:

$$A = (\bar{c}^g_{p,g} - 1) \, \bar{V}_b/\beta = (\bar{c}^g_{p,g} - 1) \quad \bar{a}_o^3/\beta \quad ,$$

$$B = \bar{c}^l_{p,v} \, \bar{n}_g \, \bar{P}_v \quad ,$$

$$D = \bar{c}^g_{p,g} \, \dot{\bar{V}}_b/\beta = \bar{c}^g_{p,g} \cdot 3 \, \bar{a}_o^2 \, \dot{\bar{a}}_o/\beta \quad ,$$

$$E = \bar{c}^l_{p,v} \, \dot{\bar{n}}_g \, \bar{P}_v \quad ,$$

$$F = \bar{c}^g_{p,v} \, \bar{P}_v \, \dot{\bar{V}}_b \, /\beta - \bar{c}^l_{p,g} \, \dot{\bar{n}}_g \quad . \tag{6.35}$$

Equation (6.34) is solved by a Runge-Kutta procedure when expressed as

$$\dot{\bar{P}}_g = \frac{E/\bar{P}_g - D \, \bar{P}_g - F}{A + B/\bar{P}_g^2} \quad , \tag{6.36}$$

where A,...,F are taken constant and known for a given time step.

The values of the specific heats, $\bar{c}^{g}_{p,g}$, $\bar{c}^{\ell}_{p,g}$ $\bar{c}^{g}_{p,v}$, and $\bar{c}^{\ell}_{p,u}$, are taken to vary only with temperature (a "semi-perfect" gas assumption) and are evaluated using the correlations of Van Wylen and Sonntag (1973, p. 683).

$$\bar{c}_p = (a + b\,\theta^p + d\,\theta^q + e\,\theta^r)/R_u \qquad (6.37)$$

where $\theta = T/100$, T is in °K, and c_p is the dimensionless specific heat. Values of the constants are:

	a	b	d	e	p	q	r
H_2O	34.19	-43.868	19.778	-0.88407	0.25	0.5	1
O_2	8.9465	0.0048044	-42.679	56.615	1.5	-1.5	-2
N_2	9.3355	-122.56	256.38	-196.08	-1.5	-2	-3

These correlations are stated to be within an accuracy of less than 0.5 percent for temperatures (in degrees K) in the range $300 \leq T \leq 3500$. For temperatures below or above this range, the specific heats are taken as being constant at the values for T=300 or T=3500 respectively.

Air is treated as a mixture of nitrogen and oxygen such that $c_p(\text{air}) = 0.21\, c_p(O_2) + 0.79 c_p(N_2)$. Since the liquid temperature is taken to be fixed for a given problem, $c^{\ell}_{p,g}$ and $c^{\ell}_{p,v}$ do not vary and are evaluated once from (6.37) for the specified liquid temperature. The specific heats dependent on T_g are evaluated each time (6.36) is solved knowing the dimensional value of the gas temperature $T_g = \bar{T}_g \cdot T_1$ where from (6.21)

$$T_g = \bar{T}_g \cdot T_l = \frac{\bar{P}_g \bar{a}_o^3}{\beta \bar{n}_g} \cdot T_l \quad . \qquad (6.38)$$

The specific heats are evaluated each time Equation (6.36) is solved using this value of T_g based on the old value of $\bar{P}_g$. If isothermal conditions are assumed, Equation (6.22) is used to solve for $\bar{P}_g$.

The quantity of noncondensible gas in the bubble at any time is obtained by rewriting equation (6.13). The interval of integration in (6.13) can be split into two intervals to separate out the current time step:

$$I(0,\bar{t}) = I(0,\bar{t}-h) + I(\bar{t}-h,\bar{t}) \quad , \qquad (6.39)$$

where h is the time step size and

$$I(a,b) = \int_a^b \frac{\dot{\bar{n}}_g}{\left[\int_{\bar{x}}^b \bar{a}_o^4 \, d\bar{y}\right]^{1/2}} \, d\bar{x} \quad . \qquad (6.40)$$

The second integral is evaluated to avoid the singularity in $(t-x)^{-1/2}$:

$$I(\bar{t}-\bar{h},\bar{t}) = \int_{\bar{t}-h}^{\bar{t}} \frac{\dot{\bar{n}}_g}{\tilde{\bar{a}}_o^2 \, (\bar{t}-\bar{x})^{1/2}} \, dx =$$

$$= \frac{-2 \, \dot{\tilde{\bar{n}}}_g}{\tilde{\bar{a}}_o^2} (\bar{t}-\bar{x})^{1/2} \Big|_{\bar{x}=\bar{t}-h}^{\bar{x}=\bar{t}} = 2\sqrt{h} \, \dot{\tilde{\bar{n}}}_g / \tilde{\bar{a}}_o^2 \quad . \qquad (6.41)$$

where the tildes denote an average values over the interval from $\bar{t}-h$ to $\bar{t}$. We approximate these average values as:

$$\tilde{\dot{n}}_g \approx \dot{n}_g(\bar{t}) \quad , \tag{6.32}$$

$$\tilde{a}_o \approx \frac{\bar{a}_o(\bar{t}) + \bar{a}_o(\bar{t}-h)}{2} \quad . \tag{6.43}$$

Expression (6.42) for $\tilde{\dot{n}}_g$ was found to be better numerically than the mean of the values of $\dot{n}_g$ at $\bar{t}$ and $\bar{t}-h$. Then

$$I(\bar{t}-h,\bar{t}) \approx 8\sqrt{h}\ \frac{\dot{n}_g(\bar{t})}{[\bar{a}_o(\bar{t}) + \bar{a}_o(\bar{t}-h)]^2} \tag{6.44}$$

Equations (6.13, 6.39, 6.44) can be combined to provide an expression for $\dot{n}_g(t)$:

$$\dot{n}_g(\bar{t}) = \frac{[\bar{a}_o(\bar{t}) + \bar{a}_o(\bar{t}-h)]^2}{8\sqrt{h}} \left[\frac{1-\bar{C}^v(\bar{t})}{\alpha} - I(0,\bar{t}-h)\right] \quad , \tag{6.45}$$

where

$$\alpha = \frac{1}{3\ C_\infty^v} \left[\frac{r_{b_o}^2}{\pi\ \tau\ D_g}\right]^{1/2} ,$$

$$I(0,\bar{t}-h) = \int_0^{\bar{t}-h} \frac{\dot{n}_g(\bar{x})}{\left[\int_{\bar{x}}^{\bar{t}-h} \bar{a}_o^4(\bar{y})\ d\bar{y}\right]^{1/2}}\ dx \quad . \tag{6.46}$$

Equation (6.45) is used to calculate $\dot{\bar{n}}_g(\bar{t})$. The value of $\bar{n}_g(t)$ can then be obtained by a simple trapezoidal rule integration:

$$\bar{n}_g(\bar{t}) = \bar{n}_g(\bar{t}-h) + h[\dot{\bar{n}}_g(\bar{t}) + \dot{\bar{n}}_g(\bar{t}-h)]/2 \quad .$$

A higher order approximation could also be easily implemented. The values of $\dot{\bar{n}}_g$ and $\bar{n}_g$ are utilized in solving (6.36) or (6.22).

The algorithm employed can be summarized as follows:

1. At a time t*, all variables are known.

2. At time t*+h, the bubble dynamics equations are solved for $\bar{a}_o$, $\dot{\bar{a}}_o$ with all other parameters evaluated at t=t*. Then, the differential equations for all other components of the bubble surface equation (see Equation 3.10) are solved with the same evaluation of the parameters at the preceding time step.

3. Equation (6.45) for $\dot{\bar{n}}_g(t^*+h)$ is solved using the values of $\bar{a}_o$, $\dot{\bar{a}}_o$ at t*+h and the value of $\bar{P}_g$ at t*. It is then integrated to obtain $\bar{n}_g(t^*+h)$.

4. Equation (6.36) or (6.22) is solved for $\bar{P}_g$ using the values of $\bar{a}_o$, $\dot{\bar{a}}_o$, and $\bar{n}_g$ at t*+h and the values of the other parameters at t*. Use of Henry's law yields $\bar{C}^v(t^*+h)$.

5. Iteration is performed between steps 3 and 4 above until the calculated values of $\bar{P}_g$ for successive iterations are within a specified difference - or error bound. During this

process, the "most current" values of the variables are used at each step of the iteration.

6. When the criterion of step 5 is satisfied, all variables are known at t=t*+h and the calculation returns to step 1 with all variables known at time t=t*+h.

This process is continued until a desired time is reached. Figure 6.1 shows a flow chart of the program GASCLD based on the above algorithm.

6.4 Numerical Examples and Interpretation

A series of numerical cases were run on a VAX 11/750 computer using the developed program GASCLD. Only a few variables were investigated in order to demonstrate the capabilities of the code and to gain some insight into the influence of gas diffusion on bubble cloud dynamics. Figures 6-2 to 6-11 illustrate the results obtained. Bubble growth has been considered following a sudden ambient pressure drop. Two arbitrary particular values of the initial and subsequent ambient pressures were considered. In these figures comparisons are made between the behavior of an isolated dynamic-controlled bubble (no gas diffusion), an isolated bubble with gas diffusion, and a multibubble configuration with gas diffusion. A preliminary investigation of the influence on bubble growth of the initial concentration of dissolved gas in the liquid and of the ratio ϵ between characteristic bubble size and characteristic interbubble distance was also conducted.

Figures 6-2 to 6-5 each show a collection of cases of normalized bubble radii, $\bar{r} = r/r_{b_o}$, versus normalized times,

$\bar{t} = t/r_{b_o}\sqrt{\rho/(P_o - P_{inf})}$. In all four figures the isolated bubble cases are presented for reference. When mass transfer is neglected at the bubble-liquid interface a polytropic compression law,

$$P_g \; V^k = (P_g \; V^k) \text{ at } t = 0 \quad , \tag{6.48}$$

has been adopted. For an isolated bubble comparisons are made between the two extreme cases of no-gas diffusion: k = 1 (isothermal behavior) and k =1.4 (adiabatic behavior), and the case where the mass transfer and the energy balance equations are solved. For both cases considered here the adiabatic assumption in the absence of gas diffusion gives closer results to the solution of the diffusion problem. Based on the perfect gas law (6.15), this result is to be expected when during the bubble growth the increase in the number of moles of gas entering the bubble overcomes the decrease in gas temperature in the product (n_g T_g) leading therefore PV to grow with V (and not remain constant as k = 1 presumes). As we will see later in Figure 6.10 the temperature drops in the initial phase of the growth but recovers rapidly to maintain its value later in the bubble growth history. In addition, with our assumptions of no direct heat exchange between the content of the bubble and the liquid, the initial phase of the bubble growth is adiabatic. Comparison between isothermal, adiabatic and complete solution results show that deviation between the three cases is more significant when the growth is pursued for a much longer nondimensional time. This is the case in Figure 6.2 where, the pressure drop being less violent than in Figure 6.3, the growth rate is slower.

Comparisons between two initial gas concentrations can be seen in Figure 6.2 As expected, for an isolated bubble, an increase in the initial gas concentration, C_o, leads to an increase in the bubble radius attained at any time mostly due to an increase in the amount of moles transferred. (As we will see below in Figures 6.6 to 6.8, this change in C_o affects more significantly the effective polytropic coefficients. In a multibubble system interactions become very significant when the bubble sizes approach the interbubble distance. This is reflected by an oscillation in the bubble radius similar to that obtained in the heat transfer problem. Initially during the bubble growth the modification of the imposed pressure field by the presence of the other bubbles in the cloud reduces the bubble size achieved. At any instant the bubble radius is smaller than that of an isolated bubble. Two such radii are shown in the figures (R_2 and R_3) and correspond to the sketch in Figures 3.1 and 8.5. R_2 is the measurement of the bubble radius along the cloud center direction, while R_3 is measured in the opposite direction. Figure 6.3 shows the variation of these two dimensions as functions of time for a set of values of the spacing parameter ε. It is obvious from this figure that bubble interaction and deformation increase when the spacing between bubbles is reduced. The presence of multiple bubbles introduces a flattening of the bubble on its side closer to the cloud center. This side has a slower growth than the other side. The computed shrinking and oscillation of the bubble shape in the latter stage of the growth needs to be investigated to assure it does not result from a failure of the asymptotic approach. This behavior, seen in Figure 6.3 for ε =0.2, occurs at larger times for the smaller values of ε. All the computations presented here were performed with a logarithmic increment in the time steps. Figures 6.4 and 6.5 present some of the results of

Figures 6.2 and 6.3 with logarithmic time scales. A smoother behavior of the curves can be seen with these scales.

Figures 6.6 to 6.10 show for various conditions the time variations of the effective gas polytropic coefficients when gas diffusion is taken into account. The two effective coefficients used in these figures are defined as follows. The total effective polytropic coefficient, K is defined base on the Relation (6.48) and is computed at each time step using

$$K = (\text{Log } P_g/P_{g_o})/(\text{Log } V/V_o) \quad . \tag{6.49}$$

The local effective polytropic coefficient, K_ℓ, is based on a compression law which applies locally between two computation steps

$$(P_g \ V^{K_\ell})_i = (P_g \ V^{K_\ell})_{i+1} \quad . \tag{6.50}$$

It is therefore computed using the relation

$$K_\ell = (\text{Log } P_{g_i}/P_{g_{i+1}})/(\text{Log } V_i/V_{i+1}) \quad . \tag{6.51}$$

Figures 6.6 to 6.9 show that the total effective polytropic coefficient drops rapidly, at the beginning of the growth from the value 1.4 to a minimum value which depends on the initial gas concentration, C_o. As seen in the figures this value can become significantly smaller than one. Since at these later times the gas temperature becomes practically constant, the lower is the minimum value of K the stronger is the relationship between the number of moles of gas diffusing into the bubble and the bubble volume change. This can be reflected by the approximate equation

$$(V/V_o)^{1-K} = n_g/n_{g_o} \quad . \qquad (6.52)$$

derived from the ideal gas law with T_g assumed constant. This might explain why the minimum value of K is smaller when C_o is increased. The local effective coefficient of compression, K_ℓ decreases much more significantly than K. From the initial value of 1.4, K_ℓ decreases practically to 0 later during the growth expressing the fact that P_g and T_g become practically constant during the growth.

The variation of both K and K_ℓ are much more sensitive to the initial conditions, (such as initial gas concentration, C_o, and initial bubble size, R_o), than the actual bubble radius history. This is probably due to the fact that K and K_ℓ express only the gas thermodynamic behavior while the bubble radius behavior includes gas and vapor thermodynamic and dynamic phenoma (pressure drop). These results are well illustrated in Figure 6.9 where the influence of the initial bubble radius is seen. No difference between the two cases of initial bubble radii was seen in the radii versus time curves. However, the effective gas polytropic coefficients are very much dependent on these initial conditions. Figure 6.10 presents the temperature histories for these two initial bubble radii. This figure is typical of all temperature versus time curves. Initially, the temperature drops significantly and attains a minimum. Later, the temperature inside the bubble recovers to reach the initial temperature and remains practically constant. The minimum temperature achieved and the time to achieve this minimum are functions of the initial conditions. This result is related to the variations of K and K_ℓ. The influence of temperature change on the effective coefficients K can be seen

in Figure 6.11 where the solution based on the energy equation is compared with that where the temperature was imposed to remain constant.

The above results should be extended to actual pressure fields where the pressure variations are more realistic than a sudden pressure drop and, more importantly, to longer computation times where gas diffusion effects become more significant. For such more practical situations the influence of the magnitude of the pressure drop, $P_o - P_{inf}$, should be investigated carefully.

7.0 CONTINUUM MEDIUM APPROACH

7.1 Introduction

One major assumption of the approach presented above is that in first approximation the imposed ambient pressure is assumed to be instantaneously transmitted to the vicinity of each bubble in the cloud. Therefore, both the compressibility of the bubble medium and the influence of the liquid motion generated by the other bubbles on the dynamics of the bubble considered were neglected in the first order approximation. This limits the validity of the study to very low void fractions. The incompressibility assumption is valid as long as the fluid velocity does not approach the speed of sound. For single bubble dynamics, this does not usually happen until the final phase of the collapse. Here, however, two factors contribute to limit the validity of the assumption. First, the rate of implosion is higher for a cloud than for a single bubble, and second, more importantly, the velocity of sound drops considerably when the void fraction increases. This underlines the need to account for the behavior of the cloud as a whole in order to determine a more accurate value of the local pressure driving the collapse of the individual bubbles. In addition, this would have the advantage of limiting, for the following orders of approximations, the number of bubbles directly influencing the considered one through a time delay of the propagation of the information from one bubble to another. Indeed, the asmyptotic theory shows that the effective parameter of the expansions is εc_1, (where c_1, defined by (3.13), is a direct function of the number of bubbles), rather than $\varepsilon = r_{b_o}/\ell_o$. Introducing a motion equation for the bubbly medium would limit the number of influencing bubbles to those in

the direct vicinity of the considered one, through a time delay of the propagation of the information from one bubble to another. In summary, if we account for a motion equation in the cloud medium, the first order approximation of the preceding approach becomes more accurate, and as a consequence the following corrections will be smaller, making the approach valid for higher void fractions, α.

7.2 Volume Average Method

Basically the classic methods used to describe a two-phase medium are not much different from the singular perturbation method presented above. The final description deals only with the macroscale of the cloud.

The description of the macroscale of the cloud can be obtained by averaging the various physical quantities defined in the microscale. The two-phase medium is assumed to be constituted of "particles" containing the host liquid and few bubbles. This "particle" is small enough to be able to distinguish the gaseous and liquid constituents, but large enough to enable one to define significant volume average quantities in the two-phase continuum. Therefore, each "particle" appears in the macroscale as a fluid point M allotted various physical and kinematic properties: $\alpha(M,t)$ is the local void fraction, $\rho_m(M,t)$ is the local medium density, $U_m(M,t)$ is the velocity, and $P_m(M,t)$ the pressure, ...,etc. In such a volume averaging description, if V_p is the volume of the particle, $X(M,t)$ the considered average quantity and $x(m,t)$ its local value in the microscale, we have the following definition:

$$X(M,t) = \frac{1}{V_p} \int_{V_p} x(m,t) \; d\,V \qquad (7.1)$$

The density of the medium is therefore defined by the relation:

$$\rho_m(M,t) = \rho_\ell \left[1-\alpha(M,t)\right] + \rho_g \, \alpha(M,t) \quad . \qquad (7.2)$$

The liquid is assumed to be incompressible and ρ_ℓ constant. The void fraction, $\alpha(M,t)$, is defined as the relative volume of gas in the particle. Usually $\rho_g \alpha$ is neglected, and the density of the medium is written:

$$\rho_m(M,t) \simeq \rho_\ell \left[1 - \alpha(M,t)\right] . \qquad (7.3)$$

If $\underline{U}_\ell(M,t)$ is the average velocity of the liquid in the particle and $\underline{U}_g(M,t)$ the average velocity of the gas, we obtain comparable results to (7.2) and (7.3):

$$\rho_m \, \underline{U}_m = \rho_\ell \underline{U}_\ell \, (1-\alpha) + \rho_g \, \underline{U}_g \, \alpha \quad , \qquad (7.4)$$

$$\rho_m \, \underline{U}_m \simeq \rho_\ell \underline{U}_\ell \, (1 - \alpha) \quad , \qquad (7.5)$$

and combining with (7.3),

$$\underline{U}_m \simeq \underline{U}_\ell \, . \qquad (7.6)$$

The continuity equation is obtained by writing the mass conservation of a volume of the bubble medium followed during its motion. Using the average quantities defined above we can write:

$$\frac{d}{dt} \int_{V(t)} \rho_m \, d \quad = \int_{V(t)} \left[\frac{d\rho_m}{dt} + \rho_m \, \nabla \cdot \underline{U}_m \; d\,V \right] = 0 \, . \qquad (7.7)$$

Here the material derivative pertains to the medium velocity U_m or, with our assumptions, to $\underline{U}_\ell$ because of Equation (7.6):

$$d/dt = \partial/\partial t + \underline{U}_\ell \quad \nabla \quad . \tag{7.8}$$

Since Equation (7.7) is valid for any volume V, we obtain the general equation:

$$\frac{\partial \rho_m}{\partial t} + \nabla \cdot (\rho_m U_m) = 0 \quad . \tag{7.9}$$

A similar equation can be written concerning the number of bubbles, n(M,t). Neglecting any complete bubble disappearance or sudden generation, as well as bubble splitting and coalescence, we can write:

$$\frac{Dn}{Dt} + n \nabla \cdot \underline{U}_g = 0 \quad , \tag{7.10}$$

the material derivative, D/Dt, being defined as:

$$D/Dt = \partial/\partial t + \underline{U}_g \nabla_{\cdot} \quad . \tag{7.11}$$

The momentum equation of the bubbly medium can be obtained in the same manner by using the momentum equations of both constituents in the microscale and integrating over the "particle" volume V_p. If we neglect the viscous forces, this can be written:

$$\int_{V_p} \left[\rho_i \frac{d_i U_i}{dt} + \Delta P_i \right] d V = 0 \quad , \tag{7.12}$$

the index i designating the liquid or the gaseous phase depending on the position of the element of volume dV in the microscale. If we account for the incompressibility of the liquid this equation becomes:

$$\rho_\ell (1 - \alpha) \frac{d\underline{U}_\ell}{dt} + \rho_g \alpha \frac{D\underline{U}_g}{Dt} - \rho_g \int_{V_p} \underline{U}_g \nabla \cdot \underline{U}_g \, dV \int_{V_p} \Delta P_i dV = 0 \qquad (7.13)$$

If we neglect the gas contribution to the momentum, and we account for (7.6) we obtain the following approximate classical momentum equation:

$$\rho_\ell (1 - \alpha) \frac{d\underline{U}_m}{dt} + \nabla P_m = 0 \quad . \qquad (7.14)$$

where it is assumed that

$$\int_{V_p} \Delta p_i \, d V = \int_{A_p} p_i \, \underline{n} \, ds \simeq V_p \cdot \nabla P_m \quad . \qquad (7.15)$$

7.3 Bubble-Liquid Relative Motion

The only equation left is that giving the bubble translation velocity, $\underline{U}_g$, which reflects the interaction between the two phases of the bubbly medium. The study of this equation is a whole subject of research in itself. Several contributions exist which have dealt with more and more complicated situations. When viscous drag is neglected, a very interesting general expression for the motion of a deformable bubble in a nonuniform potential flow was derived by Landweber and Miloh (1980). If we admit, however, that the liquid flow around an isolated bubble is linearly accelerated, and that the bubble remains in first approximation spherical, we can write, neglecting the bubble mass, a simpler equation as follows:

$$\frac{D\underline{U}_g}{Dt} - 3\frac{D\underline{U}_\ell}{Dt} = 3\frac{\dot{a}_0}{a_0}(\underline{U}_\ell - \underline{U}_g) \ . \qquad (7.16)$$

In this equation, the virtual mass of the bubble is considered to be $2/3\pi a_0^3 \rho_\ell$ and the material derivative is related to the bubble velocity as discussed by Prosperetti and Van Wijngaarden (1976).

When other bubbles are present in the flow, corrections are to be introduced in this expression, following Landweber's calculations. Van Wijngaarden (1976) performed similar corrections for a rigid sphere and obtained the expression:

$$\frac{d}{dt}\left[\frac{1}{2}(1 + 2.78\ \alpha)(\underline{U}_g - \underline{U}_\ell)\right] = (1 - \alpha)\frac{d}{dt}\underline{U}_\ell \ . \qquad (7.17)$$

A relationship similar to (7.16) or (7.17) was implemented in the program CLDMAIN2 to account for gravity effects.

7.4 Micromorphic Continuum Description

In classical continuum mechanics the fluid is described geometrically by a field point M and kinematically by a velocity field $\underline{U}(M)$. The averaging approach of the cloud medium, as described in the preceding paragraph, is in this sense classical. However, when a medium contains microstructure, as is the case for a bubbly medium, a more refined description can be obtained by assigning to M, in addition to the macroscale velocity, $\underline{U}(M)$, other quantities which reflect the microscale behavior in the "particle". In a first gradient theory, in addition to the velocity field, $\underline{U}(M)$, a field of the gradients of relative velocities in the microscale scale, X, is added which defines kinematically the medium. The description can be

further refined by using higher order gradient theories. Germain (1973) considered such approaches and, using the method of virtual power, was able to derive the equation of motion of the continuum medium accounting for the macrostresses, $\underline{\underline{\sigma}}$, and the microstresses, $\underline{\underline{S}}$.

In a first gradient theory the velocity in the microscale can be written as

$$\underline{U}'(m) = \underline{U}(M) + \underline{\underline{X}}(M) \cdot \underline{Mm} \quad , \qquad (7.18)$$

where m is a point in the microscale (see Figure 7.1). Consequently the acceleration, $\underline{\Gamma}'$, of m is derived and, by equating at dynamical equilibrium the virtual power of all the internal and external forces acting on the considered particle (volume V_p) to the material derivative of the virtual power of mass velocity of V_p, one obtains a dynamical equation of the medium relating $\underline{\underline{S}}$, $\underline{\underline{\sigma}}$, and $\underline{\Gamma}'$.

To define $\underline{\underline{X}}$ we consider the motion on a scale which is of the same order as the microstructure. To do so for a bubble cloud, let us divide the cloud medium into fluid "cells" each enclosing an isolated bubble. In addition, we assume for simplicity that the bubble center of mass and the "cell" center of mass coincide at the considered time. Let $\underline{U}(M)$ be the velocity in M induced by the rest of the cloud in absence of the bubble, and $\underline{V}(B)$ the velocity of the bubble center, B. $\underline{U}(M)$ would be the value of the velocity field assigned to M in a classical fluid mechanics description.

The bubble radius is a_o and its variations with time are given by the Rayleigh Plesset equation. This radial motion of

the bubble surface induces at a point m of the cell (Figure 7.1) a velocity of value $(u_r \cdot \underline{e}_r')$, where $\underline{e}_r'$ is the unit vector of the direction Mm. The total velocity u', at m is:

$$\underline{u}'(m) = \underline{U}(M) + \frac{\dot{a}_o a_o^2}{r'^2} \cdot \underline{e}_r' + \nabla \left[\frac{a_o^3}{2r'^2} (\underline{U}(M) - \underline{V}(B)) \cdot \underline{e}_r'\right] + \ldots \quad (7.19)$$

where r' is the distance between M and m. The second term in this expression is a source term due to the spherical bubble oscillations, while the last term is a dipole due to the slip velocity between the spherical bubble and the fluid, and could include first order corrections of the bubble shape. For further corrections for nonsphericity of the bubble, other terms (singularities of higher orders) have to be included. By differentiating (7.19) with respect to time and space one can define an acceleration vector, Γ', and a strain rate tensor, D'. Following Germain's approach, and using the principle of virtual powers, one could then derive an equation of motion of the cloud medium. We decided instead to start with a first gradient theory and replace (7.20) by its Taylor expansion. We follow in doing so the first calculations done by Michelet (1980) in his graduate thesis.

The basic approximation used in this linearization approach is based on the fact that Equation (7.19) is only valid in the liquid portion of the "cell" ($r > a_o$). It seems therefore logical to write the velocity at m, close to the bubble boundary, as a Taylor expansion of the value of u' computed on a point of the bubble surface, S, (figure 7.1). This has the advantage of eliminating the singularity of (7.19) for r' = 0. The obtained expression for u'(m) is then:

$$\underline{u}'(m) \approx \underline{U}(M) + \left[3a_o + 4V_t \cos\theta - r' \left(2 \frac{\dot{a}_o}{a_o} + 3 \frac{V_t}{a_o} \cos\theta\right)\right] \underline{e}_r +$$

$$+ \left[2 V_t \sin\theta - \frac{3}{2a_o} r' V_t \sin\theta\right] \underline{e}_\theta \quad , \qquad (7.20)$$

where $V_t = \left|\underline{V}(B) - \underline{U}(M)\right|$.

When V_t is not accounted for, the expression of u'(m) reduces to a form comparable to (7.18), which is much easier to interpret than equation (7.20). In that case we obtain:

$$\underline{u}_o'(M') \approx \underline{U}(M) + \underline{\underline{X}} \cdot \underline{Mm} + \underline{\underline{\alpha}} \cdot \underline{e}_r \qquad (7.21)$$

where $\underline{\underline{X}}$ and $\underline{\underline{\alpha}}$ are both tensors assigned to M and defined as:

$$\underline{\underline{X}} = -2 \frac{\dot{a}_o}{a_o} \underline{\underline{I}}, \quad \underline{\underline{\alpha}} = 3 a_o \underline{\underline{I}} \quad , \qquad (7.22)$$

$\underline{\underline{I}}$ is the spherical unit tensor. We notice that in comparison to (7.18), which describes a first gradient homogeneous deformation, in (7.21) there is in addition to the gradient tensor, $\underline{\underline{X}}$, a tensor $\underline{\underline{\alpha}}$ reflecting the presence of a source in the cell. Equation (7.20) reflects in addition to this the presence of a dipole. It could be written as

$$\underline{u}'(m') \approx \underline{U}(M) + \underline{\underline{X}} \cdot \underline{Mm} + \underline{\underline{X}}' \cdot \left|\underline{Mm}\right| \underline{e}_z + \underline{\underline{\alpha}} \cdot \underline{e}_r + \underline{\underline{\alpha}}' \cdot \underline{e}_z$$

$$+ \left(6V_t \cos\theta - \frac{9}{2a_o} r' V_t \cos\theta\right) \underline{e}_r \quad , \qquad (7.23)$$

where $\underline{e}_z$ is the unit vector of the direction of $\underline{U}$ and $\underline{V}$; $\underline{\underline{X}}'$ and $\underline{\alpha}'$ play the same role as $\underline{\underline{X}}$ and $\underline{\underline{\alpha}}$ but are applied just to the direction of the translation. The last inhomogeneous term is more difficult to put in simple form.

From the expression (7.20) we can now compute the acceleration, then apply the principle of virtual power, to obtain the equation of motion. Here again in the absence of translation velocity V_t, the results are simpler to interpret. In the absence of viscous effects these results can be written as follows:

$$\rho_m \left[\frac{d\underline{U}}{dt} + 3\,\underline{K}\,\left(\ddot{a}_o - 2\,\frac{\dot{a}_o^2}{a_o}\right) \right] = -\nabla p \quad , \qquad (7.24)$$

where $\underline{K}$ depends unfortunately on the cell geometry

$$\rho_m\,\underline{K} = \int_{V_c} \rho_i\,\underline{e}_r \; dV \quad . \qquad (7.25)$$

If the cell and the bubble are symmetrical with regard to the center of mass M, then $\underline{K} \equiv \underline{0}$, and (7.25) reduces to the classical equation of motion (7.14). Although it is unfortunate that the cell shape seems to play a role in the model, $\underline{K}$ might rather reflect an effect of the nonsphericity of the bubble.

When V_t is taken into account a whole series of "inertia" integrals like (7.25) appear in the calculations. In order to see what such a model might indicate we considered the case of a spherical bubble in a spherical cell. In this case the motion equation becomes:

$$\rho_m \left\{ \frac{d\underline{U}}{dt} + \frac{\dot{a}_o}{a_o} \left[3 + \frac{3}{4}\,\frac{R}{a_o} - 6\,\frac{a_o}{R} + 0(\alpha)\right](\underline{V} - \underline{U}) \right\} = -\nabla p. \qquad (7.26)$$

Here, R is the radius of the cell, and if we write $R \approx a_o \alpha^{-1/3}$, we have the result:

$$\rho_m \left\{\frac{d\underline{U}}{dt} + 3\,\frac{\dot{a}_o}{a_o}\left[\alpha^{-1/3}\left(\frac{1}{4} + \alpha^{1/3} - 2\alpha^{2/3} + \ldots\right)\right](\underline{V} - \underline{U})\right\} = -\nabla p \qquad (7.27)$$

This surprising result (dependence on $\alpha^{-1/3}$) might be compared with that obtained for the apparent viscosity of a bubbly flow, which is $4\mu/3 \cdot \alpha^{-1}$ (Batchelor (1967), Van Wijngaarden (1972)). In addition, due to the linearization of the velocity field (first gradient theory) this model loses it validity for low α's.

7.5 Example of a Spherically Symmetrical Cloud

Let us consider a finite-sized spherical cloud of bubbles and define its radius, R(t), at time t, as the position of the last outer shell of bubbles. The space is therefore divided into two regions. For $r > R(t)$, the medium is an incompressible liquid of density ρ_ℓ, while the interior of the sphere, $r<R(t)$, is filled with a two-phase medium which can be defined as in Section 7.3. We define at a point M(r), a radial liquid velocity $u_\ell(r,t)$ and a radial bubble translation velocity $u_g(r,t)$. Similarly, we define a local void fraction $\alpha(r,t)$, density $\rho_m(r,t)$, bubble radius $a_0(r,t)$, number density $n(r,t)$, and medium velocity $u_m(r,t)$. The matching between the two media states that at $r = R(t)$ there is a continuity of velocities and pressures:

$$R(t) = u_g(r,t) \quad , \qquad (7.28)$$

$$P_\ell(R,t) = \lim_{r' \to \infty} p'(R, r', t) \quad , \qquad (7.29)$$

where r' is the distance in the microscale between a bubble center and a cell field point. The continuity and momentum equations in the liquid medium (r>R(t)) are easy to solve and give, after neglecting viscous effects:

$$u_\ell(r) = \dot{V}_g/4\pi r^2 \quad , \tag{7.30}$$

$$\frac{\partial P_\ell}{\partial r} = -\frac{\rho_\ell}{4\pi}\left[\frac{\ddot{V}_g}{r^2} - 2\frac{\dot{V}_g^2}{r^5}\right] \quad . \tag{7.31}$$

V_g is the total volume of the bubbles in the cloud,

$$V_g = 4\pi \int_0^R \alpha\, r^2\, dr \quad . \tag{7.32}$$

Inside the bubbly medium, due to the spherical symmetry, the continuity equation also gives

$$u_\ell(r,t) = \frac{\dot{V}(r)}{4\pi r^2} \; ; \; r < R(t) \quad , \tag{7.33}$$

with

$$V(r) = 4\pi \int_0^r \alpha(x,t)\, x^2\, dx \quad . \tag{7.34}$$

If we are interested in the problem of the collapse of the cloud under an imposed ambient pressure variation, $P_\infty(t)$, (20) can be integrated between the cloud radius and infinity to give:

$$-P_\infty(t) + P_\ell(R) = \frac{\rho_\ell}{4\pi}\left[\frac{\ddot{V}_g}{R} - \frac{1}{2}\frac{\dot{V}^2}{R^4}\right] . \tag{7.35}$$

Using (7.29), $P_\ell(R)$ can be related to the behavior of any individual bubble of radius a_0 in the last outer shell of the

cloud, using the Rayleigh-Plesset equation. Equation (7.35) becomes:

$$-P_\infty(t) + P_v + P_{g_0}\left(\frac{a_0}{a}\right)^{3k} =$$

$$\frac{\rho_\ell}{4\pi}\left[\frac{\ddot{V}_g}{R} - \frac{1}{2}\frac{\dot{V}_g^2}{R^4} + a_0\ddot{a}_0 + \frac{3}{2}\dot{a}_0^2\right] \quad . \qquad (7.36)$$

The cloud radius motion can be obtained by using an equation of the bubble motion, for example, (7.16). This gives the following second relation between R, a_0, and V_g:

$$\ddot{R} + 3\frac{\dot{a}_0}{a_0}\dot{R} = \frac{3}{4\pi R^2}\left[\ddot{V}_g - \frac{\dot{V}_g^2}{2R^3} + \frac{\dot{a}_0}{a_0}\dot{V}_g\right] \quad . \qquad (7.37)$$

A third equation, in addition to (7.36) and (7.37), is needed to solve for R, a_0, and V_g. Without an assumption on a proportionality between $V_g(t)$ and $a_0(t)$ or without penetrating the cloud and solving for all $a_0(r,t)$ to determine V_g, there is no hope of solving the problem. We do not think the proportionality assumption is generally justifiable even if at $t = 0$ all bubbles in the cloud have the same size, since $P(r,t)$ would not generally be the same for any location r at a subsequent time. However, an assumption similar to that done by Morch (1980) could be done stating the $\dot{V}_g = n\,\pi a^2\dot{a}$ where n is the number of bubbles in the outer shell. The need in general to solve the whole problem is to be expected and is very important because it shows that defining the cloud by just one parameter, as a unique void fraction, is not sufficient to describe its dynamics. Number and bubble size distribution are other important variables to consider.

The problem presented above can be solved by combining the multibubble approach with the global descriptions presented in Sections 3.1 and 3.3. The approach of d'Agostino and Brennen (1983) is very close to that presented in this section with the additional assumption of small radius and pressure oscillations and the neglect of bubble-liquid relative motion and bubble interactions.

8.0 CLOUD CAVITATION THROUGH A SIMULATED MULTIBUBBLE SYSTEM

8.1 Description of Experiment

Since it is difficult to measure the quantities involved within an actual cavitation cloud produced, for example, in a cavitation tunnel, we have resorted to the same techniques used to study single bubble collapse, namely spark generated bubbles. The fast discharge of high voltage condensors across two submerged electrodes produces a bubble which, once attaining its maximum volume, is not in equilibrium with the ambient pressure. The growth, rapid collapse, and motion of the bubble can be recorded by high-speed photography. In addition, the pressure fluctuations caused by the bubble's dynamics can be monitored by means of a pressure transducer. The idea we have used based on this principle consists of placing a system of nearby solid walls which, through reflections, generates a fictitious cloud of bubbles composed of the actual bubble and its images. We know from the method of images in potential flows, that solid walls behave schematically as mirrors. For this study, wall structures which depict symmetrical configurations of $N = 4, 8, 12,$ and $N > 12$ bubbles were used.

A vacuum/pressure tank was built containing the electrodes, transducer, hydrophone, and one of the various multiple wall structures. The location of the spark gap was varied in the test tank in order to control β, the ratio of the maximum characteristic radius of the bubble produced, R_o, to the distance between the electrode tips and the apex of the wall structure, d_s. β is directly related to ε, the ratio between bubble characteristic radius and the bubble spacing. This relation is a simple factor of proportionality which is geometry

dependent. The spark-generating system was capable of obtaining a voltage charge up to 16 kV on a 0.95 μfd capacitor. For the purpose of these tests, a charge voltage of 12 kV was consistently used. The system was made more versatile through the addition of an electronic circuit which allows it to fire at a controlled repetition rate which could be of a high frequency. The relative locations between the components were varied independently so as to study the effect of changing the distance between the bubble and the walls.

The signals from the transducers and/or the hydrophone were captured on a Nicolet 2090 digital oscilloscope and then stored on floppy disks for later analysis. This oscilloscope has a maximum digitizing rate of 50 ns per point and a bandwidth of up to 7 MHz with a vertical resolution of 0.4 percent. The oscilloscope was triggered either from the initial pressure pulse caused by the spark or from a signal from a variable time delay circuit if the collapse of the bubble was to be investigated using an expanded time scale. A Digital Equipment Corp. VAX 11/750 computer was interfaced with the oscilloscope allowing the digitized pressure-time data to be analyzed with a Fast Fourier Transform. Figure 8.1 is a photograph of the overall spark bubble test facility showing the spark generator, test tank, and data acquisition equipment. Figure 8.2 is a photograph showing the test tank, the electrodes, transducer, and the multiple walls structure, in this case a cone. Figure 8.3 shows a representative curve of the pressure time signal for a spark induced bubble and Figure 8.4 the Fourier transform of the same data. For this particular case, the electrodes were located 2.25 in. from the top of the cone. The ambient pressure inside the tank was 13.1 kPa.

In this study, we tested a two-sided 90 degree corner (two solid plates perpendicular to each other), a three-sided 90 degree corner (three solid plates perpendicular to each other), a pentagonal base pyramid (five equi-sized triangles held together), and a cone with a 60 degree angle at its apex. A series of tests was run varying the distance from the apex of each of the wall structures to the electrodes. For all tests, the transducer was fixed at 6 inches below the electrodes, and the ambient pressure was approximately 14 kPa. High-speed movies were taken of the bubble growth and collapse for each test, and the bubble radius history was measured from the films.

8.2 Discussion of Results

To analyze the high-speed films of the spark generated bubbles, the model shown in Figure 8.5 was used consistently, and shall also be used for the results presented in this report. It shows the selected characteristic dimensions of the bubble shape measured relative to the initial bubble center, B, and the apex of the wall structure, point O. Point O also represents the center of the fictitious symmetrical cloud configurations. Variation of R_2 with time represents a measurement of the re-entering jet advancement. From the high-speed films, it was observed that for all tests, theoretically predicted, this re-entering jet formed and was always oriented in the direction of the apex, or cloud center, point O.

The details of this jet formation (time of formation and speed of advancement) differs significantly between the various test cases. Figures 8.6-8.9 show the time histories of R2 measured for several values of β in configurations of N = 4, 8,

12, and N > 12 bubbles. These configurations correspond to the wall structures of the 2-D corner, the 3-D corner, the pentagonal pyramid, and the 60 degree cone, respectively. All the curves have been normalized using the following procedure which tends to minimize the influence of spark energy variations and ambient pressure variations between one case and another. All bubble dimensions were normalized with an average maximum bubble radius R_o,

$$R_o = (2R_1 + R_2 + R_3)/4.$$

Time was also normalized using R_o, the measured absolute pressure in the tank, P_a, and the vapor pressure, P_v. The characteristic time used for this purpose is the Rayleigh time, τ_R,

$$\tau_R = R_o \sqrt{\frac{\rho}{P_a - P_v}} \quad ,$$

where ρ is the liquid density.

Close examination of these plots suggests that increasing the number of bubbles increases the strength of the re-entering jet, (R_2 becomes more negative). While the results from the simulated 4 bubble configuration show that the jet did not penetrate past the original center of the bubble, B, at all, the results from the simulated 12 bubble configuration and the circular cone tests show a penetration past this point of more than 40% of the maximum radius in some cases. Since the strength of the re-entering jet gives an indication of the degree of erosion from cavitation, these results verify the theoretical predictions about the increased cavitation erosion,

(increased strength of the collapse), from a cloud as compared to a single bubble.

Another trend which is noticeable from these results is that the jet penetrates further inward for higher values of β (or ε). This trend is shown in Figures 8.6-8.9 for all of the bubble configurations, but becomes much more noticeable for the higher density configurations (pyramid and cone tests) and the closer interacting bubbles. Since higher β's correspond theoretically to higher void fractions, this result agrees with the theory in that stronger collapses are occurring for these cases. This is also shown, perhaps more clearly, in Figure 8.10, which presents the variation of the minimum value of R_2 with β. One can also see that for the N=4 and N=8 bubble cases, a strong minimum also occurs at $0.09 < \beta < 0.11$. This minimum is noticed slightly for the N=12 bubble case and not at all for $N > 12$ bubbles. This result which proved to be hard to check with certainty with our testing facility indicates that there exist optimum values of β (or ε) for maximum collective effect (increased collapse intensity, erosion, or noise capability).

Figures 8.11-8.14 show the radius histories for R3, the measurement of the bubble radius along a direction toward the center of the cloud. From these results, one can see that this measurement is closely tied to R2. After the first collapse, R3 is seen to grow with increased β, and the bubble moves closer to the center of the cloud. Again, the net result is that the void fraction for the simulated cloud increases, subsequently increasing the strength of the collapse as long as the generated bubble does not touch the walls.

Figure 8.15 shows the period of bubble oscillation with respect to β for the various symmetrical configurations. It suggests a lengthening effect in the bubble period for small and large values of β, with a minimum period occuring in the region $.07 < \beta < .13$ for all the cases considered. One can see that the strongest minimum occured during the tests run with the 60° circular cone. The data from this figure and that of Figure 8.10 suggest an optimum value for β for maximum noise and erosion within the range considered for the test. This optimum seems to be at or near $\beta = 0.1$ for all of the bubble configurations. This result is consistent with the noise measurements performed using a hydrophone. Figure 8.16 shows the peak pressures plotted against β for each of the bubble configurations. One can see that the highest pressures were recorded within a small range of β, $(0.7 < \beta < 0.13)$. Also, the peak pressure increases with higher bubble density configuration (higher N here) as the theory predicts. This data again suggests the existence of an optimum value for β fairly close to that mentioned above. At this optimum value, the effect of high field pressures and large jet penetration seem to exist simultaneously.

For all of the tests considered above, the designated original center of the bubble was seen to move more or less significantly toward the center of the cloud. This is shown graphically in Figures 8.17-8.20, which show the motion of the bubble center. The distance, $\delta = R_3 - R_2$, is shown versus time for the different bubble configurations. One can see that very little bubble "center" motion was occuring before the first collapse. However, once collapsed, the bubbles both grow again and move rapidly toward the center of the cloud. The shift toward the center is greater for the higher density bubble

configuration. This, again, relates directly to the results discussed above, since large values for δ correspond to smaller values for R_2, or larger penetration of the re-entering jets. Figures 8.21 and 8.22 show typical sequences of pictures taken from high speed movies. Bubble deformation and motion towards the cone apex can be clearly observed.

8.3 Conclusions

A very extensive set of experiments was run to study the influence of bubble number and spacing on the dynamics of a simulated multibubble system. High speed photography and noise measurements allowed us to follow with precision the dynamics of spark-generated bubbles. However, as already discussed in Section 4.4, a major impediment to confident conclusions is the repeatibility of the tests. Indeed, the greatest source of error in the interpretation of the results is the amount of gas in the bubble which is not easily controlled. With this in mind, there is a strong indication that the collapse of the simulated cloud is very intense for an optimum value of ε, the ratio of characteristic bubble size to bubble interdistance. When ε increases (starting from zero) the bubble period of oscillation increases first, and the collapse pressure decreases slightly. Later, a strengthening of the implosion occurs accompanying an increase of bubble collapse and a shortening of the bubble period. These results match, qualitatively at least, the predicted theoretical behavior. As ε keeps increasing, the experiments show other pressure peaks, or a collapse period minimum for certain particular values of ε. This result, at first unexpected, seems to correspond to theoretical predictions for the case of high gas content in the bubbles (see Section 4.4).

9.0 ACOUSTIC DAMPING OF A PRESSURE FIELD BY A BUBBLE SCREEN

9.1 Objectives

In order to complement the spark-generated bubble experience where simulated symmetrical cloud configurations were submitted to strong oscillations, the acoustical behavior of a bubble cloud (screen) was investigated. Here no symmetry of the bubble configuration or size was involved and the imposed pressure oscillations were moderate. The main objective of this preliminary study was to find correlations between bubble size distribution and bubble concentration and the transmission of various frequency sound waves through the cloud. From single bubble studies it is known that there is a linear relation between bubble size and bubble natural frequency. The acoustic behavior of the bubble is also known to be a function of the relative magnitudes of the natural frequency and the frequency of the excitation. Acoustic resonance occurs when both frequencies are the same. In the present tests interaction between bubbles of different sizes in the screen come into play, and the overall results should account for these effects.

9.2 Description of Experiment

To experimentally determine a relationship between bubble size, density, and acoustic damping, a number of tests were conducted varying the density of air bubbles in water and recording the change in amplitude of acoustic signals across a path of the bubbles. The signals ranged in frequency from 5kHz to 70kHz. Photographs were taken at the time of each test to determine numerical values for bubble size distribution.

The tests were conducted in a large plexiglass tank approximately 5 feet x 4 feet x 1 foot. The tank was filled with water to a depth of 3.5 feet. Four porous nylon tubes, HYDROPERM tubes, 5/8 inch diameter, 11 inches long, and 2 inches apart were placed in the bottom of the tank to generate bubbles. The approximate pore size for these tubes was 1-3 microns. All but the top portion of the circumference of the nylon tubes was sealed off in order to avoid the coalescence of bubbles from the sides and bottom of the tubes. Each porous tube was connected to a common pipe at one end. This pipe was then attached to a compressed air line to regulate and measure the pressure of the air being forced into the porous tubes. For the purpose of these tests, the air pressure in the tubes ranged from 6 psig to 16 psig.

Two hydrophones were placed in the water 9 inches apart and 21 inches below the surface of the water. One hydrophone served as a signal transmitter, and the other as a signal receiver. The transmitting hydrophone was a rubber booted, ceramic cylinder type with a practically flat response up to 15kHz and ±3dB deviation between 15 and 30 kHz. A KSP UT-114 hydrophone, having a flat response up to 30 kHz and ±3dB oscillations up to 50kHz, was used as a signal receiver. Signals were produced at various frequencies using a Wavetek Model 113 frequency generator, amplified with a McIntosh MC75 audio amplifier, then transmitted by the hydrophone. The signal was then picked up by the receiving hydrophone, where it was first amplified then filtered to eliminate excessive low frequency noise ($f < 500$ Hz). The received signals were monitored with a Hewlett Packard 3580A frequency analyzer, (maximum frequency of 50 kHz), a Keithley 197 digital multimeter, and a Nicolet 2090 digital oscilloscope. Figure 9.1 is a diagram of this experimental

set-up. Figure 9.2 shows a photograph of the actual tank itself with the production of bubbles by 16 psig air pressure being fed through the porous tubes. It shows the arrangement and location of the two hydrophones with bubbles passing between them.

Signals of various frequencies were first generated with no air bubbles being produced in the tank. The strengths of these signals as measured by the multimeter were recorded for later comparison with those transmitted across a stream of air bubbles. In this manner, the amount of signal damping which occurred at each frequency due to the bubbles could be determined. This could then be related to a characteristic bubble size distribution by analyzing the photographs taken at the time of each test.

9.3 Experimental Results and Discussion

Figure 9.3 shows the results of some of the early tests run with the above described apparatus. The values for the air pressure ranged from 8 psig to 16 psig and the results were somewhat encouraging. The highest damping (ratio of rms signal emitted minus signal detected to signal emitted) occurred at the higher bubble densities, as is expected. However, the sharp drop in the amount of damping which occurred at around 40 kHz for most of the tests could not be explained from the characteristics of the bubbles themselves.

After some searching, it was discovered that the behavior of the curves shown in Figure 9.3 was due, in fact, more to the response of the hydrophones than to the size of the bubbles. To correct this, the receiving hydrophone was replaced with the one described above; whereas before, this hydrophone had been

one similar to the transmitting hydrophone. With two practically identical hydrophones being used, the variations of the frequency response which were occurring at the higher frequencies were being overly amplified. Figure 9.4 shows the calibrated frequency responses of both hydrophones.

With the new receiving hydrophone in place, a new series of tests was conducted to determine the range of frequencies at which the most acoustic damping would occur. Figure 9.5 shows the results of a test run at an air pressure of 10 psig. The plot presents both the percentage damping which occurred with bubbles and the amplitude of the received signal with no bubbles being generated in the tank. It suggests that most of the damping is occurring with frequencies in the range of 20-50kHz. But the response of the signals with no bubbles is still suspicious with sharp spikes at about 35 and 50kHz. To determine any effect this may still be having on the shape of the damped signal, a voltmeter was added to the experimental set-up to monitor the input signal to the transmitting hydrophone. A new test was run maintaining the output signal constant in the absence of bubbles and recording the input voltage necessary to do so over the range of frequencies of interest. Then, with bubbles being produced, the measured input voltage at each particular frequency was matched to that recorded with no bubbles. The corresponding amplitude of the output signal was then recorded. The results of this test are shown in Figure 9.6. One can see that, although the maximum amount of damping is slightly lower than that shown in Figure 9.7, the overall behavior is still very much the same.

Figures 9.7 and 9.8 are photographs taken from the front of the tank of the bubbles at 10 and 16 psig air pressures,

respectively. The photos suggest that there exists a range of bubble sizes and that the sizes changed very little with the increasing air pressure in the tubes. This would explain qualitatively the results presented above. The distribution of bubble sizes is responsible for the range of frequencies over which acoustical damping of the signals has occurred. Similar results for tests of various air pressures in the porous tubes suggest that the bubble sizes were similar for all the tests, as is evidenced by these two photographs.

In the two photographs, Figures 9.7 and 9.8, can be seen three small wires, 5, 10, and 15 mils, used for scaling purposes when analyzing the photographs for bubble size distribution. Figure 9.9 shows the spectrum of bubble radii as was determined from the photo in Figure 9.7. It shows that most of the bubble radii fall within a range of 0.05 mm to 0.30 mm. This is only a rough estimate of the sizes due to the fact that the bubbles are too small to be accurately measured. However, when comparing to theoretical considerations, these results seem to be accurate. Figure 9.10 shows graphically the theoretical relationship between bubble size and resonance frequency for an isothermal compression law. From it, one can see that the particular bubble size range given above corresponds theoretically to frequencies of 10-55kHz. This is a very good match with the experimental results presented above. The wide range of frequencies that are significantly damped ($15 < f < 60$ KHz, in Figure 9.6) corresponds to the measured bubble sizes. However, as seen in Figure 9.9, the acoustical measurements seem to indicate a higher content of smaller bubbles than visually observed. This could be due to higher modes of bubble oscillations or to deviations from the simple resonance frequency-bubble size relationship shown in Figure 9.10.

To further verify the relationship between bubble size and acoustically attenuated frequencies, the experimental apparatus described earlier was slightly altered in two separate ways in an effort to increase the size of the bubbles being produced in the tank. In addition to these alterations, bubbles were also produced by electrolysis with electrical wires. These bubbles proved to be too small for our purposes (i.e., natural frequency too high for the instrumentation). The first change consisted of placing in the tank a set of stainless steel sintered tubes, (pore size ≈ 5 microns), in much the same arrangement as the original nylon tubes. These tubes were again sealed along all but the very top portion of the circumference. Signals of frequencies ranging from 1-50 kHz were generated in the tank and the results showed that a considerable amount of damping was occurring at practically all the frequencies within this spectrum. While these results were useful in showing attenuation of lower frequencies than the HYDROPERM tubes, they did not exhibit the definite shift in frequency bandwidth as had been hoped for with this new apparatus. Apparently, with the sintered tubes, bubbles with a very wide range of sizes were being produced.

As a second attempt to produce bubbles of a noticeable difference in size from those produced by the nylon tubes, an aluminum tube with drilled holes, 0.006 inch diameter, was used to generate bubbles at the bottom of the test tank. Figures 9.11 and 9.12 show photographs of the bubbles produced from this apparatus taken at air pressures of 3 and 7 psig, respectively. Again, inspection of these two figures shows that the size distribution of the bubbles being produced at these pressures changed very little if at all. As before, a size distribution was determined from the photographs and is given in Figure

9.13. This figure suggests that most of the bubble radii were within a range of 1.22-1.45 mm. From Figure 9.10, the damped frequencies for this range of bubble sizes should fall between 1.9 and 2.2 kHz. Figure 9.14 shows the actual experimental results of the tests run with these bubbles. Problems related to data reproduction at various dates can be observed in this figure. Peak damping occurred at about 2 kHz and a much narrower bandwidth of frequencies was being attenuated by the presence of the bubbles. This corresponds very well with theoretical considerations since a spectrum of larger bubble radii (>1 mm) results in very little variation in resonant frequency, whereas a range of bubble radii <0.5 mm will produce a much larger bandwidth of resonant frequencies. For the purpose of these tests, no results could be obtained at frequencies lower than 2 kHz because of an increased noise to signal ratio at these frequencies, but the results do show the shift toward lower frequencies with increased bubble size as was expected. This set of tests give some preliminary but very useful information on the study of acoustic wave propagation through a bubbly medium .

10.0 CONCLUSIONS AND SUMMARY

The main achievement of the study described in this report is the extension of the study of single bubble dynamics to multibubble dynamics. Within the restriction that characteristic bubble size is small compared to interbubble distance, the dynamics of a bubble cloud was investigated. Dynamic effects in the absence of heat and mass transfer were first considered. The matched asymptotic expansion method was used and enabled derivation of differential equations for the bubble shape components at the various orders of approximation. These were solved numerically using a multi-Runge-Kutta procedure, and the corresponding numerical code was implemented.

Later, heat then mass transfer were accounted for. When, during a significant portion of the imposed pressure field history, the liquid is superheated (its temperature is higher than the liquid vaporization temperature at the imposed pressure) or gas supersaturated (the concentration of dissolved gas is higher than the saturation concentration at the noncondensible gas pressure in the bubbles), heat and mass transfer at the interface occur at a rate high enough to interfere with the dynamics of the bubble growth or oscillations. In that case, the dynamic equation of a bubble in the cloud is coupled to the heat or mass transfer equation by the value of one (or both) of the partial pressures of the liquid vapor and noncondensible gas inside the bubble which are then transfer dependent. We have solved this problem when (as for single isolated bubbles) the liquid properties or conditions are such that the variation of the liquid temperature or the gas concentration in the liquid occurs primarily in a thin boundary layer at the bubble wall. In that case an integral equations

relates bubble dynamics and heat or mass transfer at the bubble interface. Two numerical codes were developed to deal with the two transfer problems.

Other aspects of the problem were also considered in this study but were not pursued as deeply as the multibubble approach due either to limited time and resources or to their showing little promise based on initial feasibility efforts. The most promising of these approaches have been summarized in this report. Some others, such as the determination of the unsteady pressure field generated behind an oscillating sheet cavity have not been addressed in this report. The task turned out to be much more involved than originally thought if a significant new contribution was to be achieved. The effort was redirected towards a more thorough analysis of the other tasks.

A continuum medium approach was developed for the general description of the two phase medium composing the cloud that shows promise. As do most continuum approaches, this method applies to the case of low void fractions. It enables expression of the conservation equations in the cloud medium. The micromorphic method used consists in decomposing the medium into cells in which the bubble dynamics are considered. One shortcoming is the appearance of an additional term arising from the averaging procedure which depends on the geometry of the cell. Dependence of the equations on an inverse power of the void fraction indicates they are invalid for extremely low void fractions. These difficulties are classic with averaging methods and can now be dealt with using newly developed renormalization techniques. This should be the next step towards the improvement of this continuum theory.

A fundamental experimental program was conducted in parallel with the theoretical effort described here. Systematic observations of bubble dynamics using high speed photography and measurements of acoustical pressures were conducted. Spark-generated bubbles were produced at precise locations near complex solid wall geometries. By application of the method of images, the bubble behavior near the solid boundaries is similar to that in the presence of a set of bubble images in the wall. By varying the wall geometry the number of simulated interacting bubbles can be varied. The interbubble distance was set by controlling the distance between the electrode tips and the solid walls. The size of the bubble generated was varied by changing the discharge voltage and the tank ambient pressure. Observations confirmed and complemented the theory since cases of both low and high void fractions could be studied. Within the experimental error, (mainly due to a lack of control of the amount of gas in the bubble), preferred void fractions (or ratios of bubble characteristic radius to interbubble distance) which generated the strongest bubble collapse and the highest pressures were observed. These results qualitatively confirmed the theoretical results.

A set of experiments of a more preliminary nature concerned sound wave propagation through a sheet of bubbles. Bubble sheets were generated in a large tank using microporous, sintered, and drilled tubes. Sound pressure waves were then emitted on one side of the sheet using an active hydrophone. The transmitted wave was detected with another hydrophone. By varying the frequency of the emitted signals and the characteristics of the bubble generator, correlations could be made between the attenuation of the acoustic wave through the bubble screen and the size distribution of the bubbles.

Several numerical codes were implemented as a result of the multibubble cloud theory developed in this program. These programs consider several aspects of the problem. CLDMAIN neglects heat and mass transfer and allows the user to study the behavior of a symmetrical bubble cloud configuration. In its latest verison, CLDMAIN2, several pressure field shapes can be investigated -- e.g., sudden pressure rise, pressure drop for a finite time period, pressure field due to a venturi or over a foil shape, ... etc. The error at each step of computation can be bounded by an imposed value. This procedure is used to continuously adjust the calculation time step to minimize both errors and total computation time. This code has been extensively exercised to investigate bubble cloud behavior. Due to the symmetry of the cloud, very dramatic results can be observed. A cumulative effect is observed which tends to reinforce any pressure deviations from the ambient value due to bubble dynamics. For instance, during the initial bubble growth period the positive deviations in the presence of several bubbles reinforce each other to slow down the initial bubble growth. This effect can, however, be reversed later when the deviation pressure becomes negative and can lead to large bubble sizes. The most dramatic effect is observed during bubble collapse. It is known that large pressure rises are generated at the end of the collapse. These pressures are increased when several bubbles are present and also reinforce the collapse of each individual bubble. Therefore, collective bubble collapse can generate pressures orders of magnitude higher than those produced by single bubble collapse. The cumulative effect is mainly due to the fact that each bubble ends its collapse under the influence of pressures generated by the collapse of the other bubbles orders of magnitude higher than the imposed ambient pressure. This would tend to explain the observed high

erosion intensities and the bending of some propeller trailing edges.

When the bubble cloud geometry is asymmetrical the pressures generated by the various bubbles are not necessarily in phase. Cumulative effects are therefore reduced in intensity and the very large increases in the collapse energy found with the symmetrical CLDMAIN code are tempered. A similar result is obtained when bubble initial sizes are not identical or when a finite sound speed is taken into account to delay pressure propagation from one bubble to another. Two main codes have been developed to deal with these asymmetries: MULTIBBL and MULTICOMP. For both codes the user inputs bubble size and distribution, and the program computes the individual bubble dynamics under the influence of the other bubbles in the cloud. In addition, MULTICOMP accounts for time delays between the arrival of pressure signals from different bubbles based on a finite sound speed imposed by the user.

For heat and mass transfer, two separate codes have been implemented: HOTCLDS and GASCLD. Both consider a symmetrical cloud configuration and couple the multibubble dynamics problem with the problem of heat or mass transfer at the bubble liquid interface. Mass and heat transfer are both seen to reduce bubble growth rate. Bubble interactions also play a significant role in bubble growth -- mainly by modification of the pressure field. This interaction results in a reduced growth rate which makes the bubble radius at any given time smaller than would be found for an isolated bubble. The temperature drop at the bubble wall in a multibubble configuration is smaller than would be found for an isolated bubble. The dissolved gas concentration in the liquid exhibits similar behavior. The effective gas

compression law is seen then to vary rapidly from an adiabatic behavior at the beginning of the growth to an isothermal behavior.

In conclusion, we have conducted an in-depth study on the fundamental aspects of multibubble cloud cavitation. The results of this study explain the intense erosion associated with the phenomena. Several codes were developed and implemented as a result of the theoretical study and can be used as tools for further study of various aspects of the problem under particular conditions of interest.

11.0 REFERENCES

Bark, G., and Van Barlekom, W. B. (1979), "Experimental Investigations of Cavitation Noise," 12th Symposium on Naval Hydrodynamics, 470.

Bark, G., (1985), "Development of Distortions in Sheet Cavitation on Hydrofoils," ASME International Symposium on Jets and Cavities, Miami, Florida, Nov. 17-22, FED Vol. 31 pp. 215-225

Batchelor, G. K. (1967), An Introduction to Fluid Dynamics, Cambridge, the University Press.

Baumeister, K.J. and Hamill, T.D., 1969, "Hyperabolic Heat Conduction Equation - A Solution for the Semi-Infinite Body Problem," ASME Journal of Heat Transfer, pp 543-548.

Billet, M. L., (1984), "Cavitation Nuclei Measurements," International Symposium on Cavitation Inception - 1984, ASME FED-Vol. 16, pp. 33-42.

Bovis, A. G., and Chahine, G. L. (1981), "Etude Asymptotique de L'Interaction d'une Bulle Oscillante avec une Surface Libre Voisine," J. de Mécanique. 20, 3, 537.

Caflish, R. E., Miksis, J., Papanicolaou, G. C., and Ting, L. (1985a), "Effective Equations for Wave Propagation in Bubbly Liquids," J. Fluid Mechanics, Vol. 153, pp. 259-273.

Caflish, R. E., Miksis, J., Papanicolaou, G. C., and Ting, L. (1985b), "Wave Propagation in Bubbly Liquids at Finite Volume Fraction," J. Fluid Mechanics, Vol. 160, pp. 1-14.

Cha, Y. S. and Henry, R. E., (1981), "Bubble Growth During Decompression of a Liquid," Journal of Heat Transfer, Vol. 103, pp. 56-60.

Chahine, G. L. (1981), "Asymptotic Theory of Collective Bubble Growth and Collapse," Proc. 5th International Symp. on Water Column Separation, IAHR, Obernach, Germany.

Chahine, G. L. (1982), "Experimental and Asymptotic Study of Non-spherical Bubble Collapse," Appl. Sci. Res., 38, 187.

Chahine, G. L., and Bovis A. G. (1981), "Pressure Field Generated by Nonspherical Bubble Collapse, Cavitation Erosion in Fluid Systems," ASME, New York, 27.

Chahine, G. L. (1982a), "Pressures Generated by a Bubble Cloud Collapse," ASME, Cavitation and Ploy phase Flow Forum, St. Louis, pp. 27-31.

Chahine, G. L. (1982b), "Cloud Cavitation - Theory," Proceedings, 14th Symposium on Naval Hydrodynamics, Ann Arbor, 23-27 August.

Chahine, G. L. (1982 c), "Pressure Field Generated by the Collective Collapse of Cavitation Bubbles," Proceedings, IAHR Symposium on Operating Problems of Pump Stations and Power Plants, Amsterdam, Holland, September, pp. 2-1, 1-12.

Chahine, G. L. and Liu, H. L. (1983), "Collective Bubble Growth in a Superheated Liquid Following a Sudden Depressurization," 6th International Symposium on Hydraulic Transients in Power Station, Cloucester, England, Sept. 19-20.

Chahine, G. L. and Liu, H. L. (1984), "Collective Effects on the Growth of Vapour Bubbles in a Superheated Liquid," Journal of Fluids Engineering, Vol. 106, pp. 486-491.

Chahine, G. L. and Liu, H. L. (1985), "A Singular Perturbation Theory of the Growth of a Bubble Cluster in a Super-heated Liquid," Journal of Fluid Mechanics, 156, pp. 257-274.

Chahine, G. L. and Shen, Y. (1985), "Bubble Dynamics and Cavitation Inception in Cavitation susceptibility Meters," ASME, Intn'l Symp. Fundamental Aspects of Gas Fluid Flows, Miami Beach, Floriday, Nov. 17-22, pp. 137-146.

Chahine, G. L. and Sirian, C. R. (1985), "Collapse of a Simulated Multibubble System" ASME Cavitation and Multiphase Flow Forum, Albuquerque, New Mexico, June.

d'Agostino, L. and Acosta, A. J., (1983) "On the Design of Cavitation Susceptibility Meters," 20th American Towing Tank Conference.

D'Agostino, L and Brennen, C. E. (1983), "On the Acoustical Dynamics of Bubble Clouds," ASME Cavitation and Polyphase Flow Forum 1983, pp. 72-76, Houston, Texas.

Dalle Donne M. and Ferranti, M. P., (1975), "The Growth of Vapor Bubbles in Superheated Sodium," International Journal of Heat Mass Transfer, Vol. 18, pp. 477-493.

Darrozes, J. S., (1971), "The Method of Matched Asymptotic Expansions Applied to Problems Involving Two Singular Perturbation Parameters," Fluid Dynamics Trans., Vol. 6, Part 2, pp. 119-129.

Darrozes, J. S. and Chahine, G. L., (1983), "Les Recherches sur le Phénoméne de Cavitation Effectués a l'Ecole Nationale Superieure des Techniqus Avancés," Sciences et Techniques de l'Armement 1er Fascicule.

Ellis, A. T. (1955), "Techniques for Pressure Pulse Measurements and High-Speed Photography in Ultrasonic Cavitation," Proceedings, Symposium on Cavitation in Hydrodynamics, Teddington, Egnland.

Forster, H. K. and Zuber, N., (1954), "Growth of a Vapor Bubble in a Superheated Liquid," Journal of Applied Physics, Vol. 25, No. 4, pp. 474-478.

Germain, P. (1973), "The Method of Virtual Power in Continuum Mechanisms, Part 2: Microstructure," SIAM J. Appl. Math. 25, 3, 556.

Hammitt, F. G. (1980), Cavitation and Multiphase Flow Phenomena, McGraw Hill International Book Company.

Hansson, I., and Mørch, K. A. (1980), "The Dynamics of Cavity Clusters in Ultrasonic (Vibratory) Cavitation Erosion," J. of Applied Physics, 51, 4651.

Ishii, M. (1975), Thermo-fluid Dynamic Theory of Two-Phase Flow, Eyrolles, Paris.

Johnson, V. E., and Hsieh, T. (1966), "The Influence of the Trajectories of Gas Nuclei on Cavitation Inception," Proc. 6th Naval Hydrodynamics Symp., Washington, D.C.

Jones, O. C., Jr. and Zuber, N., (1978), "Bubble Growth in Variable Pressure Fields," Journal of Heat Transfer, ASME Trans., Vol. 100, pp. 453-459.

Keller, A. P., (1984), "Scale Effects at Beginning Cavitation Applicated to Submerged Bodies," International Symposium on Cavitation Inception, ASME, FED-Vol 16, pp. 43-47.

Landweber, L., and Miloh, T. (1980), "Unsteady Lagally Theorem for Multipoles and Deformable Bodies," J. Fluid Mech. 96, 33.

Lecoffre, Y. and Bonnin, (1979), "Cavitation Tests and Nucleation Control," International Symposium on Cavitation Inception, The ASME Winter Annual Meeting New York, New York, December 2-7, pp. 141-147.

Matsumoto, Y. and Shirakua, M. (1982), "Mechanism of Cavitation Nuclei Suspension," Proceedings, IAHR Symposium on Operating Problems of Pump Stations and Power Plants, Amsterdam, September, Paper 4.

Michelet, M. G. (1980), "Etude des Milieux Micromorphiques," ENSTA, Filliere de Recherche Post-Scolaire, rapport de DEA No. 2.

Micksis, M. J. and Ting, L. (1986), "Wave Propagation in a Bubbly Liquid with Finite Amplitude Asymmetric Bubble Oscillations, J. Acoust. Soc. Am., 29 (3), March, pp. 603-618.

Morch, K. A. (1977), "Concerted Collapse of Cavities in Ultrasonic Cavitation," Proc. Acoustic Cavitation Meeting, London, 62.

Mørch, K. A. (1980), "On the Collapse of Cavity Clusters in Flow Cavitation," Proc. 1st International Conference on Cavitation and Inhomogeneities in Underwater Acoustics, Springer Series in Electrophysics, 4, 95.

Mørch, K. A. (1982), "Energy Considerations on the Collapse of Cavity Clusters," Appl. Sci. Res. 38, 313.

Ng, K. c. and Ting, L. (1986), "Wave Propagation Through a Thin bubbly Layer," J. Acoust. Soc. Am., 79 (4), April, pp. 924-926.

Oldenziel, D. M., (1982), "A New Instrument in Cavitation Research: The Cavitation Susceptibility Meter," ASME Journal of Fluids Engineering, 104, pp. 136-142, June.

Plesset, M. S., (1980), "New Problems in Two-Phase Flows," Proc. 10th IAHR Symposium on Hydraulic Machinery and Equipment Associated With Energy Systems in the New Decade of the 1980's, Tokyo, October, pp. 31-40.

Plesset, M. S. and Prosperetti, A., (1977), "Bubble Dynamics and Cavitation," Annual Review Fluid Mechanics, 9, pp. 145-185.

Plesset, M. S. and Zwick, S. A., (1952), "A Nonsteady Heat Diffusion Problem with Spherical Symmetry," Journal of Applied Physics, Vol. 23, No. 1, pp. 95-98.

Prosperetti, A., and Van Wijngaarden (1976), "On the Characteristics of the Equation of Motion for a Bubbly Flow and the Related Problem of Critical Flow," J. Eng. Math, 10, 2.

Prosperetti, A. and Plesset, M. S., (1978), "Vapor-Bubble Growth in a Superheat Liquid," Journal of Fluid Mechanics, Vol. 85, Part 2, pp. 349-368.

Rubinstein, J. (1985), "Bubble Interaction Effects on Waves in Bubbly Liquids," J. Acoust. Soc. Am., 77 (6), June, pp. 2061-2066.

Shen, Y. T., Gowing, S., and Pierce, R., (1984), "Cavitation Susceptibility Measurements by a Venturi," International Symposium on Cavitation Inception, ASME, FED-Vol. 16, pp. 9-19.

Shen, Y. T. and Gowing S., (1985), "Scale Effect on Bubble Growth and Cavitation Inception in Cavitation Susceptibility Meters," ASME Cavitation and Multiphase Flow Forum, 1985, Albuquerque, NM.

Shen, Y. T., and Peterson, F. B. (1979), "Unsteady Cavitation on Any Oscillating Hydrofoil," 12th Symposium on Naval Hydrodynamics, 362.

Shen, Y. T. and Peterson, F. B., (1983), "Cavitation Inception - A Review - Progress Since 19th ATTC," 20th American Towing Tank Conference.

Shima, A., Takayama, K., Tomita, Y. and Ohsawa, N. (1983), "Mechanism of Impact Pressure Generation from Spark-generated Bubble Collapse Near a Wall," AIAA Journal, Vo. 21, 1, January.

Tanabayshi, H., and Chiba, N. (1977), "Unsteady Cavitation of Oscillating Hydrofoil," Mitsubishi Technical Bulletin 117, Mitsubishi Heavy Industries, Ltd., Tokyo, Japan.

Theofanous, T., Biasi, L., Isbin, H. S., and Fauske, H., (1969), "A Theoretical Study of Bubble Growth in Constant and Time Dependent Pressure Fields," Chemical Engineering Science, Vol. 24, pp. 885-897.

Tulin, M. P. (1980), "An Analysis of Unsteady Sheet Cavitation," 1980 ITTC Conference, Ann Arbor, Michigan.

Tulin, M. P., and Hsu, C. C. (1980), "New Applications of Cavity Flows Theory," 13th Symposium on Naval Hydrodynamics, Tokyo, Japan.

Van Dyke, M., (1964), Perturbation Methods in Fluid Mechanics, Academic Press.

Van Wylen, G. J. and Sonntag, R. E., (1973), Fundamentals of Classical Thermodynamics, Second Edition, Wiley.

Van Manen, J. D. (1963), "Bent Trailing Edges of Propeller Blades of High Powered Single Screw Ships," International Shipbuilding Progress, 10, 101, 3.

Van Wijngaarden, L. (1964), "On the Collective Collapse of a Large Number of Gas Bubbles in Water," Proc. 11th International Cong. of Appl. Mechanics, Springer, Berlin, 854.

Van Wijngaarden, L. (1972), "One-dimensional Flow of Liquids Containing Small Gas Bubbles," Annual Review of Fluid Mech., 4, 369.

Van Wijngaarden, L. (1976,a), "Hydrodynamic Interaction Between Bubbles in a Dilute Gas Bubble Liquid Mixture," J. Fluid. Mech., 77, 1, 27.

Van Wijngaarden, L. (1976,b), "Some Problems in the Formulation of the Equations for Gasliquid Flows," Theor. and Appl. Mech., ed. W. T. Koiter, North Holland Publishing Company.

Van Wijngaarden, L. (1980), "Sound and Shock Waves in Bubbly Liquids," Proc. 1st International Conference on Cavitation and Inhomogeneities in Underwater Acoustics, Springer Series in Electrophysics, 4, 127.

Van Wijngaarden, L. (1982), "Bubble Interaction in Liquid/gas Flows," Appl. Sci. Res., 38, 331.

Zuber, N. (1964), "On the Disperse Two-phase Flow in the Laminar Flow Regime," Chem. Eng. Sci., 10. 897.

Zwick, S. A. (1959), "Behavior of Small Permanent Gas Bubbles in a Liquid," J. Math and Phys., 37, 339.

TABLE 1. VALUES OF THE NUMERICAL CONSTANTS USED IN THE COMPUTATIONS

N	C_1	C_2	C_3
1	0	0	0
2	1	1	1
3	2	1.732	1.25
5	3	2	1
12	8.616	4.53	0.41

N: Number of bubbles

$c_1 = \sum \lambda_{ij}$

$c_2 = \sum (\lambda_{ij})^2 \cos\theta^{ij}/\cos\theta^{ig}$

$c_3 = \sum (\lambda_{ij})^3 (3\cos^2\theta^{ij}-1)/(3\cos^2\theta^{ig}-1)$

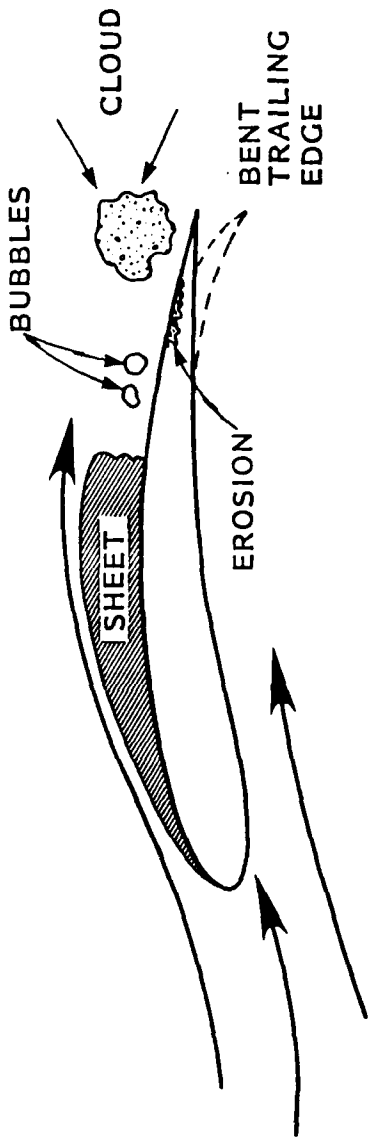

FIGURE 1.1 - TYPES OF CAVITATION ON FOIL

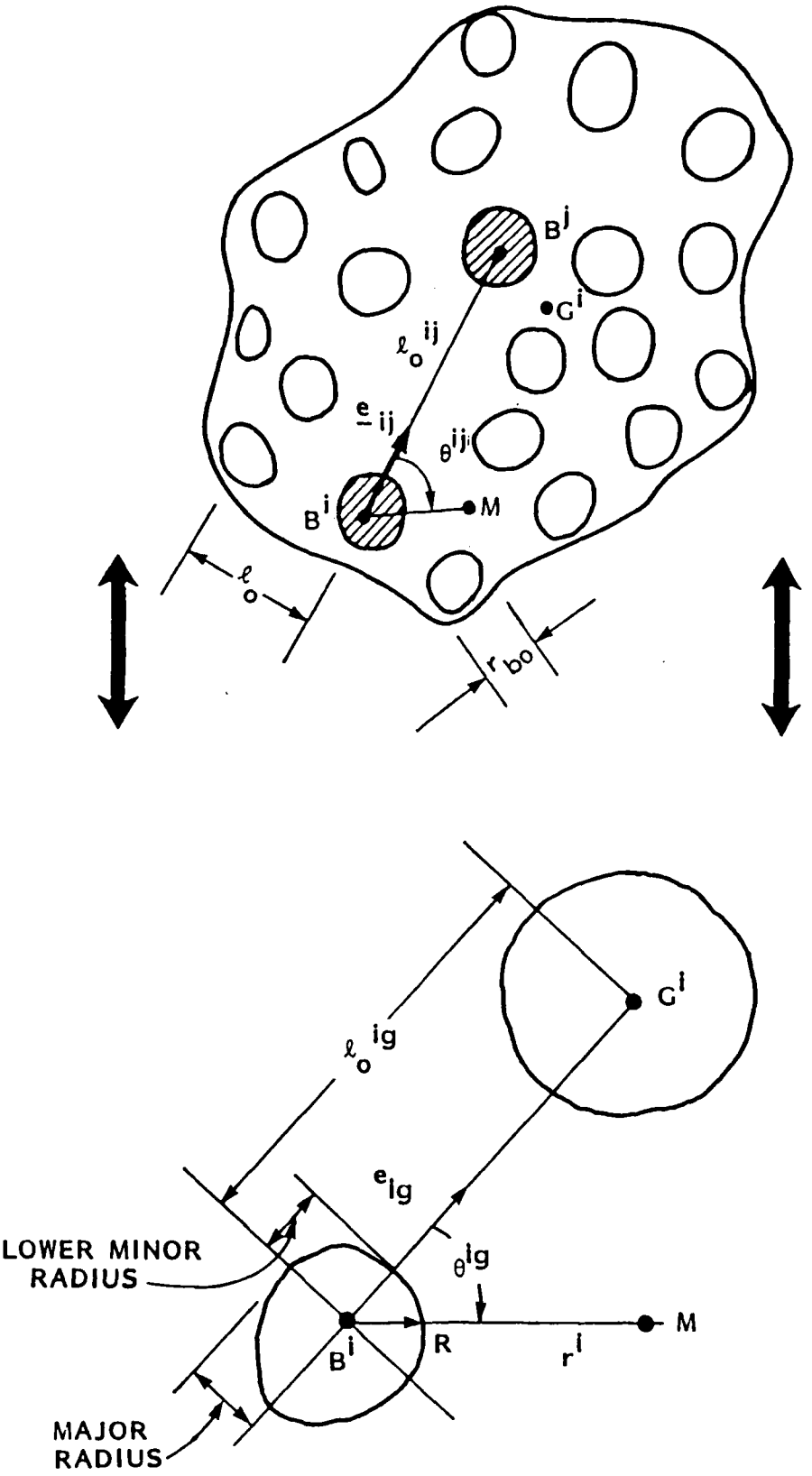

FIGURE 3.1 - MULTIBUBBLE INTERACTION EQUIVALENCE CONCEPT

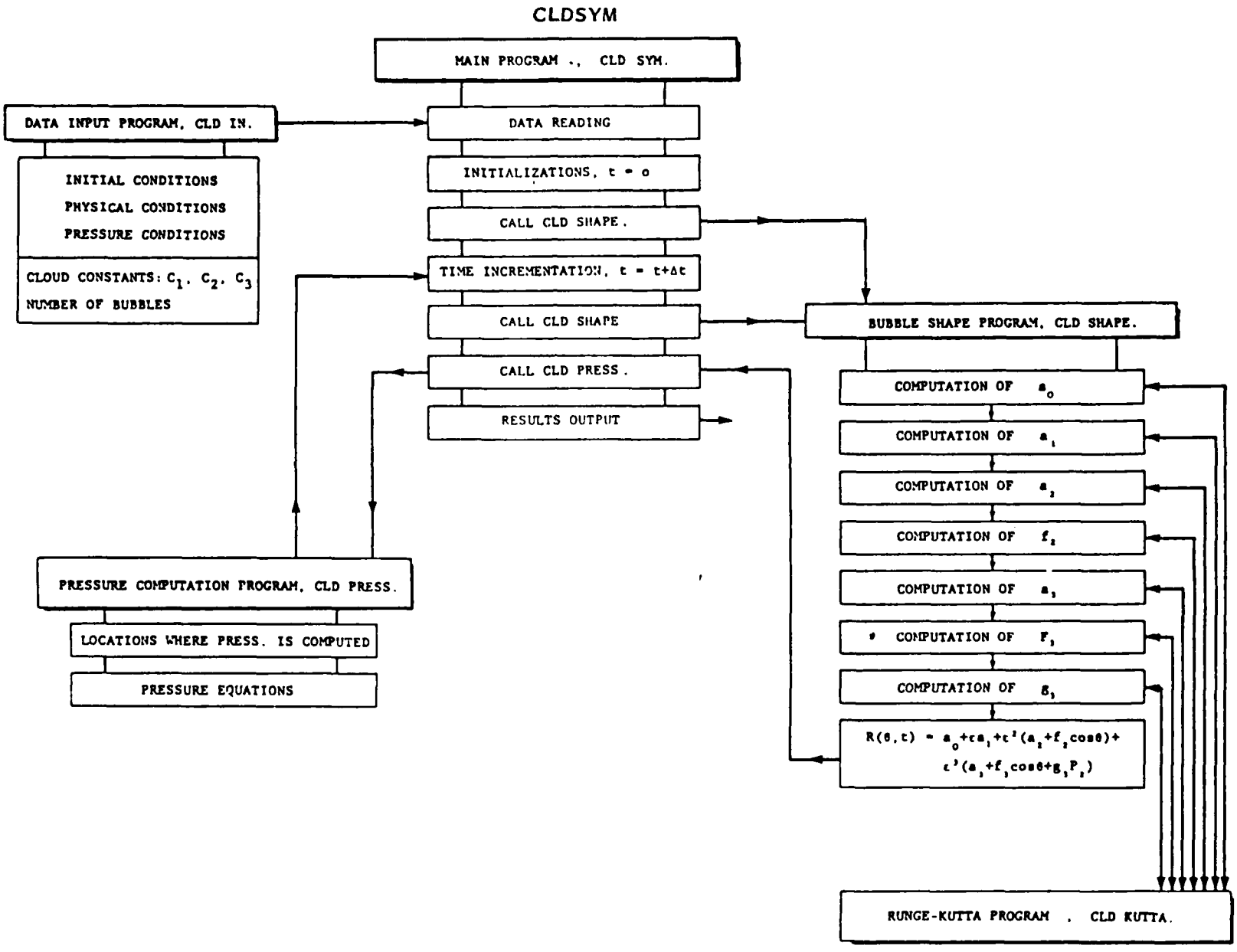

FIGURE 4.1 - BUBBLE CLOUD DYNAMICS PROGRAM FLOW CHART.
EQUI-SIZED SYMMETRICALLY DISTRIBUTED BUBBLES

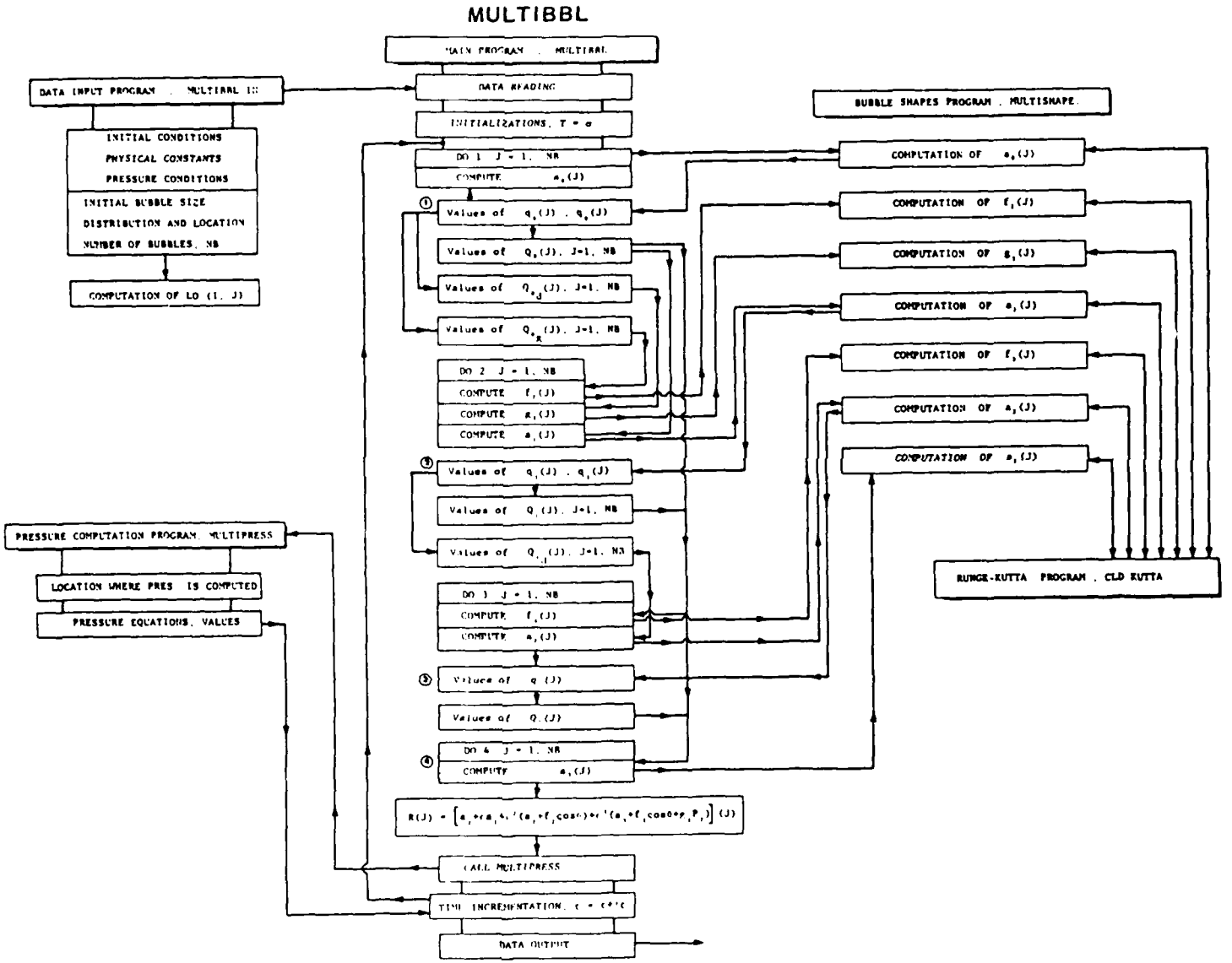

FIGURE 4.2 - BUBBLE CLOUD DYNAMIC PROGRAM FLOW CHART.
NON-EQUAL BUBBLE SIZES

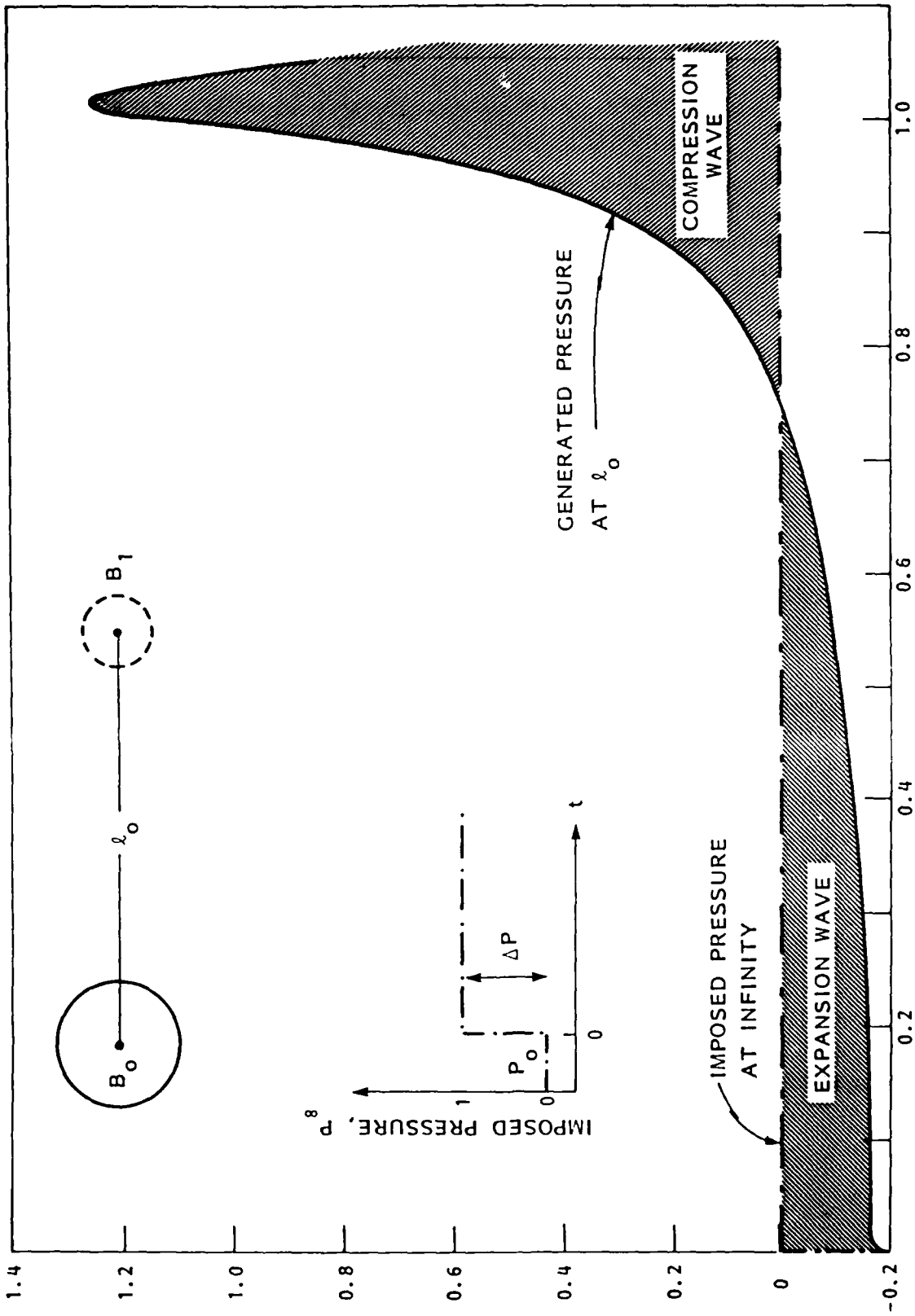

FIGURE 4.3 - PRESSURE VARIATION VERSUS TIME AT A DISTANCE ℓ_o FROM AN ISOLATED SPHERICAL BUBBLE

$P_{g_o} = 0.1$, $W_e = 100.$, $\epsilon = r_o/\ell_o = 0.33$

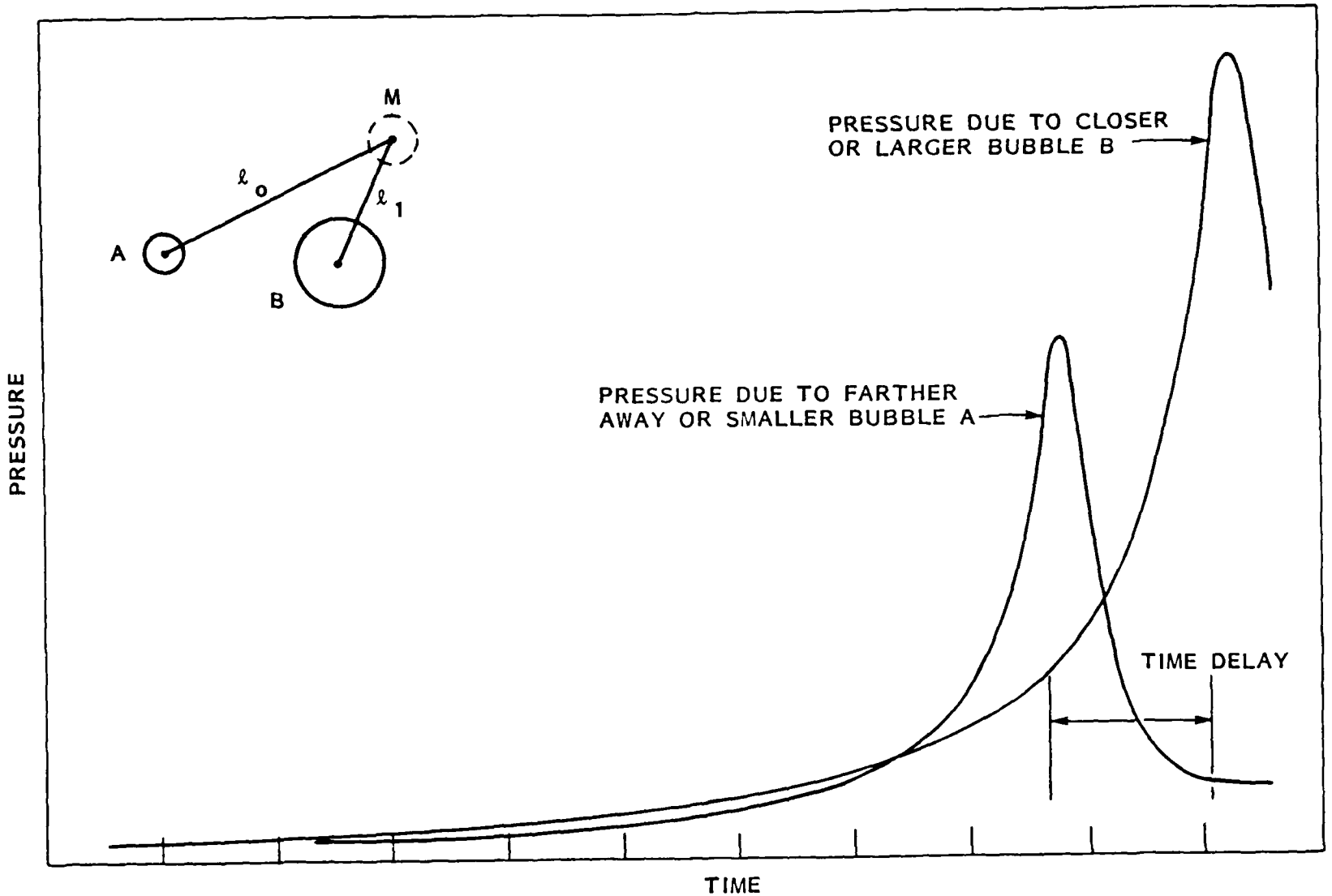

FIGURE 4.4 - PRESSURES GENERATED AT A POINT M BY TWO COLLAPSING BUBBLES: BUBBLE A, SMALLER OR FARTHER AWAY; BUBBLE B, LARGER OR CLOSER

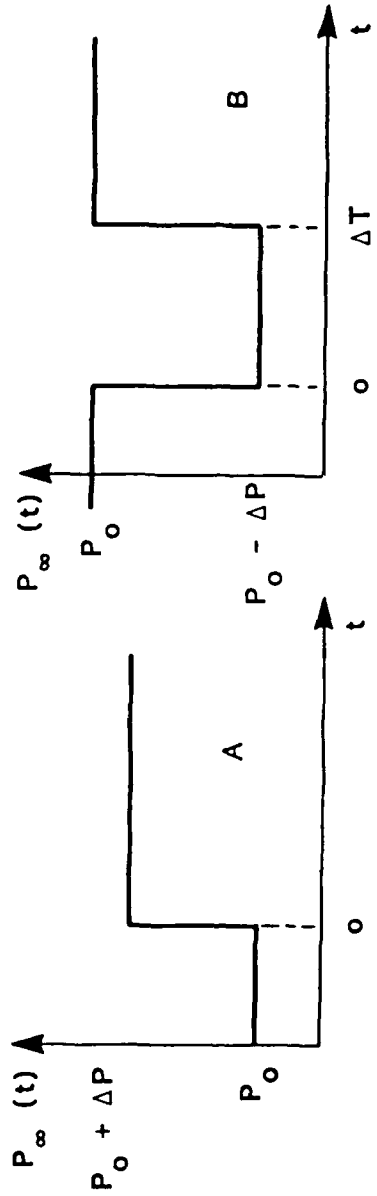

FIGURE 4.5 - IMPOSED AMBIENT PRESSURE FUNCTIONS

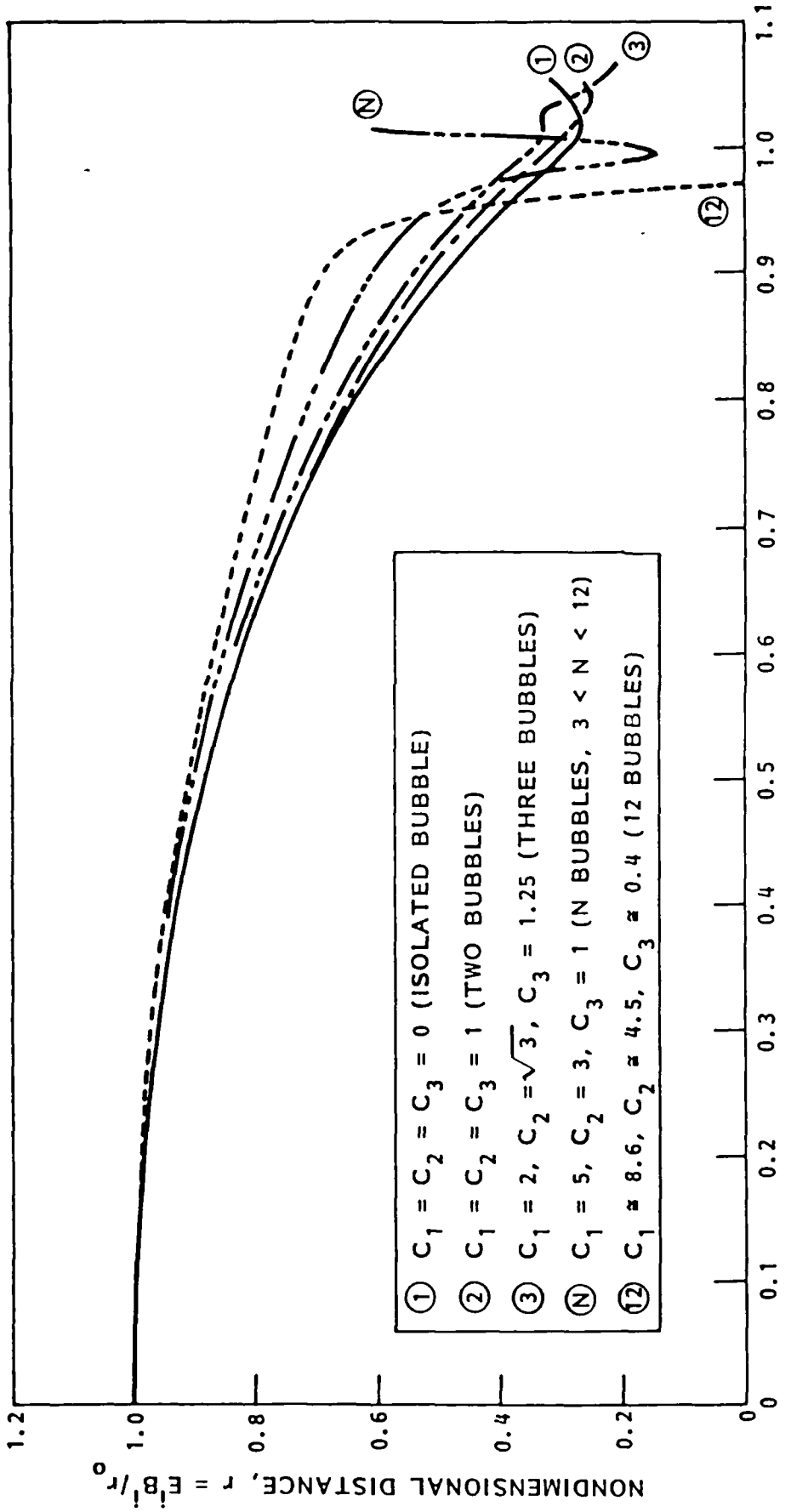

FIGURE 4.6 - MOTION OF THE BUBBLE WALL TOWARD THE CLOUD: $\varepsilon = 0.05$, $P_{g_o} = 0.1$, $K = 1.4$, POSITIVE PRESSURE STEP

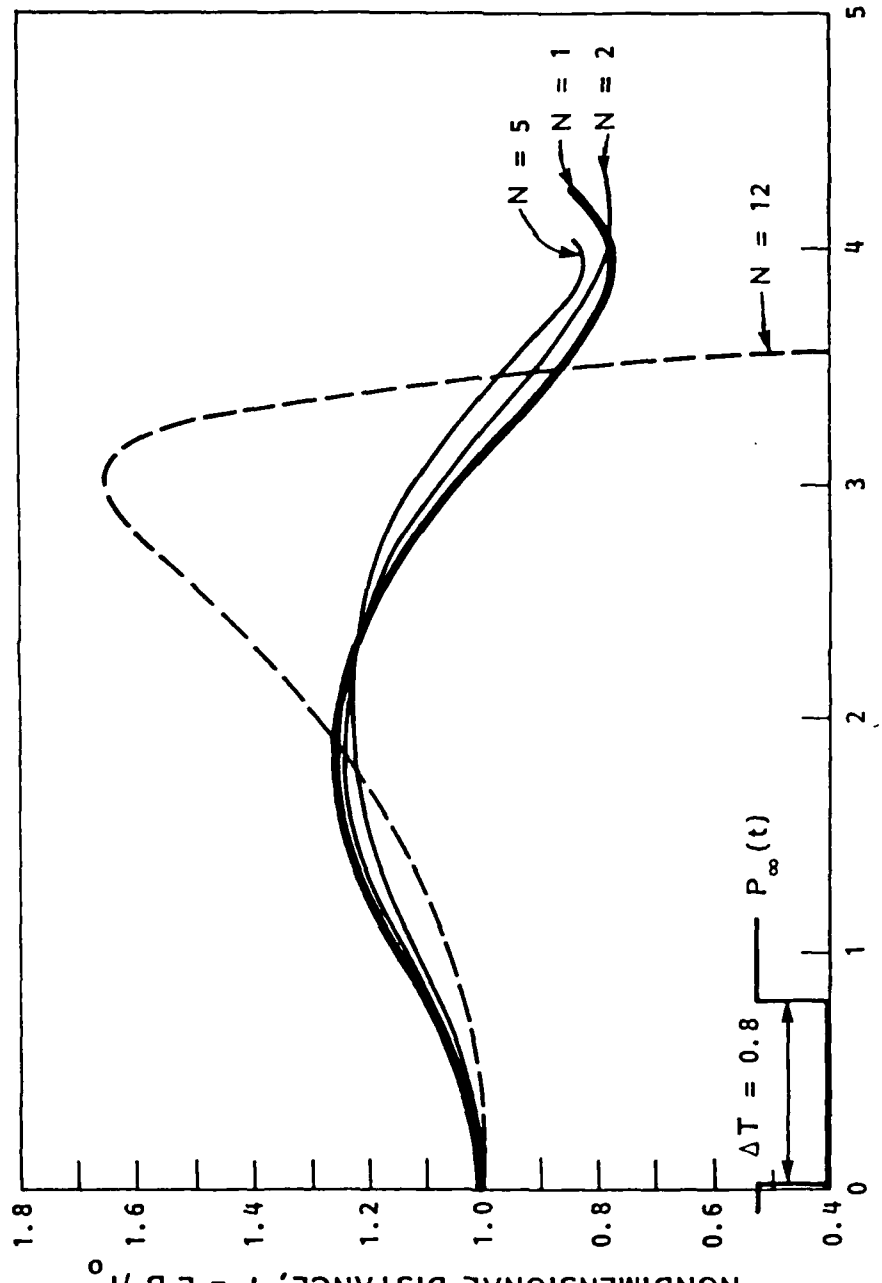

FIGURE 4.7 - MOTION OF THE BUBBLE WALL TOWARD THE MULTIBUBBLE CLOUD CENTER $W_e = 100.$, $P_{go} = 0.53$, $K = 1.4$, $\epsilon = 0.1$. DURATION OF THE PRESSURE DROP $\Delta T = 0.8$.

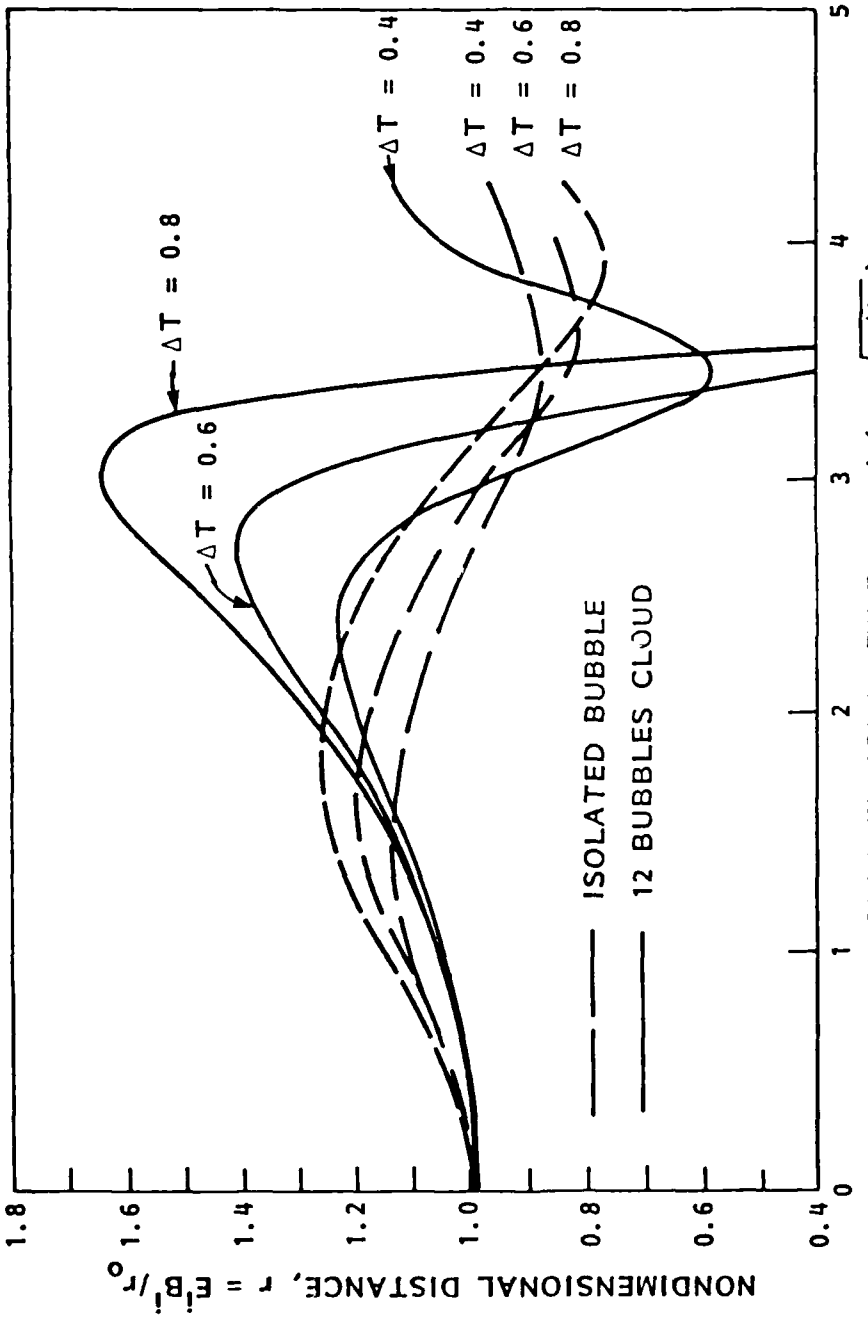

FIGURE 4.8 - INFLUENCE OF THE PRESSURE DROP DURATION ON THE BUBBLE WALL MOTION TOWARD THE CLOUD CENTER, $W_e = 100.$, $P_{g_o} = 0.53$, $K = 1.4$, $\epsilon = 0.1$, $N = 12$

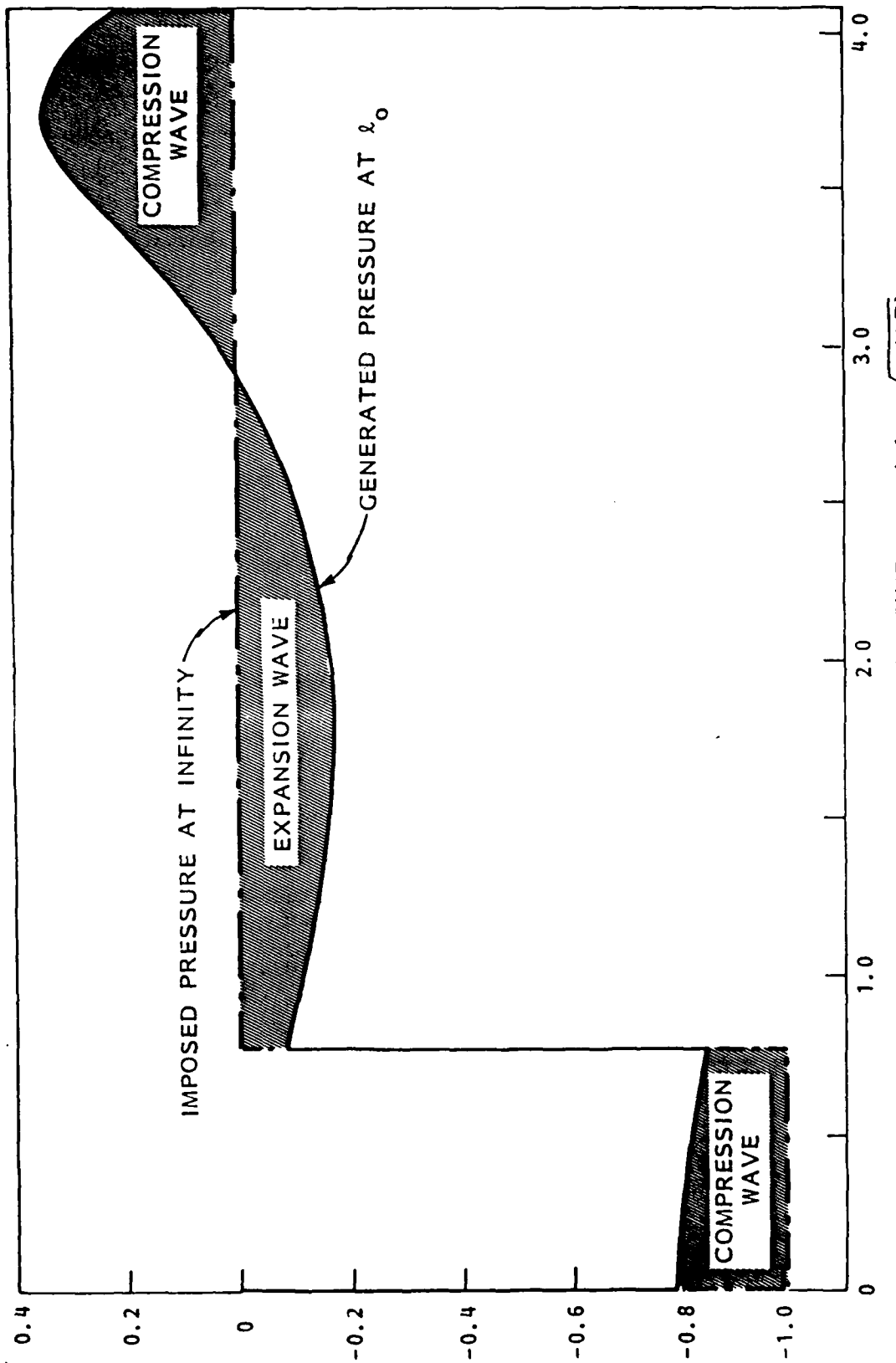

FIGURE 4.9 - PRESSURE VARIATION VERSUS TIME AT A DISTANCE ℓ_o, FROM AN ISOLATED SPHERICAL BUBBLE, FINITE TIME AMBIENT PRESSURE DROP $P_{g_o} = 0.53$, $W_e = 100.$, $\epsilon = r_o/\ell_o = 0.2$, $\Delta T = 0.8$

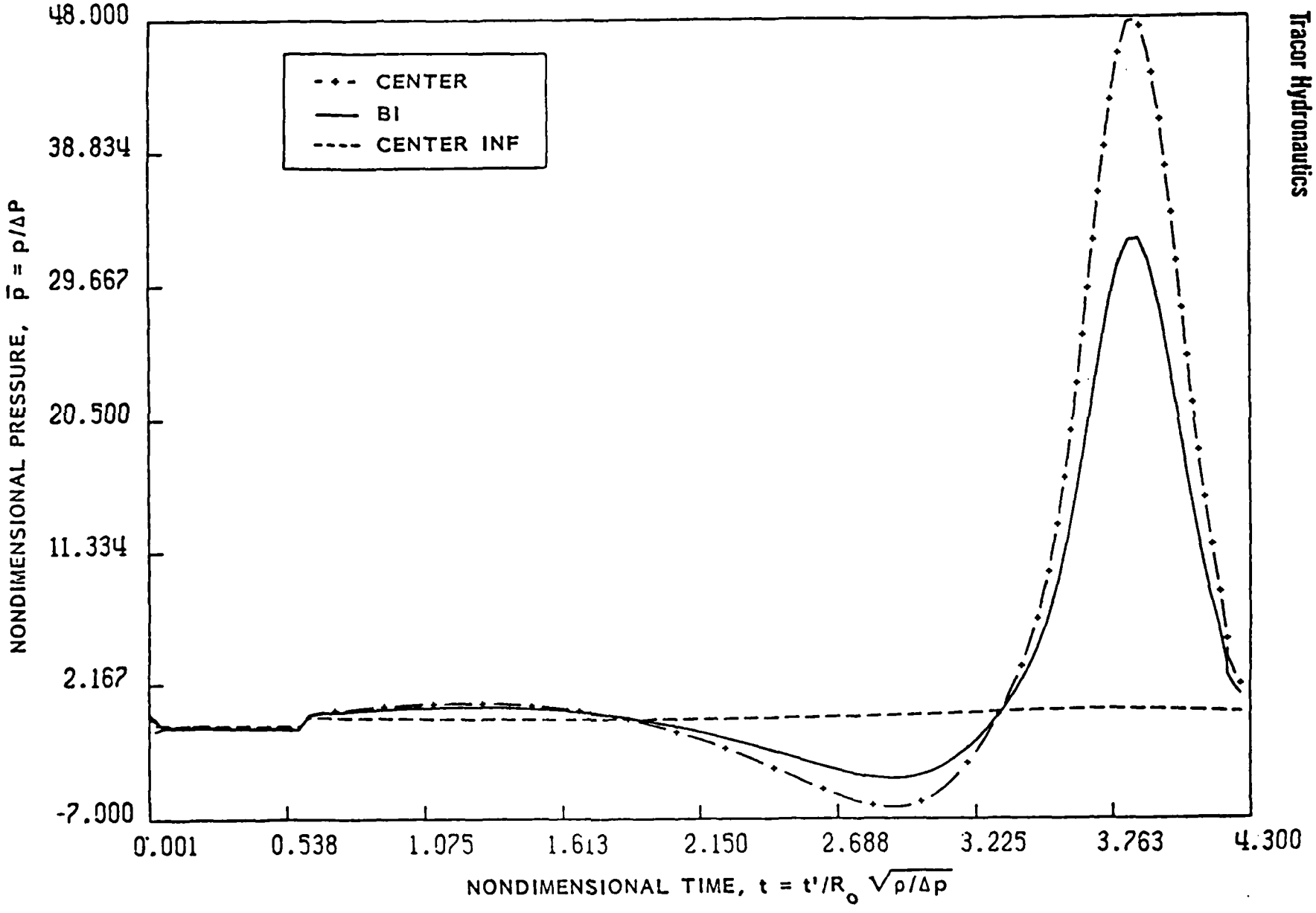

FIGURE 4.10 - PRESSURE VERSUS TIME AT DIFFERENT LOCATIONS, $\epsilon = 0.1$, $W_e = 100.$, $\bar{P}_{g_o} = 0.54$, $K = 1$, 12 BUBBLES, $\Delta T = 0.6$

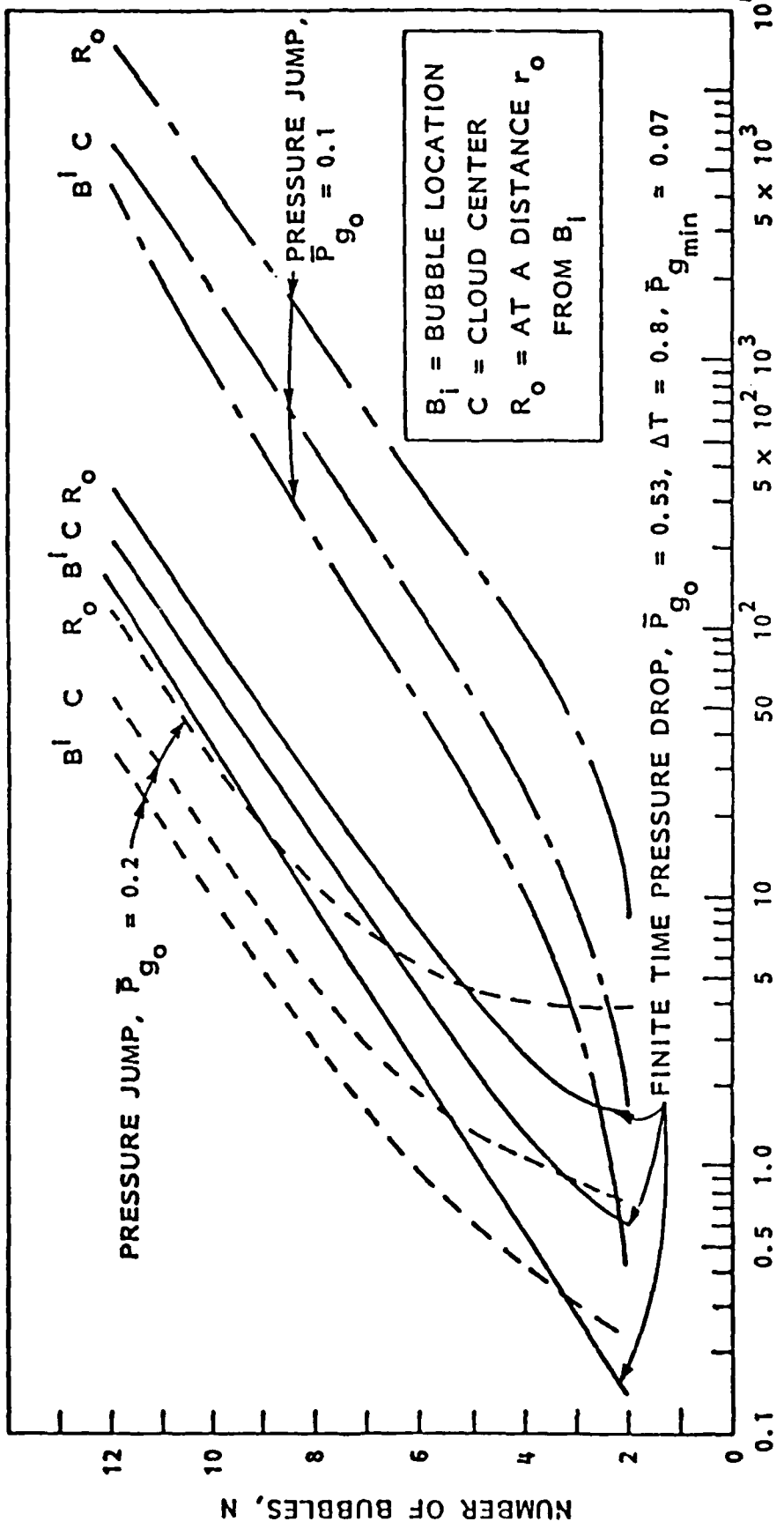

FIGURE 4.11 - VARIATION WITH THE NUMBER OF BUBBLES OF THE MAXIMUM PRESSURES GENERATED, $W_e = 100.$, $\epsilon = 0.1$

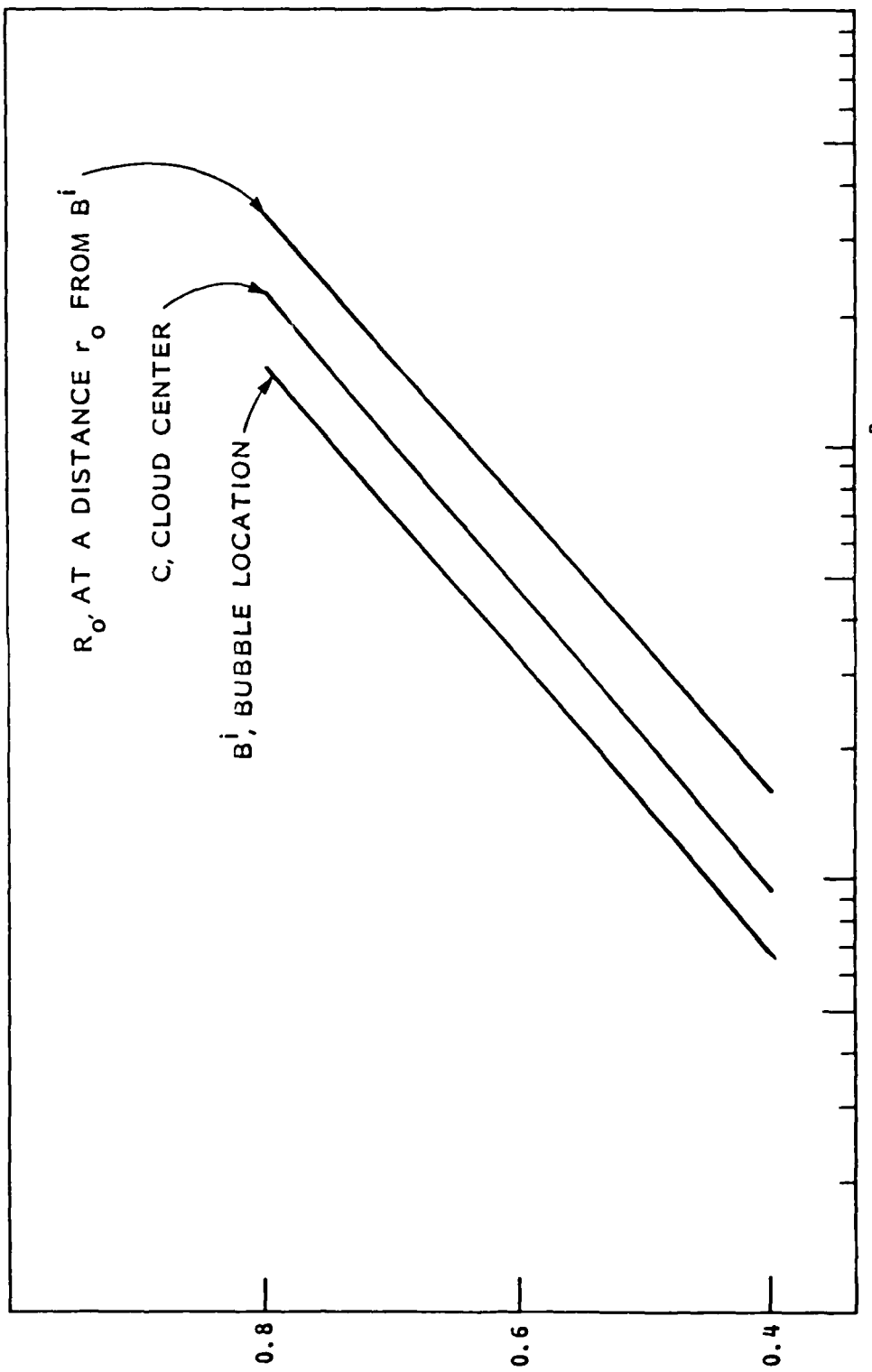

FIGURE 4.12 - VARIATION WITH THE AMBIENT PRESSURE DROP DURATION, ΔT, OF THE MAXIMUM PRESSURES GENERATED, $\bar{P}_{g_o}$ = 0.53, W_e = 100., ϵ = 0.1, N = 12

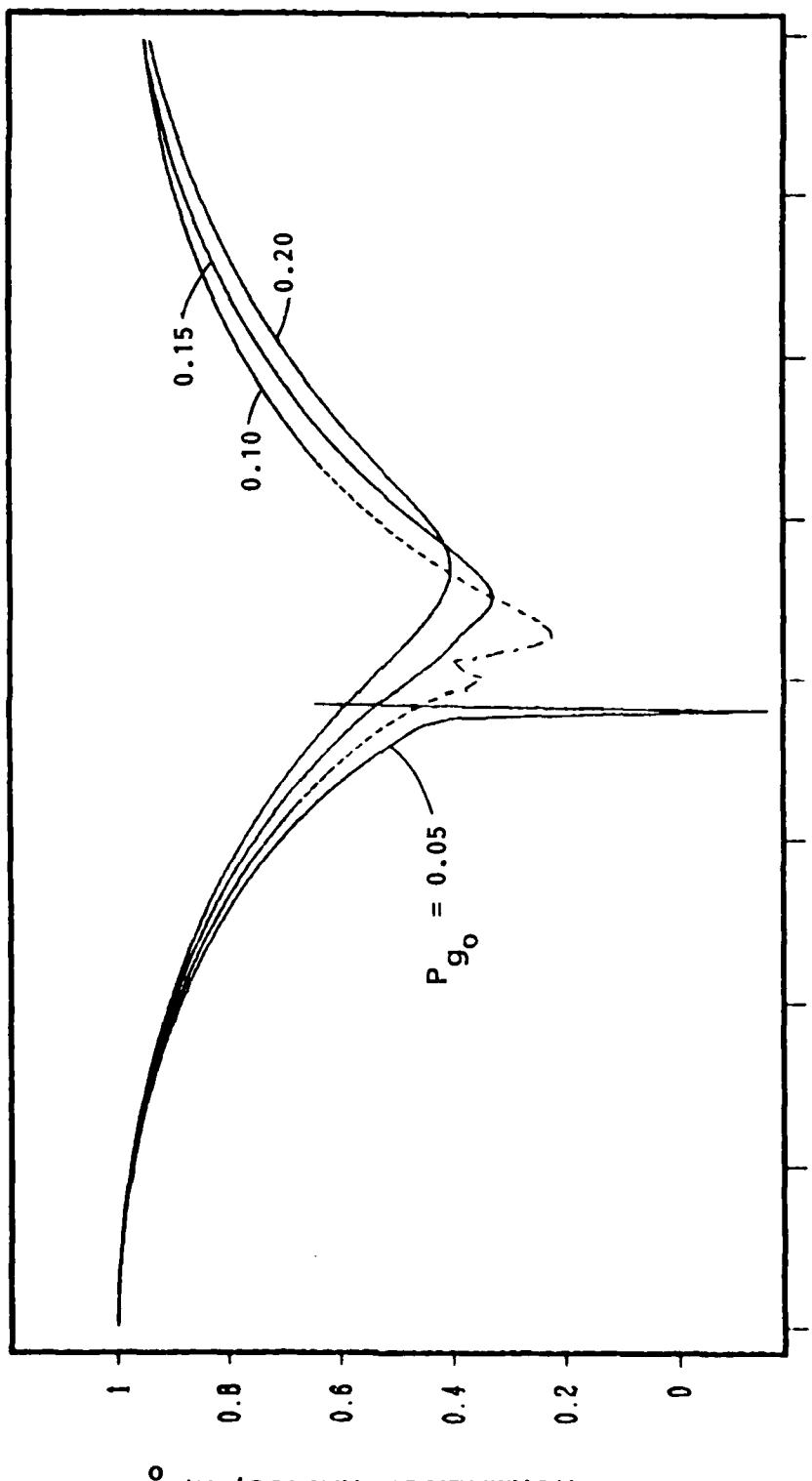

FIGURE 4.13 - INFLUENCE OF THE INITIAL GAS PRESSURE ON THE COLLAPSE OF A FOUR-BUBBLE CLOUD. $C_1 = 2.707$, $C_2 = 1.914$, $C_3 = 0.854$

$\epsilon = 0.1$

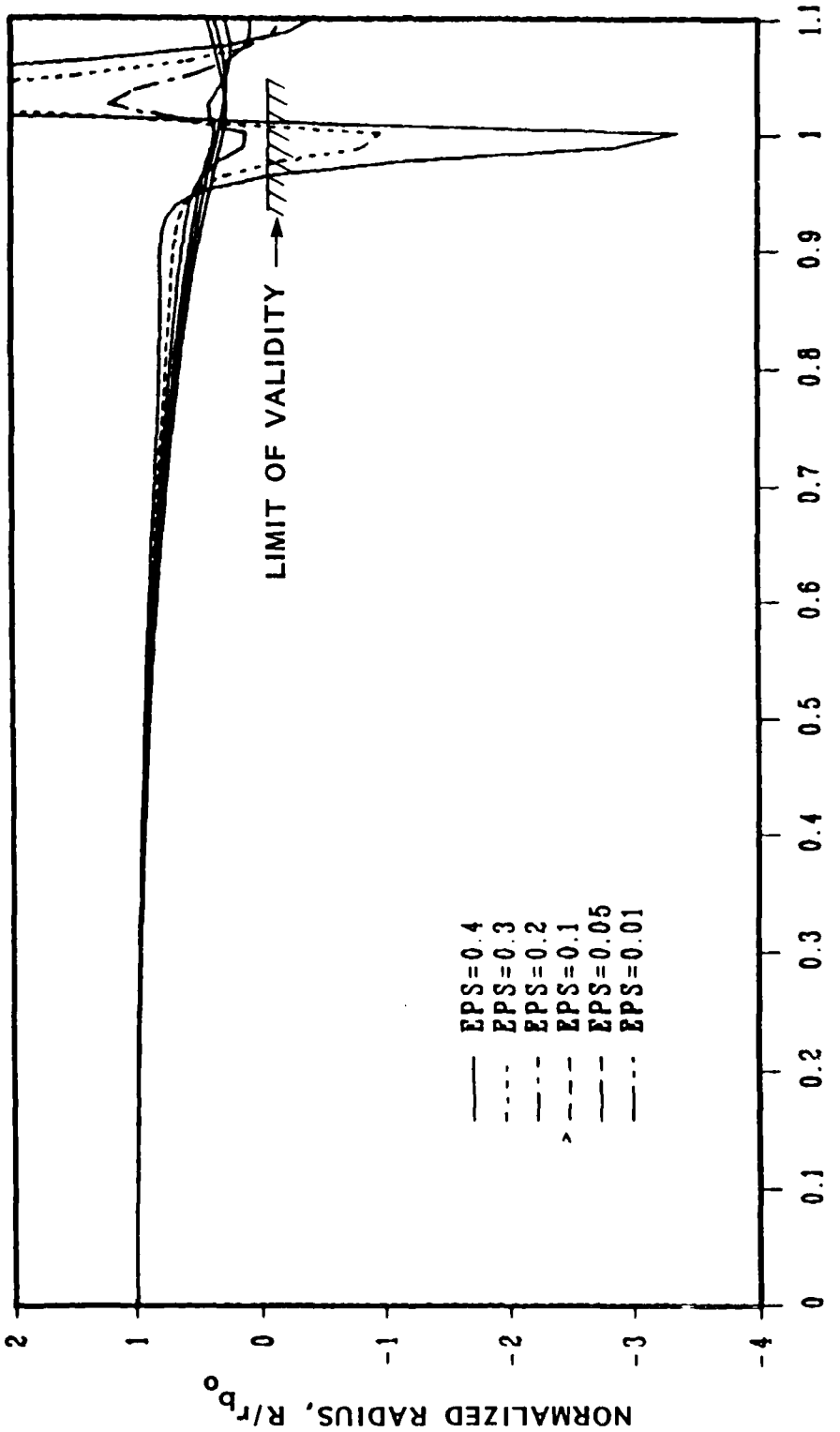

FIGURE 4.14 - INFLUENCE OF ε ON THE COLLAPSE OF A FOUR-BUBBLE CLOUD
$C_1 = 2.707$, $C_2 = 1.914$, $C_3 = 0.854$, $P_{g_o} = 0.1$

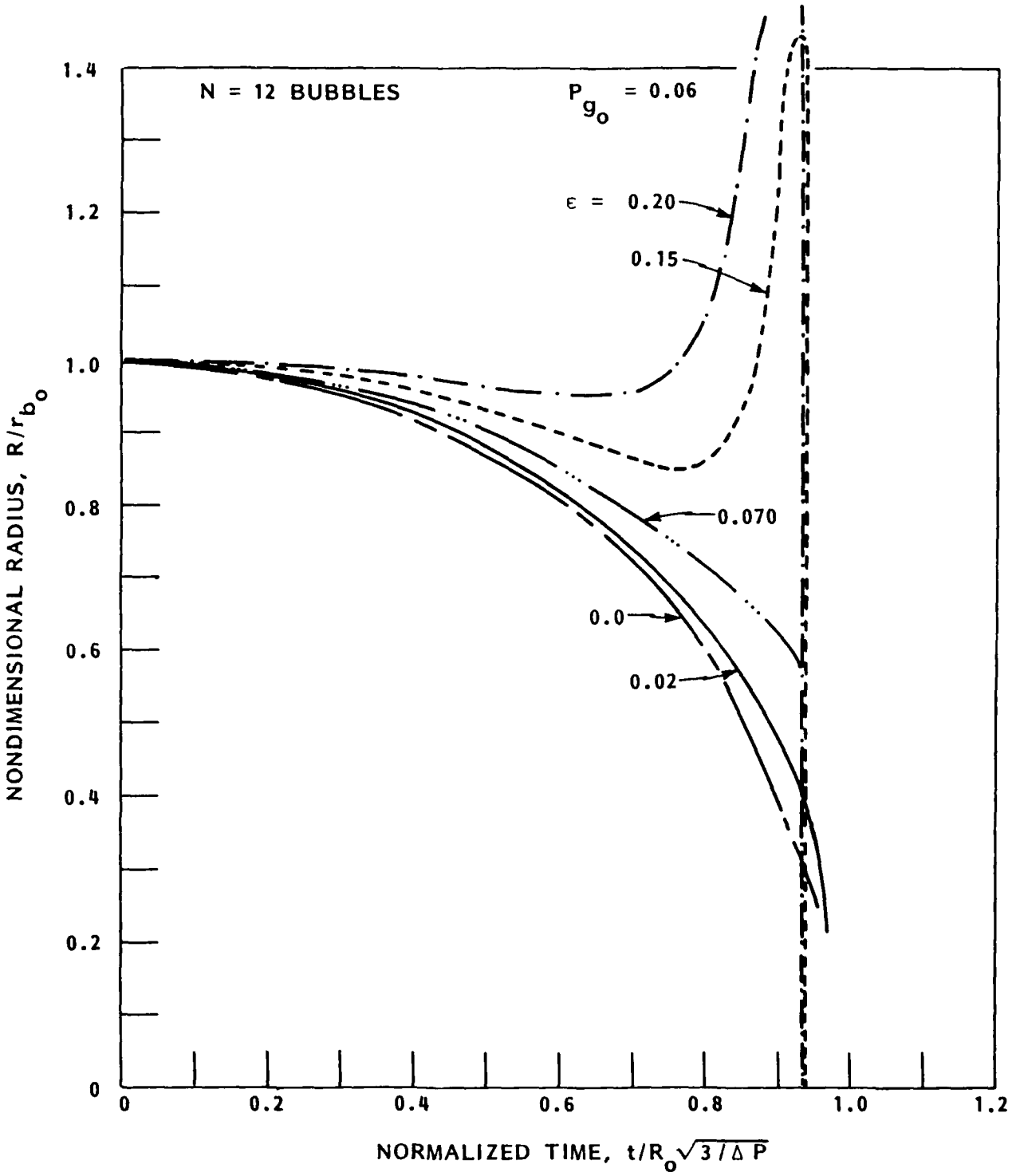

FIGURE 4.15 - INFLUENCE OF ε ON THE COLLAPSE OF A TWELVE-BUBBLE CLOUD, C_1 = 8.616, C_2 = 4.53, C_3 = 0.41, P_{g_o} = 0.06

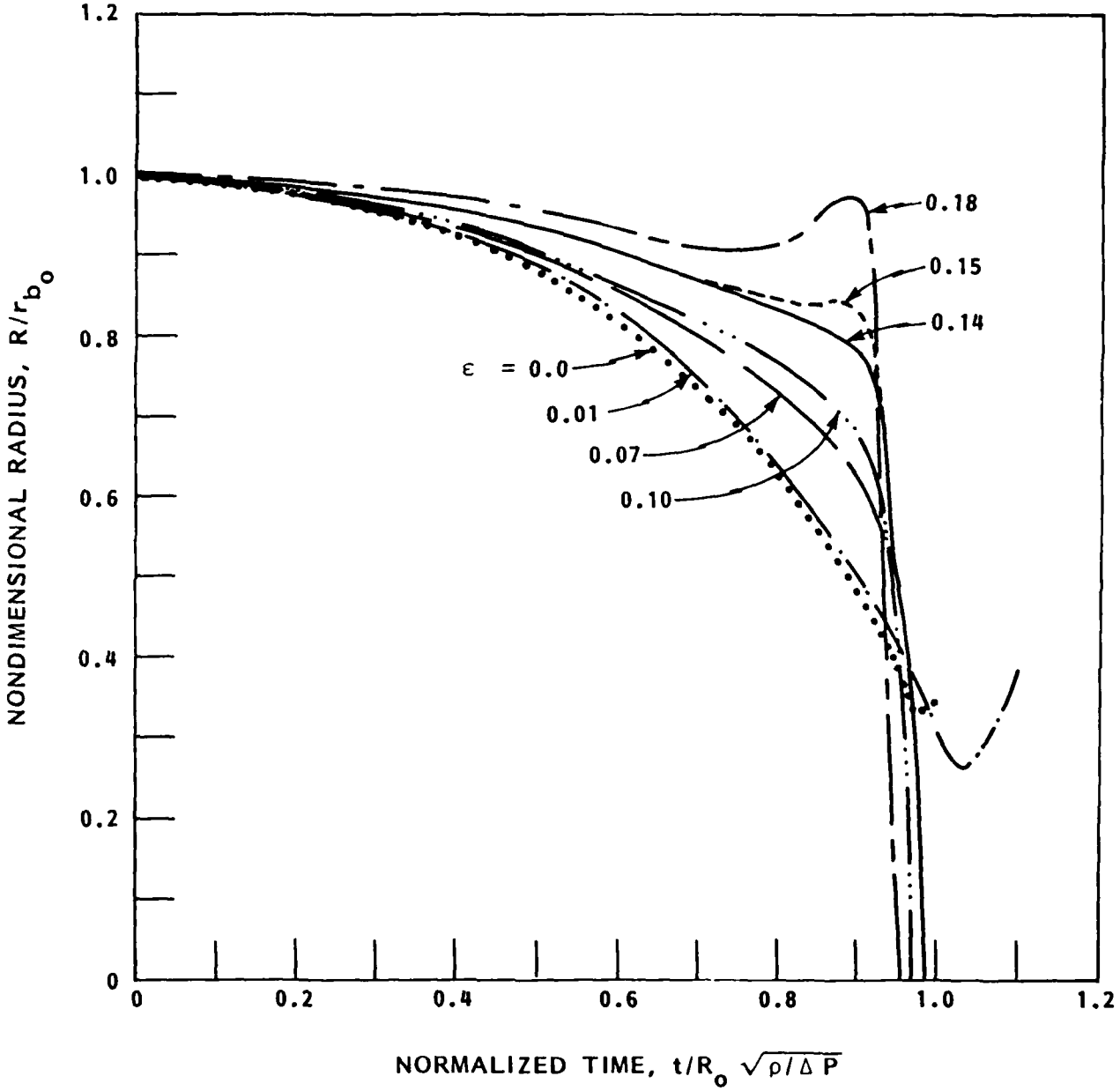

FIGURE 4.16 - INFLUENCE OF ϵ ON THE COLLAPSE OF A TWELVE-BUBBLE CLOUD, $C_1 = 8.616$, $C_2 = 4.53$, $C_3 = 0.41$, $P_{g_o} = 0.10$

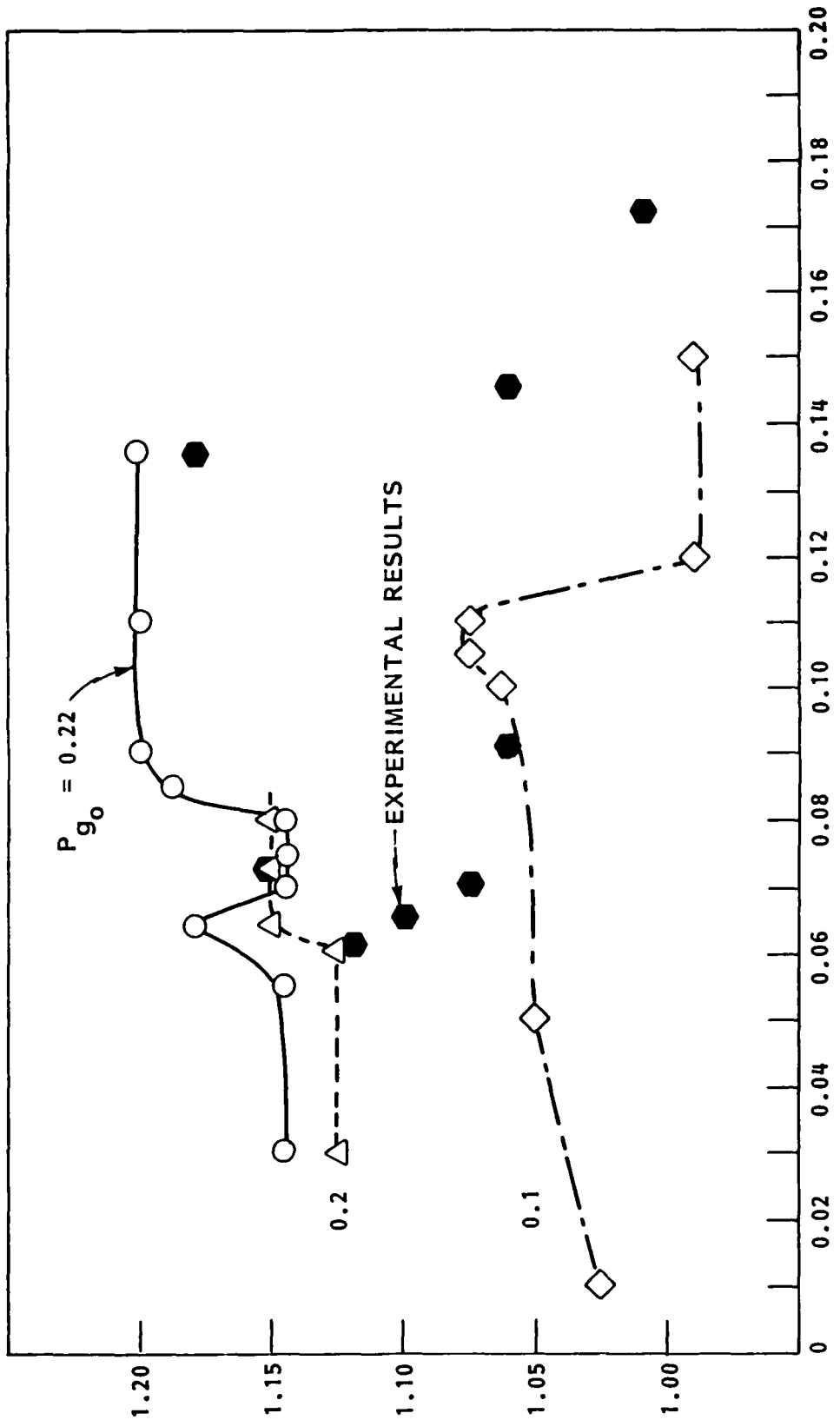

FIGURE 4.17 - INFLUENCE OF ε ON THE TIME TO FIRST COLLAPSE FOR A FOUR-BUBBLE CONFIGURATION AND VARIOUS INITIAL GAS PRESSURES

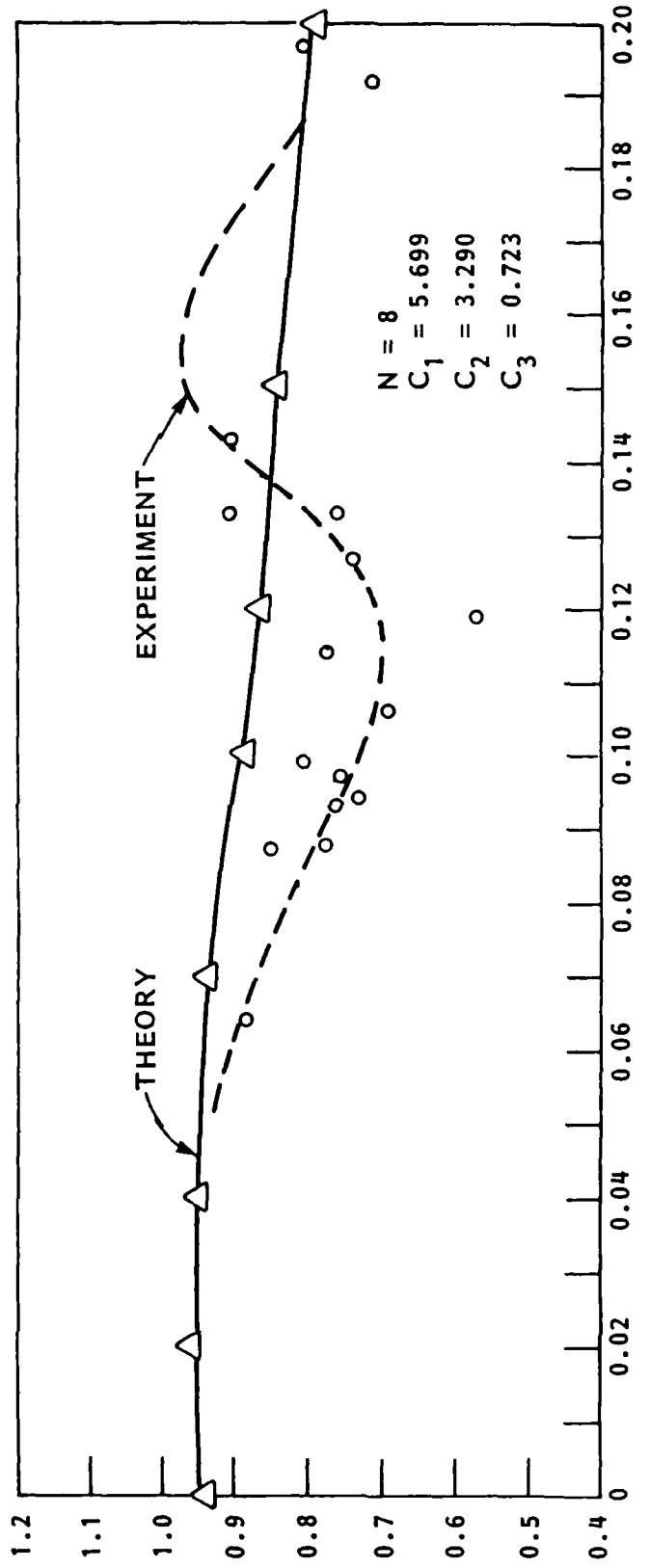

FIGURE 4.18 - INFLUENCE OF ε ON THE TIME TO FIRST COLLAPSE FOR AN EIGHT-BUBBLE CONFIGURATION. P_{g_o} = 0.05

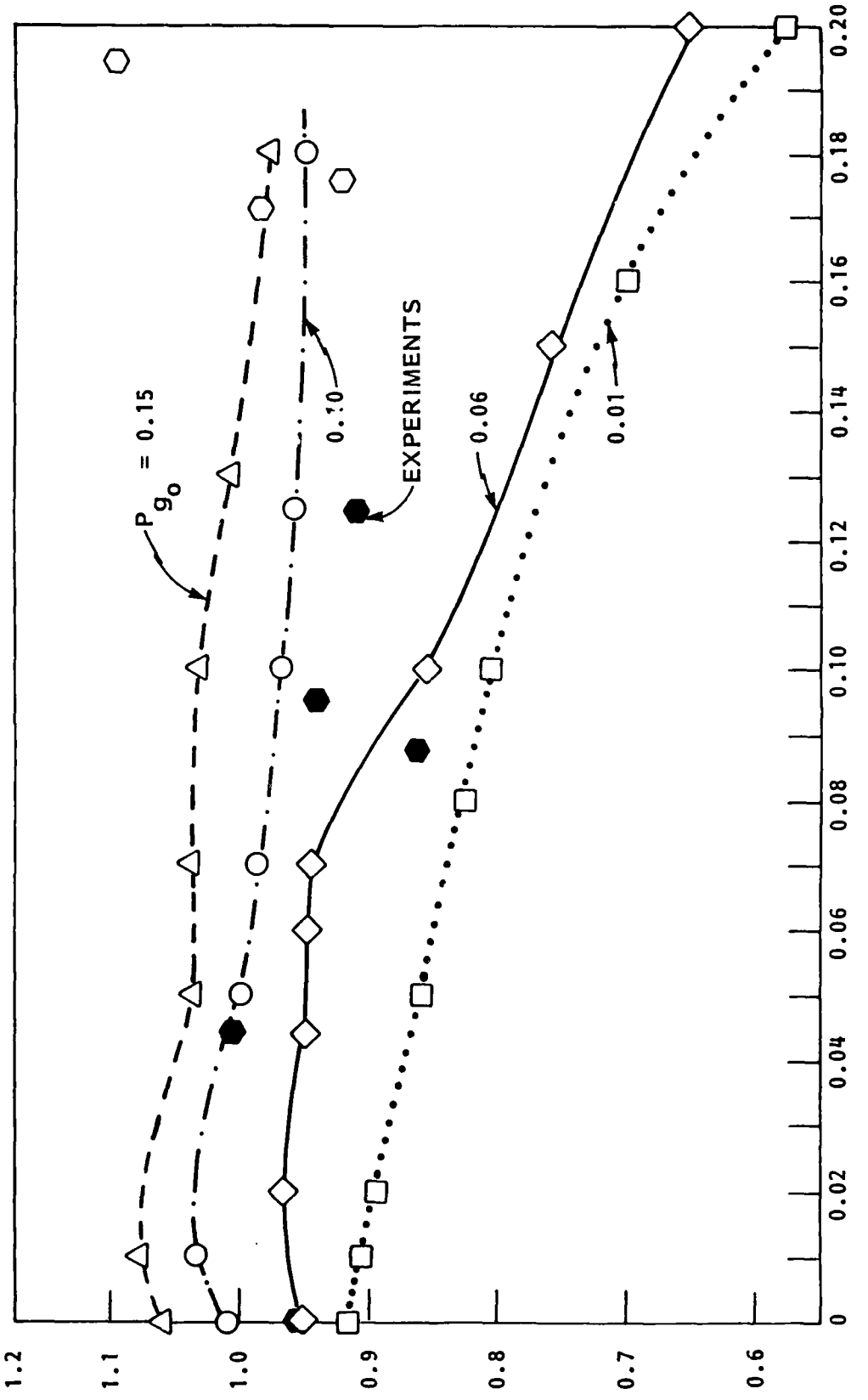

FIGURE 4.19 - INFLUENCE OF ε ON THE TIME TO FIRST COLLAPSE FOR A TWELVE-BUBBLE CONFIGURATION FOR VARIOUS INITIAL GAS PRESSURES

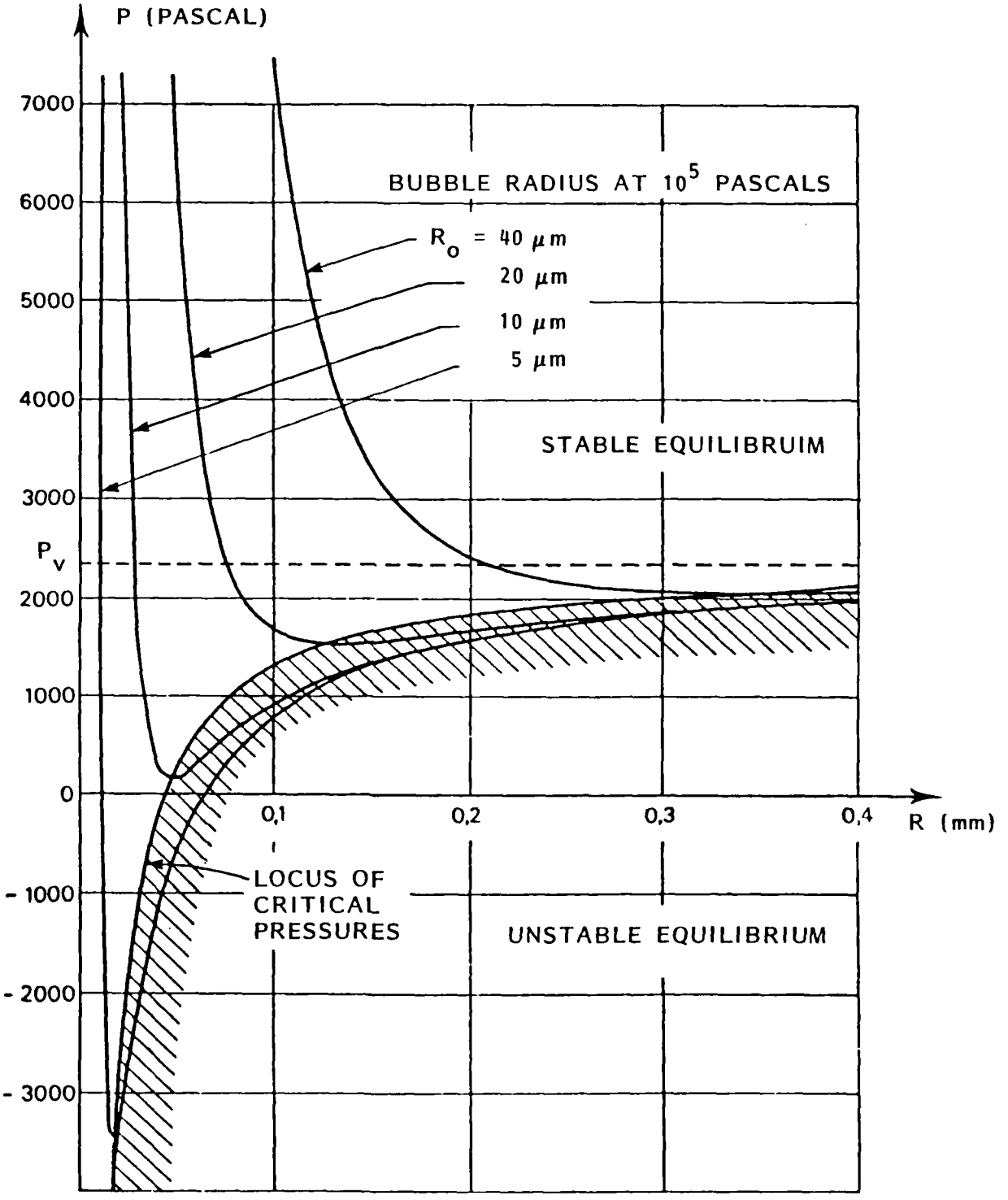

FIGURE 4.20 - VARIATION OF BUBBLE RADIUS WITH AMBIENT PRESSURE

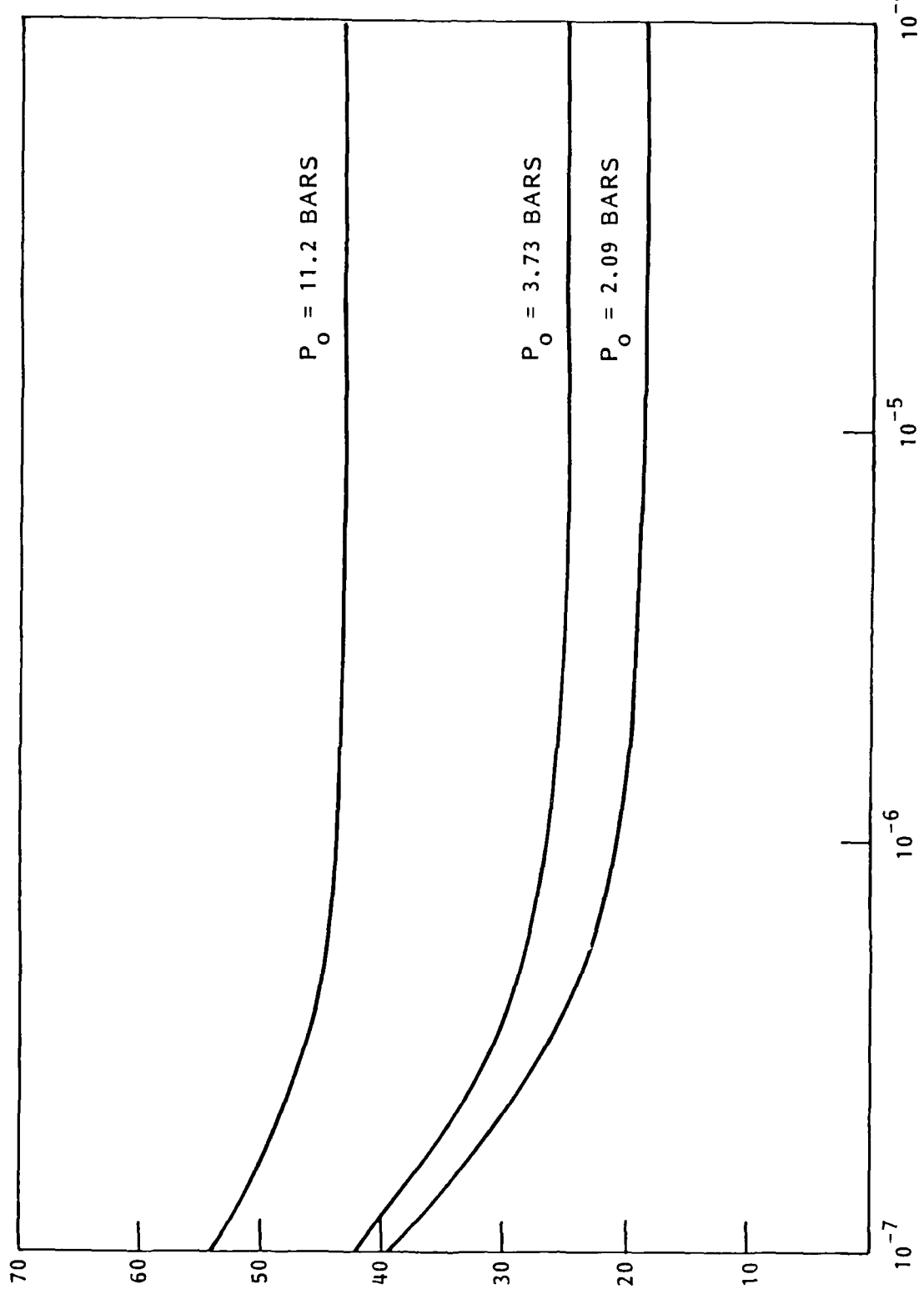

FIGURE 4.21 - CRITICAL VELOCITY AT VENTURI THROAT AS A FUNCTION OF THE INITIAL BUBBLE RADIUS. STATIC EQUILIBRIUM CASE, K = 1.4

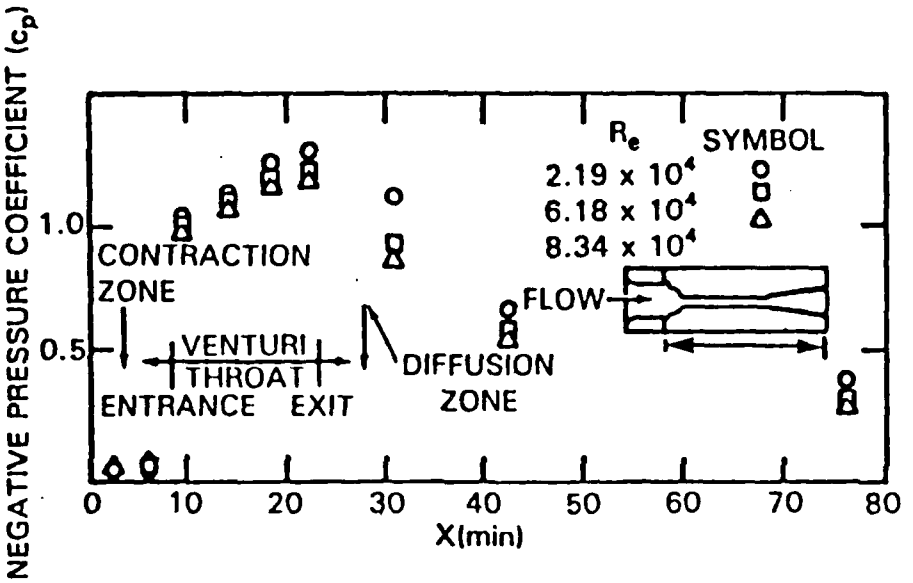

FIGURE 4.22 - PRESSURE DISTRIBUTION ALONG THE VENTURI THROAT

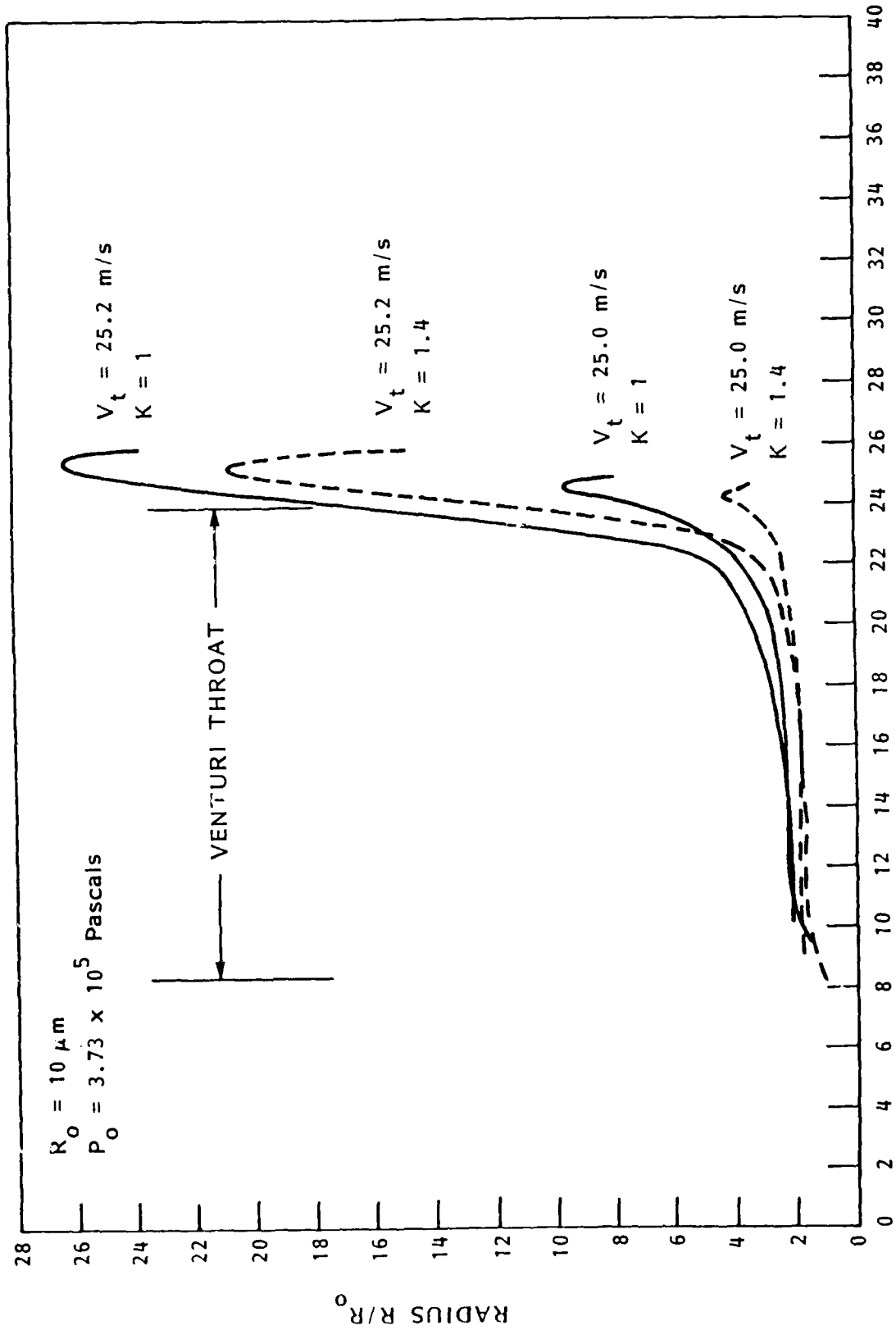

FIGURE 4.23 - BUBBLE RADIUS VARIATION DURING ITS TRAVERSE THROUGH THE VENTURI. INFLUENCE OF THROAT VELOCITY AND POLYTROPIC CONSTANT K.

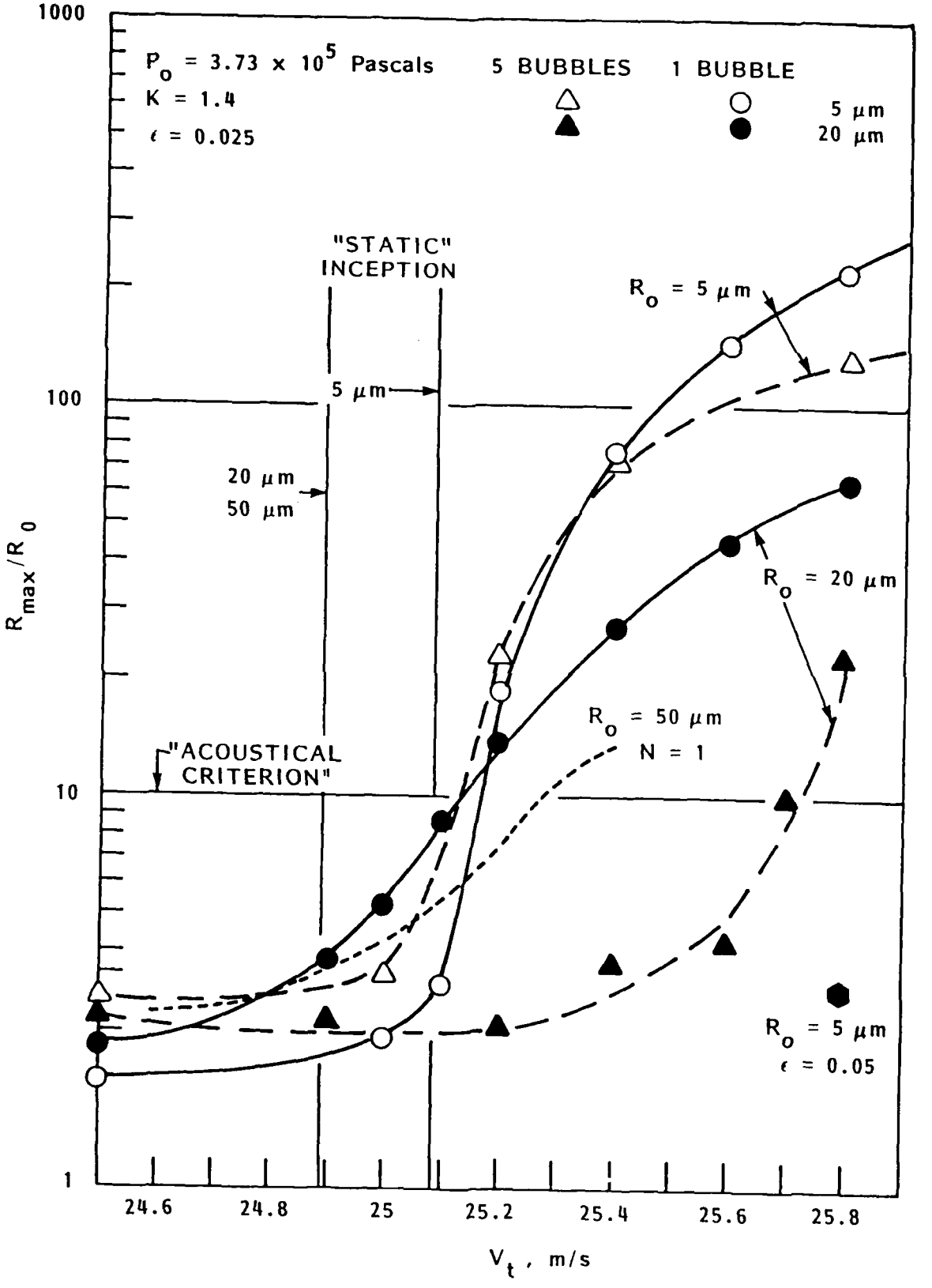

FIGURE 4.24 - NORMALIZED MAXIMUM BUBBLE RADIUS AS A FUNCTION OF THE THROAT VELOCITY. INFLUENCE OF BUBBLE SIZE AND BUBBLE NUMBER

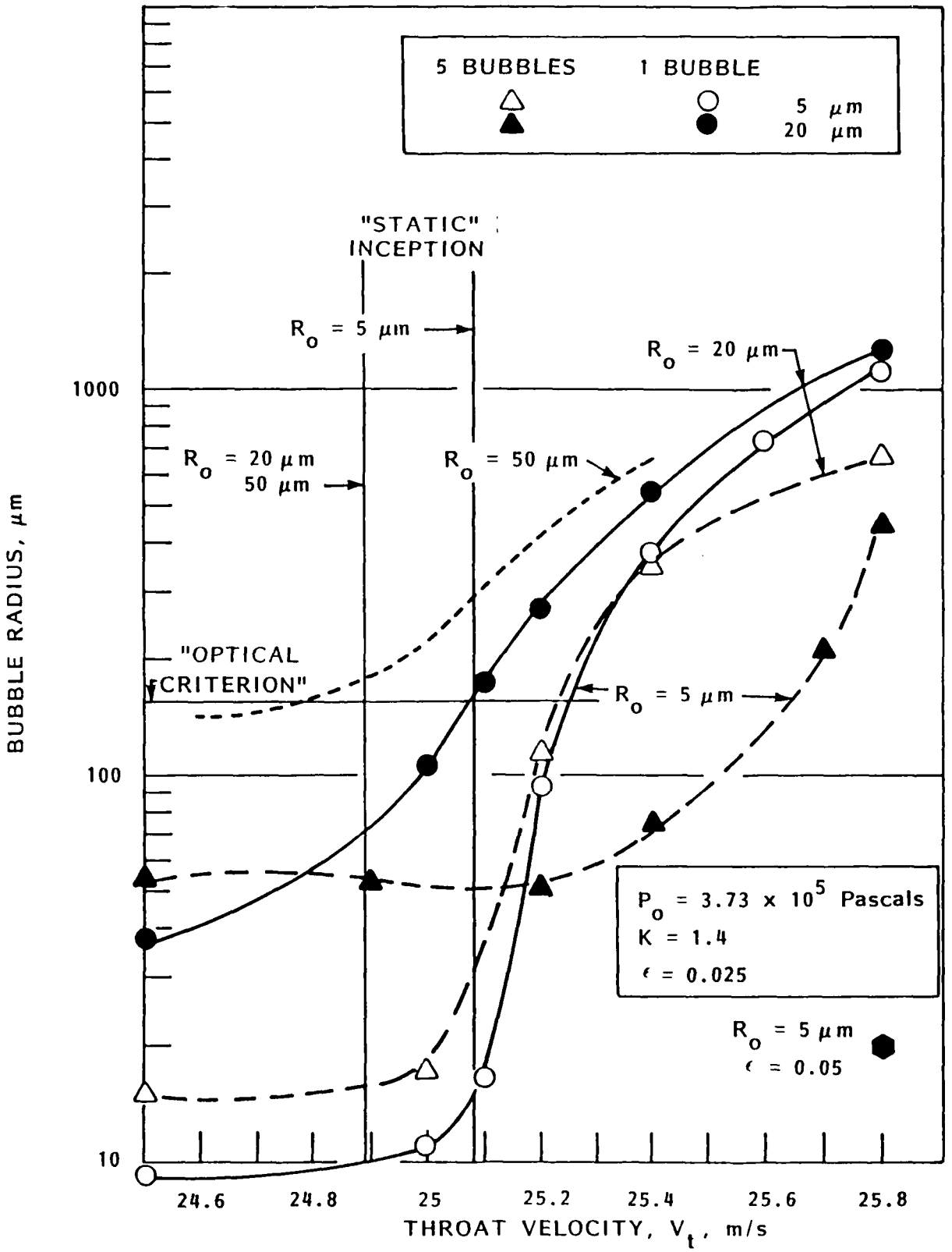

FIGURE 4.25 - MAXIMUM BUBBLE RADIUS AS A FUNCTION OF THE THROAT VELOCITY. INFLUENCE OF BUBBLE SIZE AND NUMBER

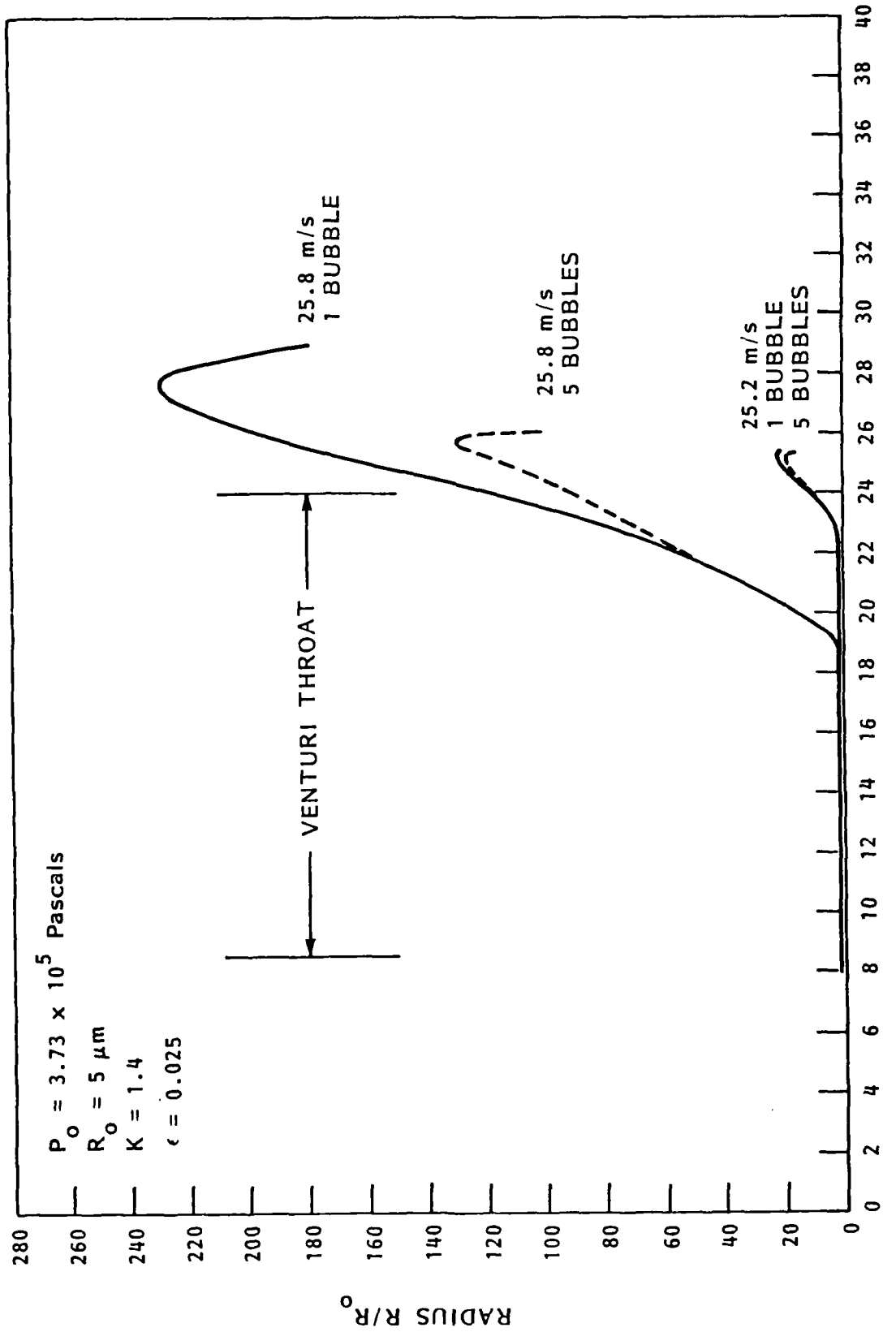

FIGURE 4.26 - INFLUENCE OF THROAT VELOCITY AND BUBBLE NUMBER ON BUBBLE RADIUS HISTORY DURING ITS MOTION THROUGH THE VENTURI

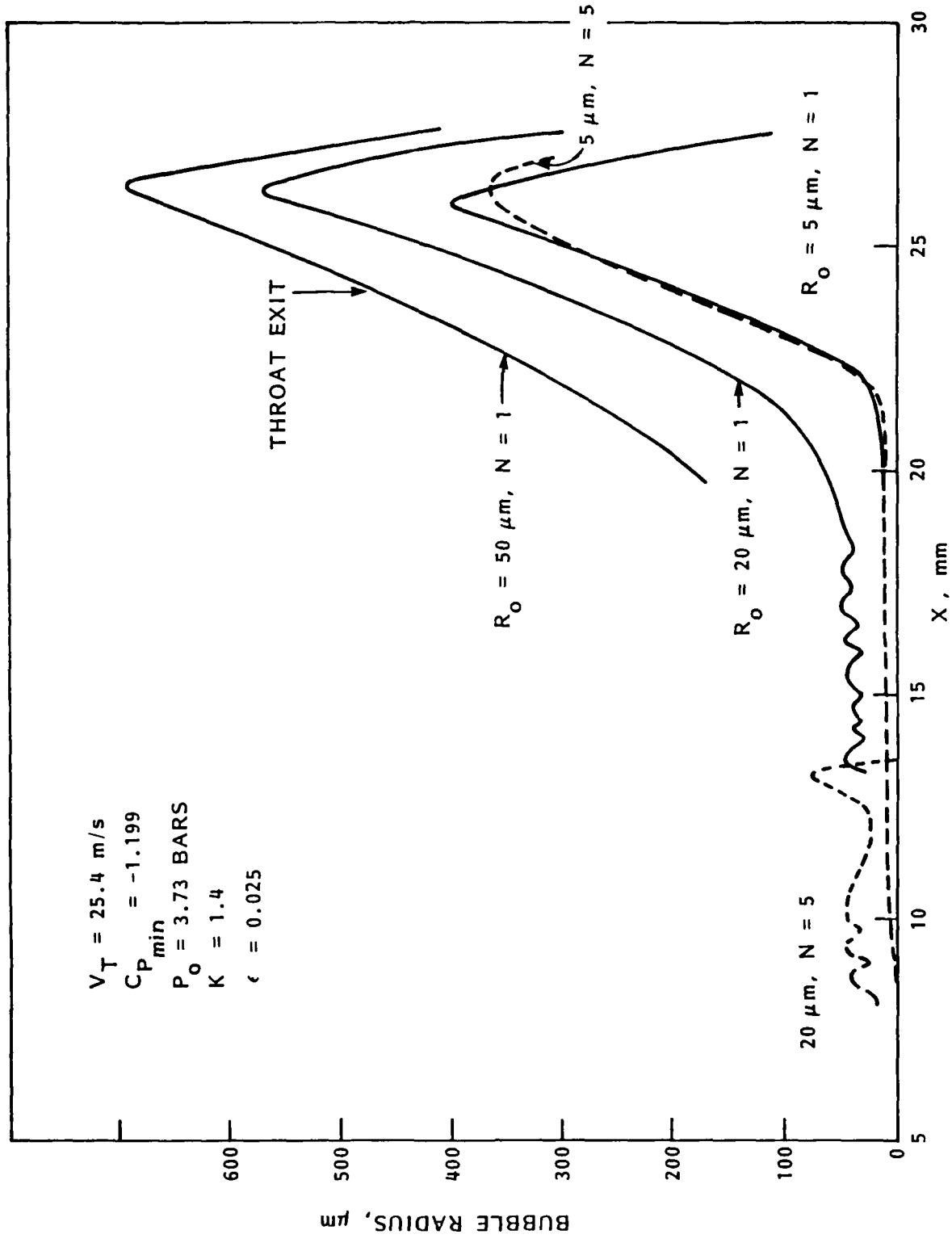

FIGURE 4.27 - BUBBLE GROWTH AND COLLAPSE IN THE VENTURI SYSTEM AT THREE DIFFERENT INITIAL BUBBLE SIZES

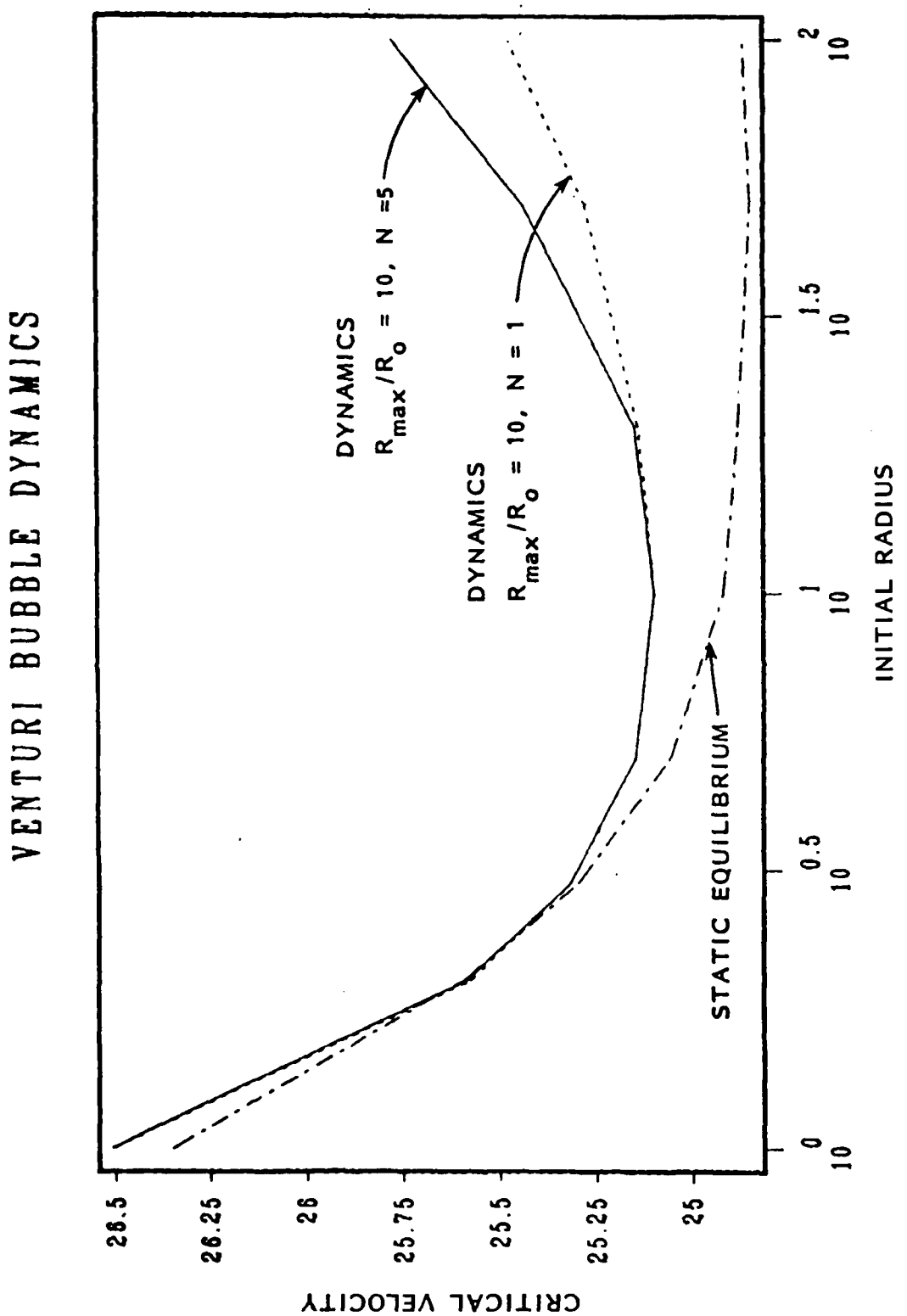

FIGURE 4.28 - COMPARISON BETWEEN DYNAMICS AND STATIC CRITICAL VELOCITY AT VENTURI THROAT AS A FUNCTION OF INITIAL BUBBLE RADIUS

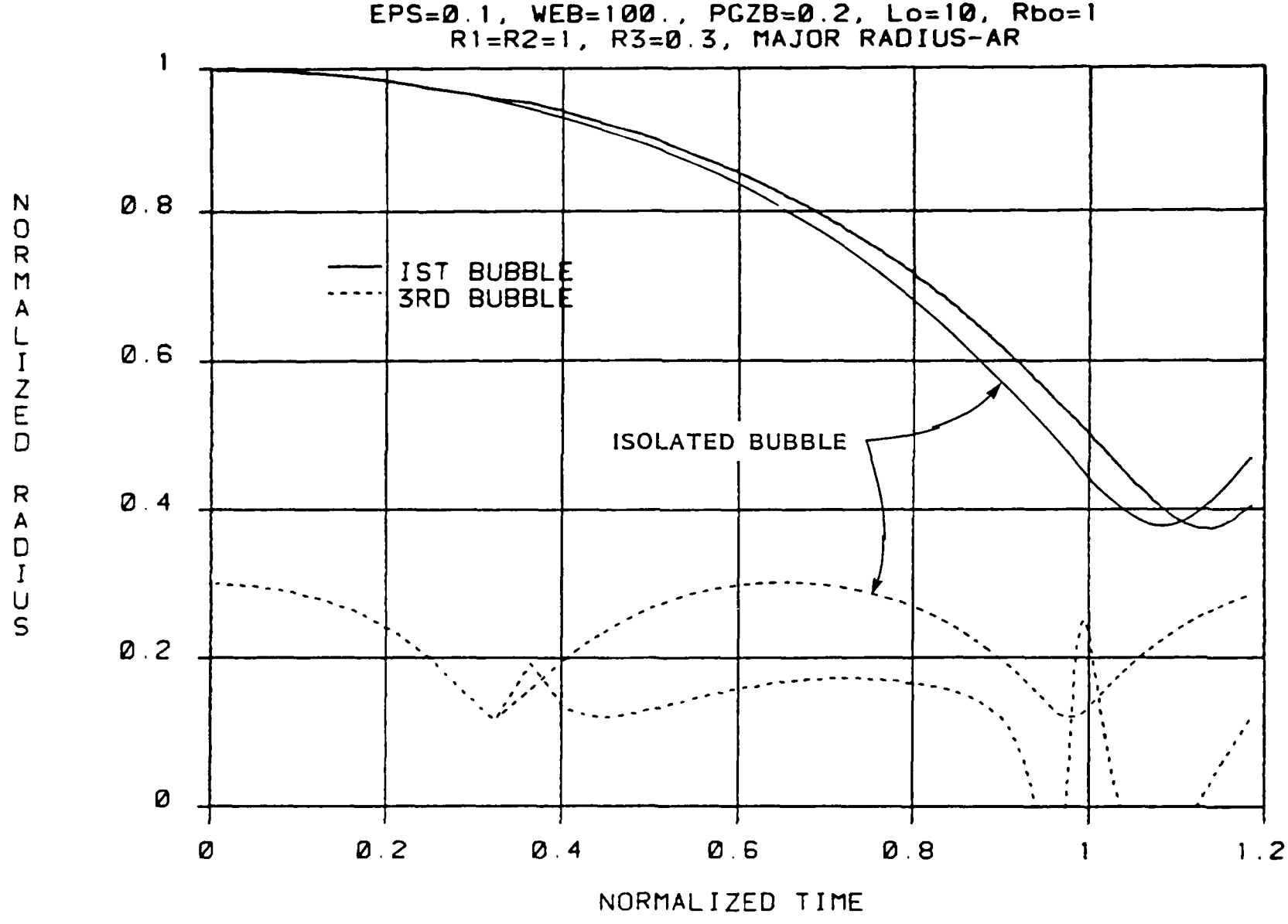

FIGURE 4.29 - COLLAPSE HISTORY OF A THREE BUBBLE CONFIGURATION. RESPECTIVE INITIAL NONDIMENSIONAL RADII OF 1, 1 AND 0.3 COMPARISON WITH THE ISOLATED BUBBLE CASES

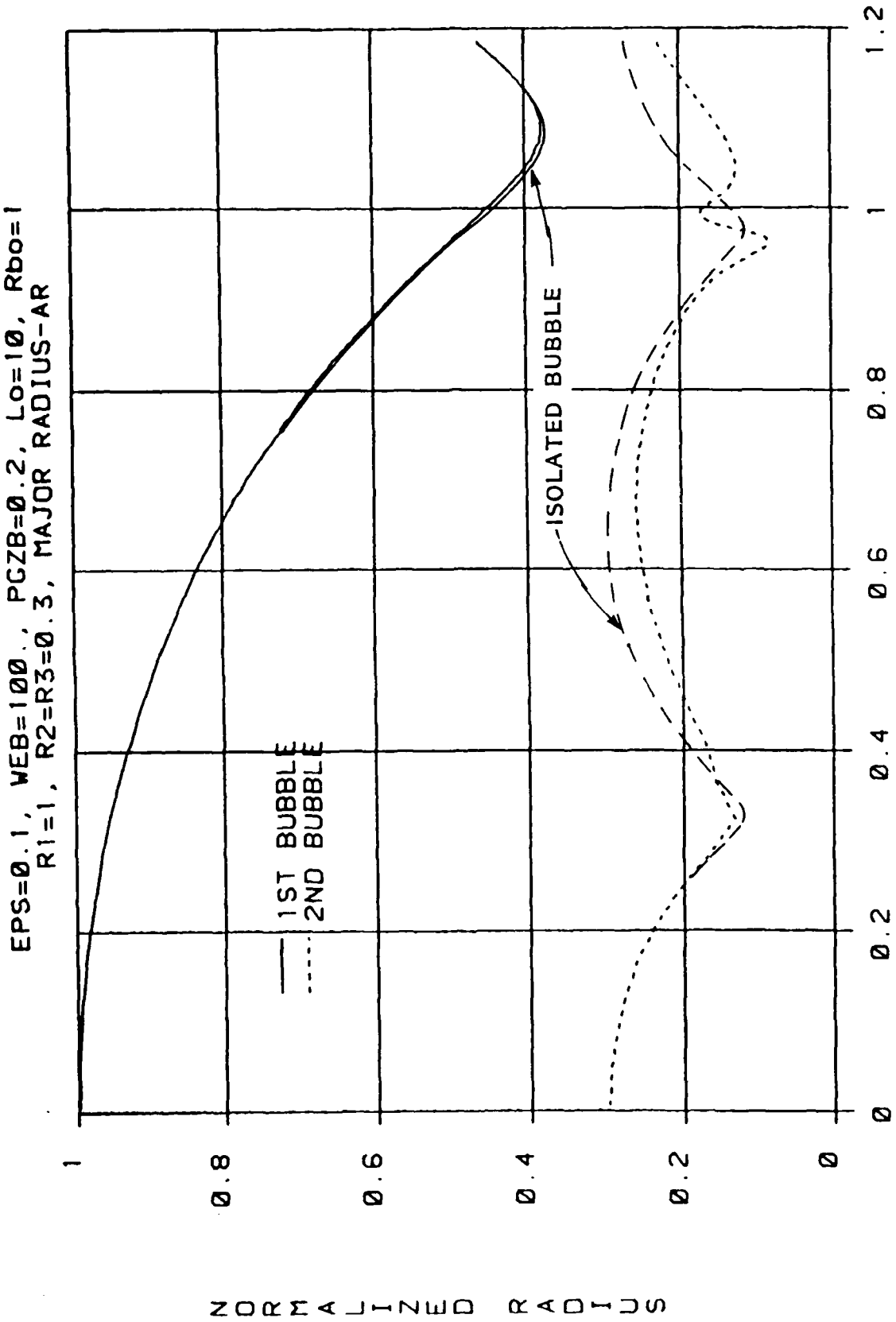

FIGURE 4.30 - COLLAPSE HISTORY OF A THREE BUBBLE CONFIGURATION. RESPECTIVE INITIAL NONDIMENSIONAL RADII OF 1, 0.3 AND 0.3 COMPARISON WITH THE ISOLATED BUBBLE CASES

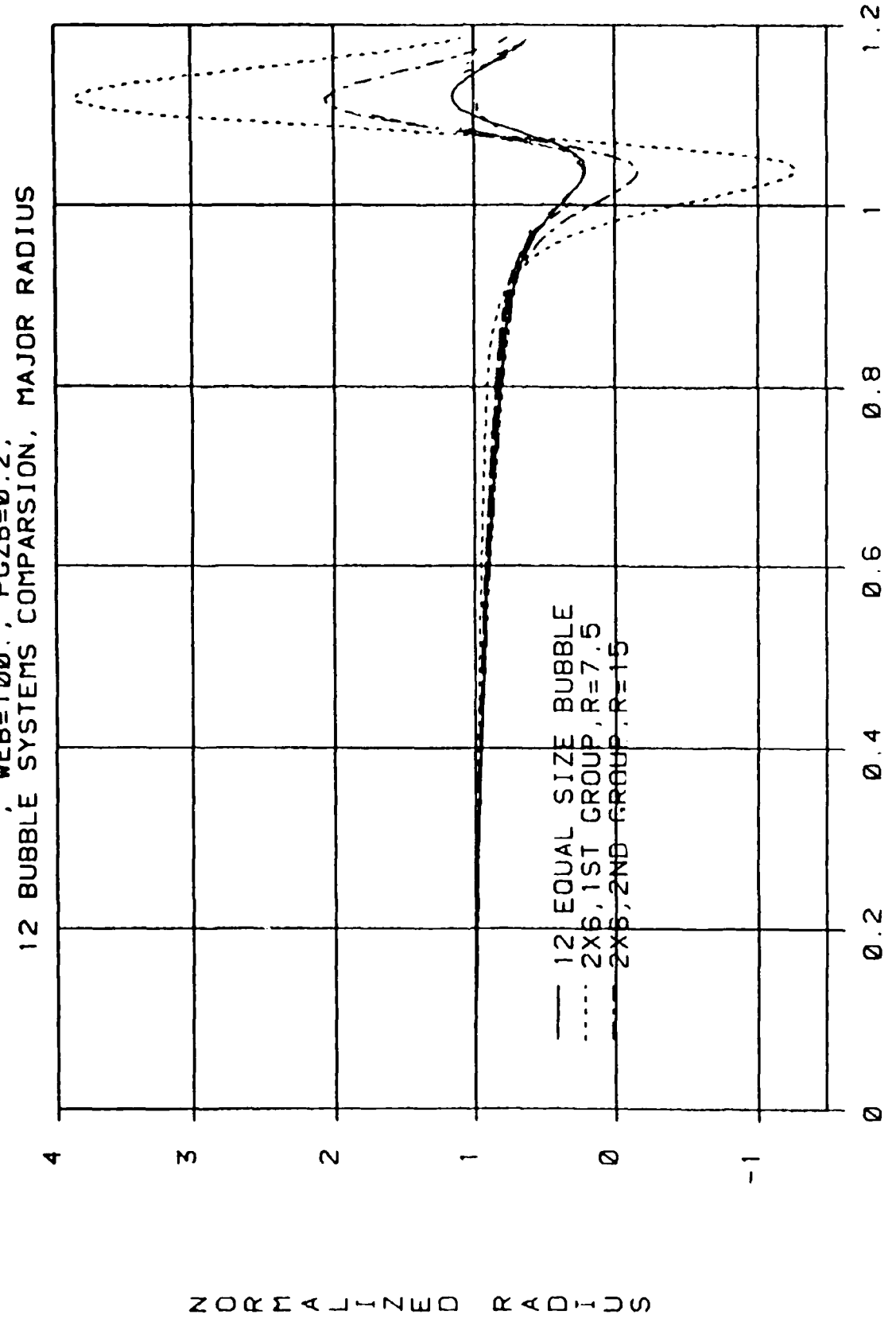

FIGURE 4.31 - COMPARISON OF THE RADIUS HISTORY FOR A SYMMETRICAL 12-BUBBLE CONFIGURATION (BUBBLES CENTERED ON SPHERE R = 15), AND A 2-LAYER 6-BUBBLE CONFIGURATION (BUBBLES CENTERED ON SPHERES R = 7.5 AND R = 15). BOTH CONFIGURATIONS HAVE THE SAME GLOBAL VOID FRACTION

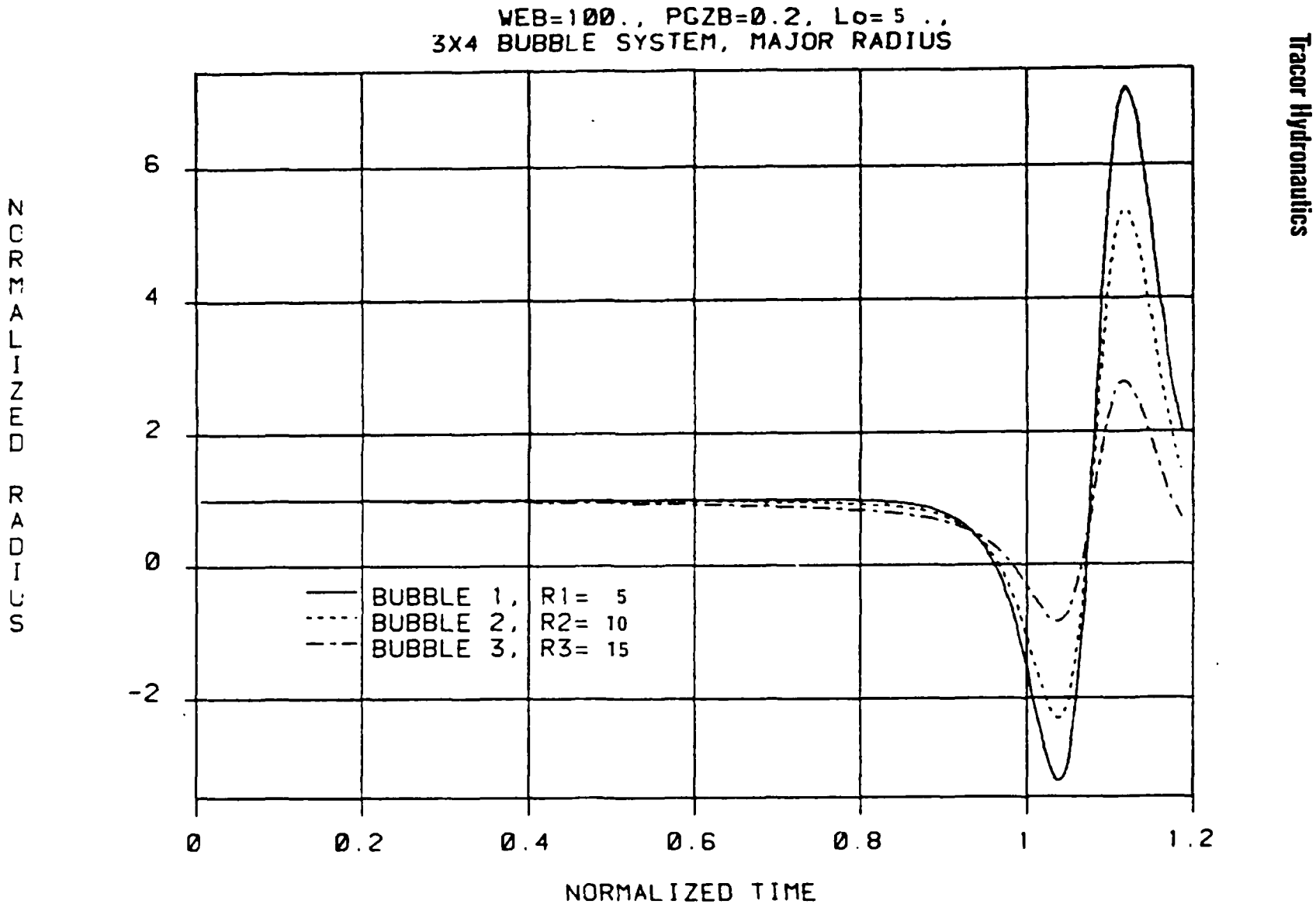

FIGURE 4.32 - COMPARISON OF THE RADIUS HISTORY FOR A 3-LAYER CONFIGURATION WITH 4-BUBBLES ON EACH LAYER. BUBBLES CENTERED ON SPHERES OF RADII 5, 10 AND 15

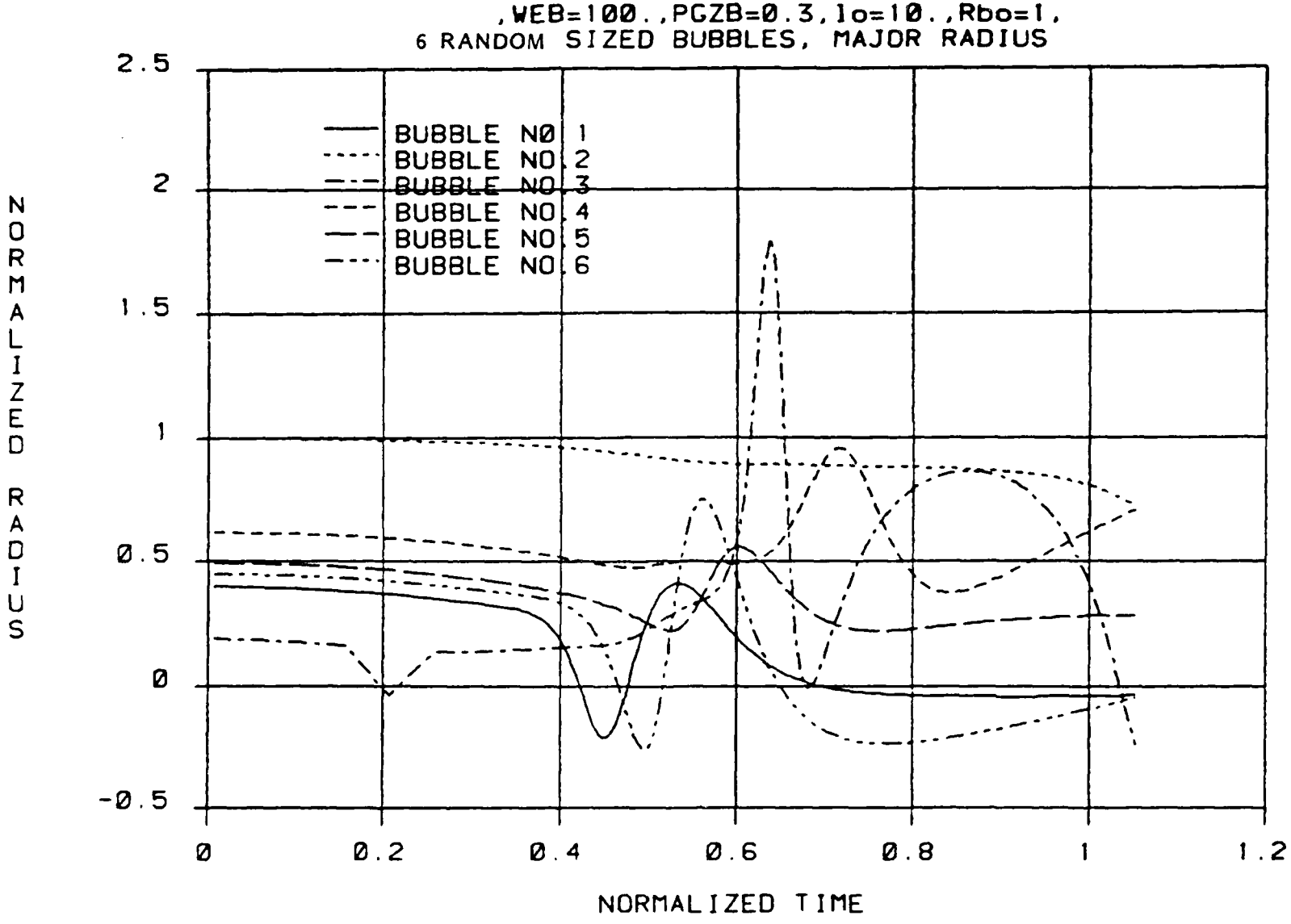

FIGURE 4.33 - BUBBLE SIZES HISTORY FOR A RANDOMLY SIZED AND RANDOMLY DISTRIBUTED 6-BUBBLE CONFIGURATION (SEE TABLE FIGURE 4.34)

BUBBLE NO.	COORDINATES			RADIUS
	X	Y	Z	
1	6	3	6	0.335
2	5	3	3	0.841
3	3	1	1	0.159
4	5	2	1	0.520
5	7	7	3	0.415
6	4	4	5	0.377

FIGURE 4.34 - RANDOM BUBBLE DISTRIBUTION AND SIZES
(Corresponds to results on Figure 4.33)

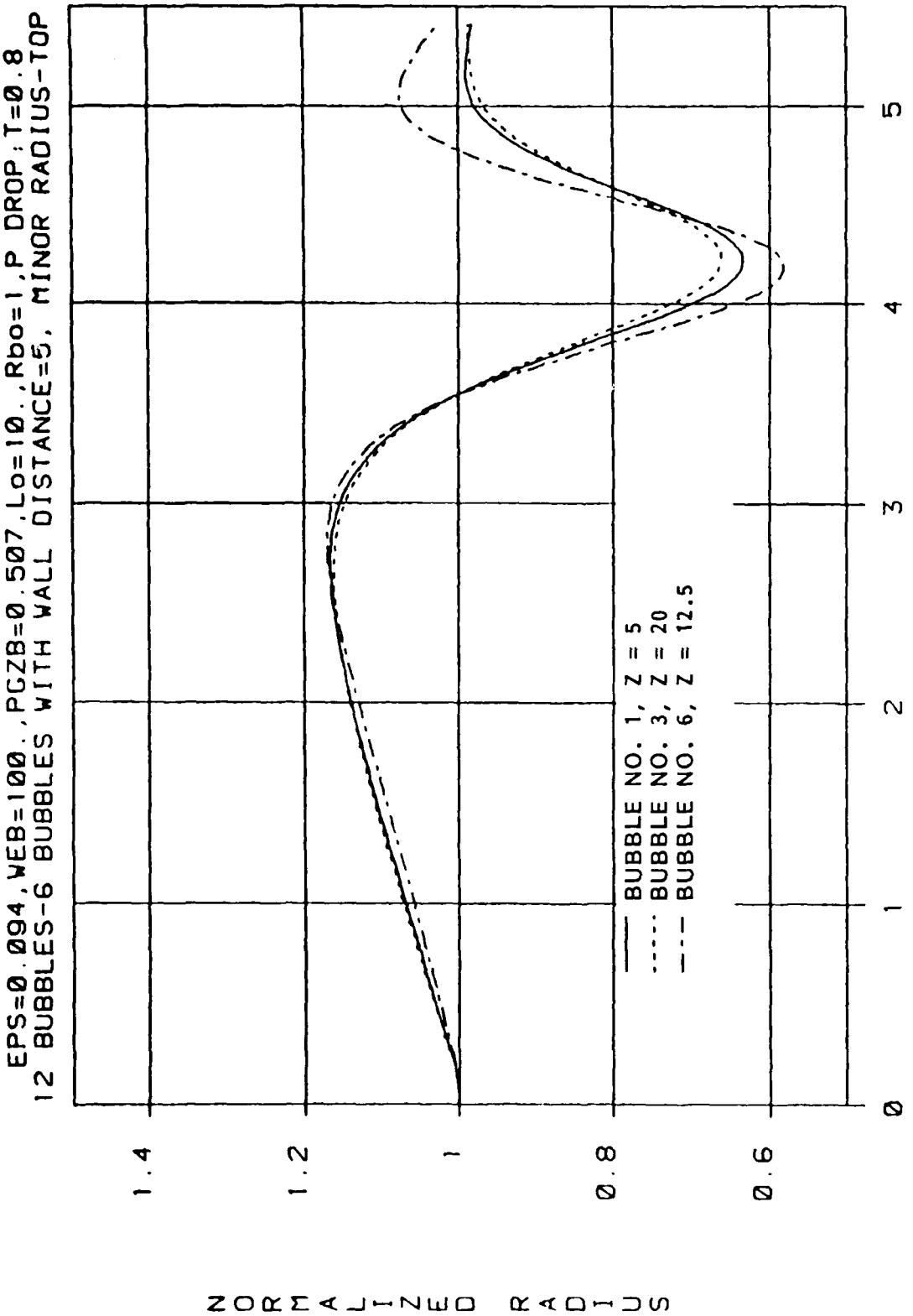

FIGURE 4.35 - GROWTH AND COLLAPSE OF A 6-BUBBLE CLOUD NEAR A SOLID WALL. RADIUS HISTORY FOR THE VARIOUS BUBBLES: NO. 1. CLOSEST TO THE WALL. NO. 3. FARTHEST FROM THE WALL NO. 6. FOUR BUBBLES IN A PLANE PARALLEL TO THE WALL.

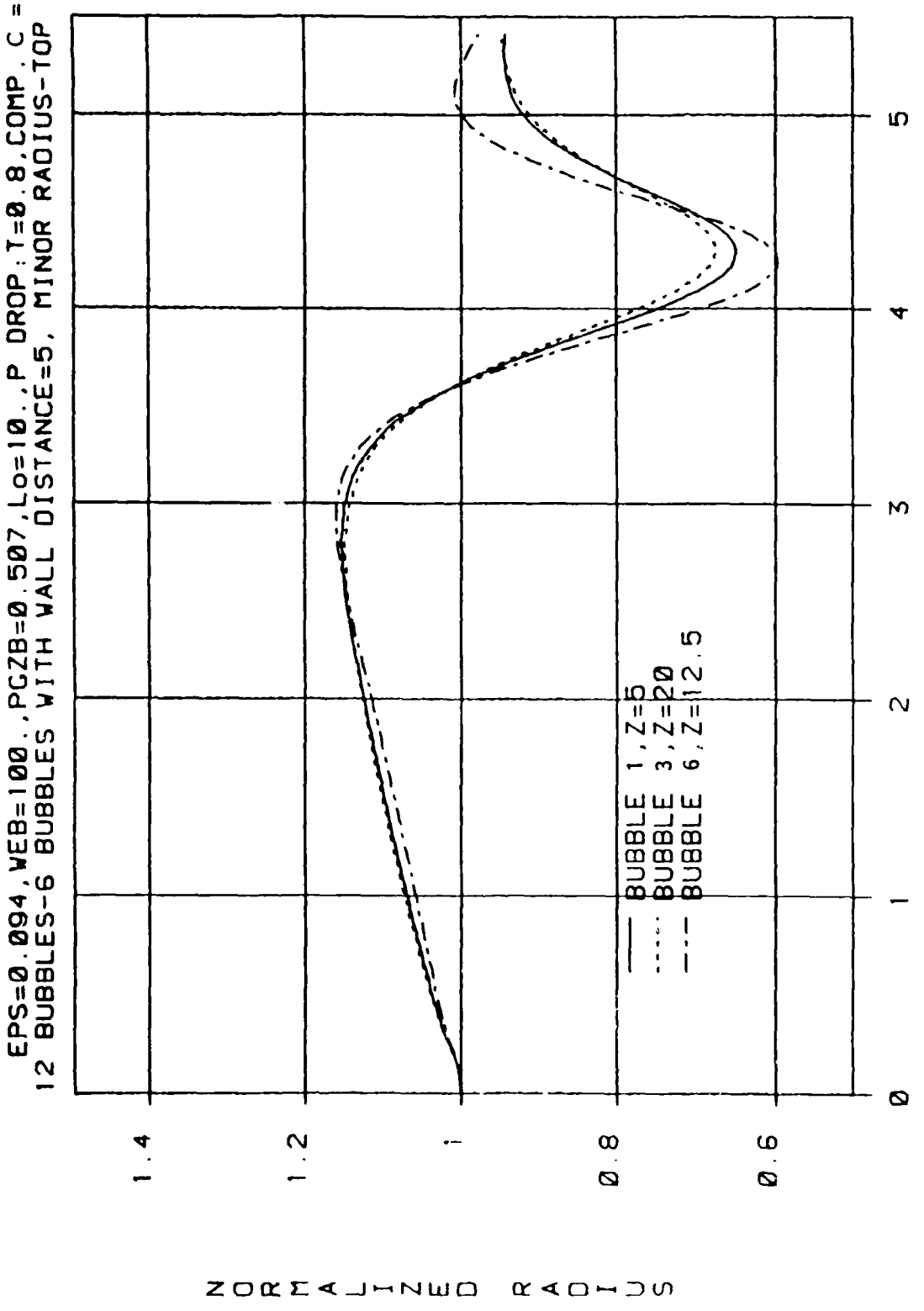

FIGURE 4.36 - EFFECT OF A FINITE SOUND SPEED ON THE GROWTH AND COLLAPSE OF A 6-BUBBLE CLOUD NEAR A SOLID WALL (COMPARE WITH FIGURE 15)

AD-A170 692 CLOUD CAVITATION AND COLLECTIVE BUBBLE DYNAMICS(U) 3/3
TRACOR HYDRONAUTICS INC LAUREL MD G L CHAHINE ET AL.
15 MAR 86 TR-83017-1 N00014-83-C-0244

UNCLASSIFIED F/G 20/4 NL

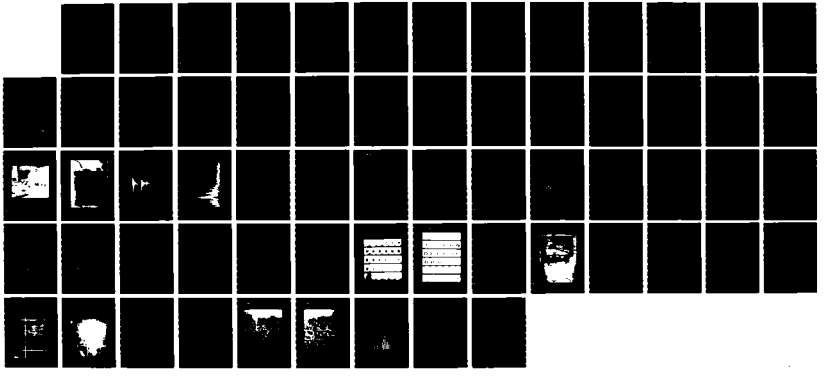

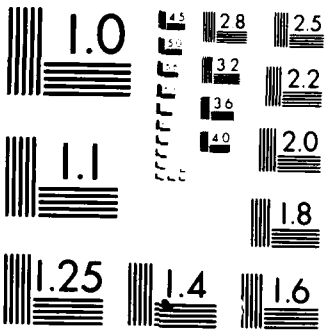

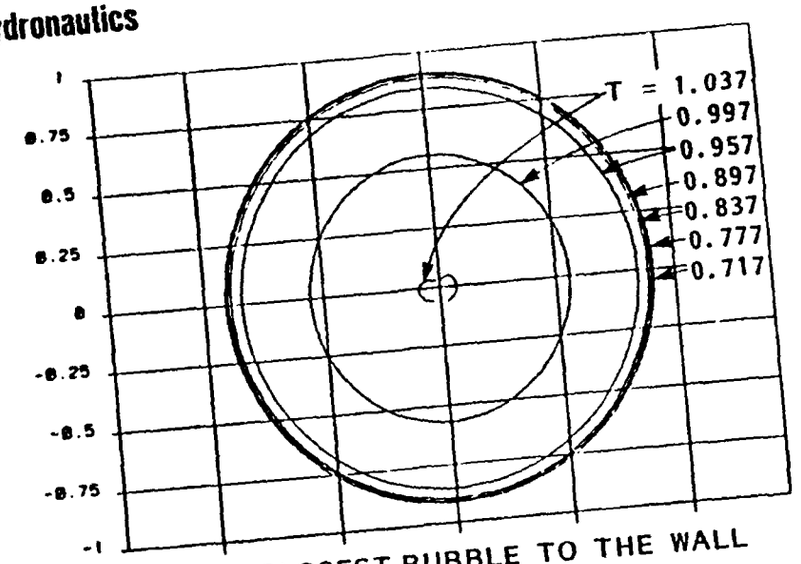

Z = 5, CLOSEST BUBBLE TO THE WALL

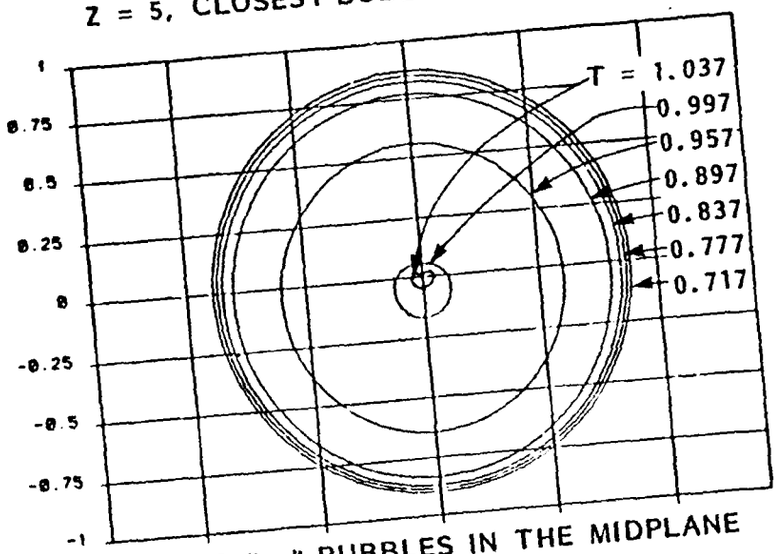

Z = 12.5, 4 BUBBLES IN THE MIDPLANE

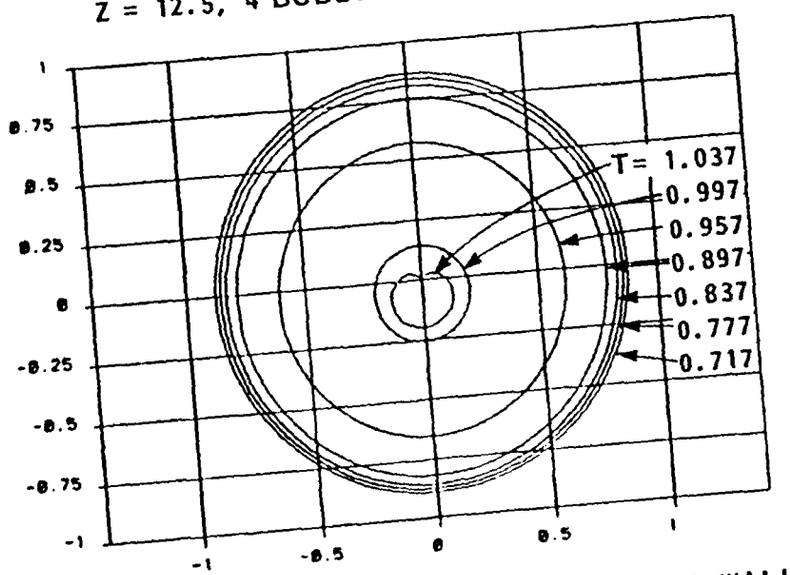

Z = 20 FARTHEST BUBBLES FROM THE WALL

FIGURE 4.37 - BUBBLE SHAPES AT DIFFERENT TIMES

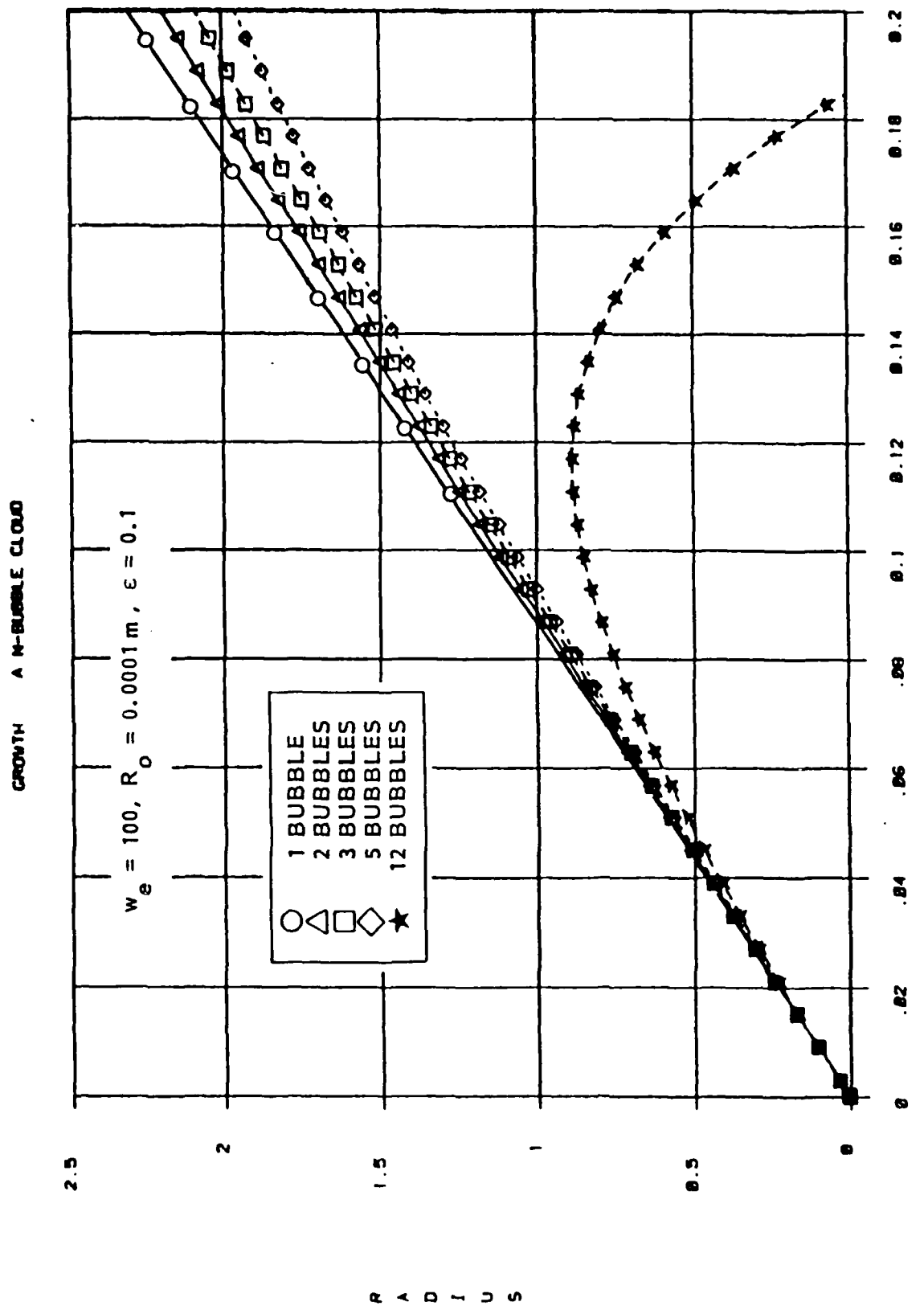

FIGURE 5.1 -GROWTH OF AN INITIALLY SHPHERICAL BUBBLE IN AN N-BUBBLE CLOUD FOLLOWING A SUDDEN PRESSURE DROP, W_e = 100, R_o = *0.0001 m*, ε = *0.1*

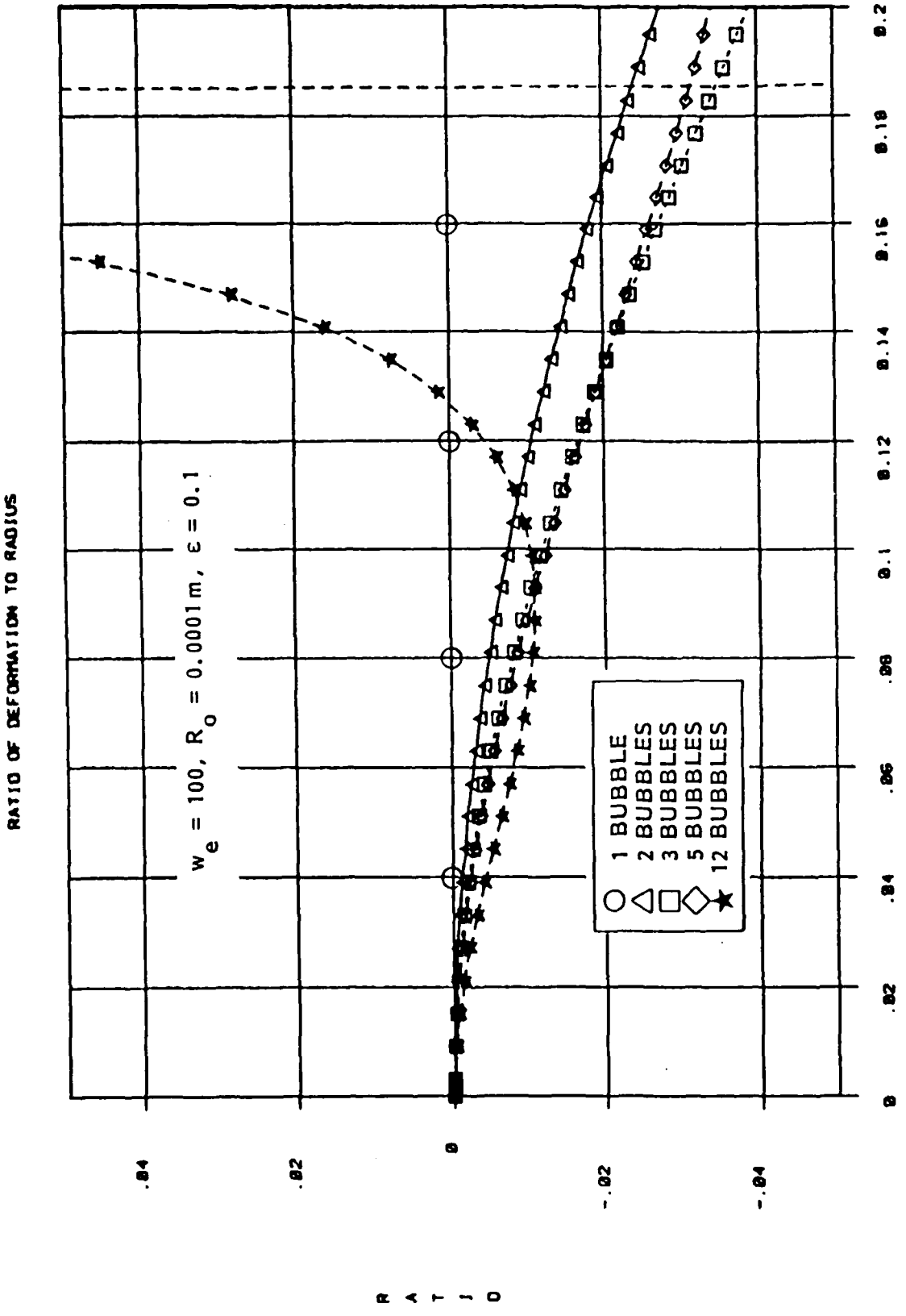

FIGURE 5.2 - RATIO OF NON-SPHERICAL TO SPHERICAL COMPONENT OF THE RADIUS VERSUS TIME FOR A BUBBLE GROWING IN AN N-BUBBLE CLOUD. W_e = 100, R_o = 0.0001 m, ε = 0.1

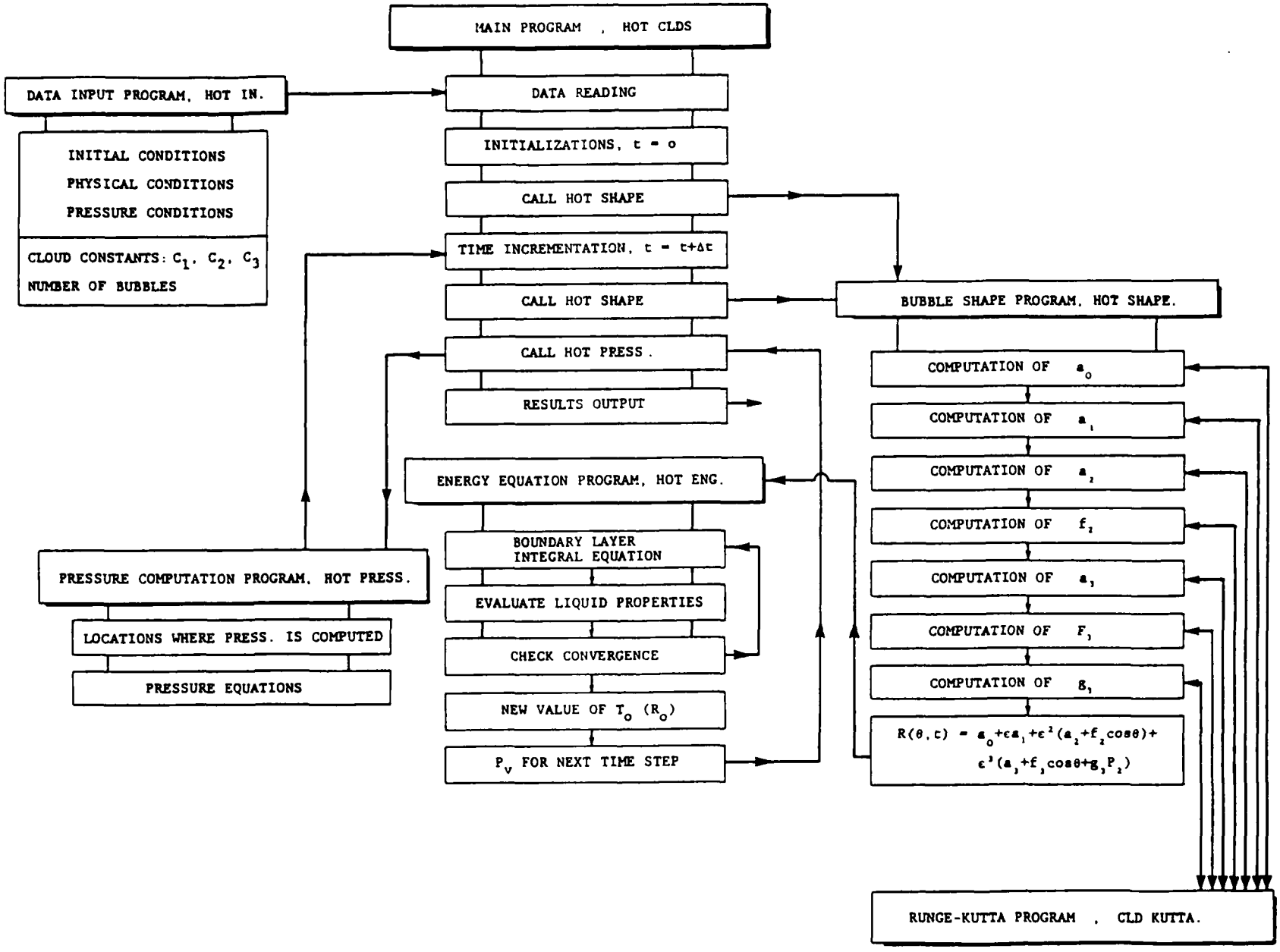

FIGURE 5.3 - PROGRAM FLOW CHART OF HOTCLDS. SYMMETRICAL CLOUD DYNAMICS ACCOUNTING FOR HEAT EXCHANGE AND PHASE CHANGE

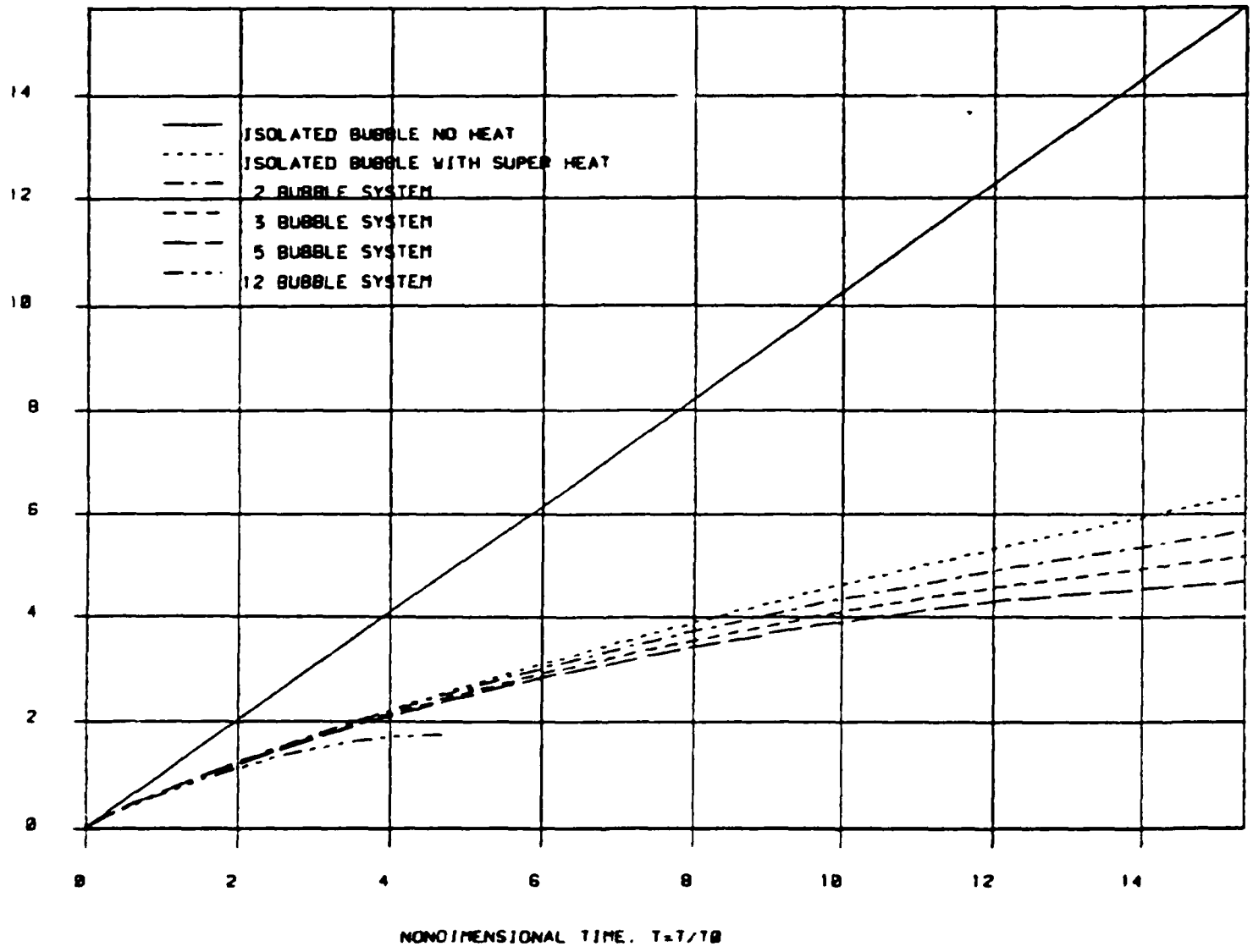

FIGURE 5.4 - INFLUENCE OF INTERACTIONS ON BUBBLE GROWTH IN A SUPERHEATED-LIQUID. BUBBLE-RADIUS HISTORY, P_o = 2 atm, P_{inf} = 0.5 atm, ϵ = 0.05, R_{b_o} = 0.01m, $R_o = 2.5 \times 10^{-5}$m, T$_b$ = 809.3°C, T_{inf} = 1177.71°C, LIQUID SODIUM

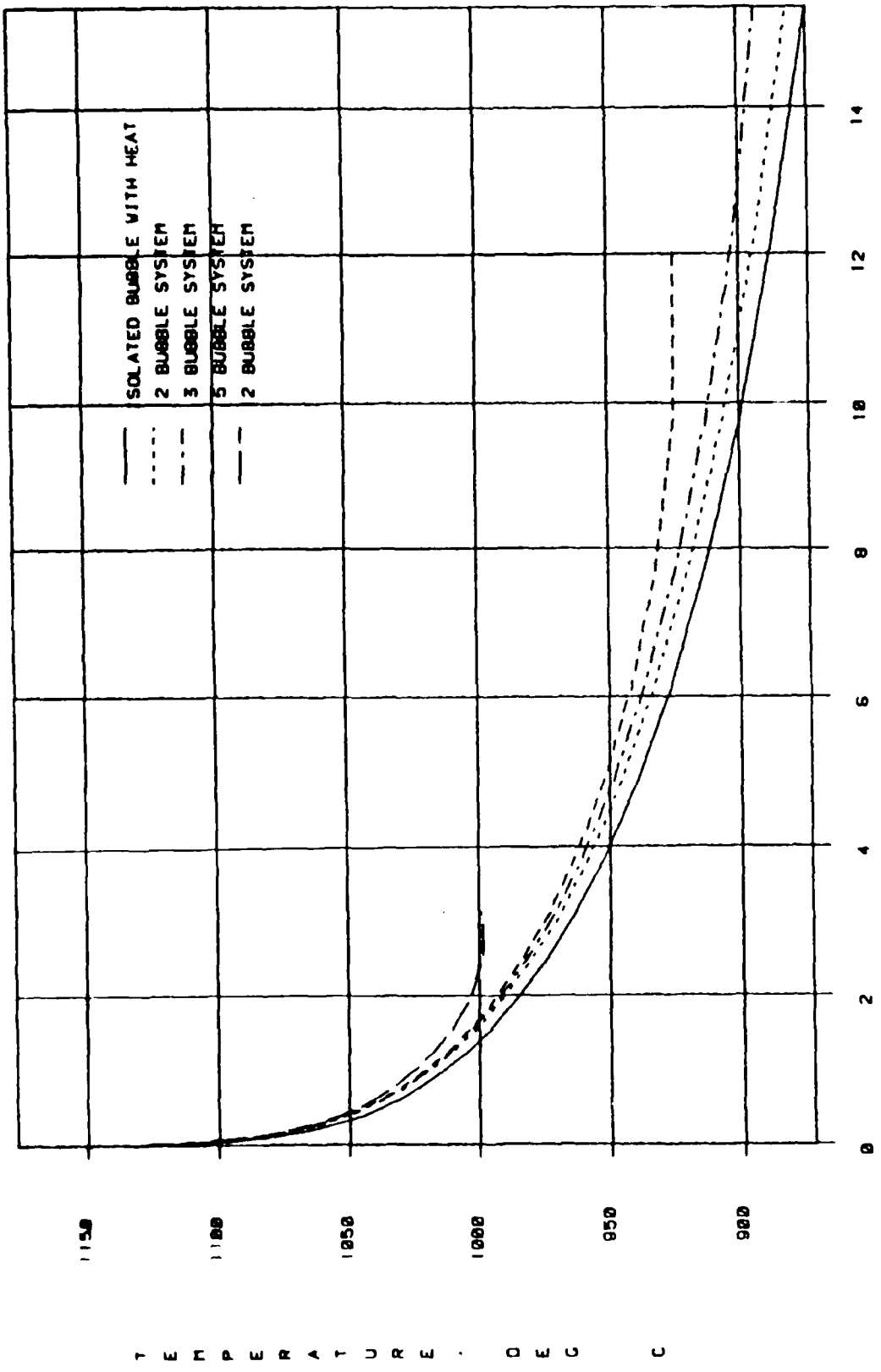

FIGURE 5.5 - INFLUENCE OF INTERACTIONS ON THE TEMPERATURE VARIATIONS AT THE WALL OF A BUBBLE IN AN N-BUBBLE CLOUD, P_o = 2 atm, P_{inf} = 0.5 atm, ϵ = 0.05, R_{b_o} = 0.01 m, $R_o = 2.5 \times 10^{-5}$ m, T_b = 809.3°C, T_{inf} = 1177.7°C, LIQUID SODIUM

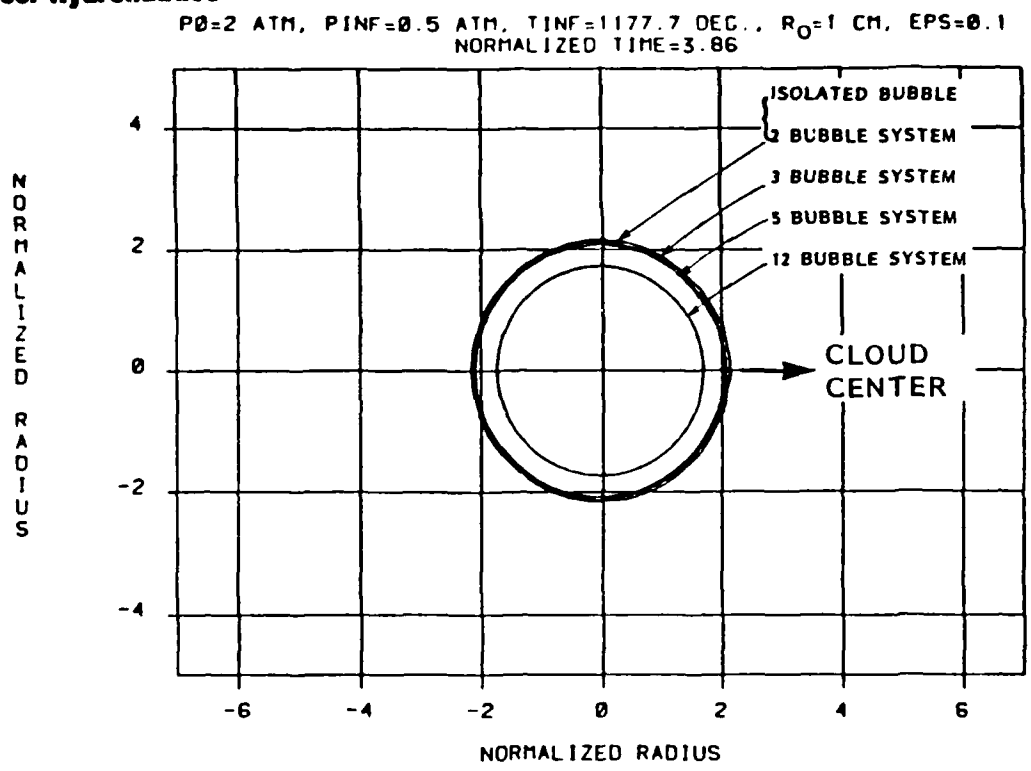

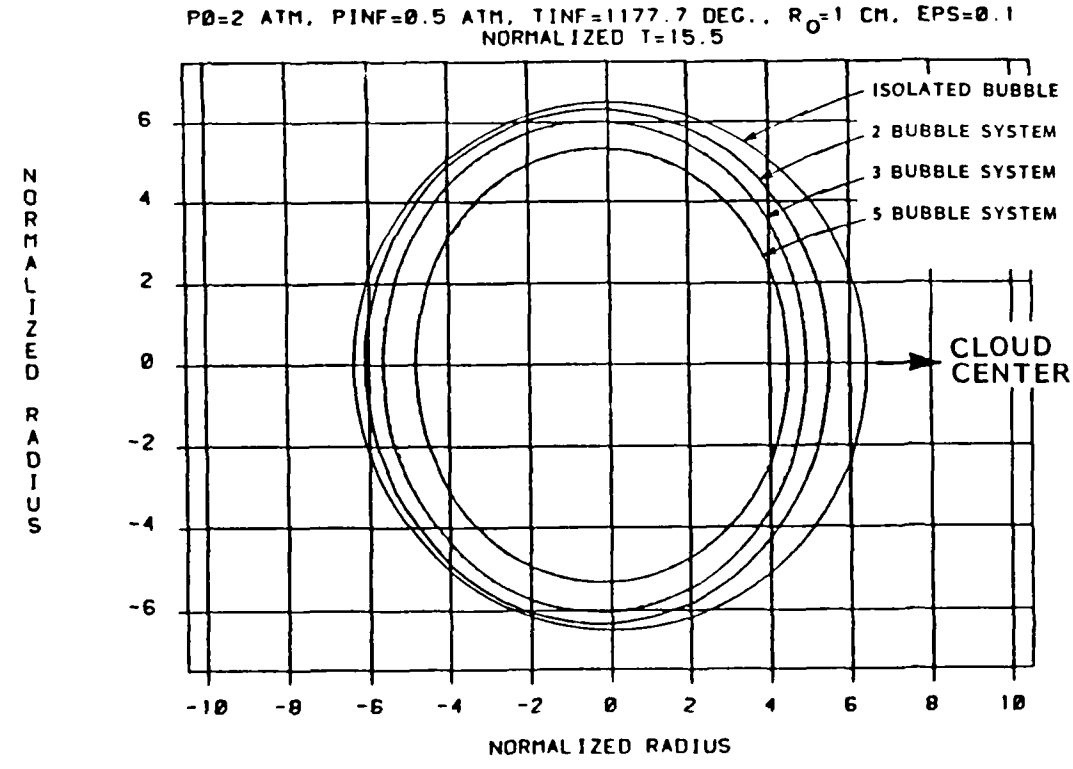

FIGURE 5.6 - VARIATION WITH TIME OF BUBBLE SHAPE CHARACTERISTICS AT TWO SELECTED TIMES, P_o = 2 atm, P_{inf} = 0.5 atm, ϵ = 0.05, R_{b_o} = 0.01 m, R_o = 2.5 x 10^{-5}m, T_b = 809.3°C, T_{inf} = 1177.71°C, LIQUID SODIUM

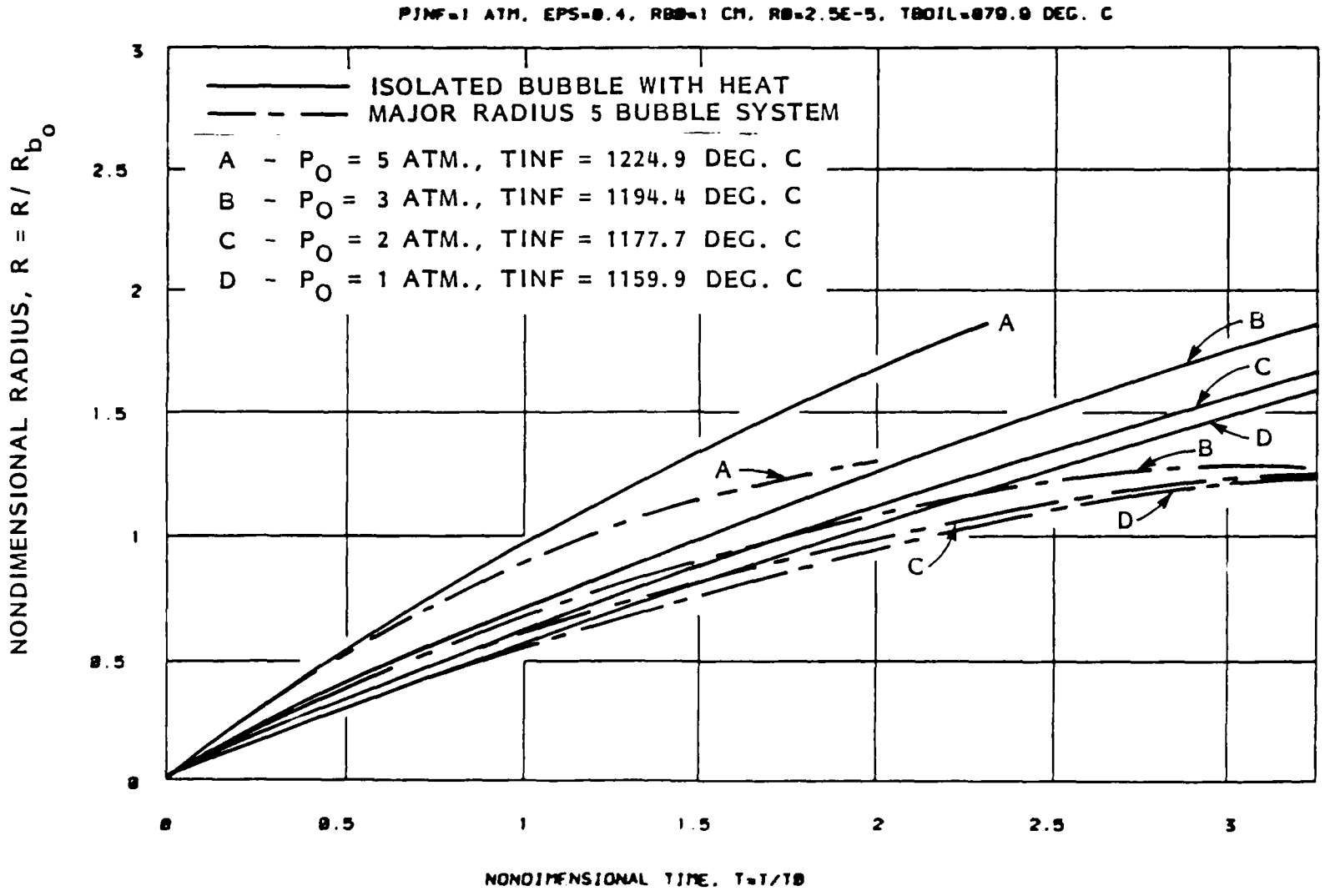

FIGURE 5.7 - INFLUENCE OF INTERACTIONS AND INITIAL CONDITIONS ON BUBBLE GROWTH IN A SUPERHEATED LIQUID, P_{inf} = 1 atm, ϵ = 0.4, R_{b_o} = 0.01 m, R_o = 2.5 x 10^{-5}m, T_b = 879.9°C: A, P_o = 5 atm, T_{inf} = 1224.9°C; B, 3 atm, 1194.9°C; C, 2 atm, 1177.7°C; D, 1 atm, 1159.9°C

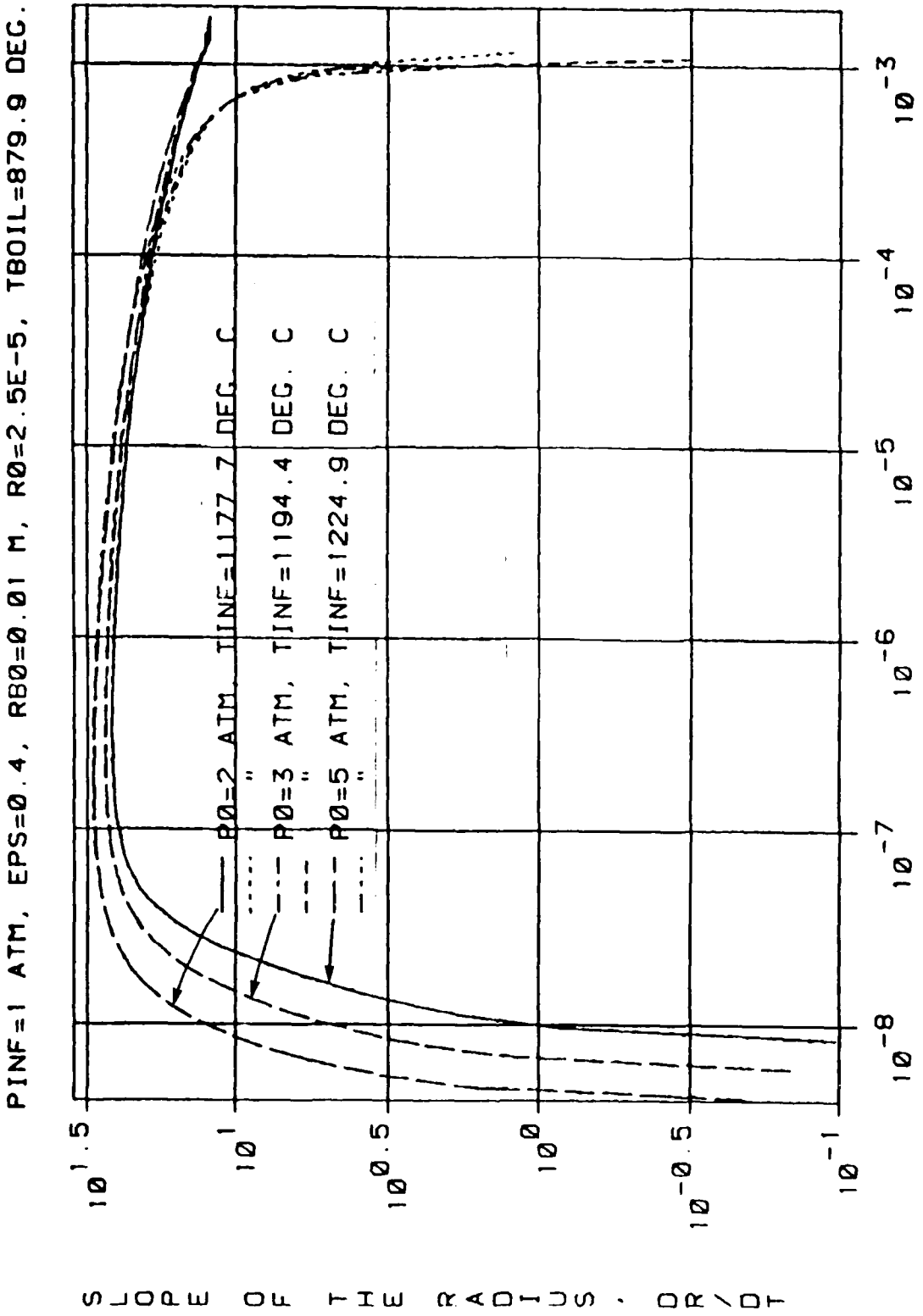

FIGURE 5.8 - INFLUENCE OF INTERACTIONS AND INITIAL CONDITIONS ON BUBBLE GROWTH RATE IN A SUPERHEATED LIQUID, P_{inf} = 1 atm, ε = 0.4,

R_{b_o} = 0.01m, R_o = 2.5 x 10^{-5}m, T_b = 879.9°CC:A, P_o = 2 atm,

T_{inf} = 1177.7°C; B, 3 atm, 1194.4°C; C, 5 atm, 1224.9°C

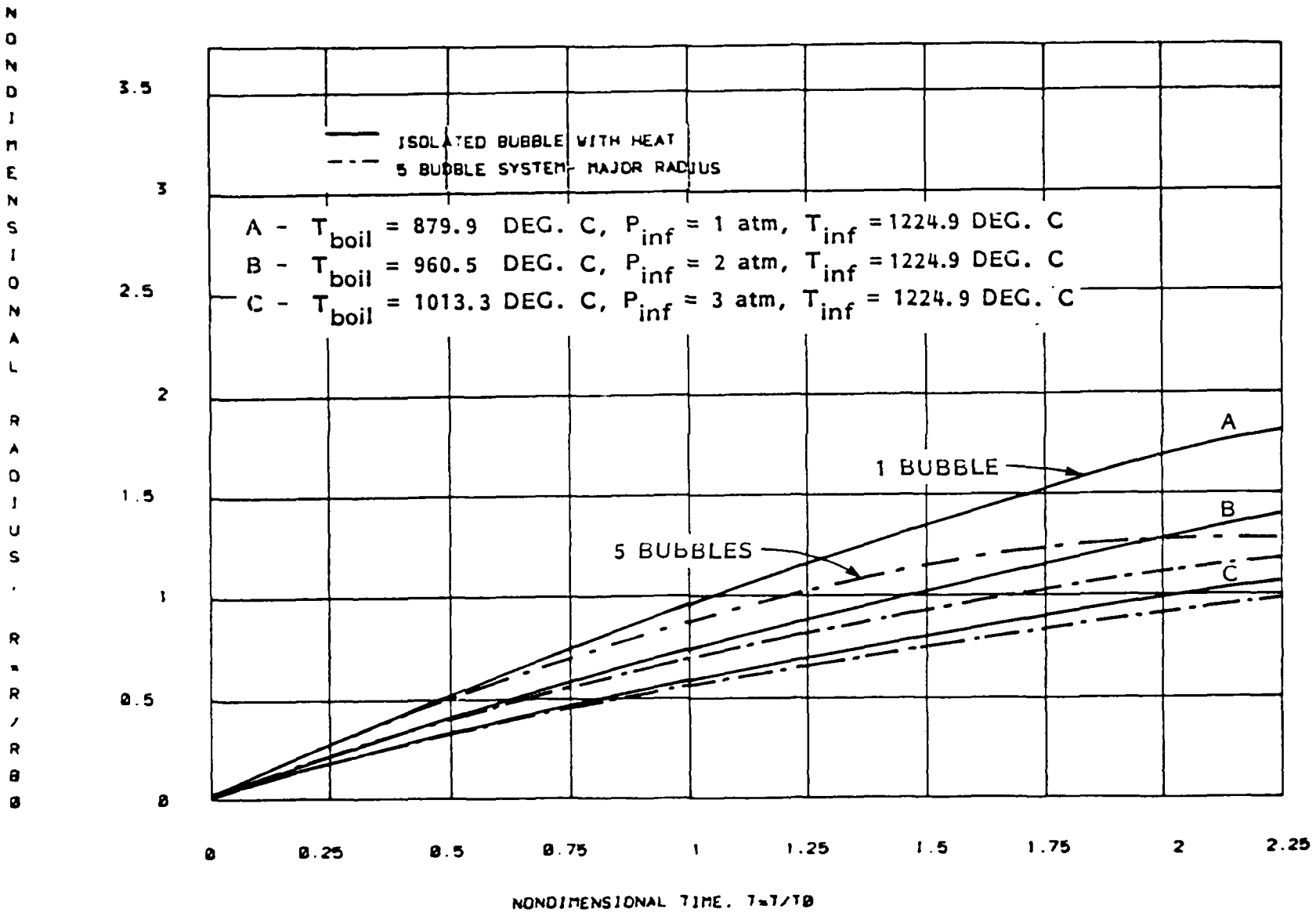

FIGURE 5.9 - INFLUENCE OF THE IMPOSED PRESSURE P_{inf} ON BUBBLE GROWTH IN A SUPERHEATED LIQUID, P_o = 5 atm, $R_o = 2.5 \times 10^{-5}$m, ε = 0.4, T_{inf} = 1224.9°C: A, T_b = 879.9°C, P_{inf} = 1 atm: B, 960.5°C, 2 atm; C, 1013.3°C, 3 atm

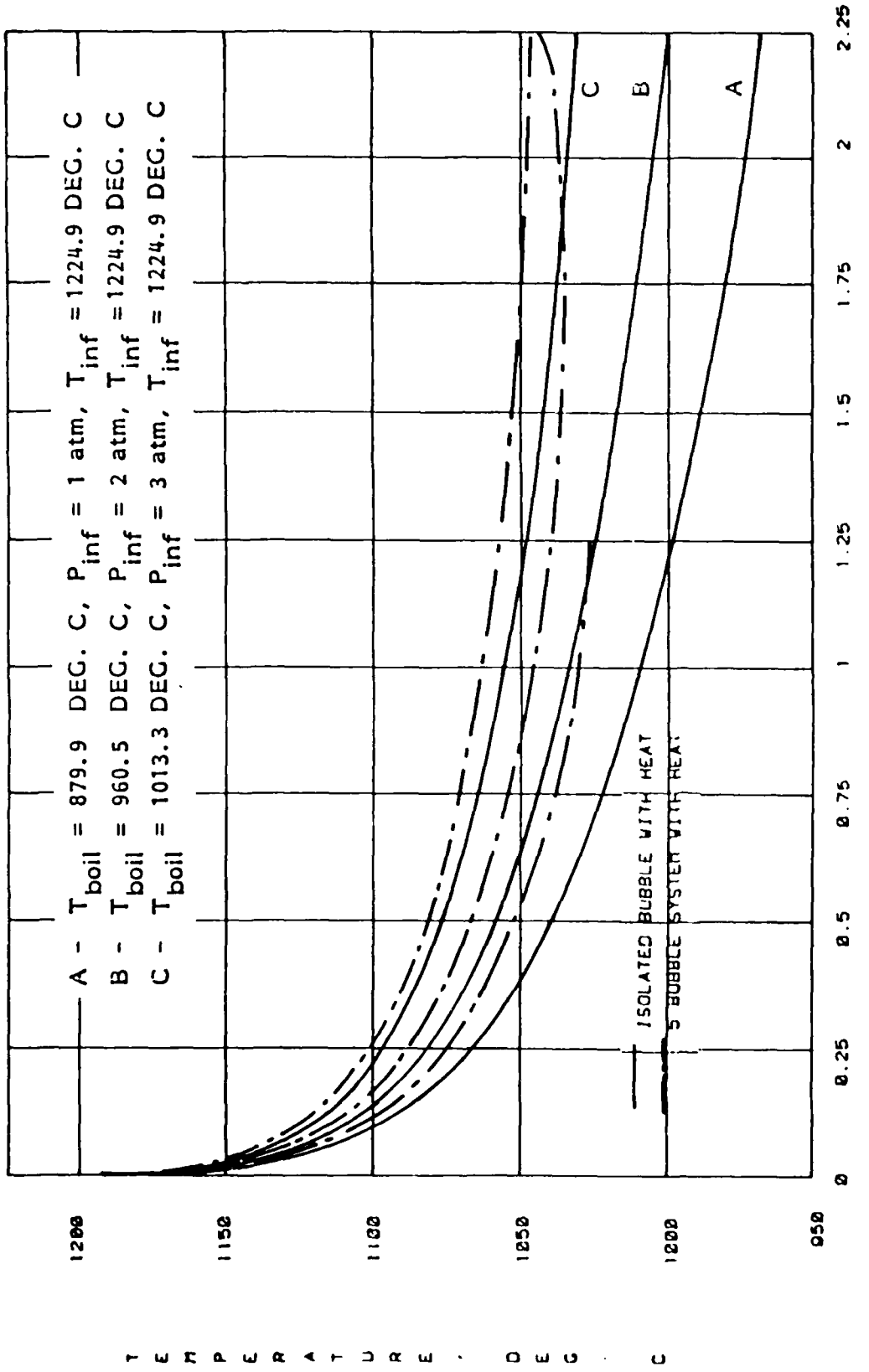

FIGURE 5.10 - INFLUENCE OF IMPOSED PRESSURE P_{inf} ON THE BUBBLE-WALL TEMPERATURE.

P_o = 5 atm, R_{b_o} = 0.01 m, R_o = 2.5 x 10^{-5} m, ε = 0.4, T_{inf} = 1224.9°C: A, T_b = 879.9°C, P_{inf} = 1 atm; B, 960.5°C, 2 atm: C, 1013.3°C, 3 atm

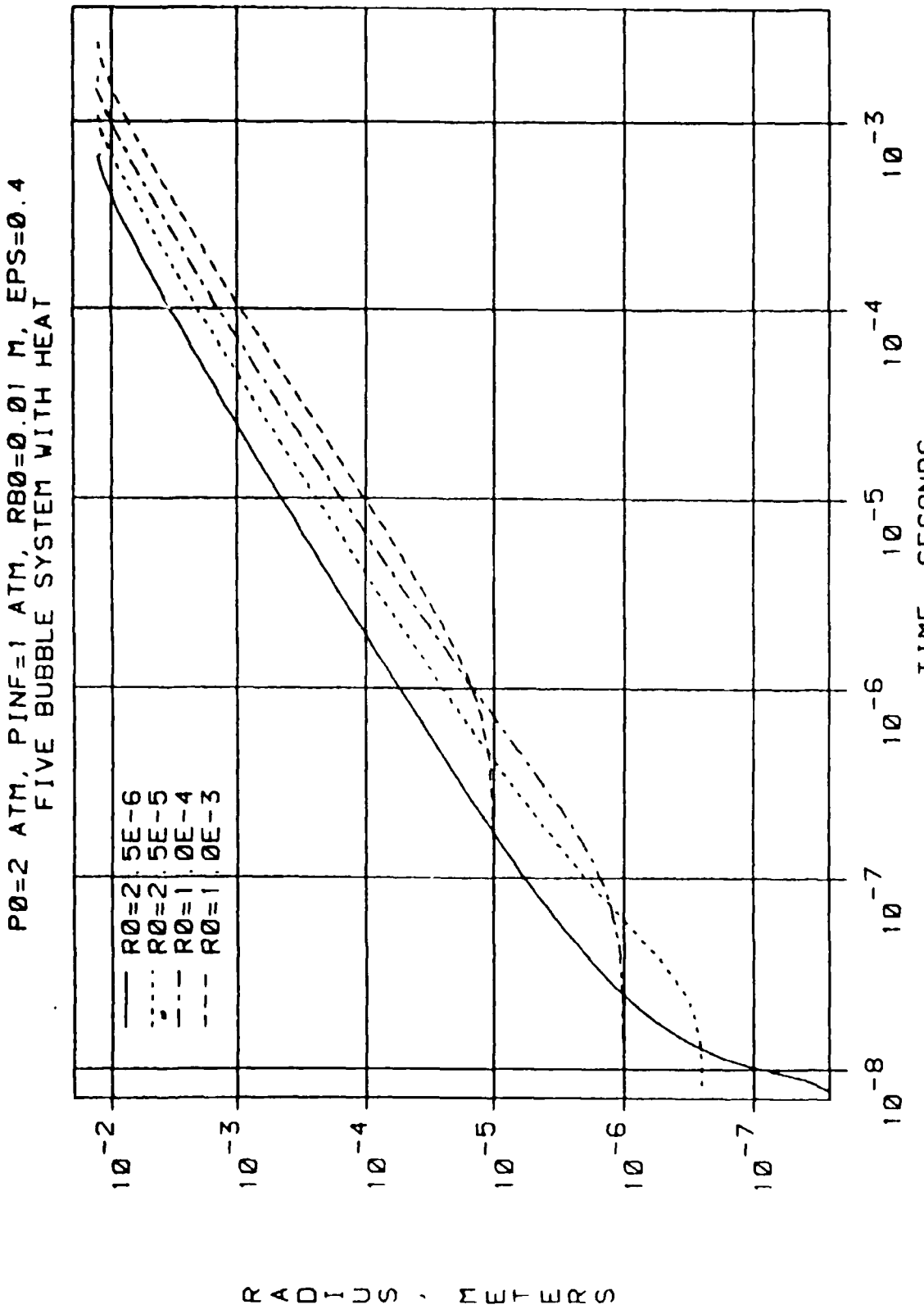

FIGURE 5.11 - INFLUENCE OF INITIAL BUBBLE SIZE ON RADIUS HISTORY, P_o = 2 atm, P_{inf} = 1 atm, ε = 0.2, R_{b_o} = 0.01m, T_b = 879.9°C: A, T_{inf} = 1518.0°C: R_o = 2,5E - 6; B, 1177.7°C, 2.5E - 5; 1051.4°C, 1.0E - 4; D, 973.2°C, 1.0E - 3

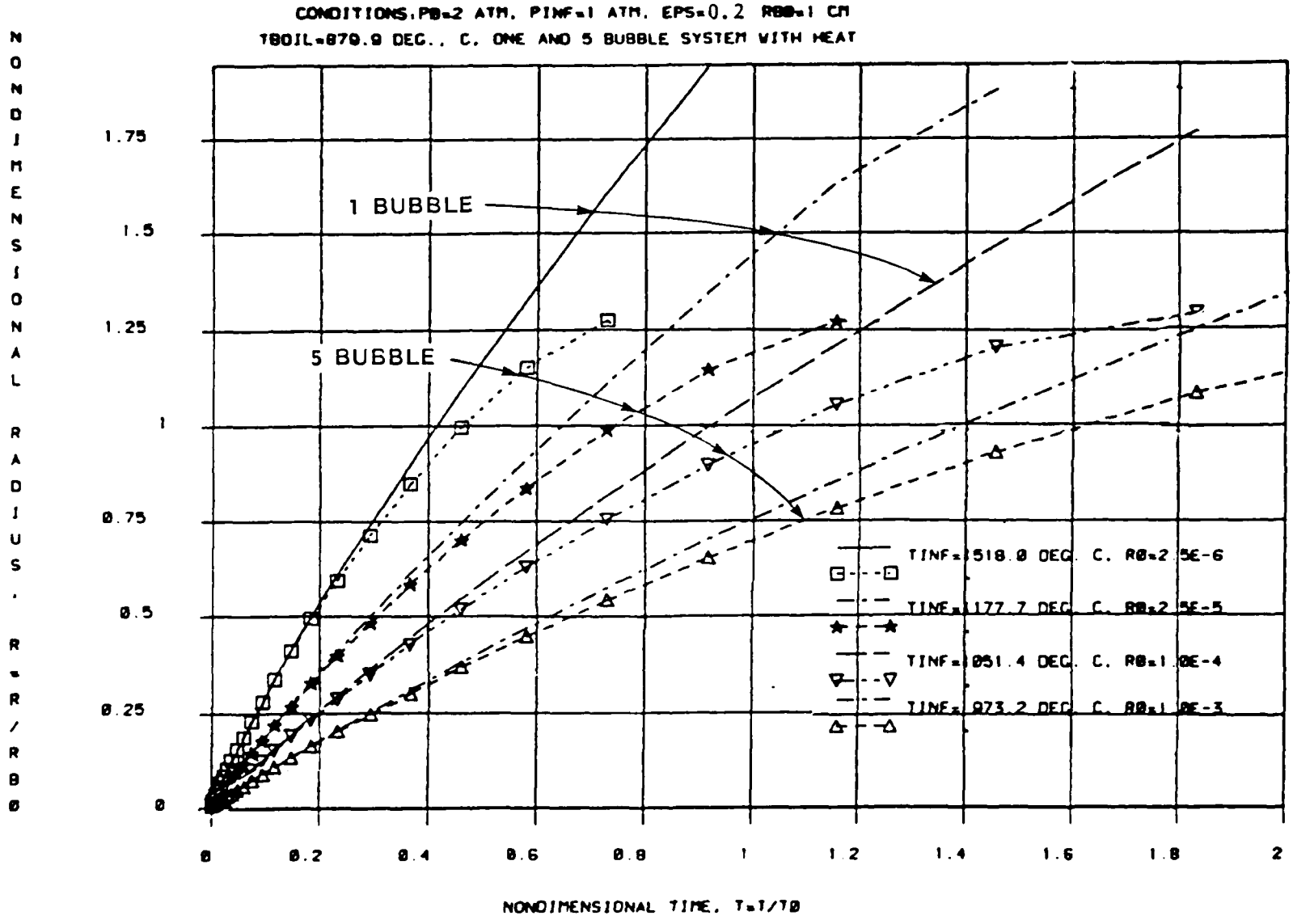

FIGURE 5.12 - INFLUENCE OF INITIAL BUBBLE SIZE AND BUBBLE INTERACTIONS ON RADIUS HISTORY. P_o = 2 atm, P_{inf} = 1 atm, ϵ = 0.2, R_{b_o} = 0.01m, T_b = 879.9°C: A, T_{inf} = 1528.0°C, R_o = 2.5E - 6; B, 1177.7°C, 2.5E - 5; C, 1051.4°C, 1.0E - 4; D, 973.2°C, 1.0E - 3

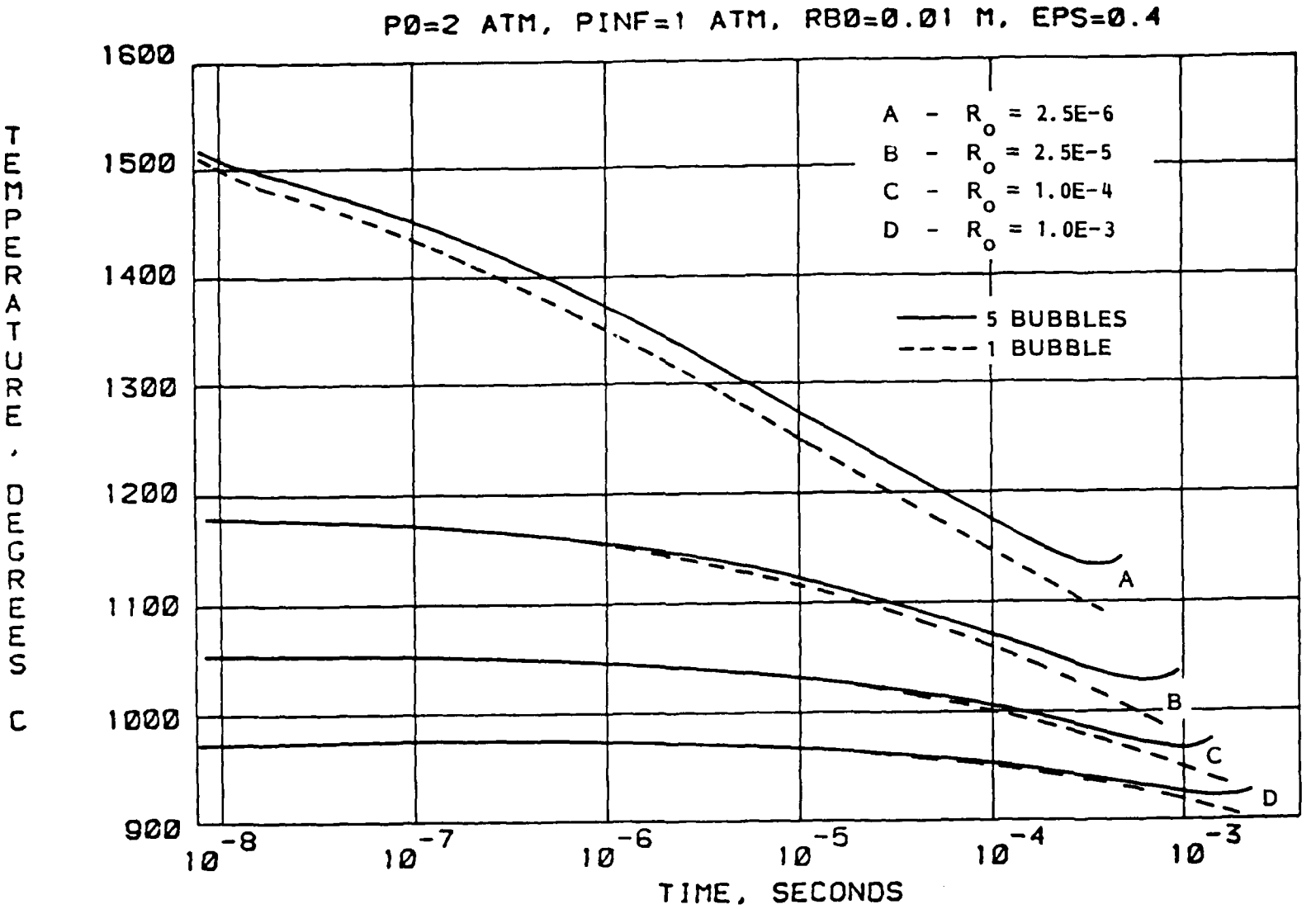

FIGURE 5.13 - INFLUENCE OF INITIAL BUBBLE SIZE ON BUBBLE-WALL-TEMPERATURE HISTORY, P_o = 2 atm, P_{inf} = 1 atm, ϵ = 0.2, R_{b_o} = 0.01 m, T_b = 879.9°C: A, R_o = 2.5E - 6; B, 2.5E - 5; C, 1.0E - 4, D, 1.0E - 3

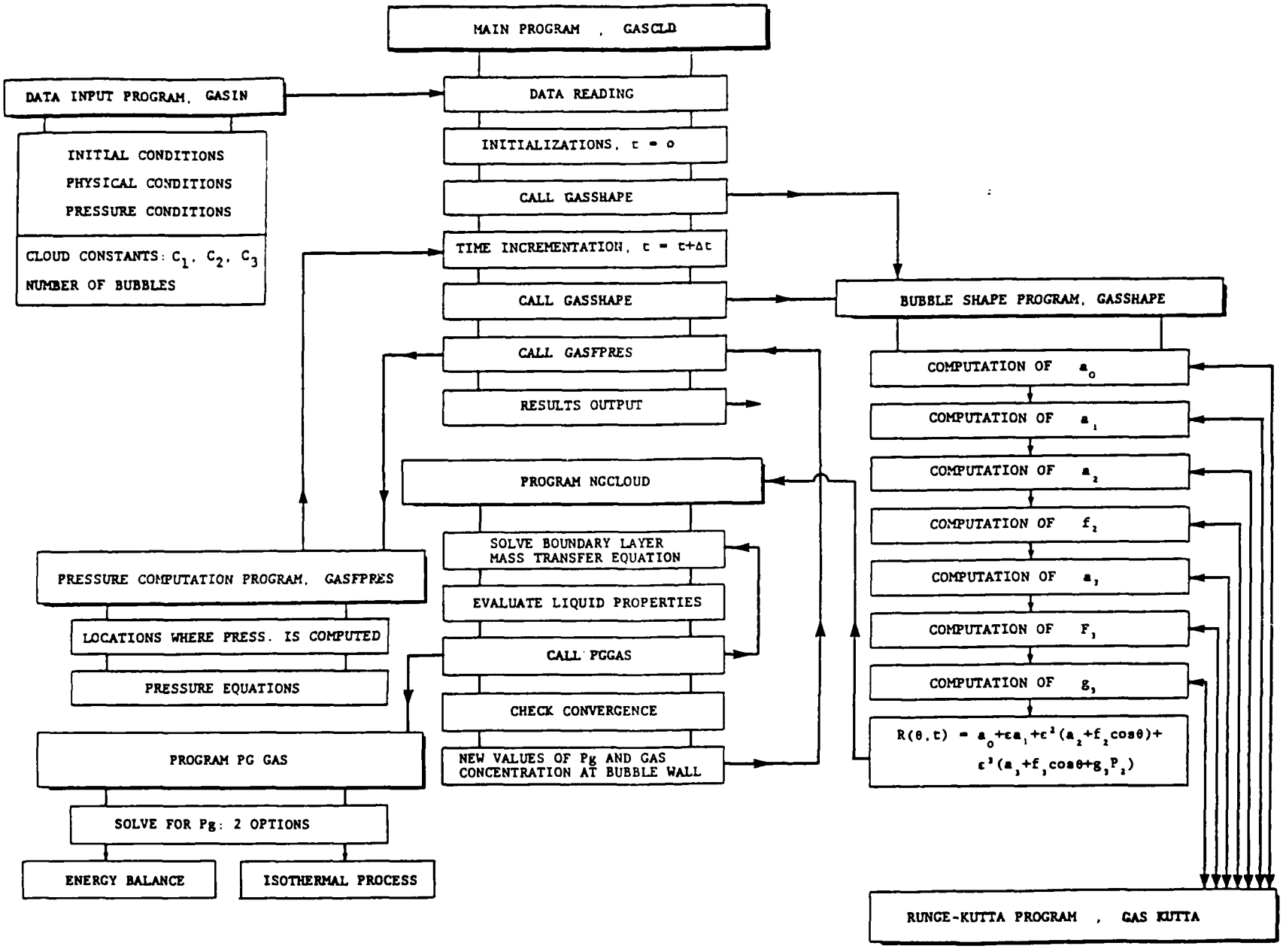

FIGURE 6.1 - PROGRAM FLOW CHART FOR GASCLD, SYMMETRICAL CLOUD DYNAMICS ACCOUNTING FOR NON-CONDENSIBLE GAS TRANSFER ACROSS THE BUBBLE WALL

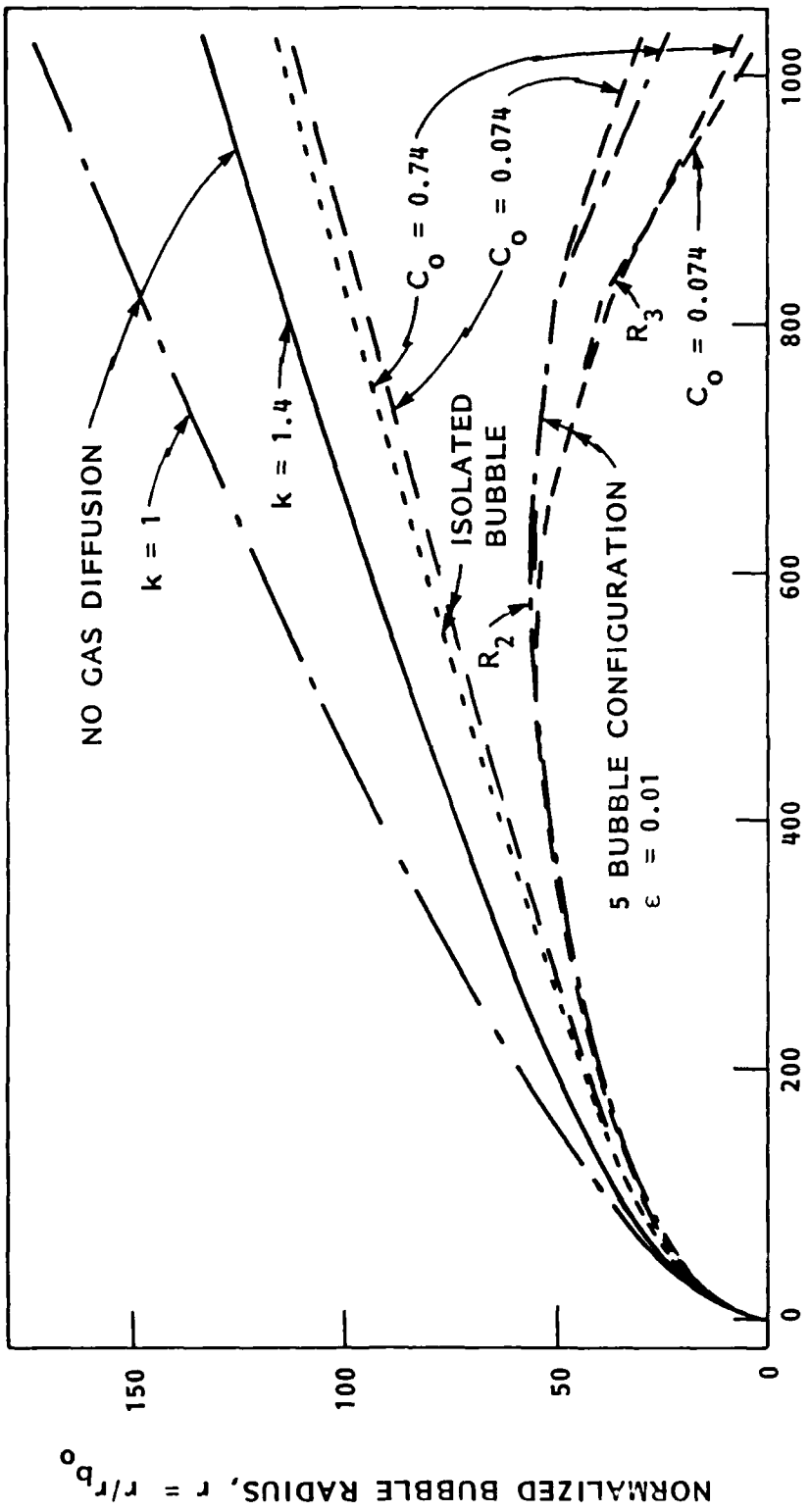

FIGURE 6.2 - BUBBLE GROWTH FOLLOWING A SUDDEN DEPRESSURIZATION (P_o = 3.78 atm, P_{inf} = 1 atm, $R_{b_o} = R_o$ = 51 μm). COMPARISON BETWEEN ISOLATED AND MULTI-BUBBLE CONFIGURATION AT TWO INITIAL DISSOLVED GAS CONCENTRATION VALUES, C_o.

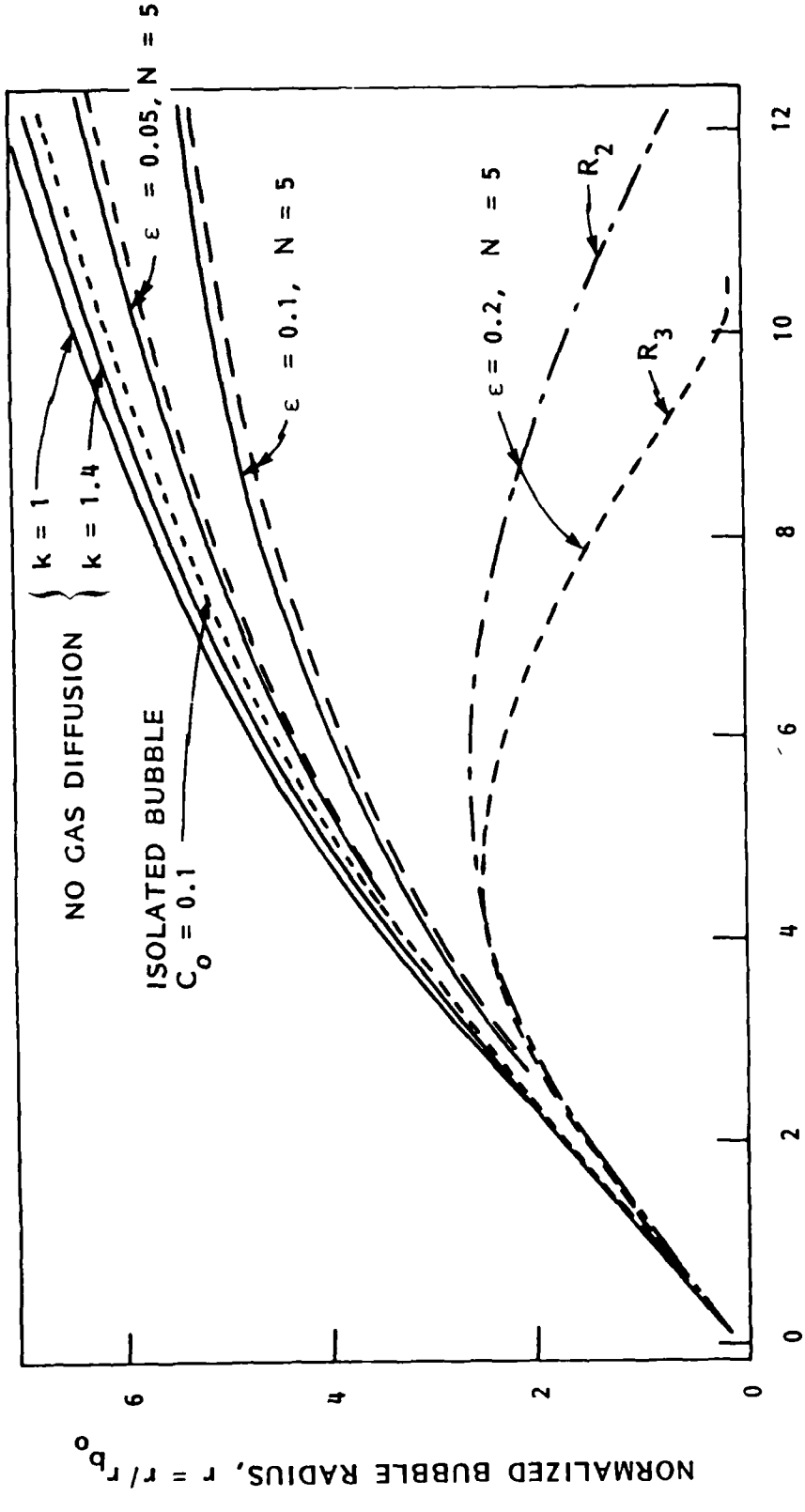

FIGURE 6.3 - BUBBLE GROWTH FOLLOWING A SUDDEN DEPRESSURIZATION (P_o = 5 atm, P_{inf} = 0.01 atm, R_{b_o} = 1 mm, R_o = 0.1 mm).

INFLUENCE OF BUBBLE SPACING PARAMETER ε, $\varepsilon = r_{b_o}/\ell_o$.

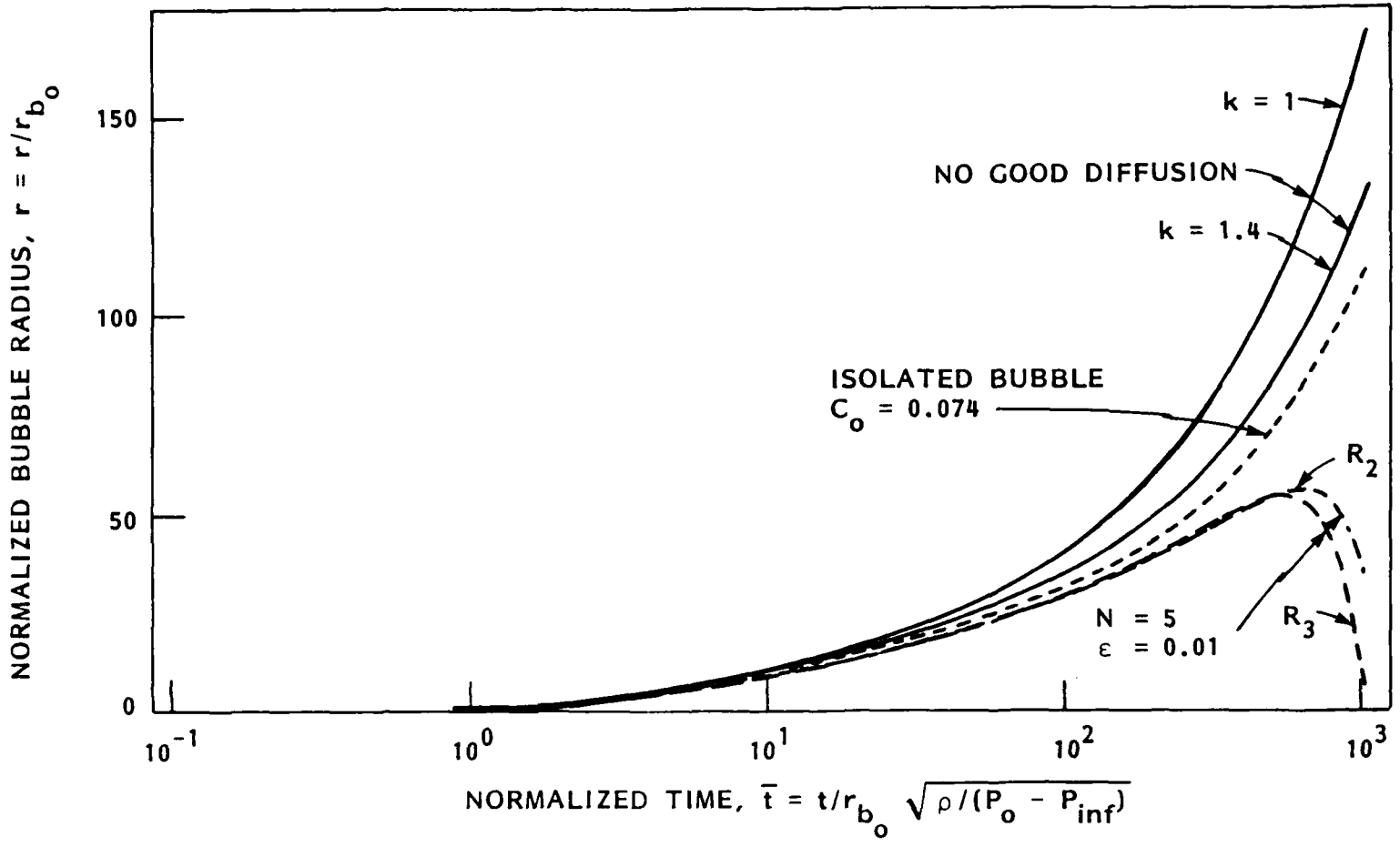

FIGURE 6.4 - BUBBLE GROWTH FOLLOWING A SUDDEN DEPRESSURIZATION (P_o = 3.78 atm, P_{inf} = 1 atm, $R_{b_o} = R_o$ = 51 μ m). COMPARISON BETWEEN ISOLATED AND MULTI-BUBBLE CONFIGURATION AT TWO TWO INITIAL DISSOLVED GAS CONCENTRATION VALUES, C_o.

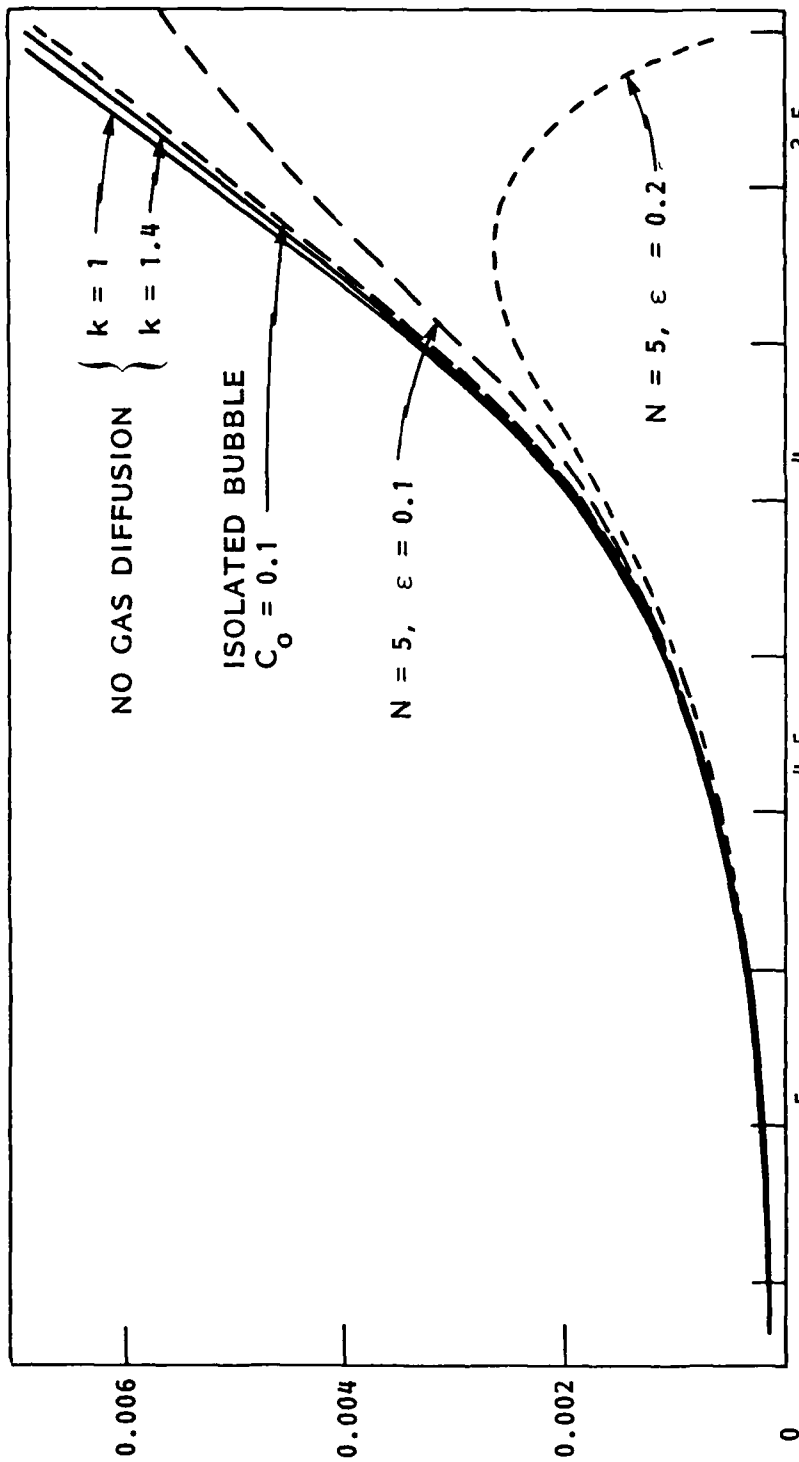

FIGURE 6.5 - BUBBLE GROWTH FOLLOWING A SUDDEN DEPRESSURIZATION (P_o = 5 atm, P_{inf} = 0.01 atm, R_{b_o} = 1 mm, R_o = 0.1 mm). INFLUENCE OF BUBBLE SPACING PARAMETER ε, ε = r_{b_o} / ℓ_o.

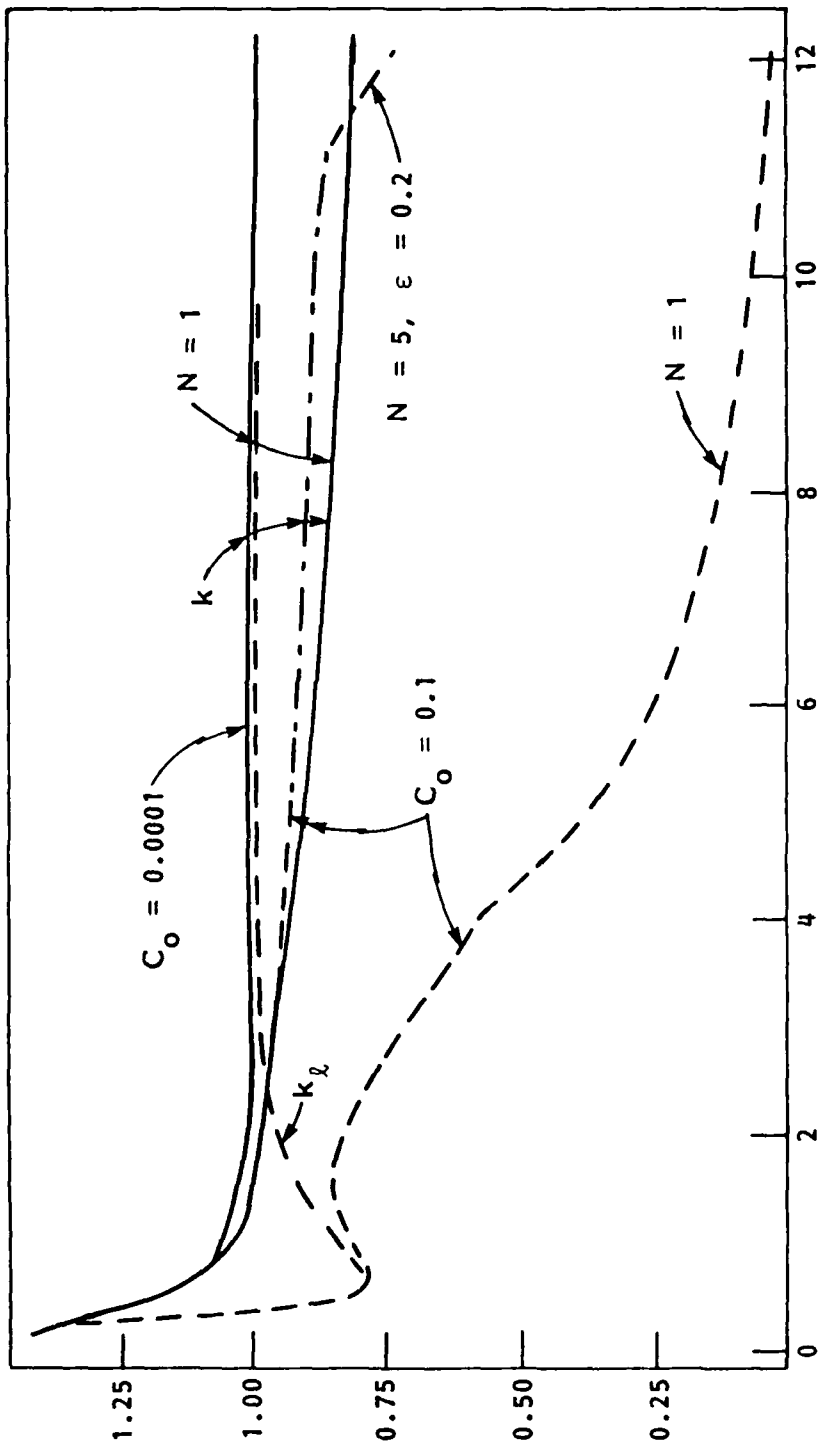

FIGURE 6.6 - VARIATION OF EFFECTIVE GAS POLYTROPIC COEFFICIENT DURING BUBBLE GROWTH FOLLOWING A SUDDEN DEPRESSURIZATION (P_o = 5 atm, P_{inf} = 0.01 atm, R_{b_o} = 1 mm, R_o = 0.1 mm)

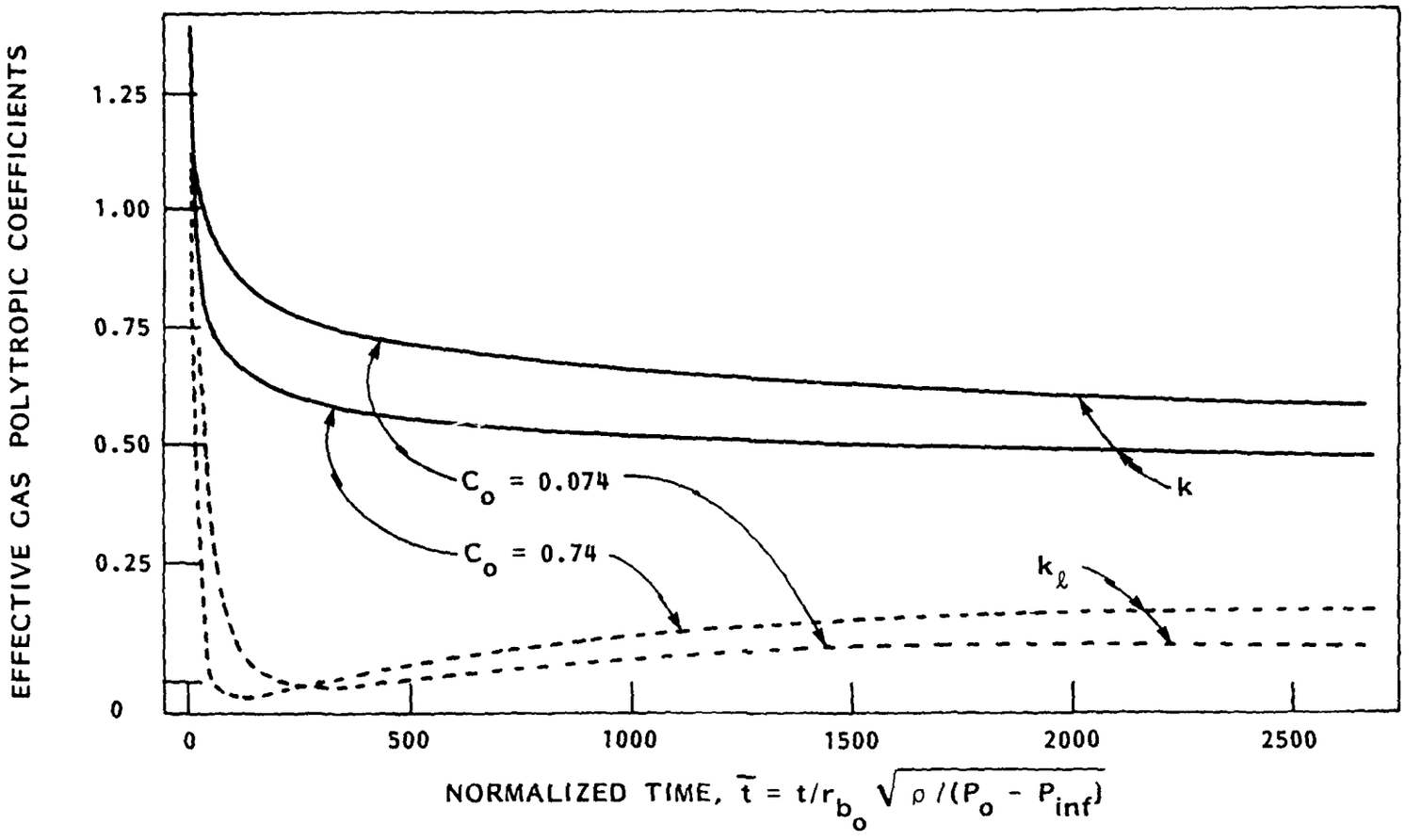

FIGURE 6.7 - INFLUENCE OF INITIAL DISOLVED GAS CONCENTRATION ON EFFECTIVE GAS POLYTROPIC COEFFICIENT (P_o = 3.78 atm, P_{inf} = 1 atm, $R_o = R_b$ = 51μ m)

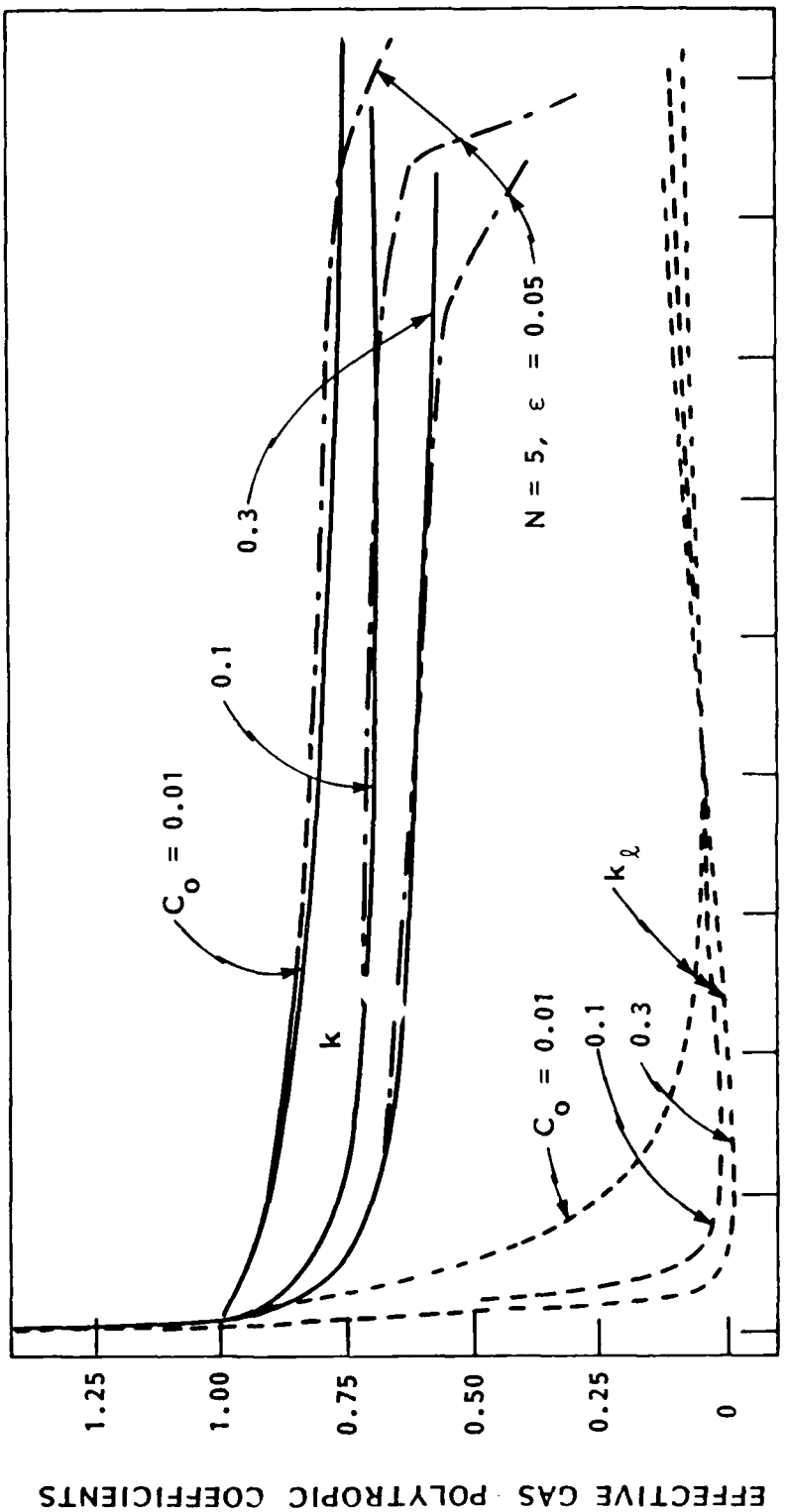

FIGURE 6.8 - INFLUENCE OF INITIAL DISSOLVED GAS CONCENTRATION ON EFFECTIVE GAS POLYTROPIC COEFFICIENTS (P_o = 5 atm, P_{inf} = 0.01 atm, R_o = 100 μm, R_{b_o} = 1 mm)

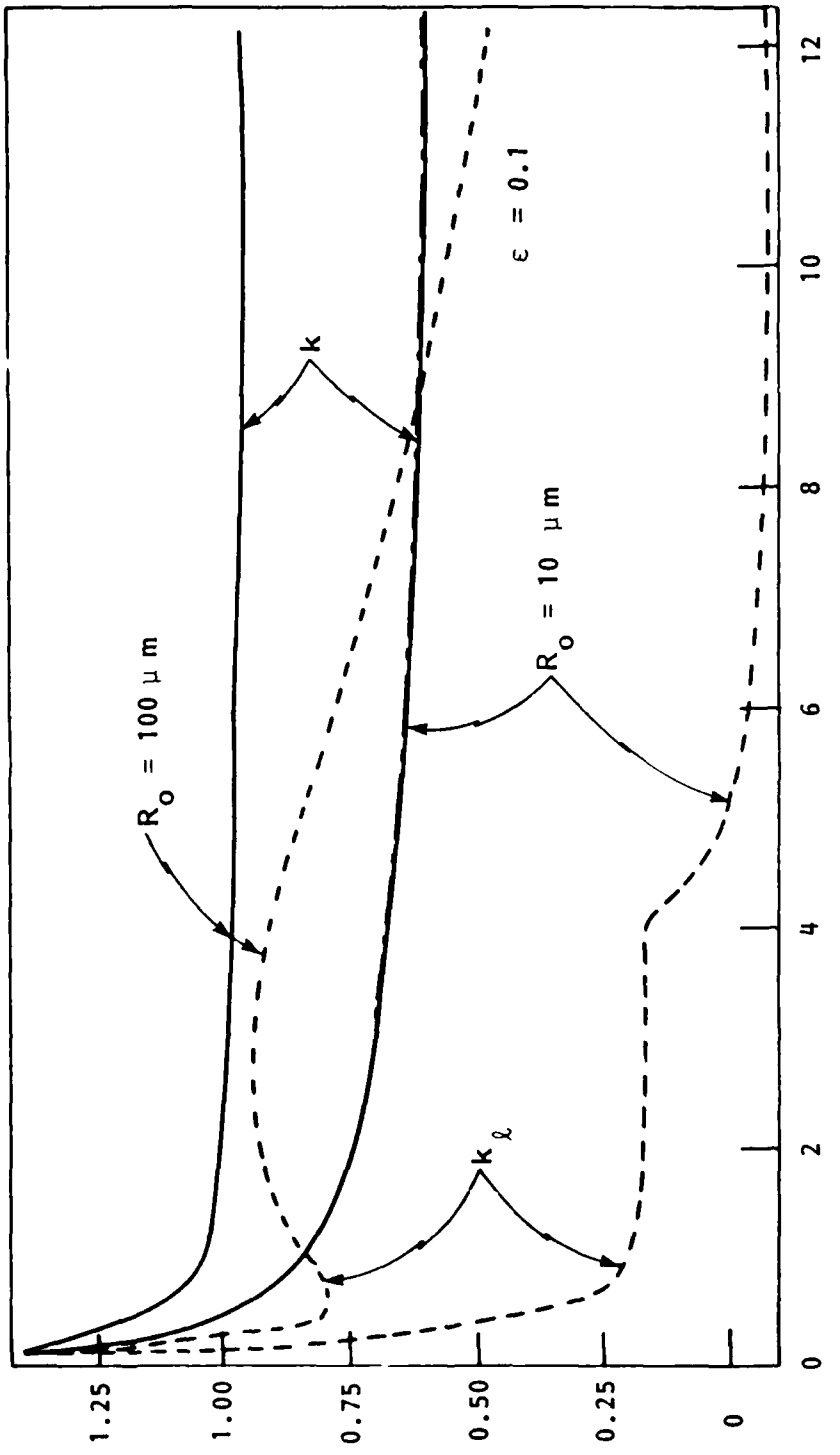

FIGURE 6.9 - INFLUENCE OF INITIAL BUBBLE SIZE R_o ON EFFECTIVE GAS POLYTROPIC COEFFICIENTS. (P_o = 5 atm, P_{inf} = 0.01 atm, R_{b_o} = 10 R_o, C_o = 0.01)

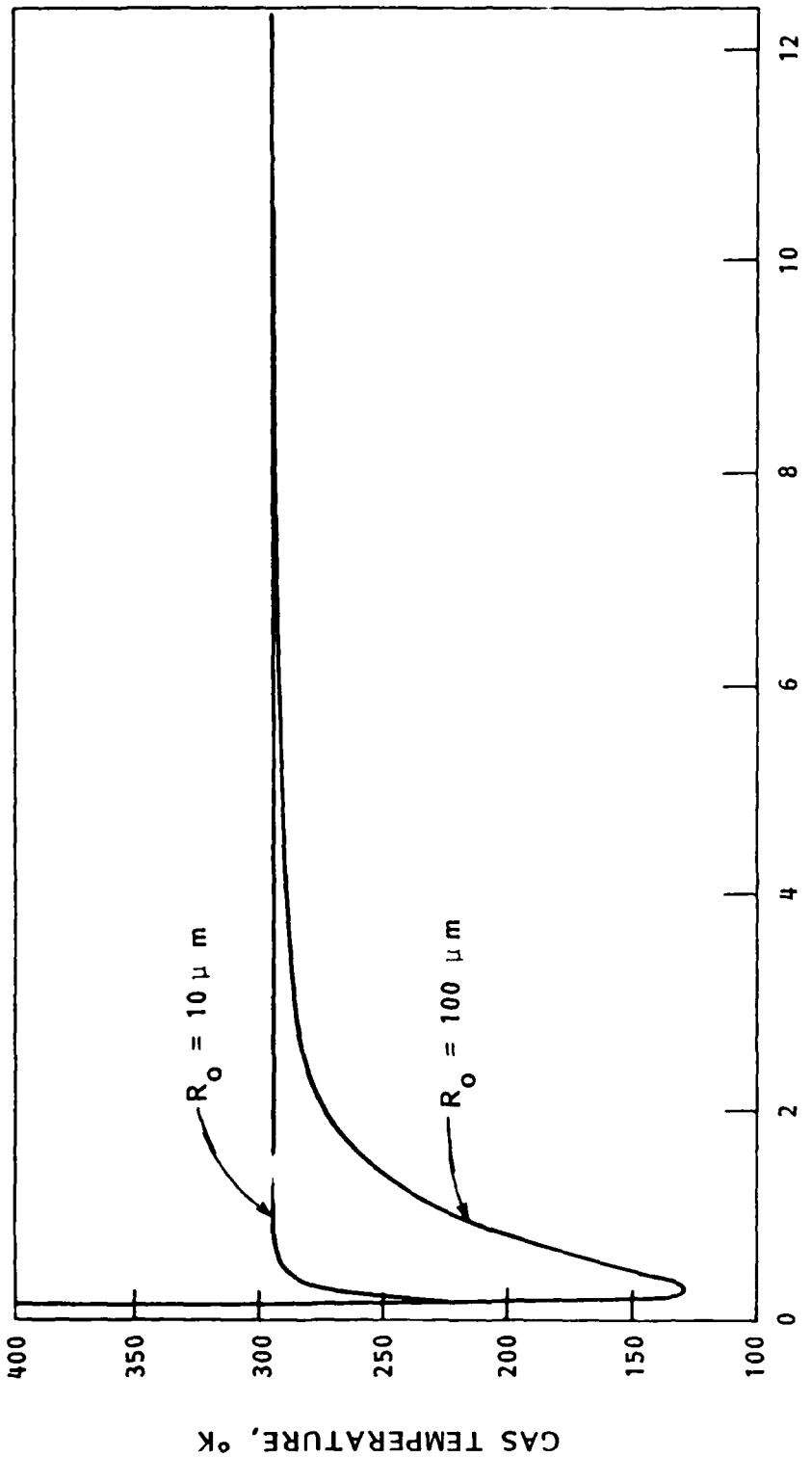

FIGURE 6.10 - NONCONDENSIBLE GAS TEMPERATURE VERSUS TIME. INFLUENCE OF INITIAL GAS SIZE. (P_o = 5 atm, P_{inf} = 0.01 atm, R_{b_a} = 10 R_o, C_o = 0.1)

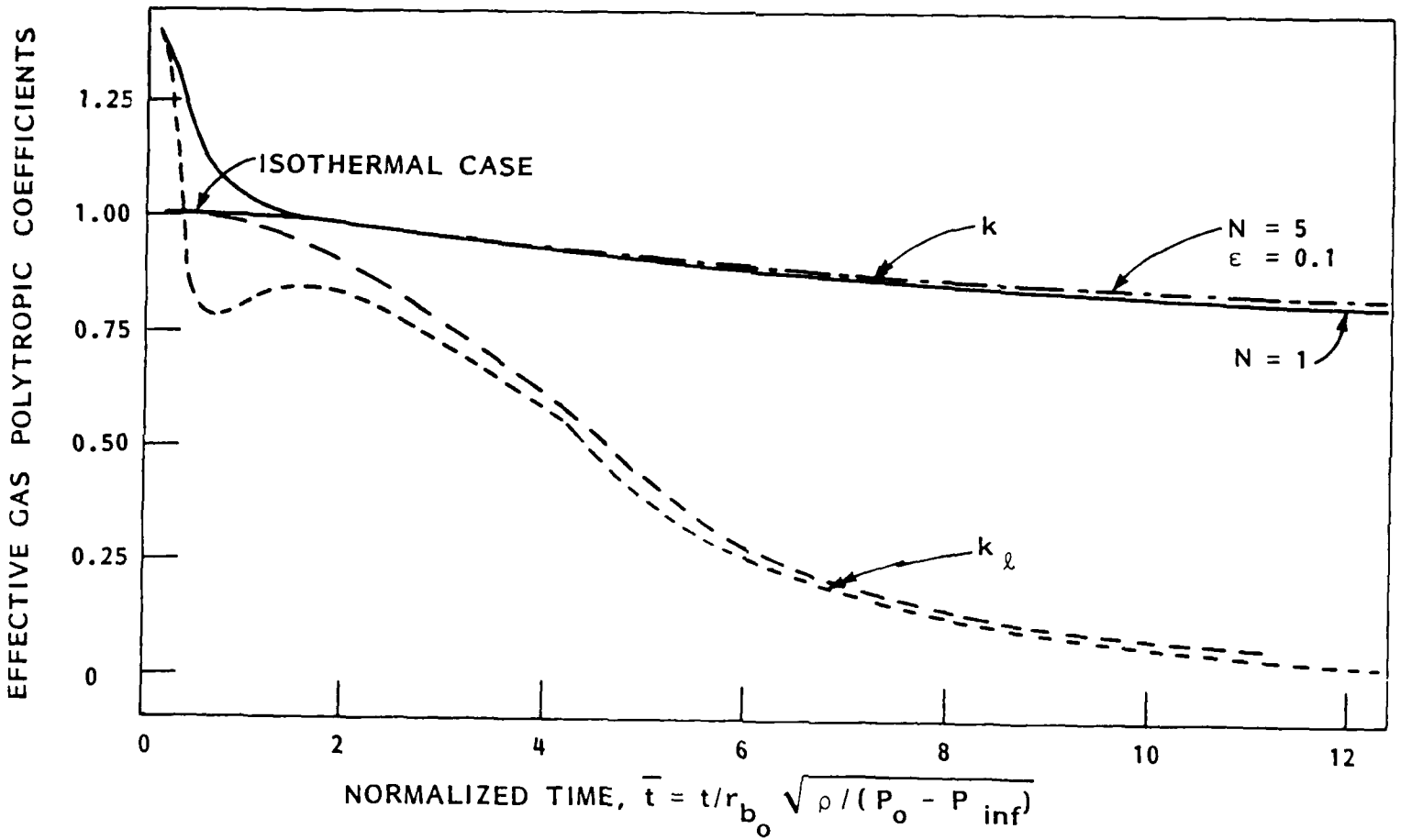

FIGURE 6.11 - EFFECTIVE GAS POLYTROPIC COEFFICIENTS VERSUS TIME. COMPARISON BETWEEN ENERGY EQUATION SOLUTIONS AND IMPOSED CONSTANT GAS TEMPERATURE CASE. (P_o = 5 atm, P_{inf} = 0.01 atm, R_{b_o} = 1 mm, R_o = 0.1 mm, C_o = 0.1)

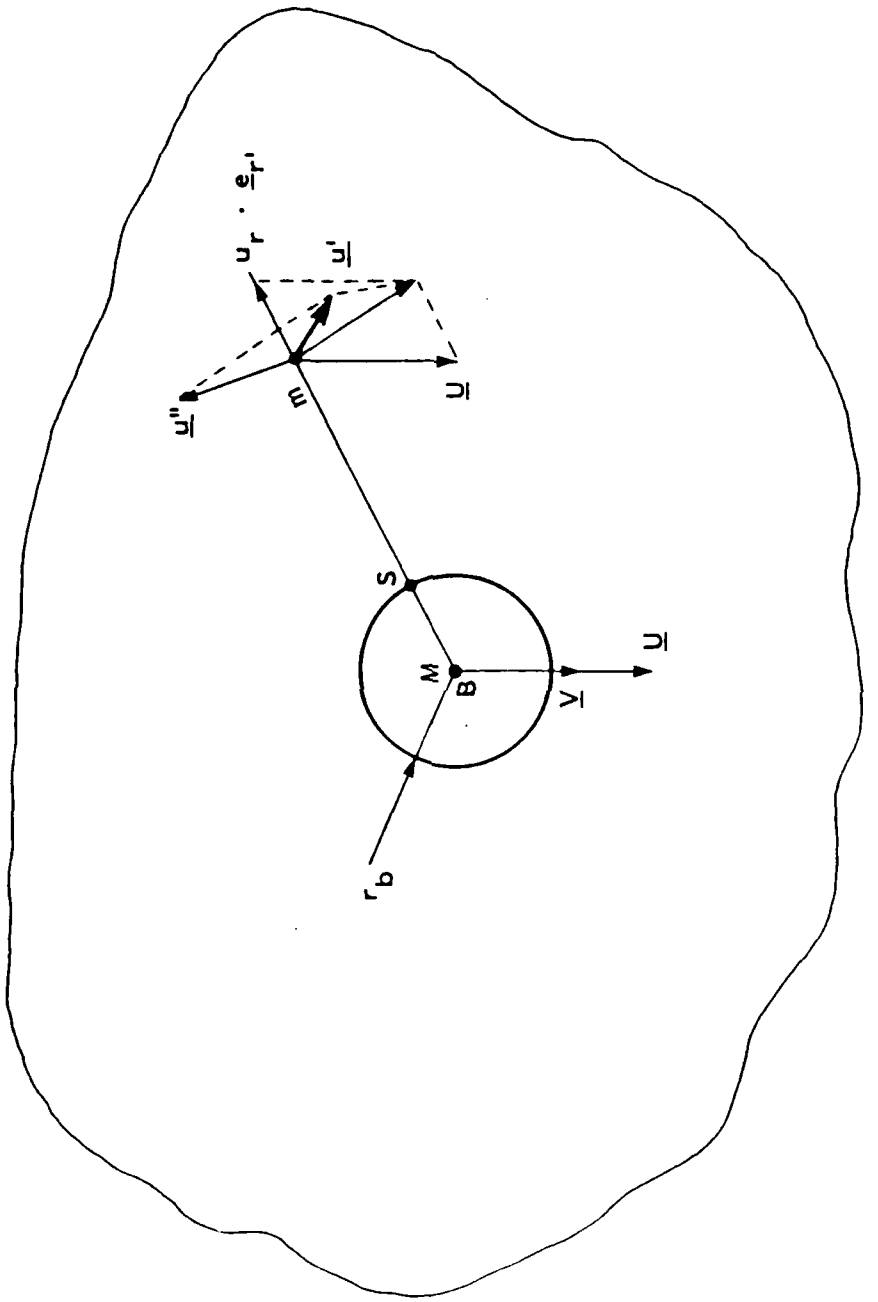

FIGURE 7.1 - SCHEMATIC OF A FLUID CELL

FIGURE 8.1 - OVERALL VIEW OF THE SPARK BUBBLE GENERATOR FACILITY

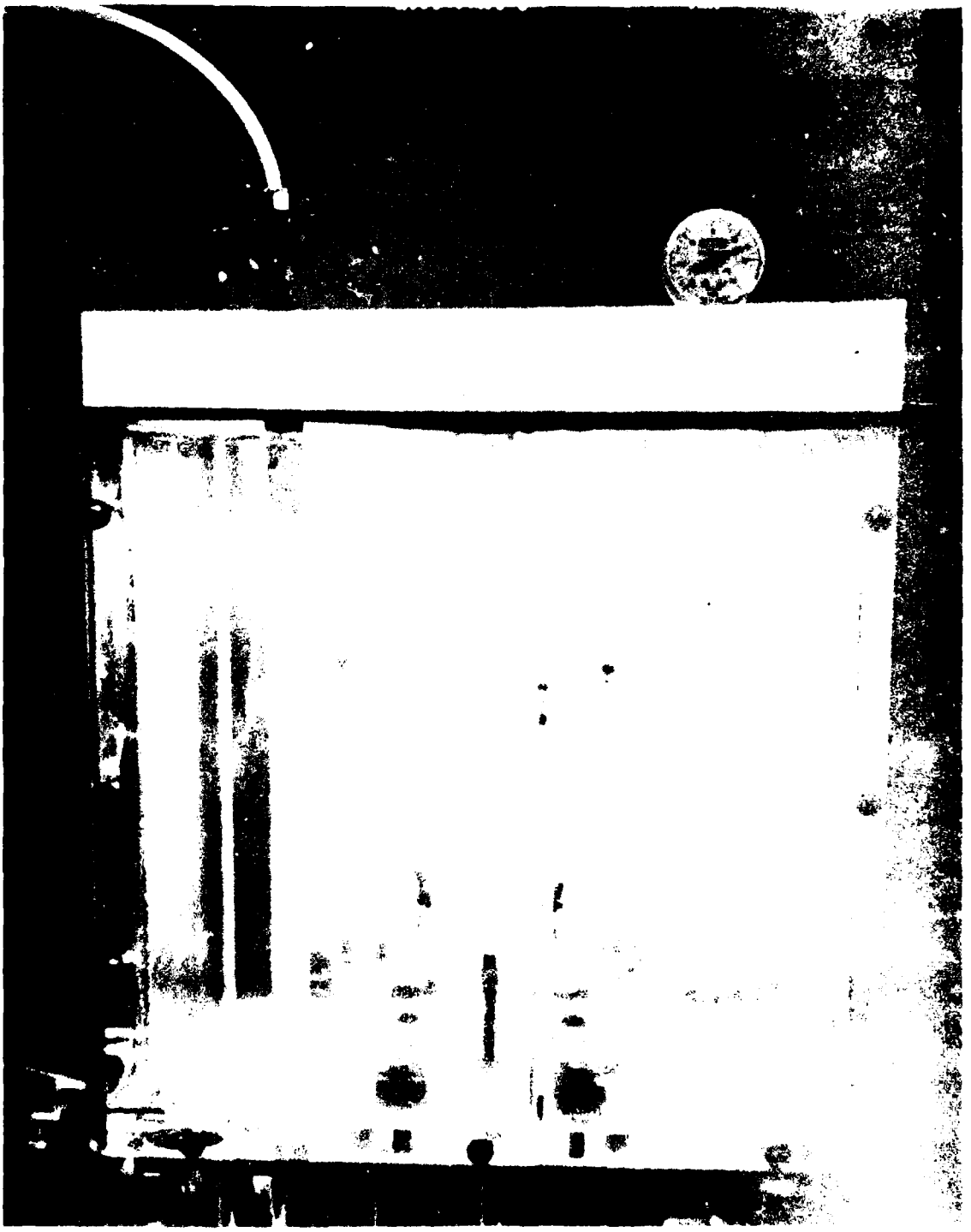

FIGURE 8.2 - EXPERIMENTAL TEST TANK SHOWING THE CONE, ELECTRODES AND PRESSURE TRANSDUCER

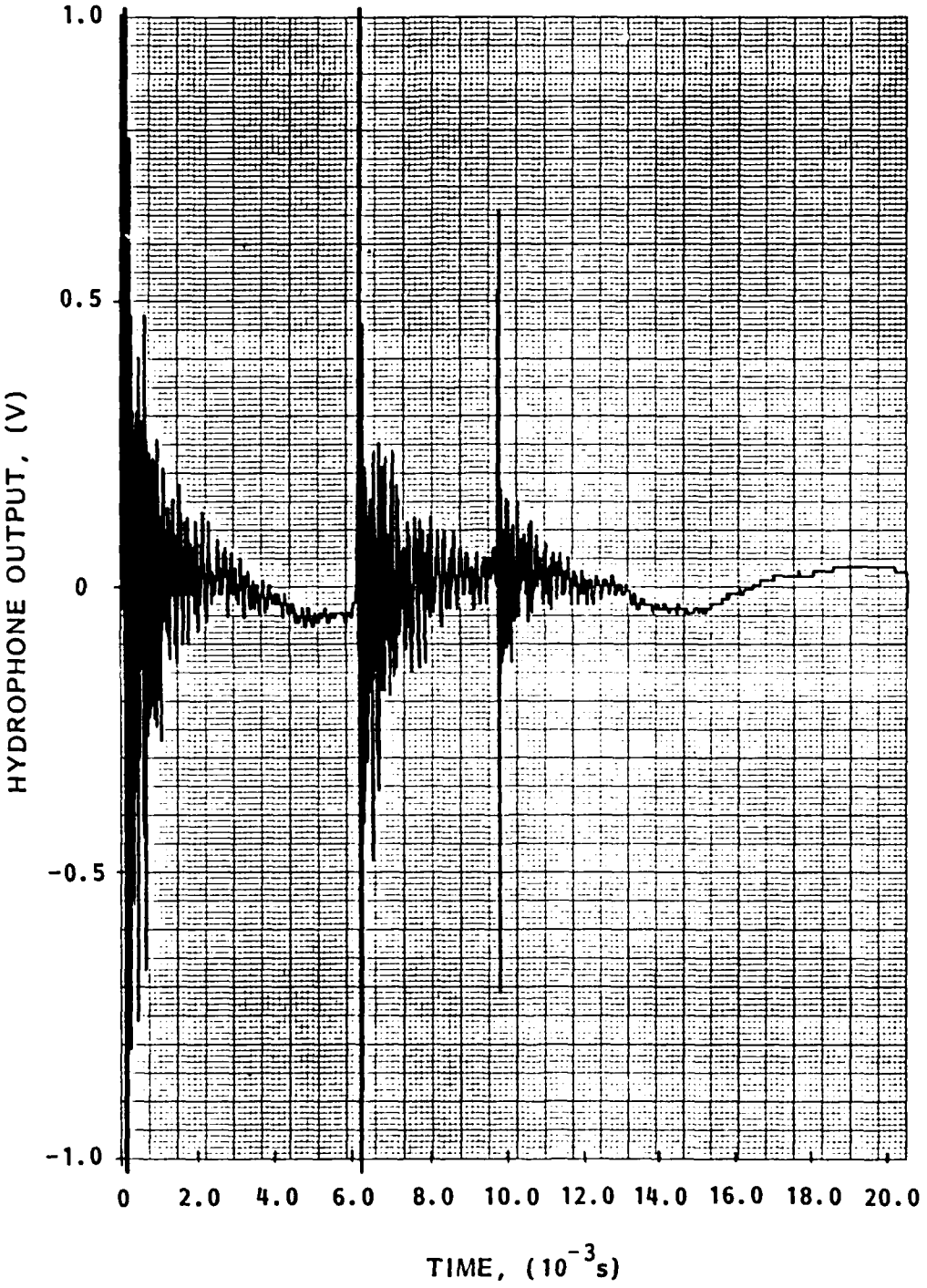

FIGURE 8.3 - PRESSURE VARIATION VS. TIME FOR SPARK INDUCED BUBBLE 2¼ INCH FROM CONE TIP

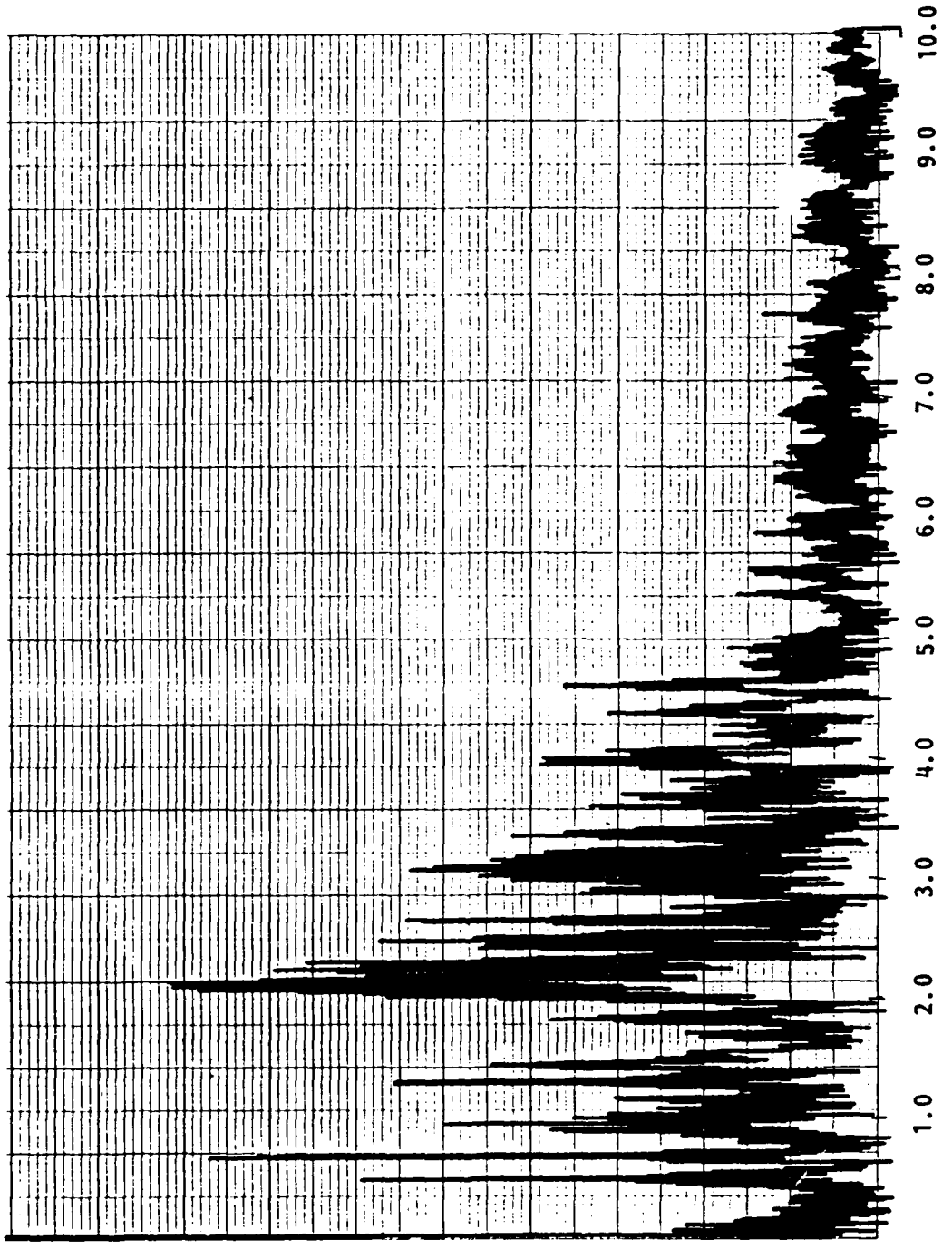

FIGURE 8.4 - FREQUENCY TRANSFORM OF DATA SHOWN IN FIGURE 26

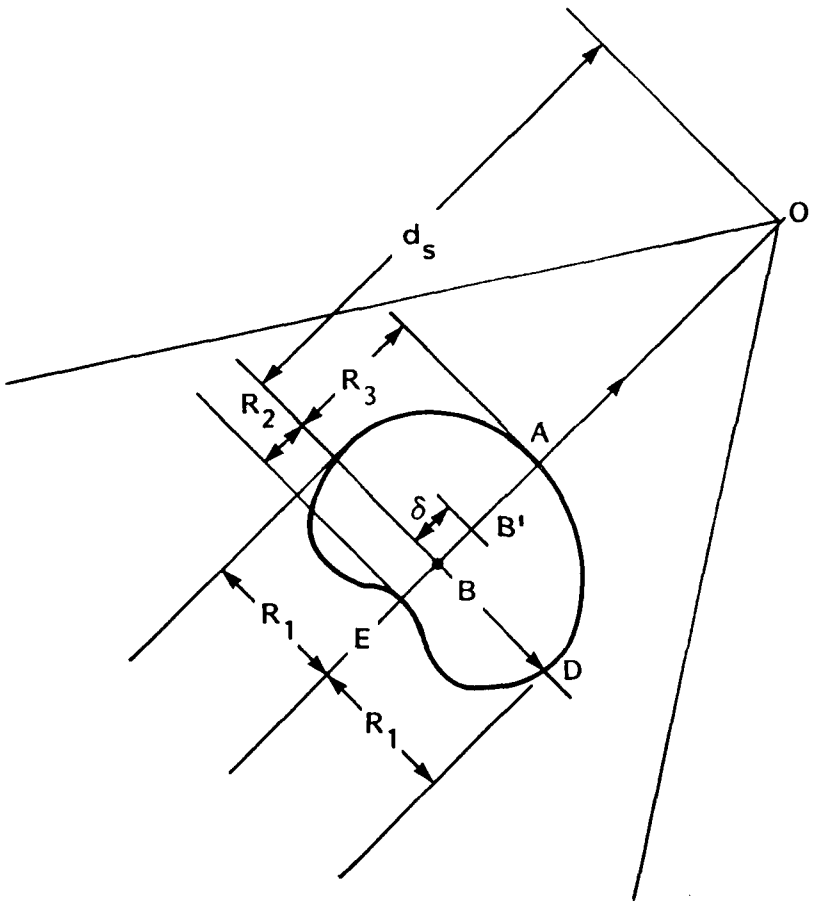

B : INITIAL BUBBLE CENTER;
OR ELECTRODE GAP

B' : NEW POSITION OF BUBBLE
CENTER

O : BUBBLE CLOUD CENTER;
OR PYRAMID APEX

FIGURE 8.5 - PRINCIPAL GEOMETRICAL CHARACTER-
ISTICS OF A BUBBLE DURING ITS MOTION

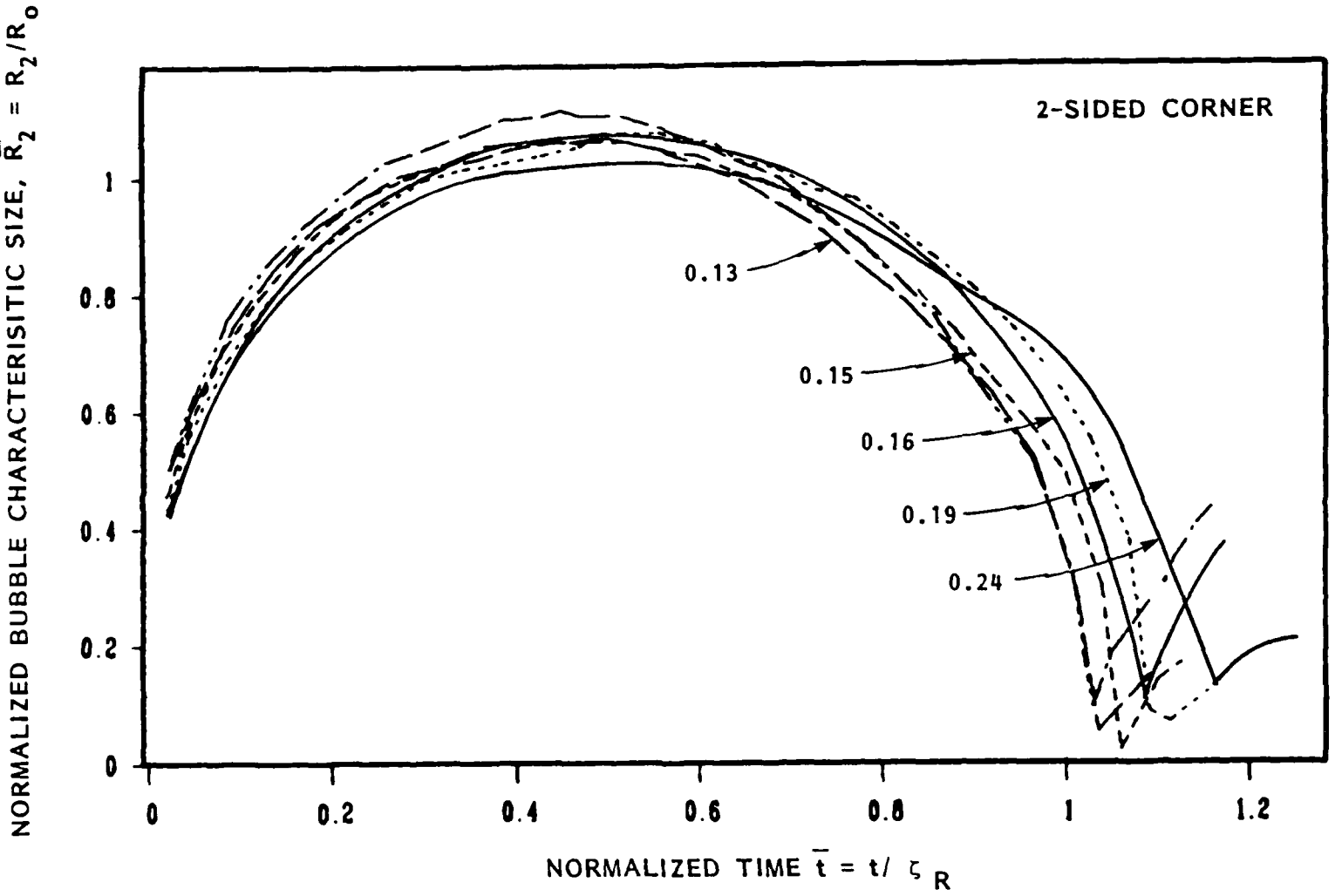

FIGURE 8.6 - VARIATION OF R_2 VERSUS TIME FOR DIFFERENT VALUES OF β. TESTS CONDUCTED WITH 2-DIMENSIONAL CORNER, (N = 4)

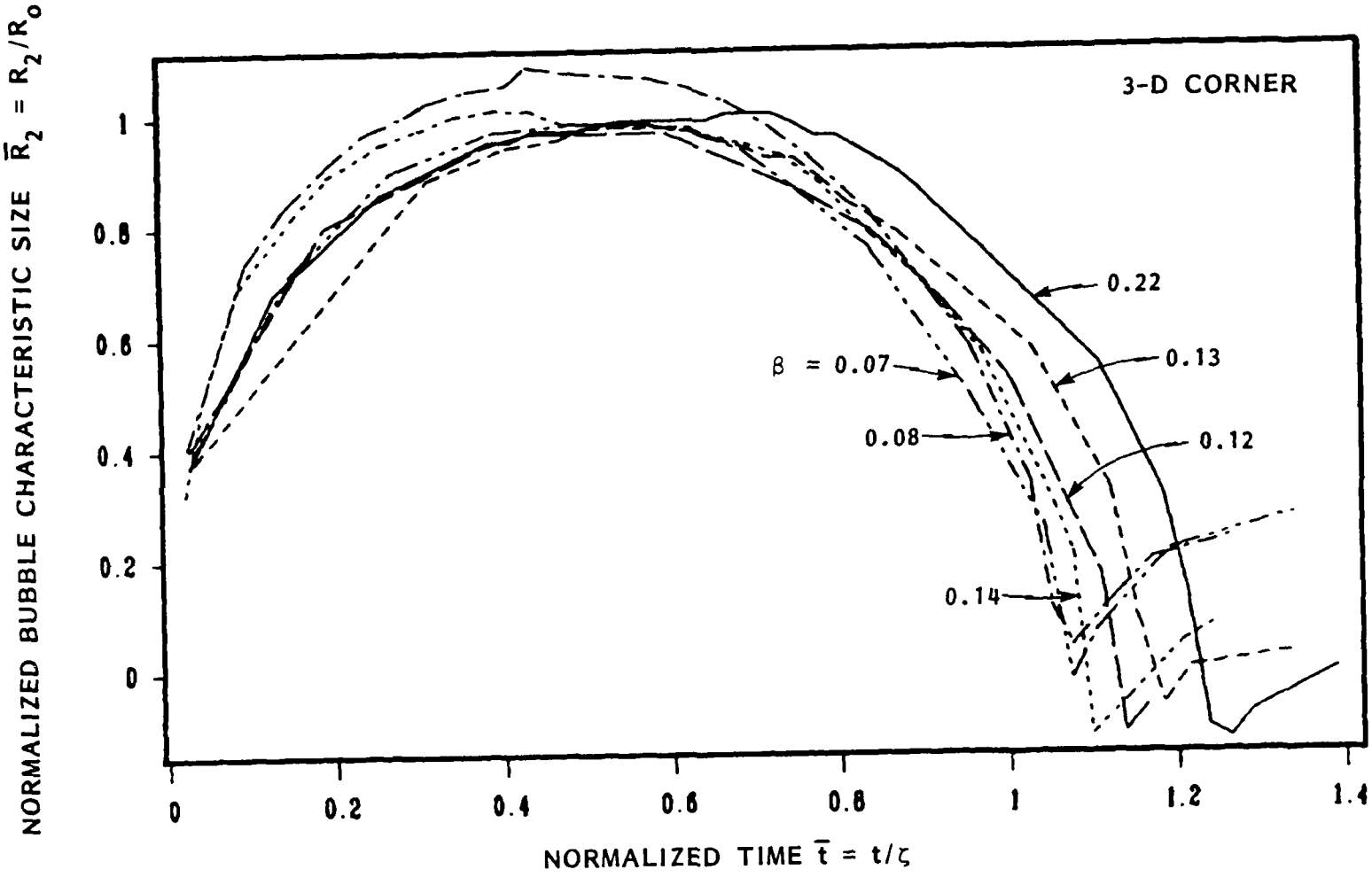

FIGURE 8.7 - VARIATIONS OF R_2 VERSUS TIME FOR DIFFERENT VALUES OF β . TESTS CONDUCTED WITH 3-DIMENSIONAL CORNER (N = 8)

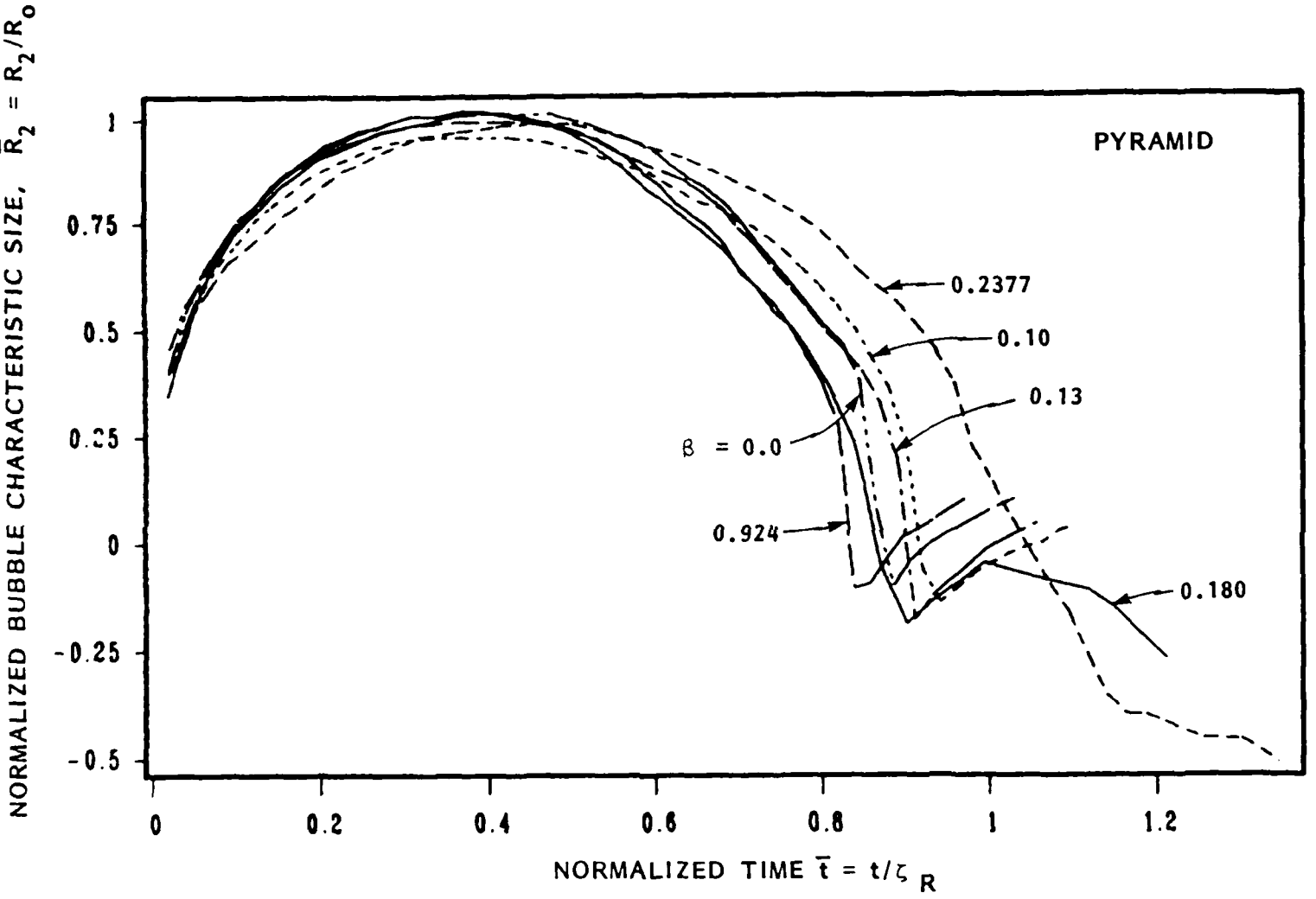

FIGURE 8.8 - VARIATIONS R_2 VERSUS TIME FOR DIFFERENT VALUES OF OF β . TESTS CONDUCTED WITH PENTAGONAL PYRAMID, (N = 12)

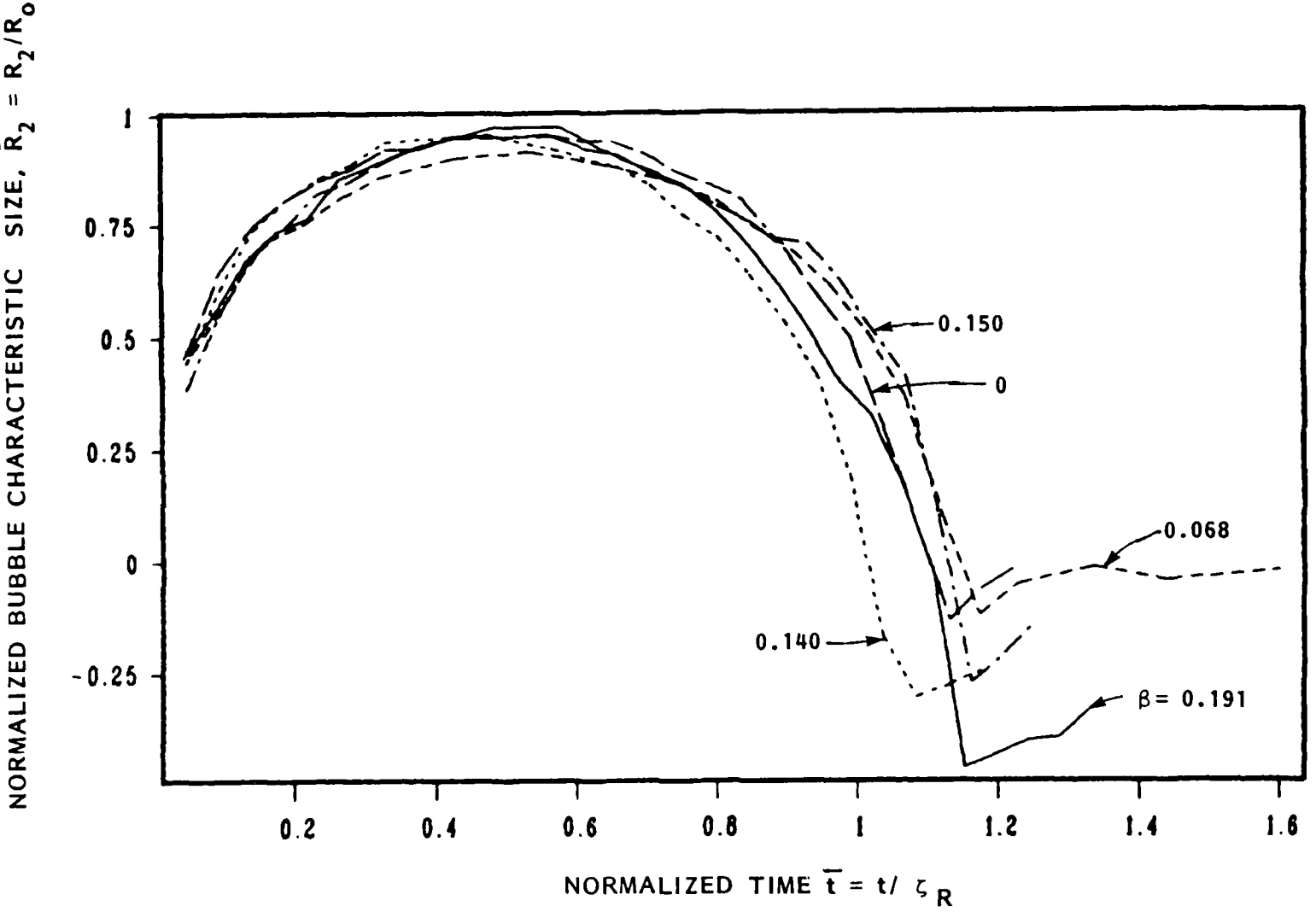

FIGURE 8.9 - VARIATIONS OF R_2 VERSUS TIME FOR DIFFERENT VALUES OF β . TESTS CONDUCTED WITH CONE (N = 12)

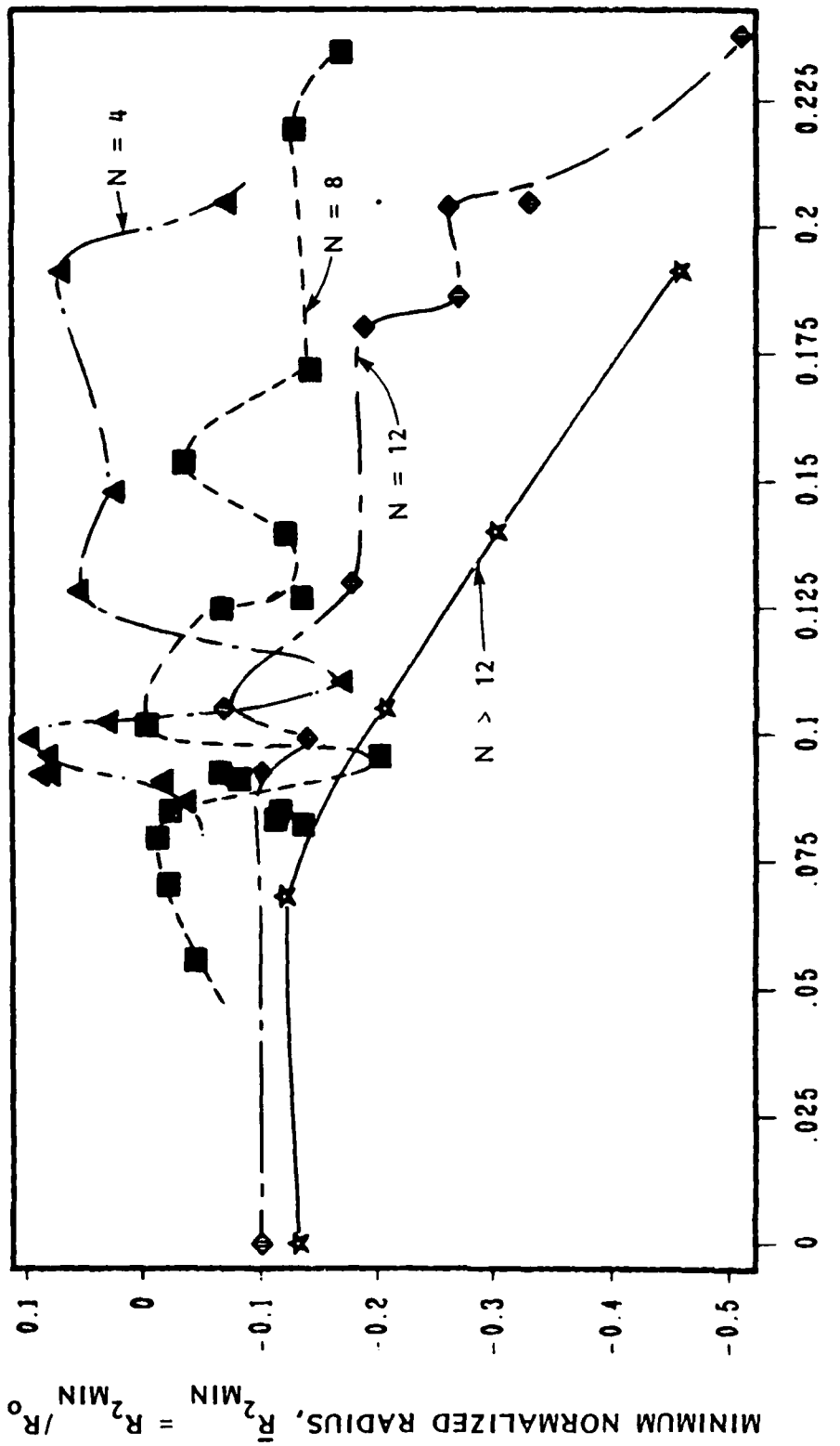

FIGURE 8.10 - MINIMUM NORMALIZED RADIUS, $\bar{R}_{2'}$ VERSUS β FOR THE VARIOUS BUBBLE CONFIGURATIONS

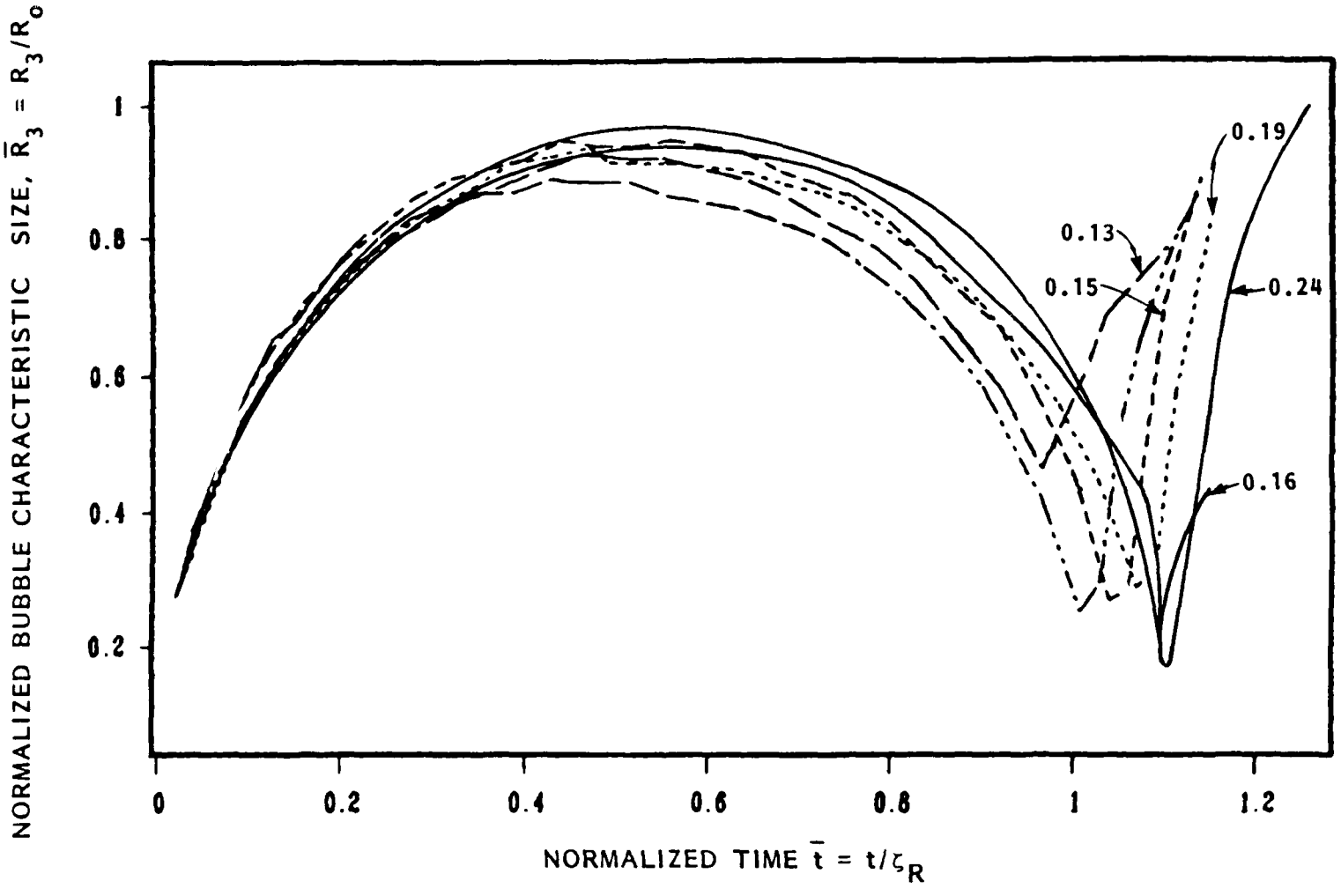

FIGURE 8.11 - VARIATION OF R_3 VERSUS TIME FOR DIFFERENT VALUES OF β . TESTS CONDUCTED WITH 2-DIMENSIONAL CORNER (N=4)

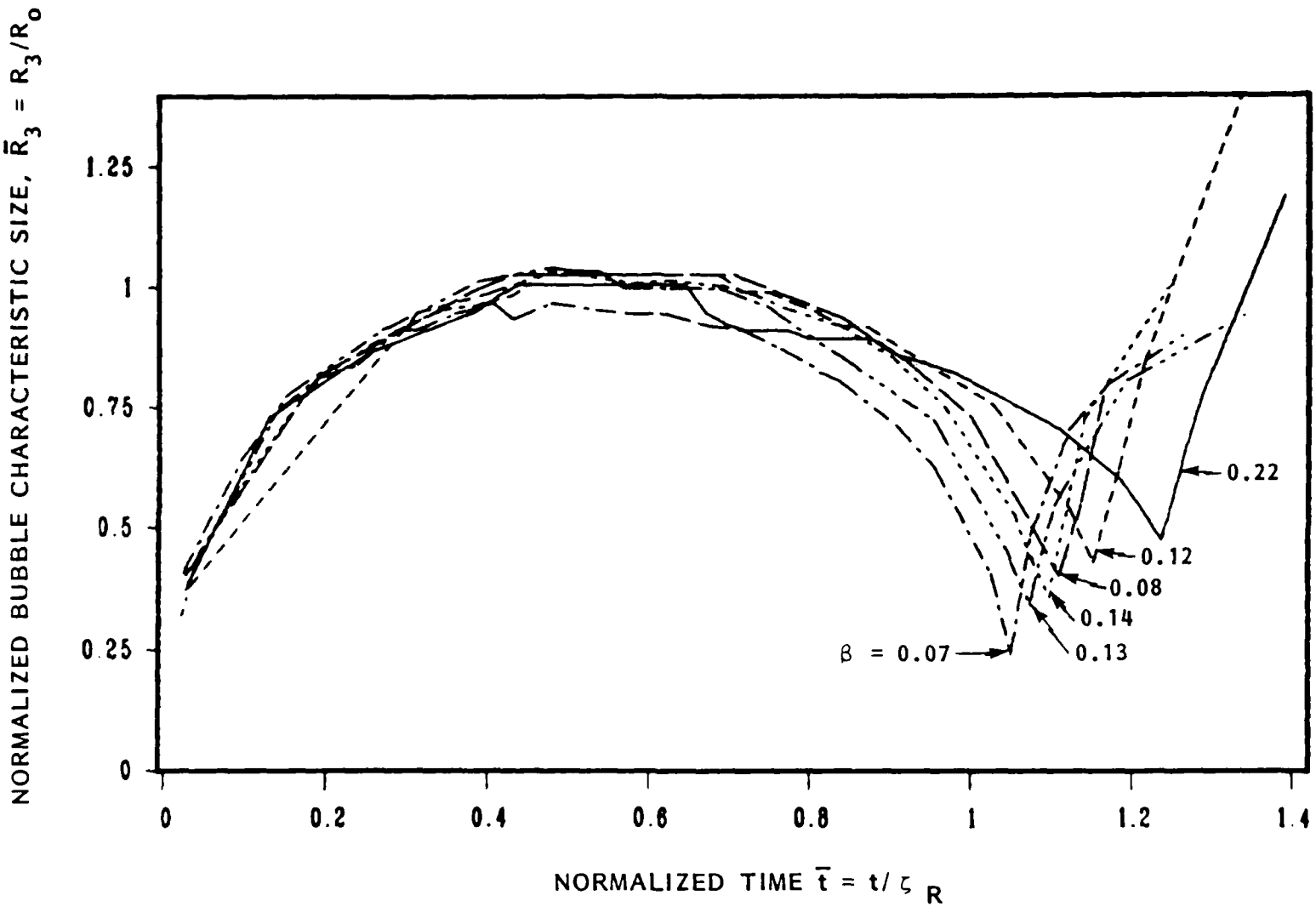

FIGURE 8.12 - VARIATION OF R_3 VERSUS TIME FOR DIFFERENT VALUES OF β. TESTS CONDUCTED WITH 3-DIMENSIONAL CORNER, (N = 8)

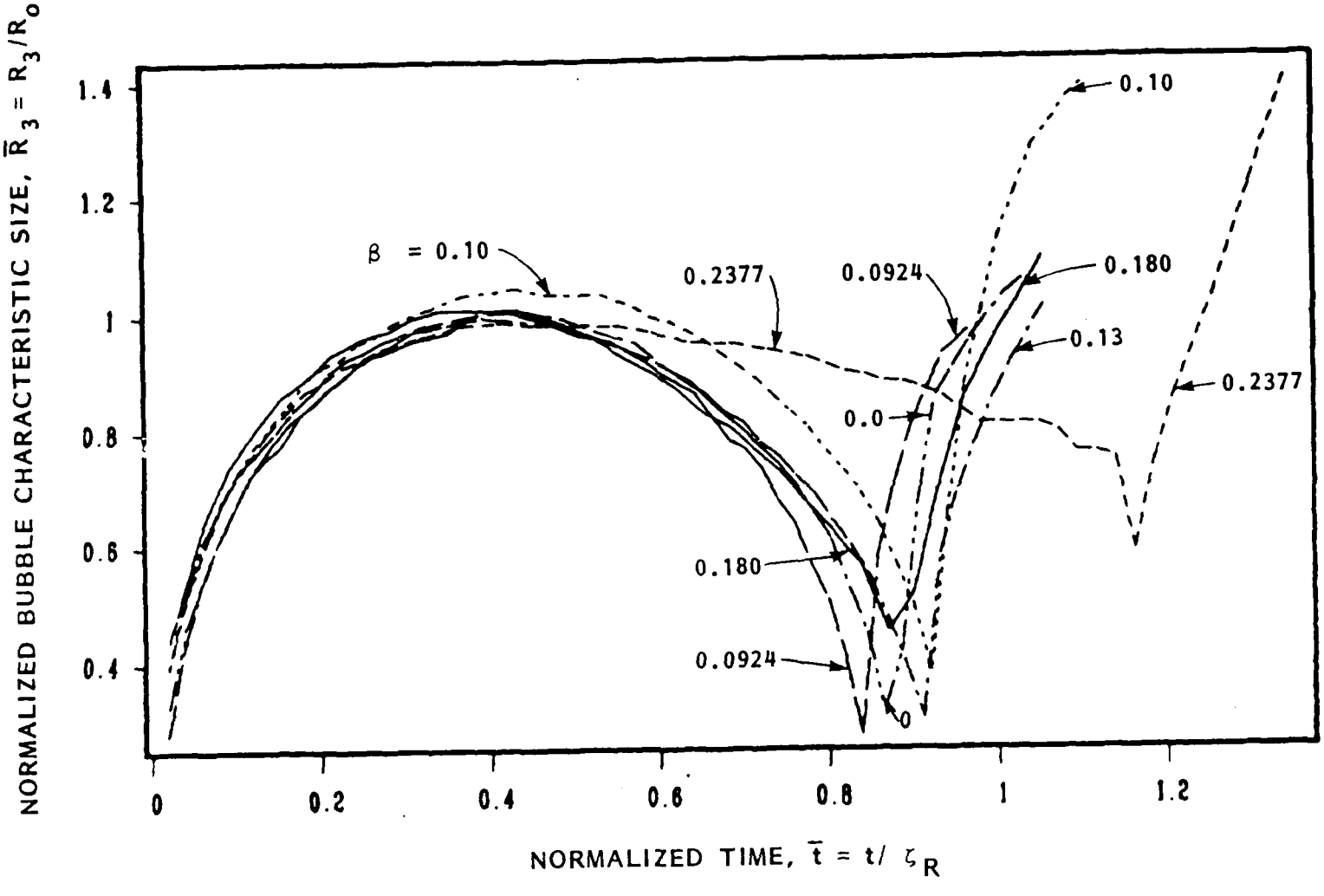

FIGURE 8.13 - VARIATION OF R_3 VERSUS TIME FOR DIFFERENT VALUES OF β. TESTS COMPUTED WITH PENTAGONAL PYRAMID (N = 12)

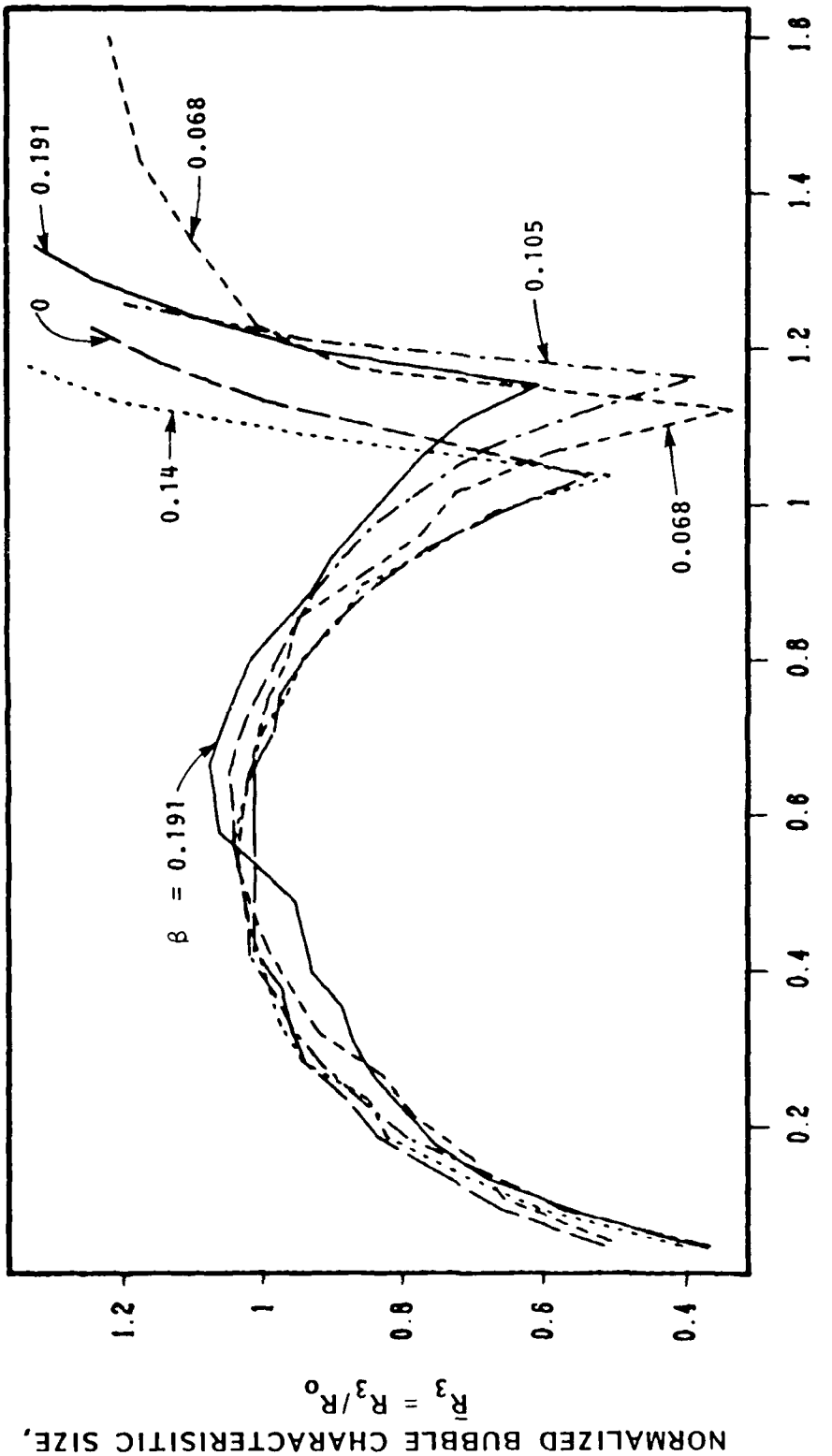

FIGURE 8.14 - VARIATION OF R_3 VERSUS TIME FOR DIFFERENT VALUES OF β . TESTS CONDUCTED WITH CONE

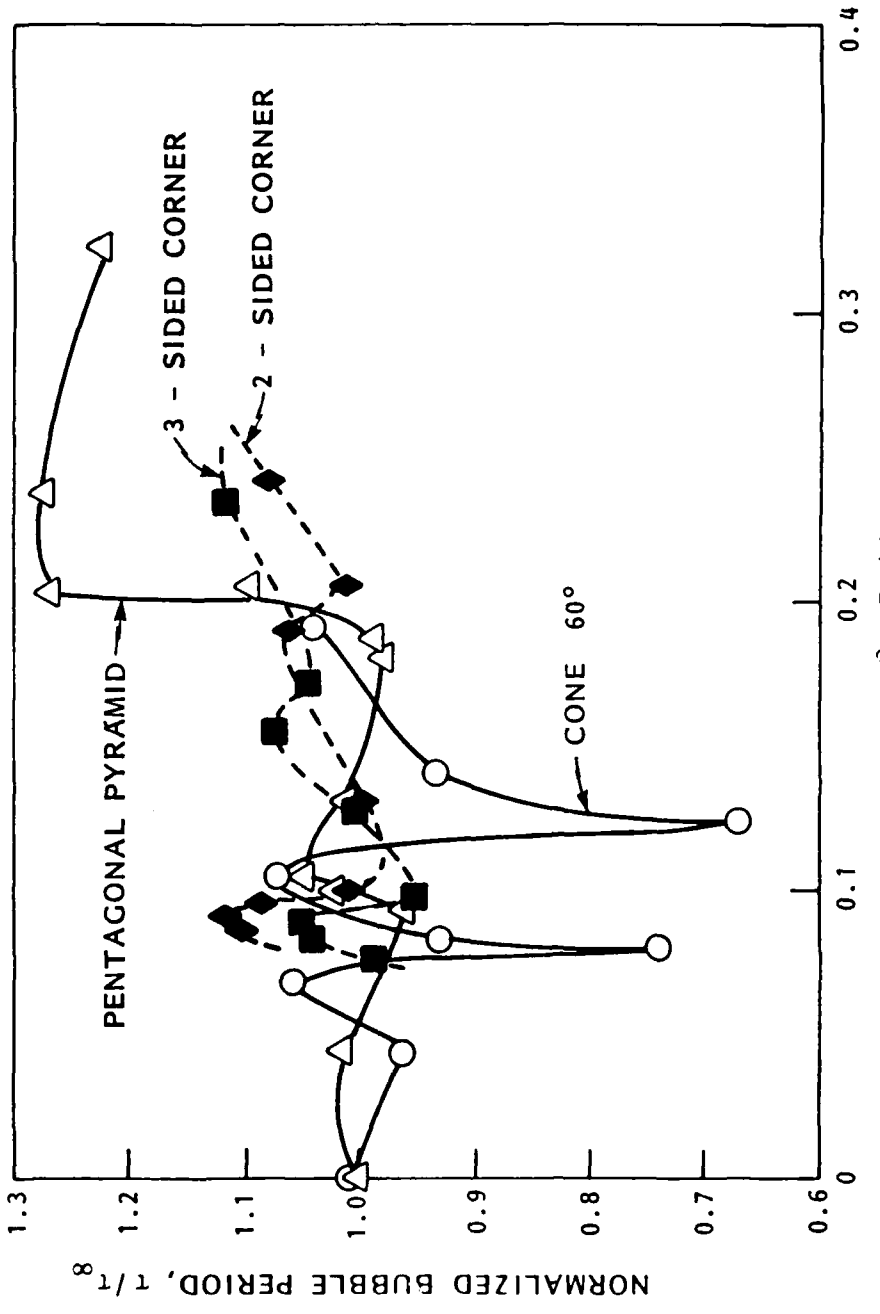

FIGURE 8.15 - NORMALIZED BUBBLE PERIOD VERSUS INVERSE NORMALIZED BUBBLE-APEX DISTANCE

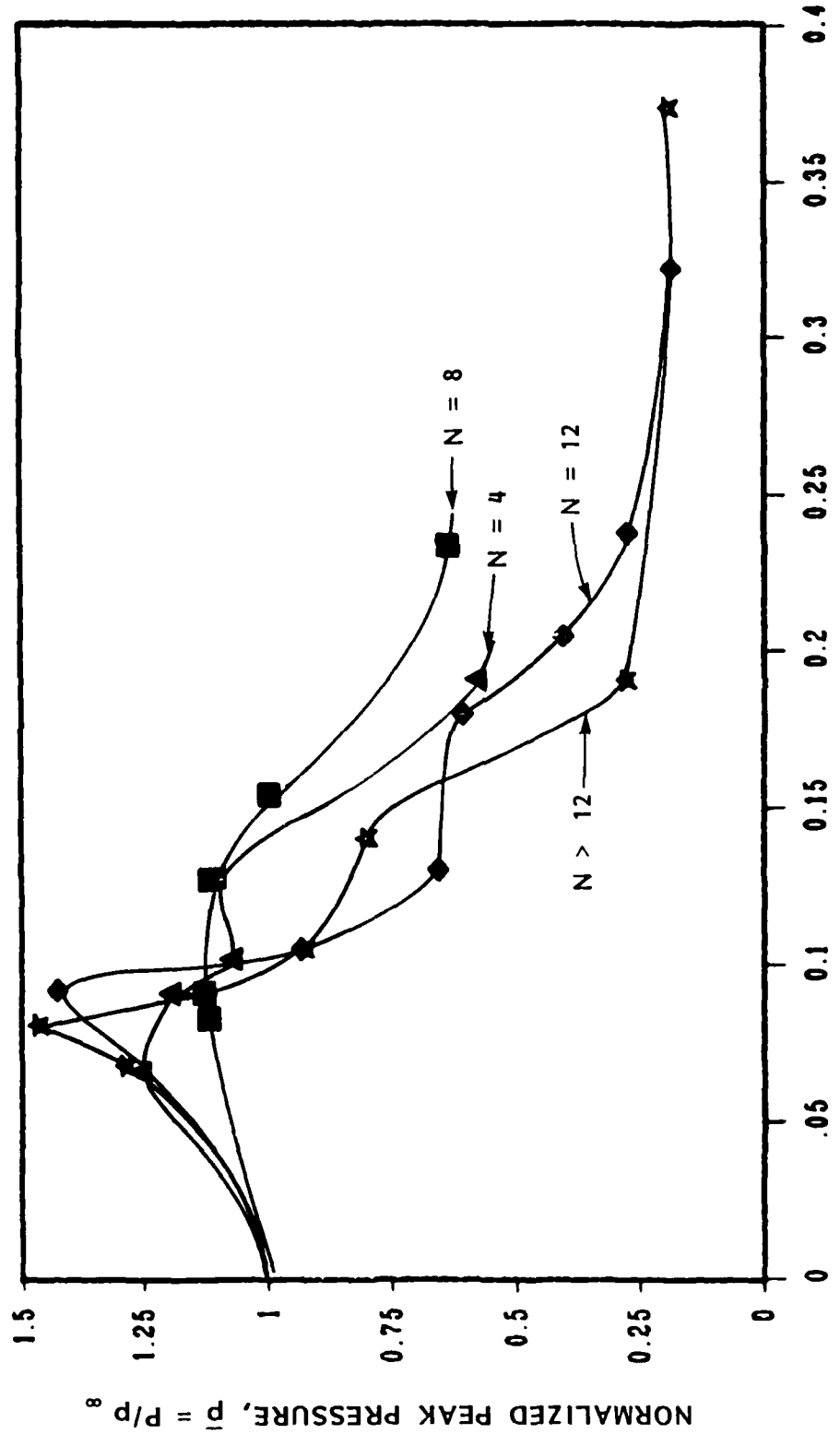

FIGURE 8.16 - PEAK PRESSURE MEASURED AT 6 in. FROM SPARK VERSUS β FOR THE VARIOUS BUBBLE CONFIGURATIONS

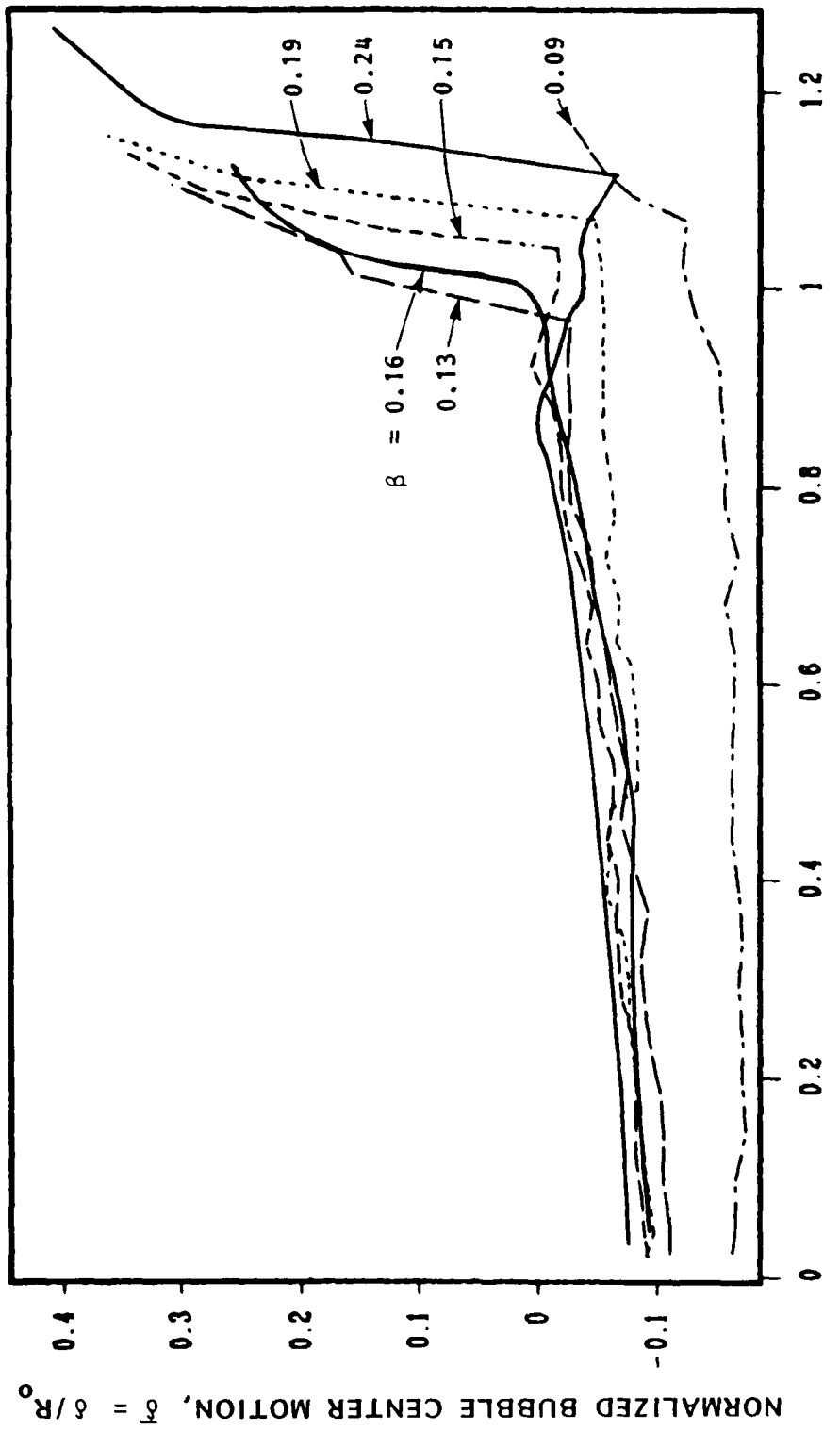

FIGURE 8.17 - MOTION OF BUBBLE CENTER VERSUS TIME FOR DIFFERENT VALUES OF β. TESTS CONDUCTED WITH 2-D CORNER

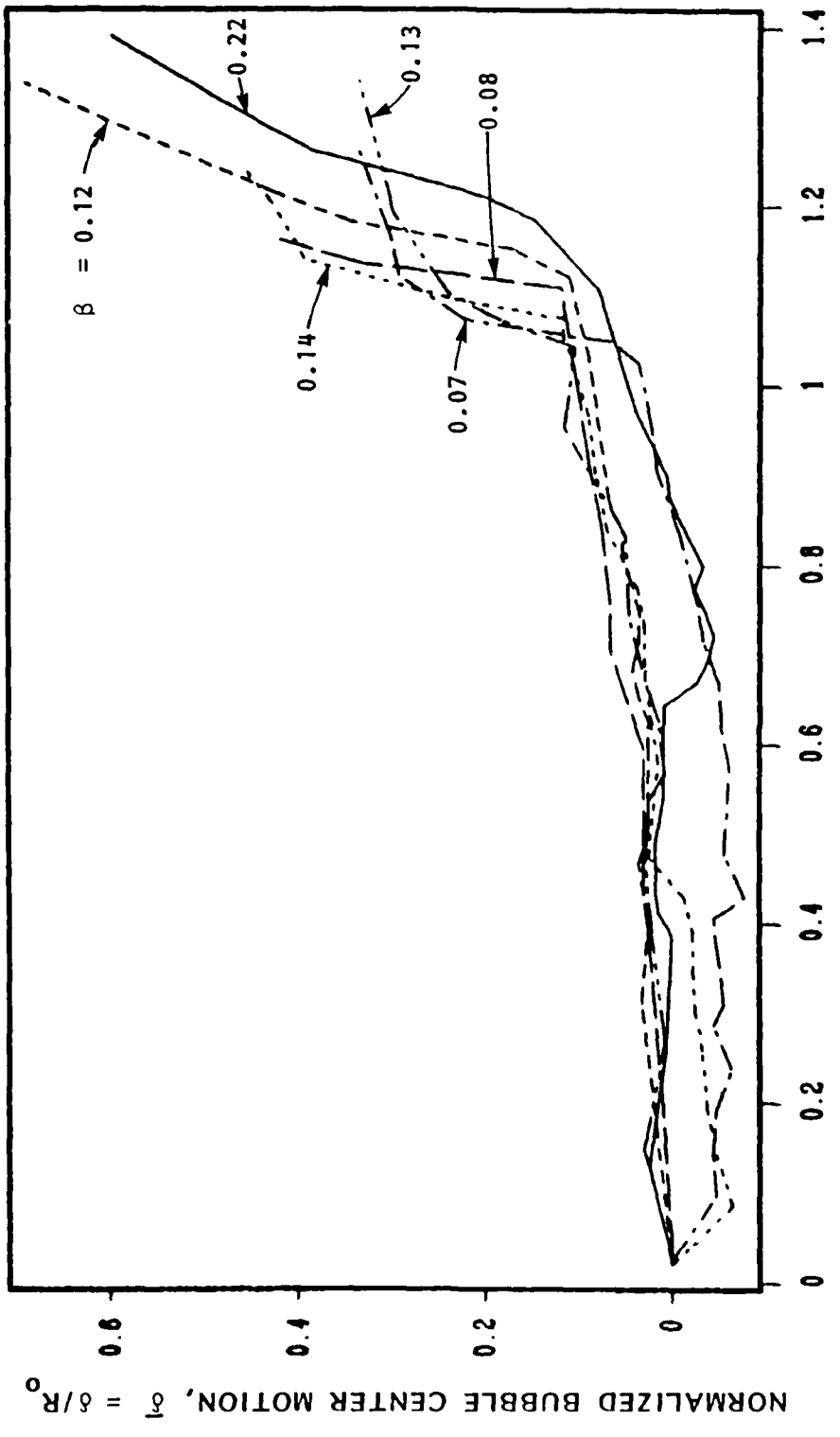

FIGURE 8.18 - MOTION OF BUBBLE CENTER VERSUS TIME FOR DIFFERENT VALUES OF β. TESTS CONDUCTED WITH 3-D CORNER

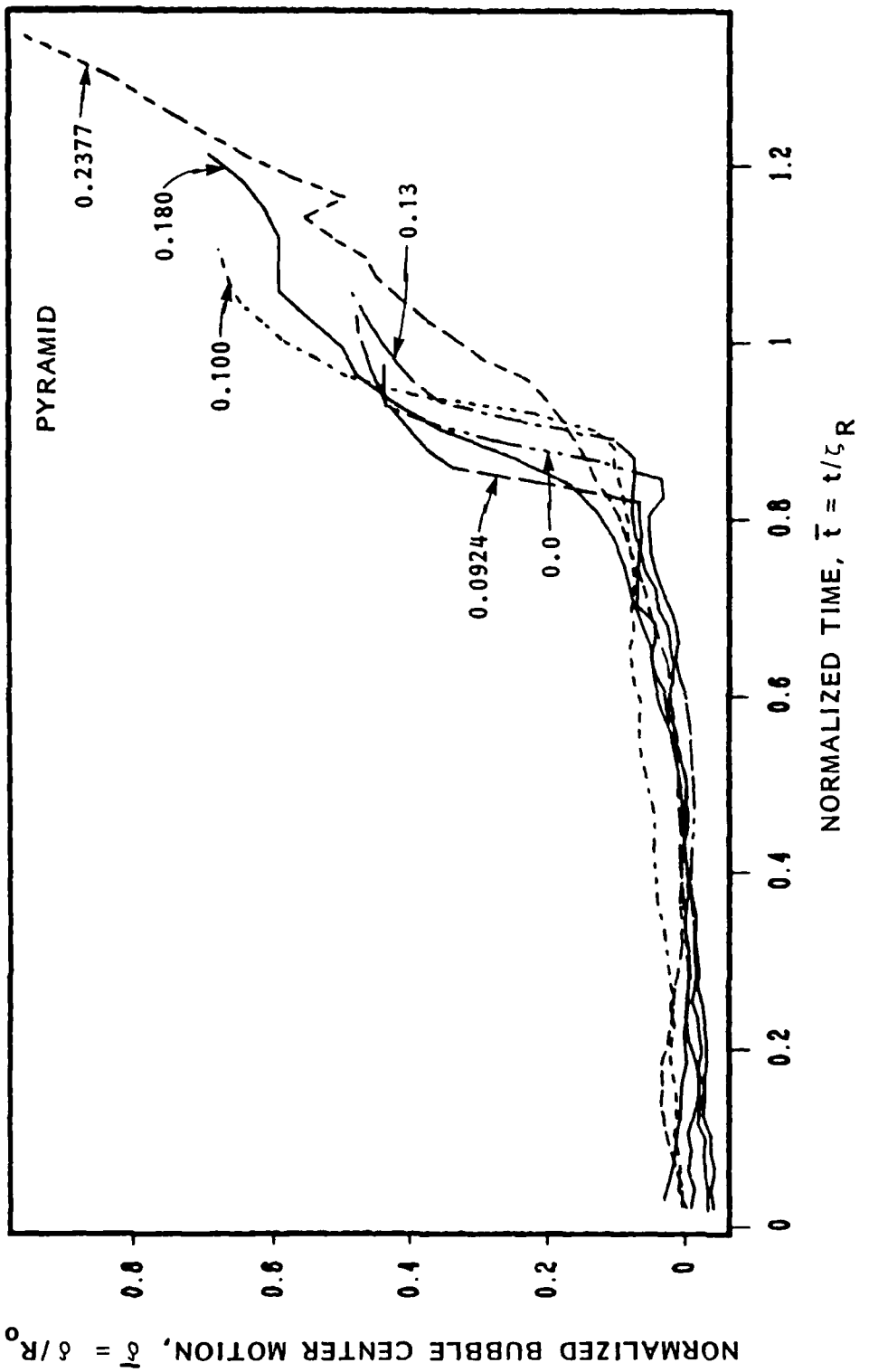

FIGURE 8.19 - MOTION OF BUBBLE CENTER VERSUS TIME FOR VALUES OF β . TSET CONDUCTED WITH PENTAGONAL PYRAMID (N = 12)

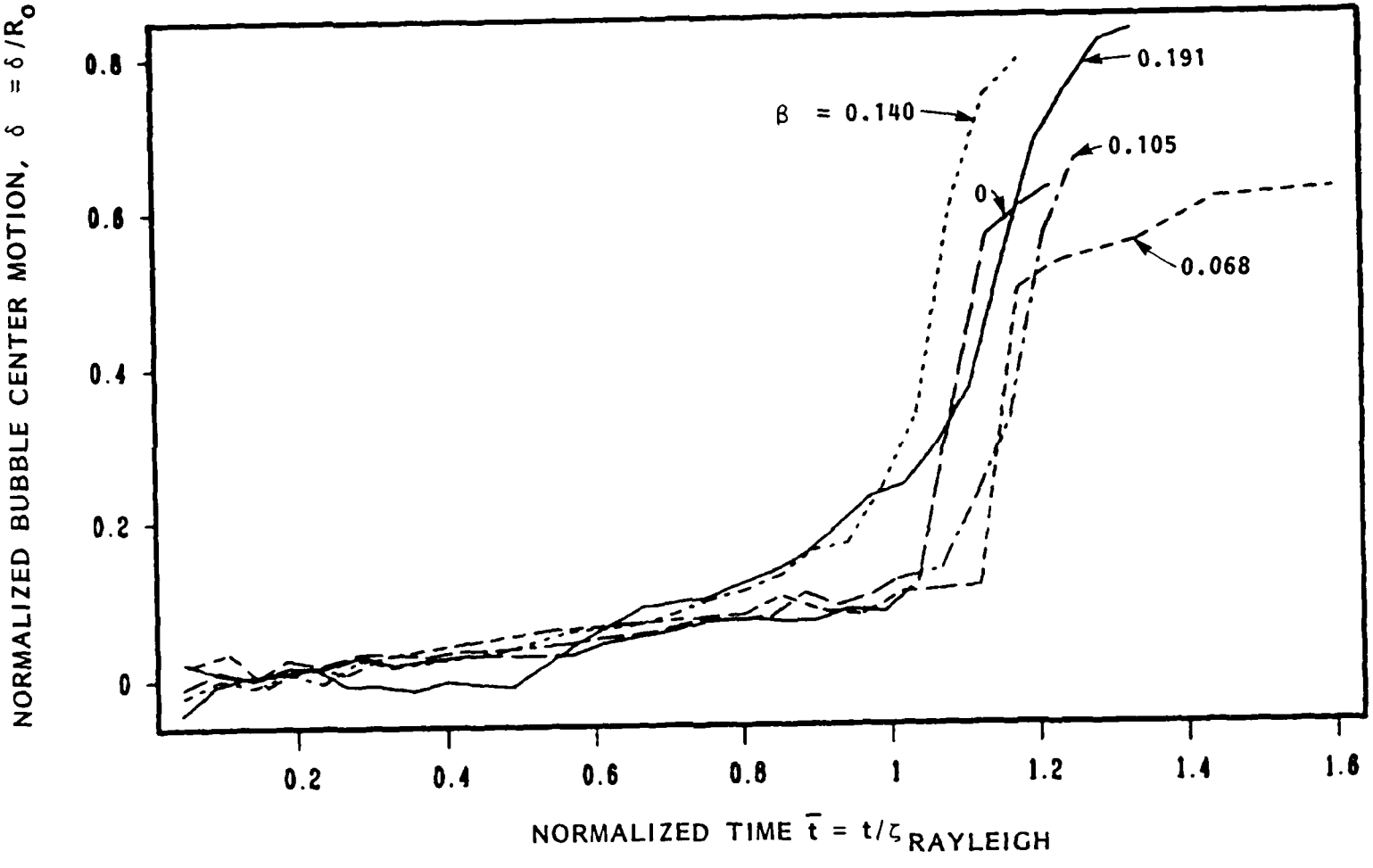

FIGURE 8.20 - MOTION OF BUBBLE CENTER VERSUS TIME FOR DIFFERENT VALUES OF β. TESTS CONDUCTED WITH CONE

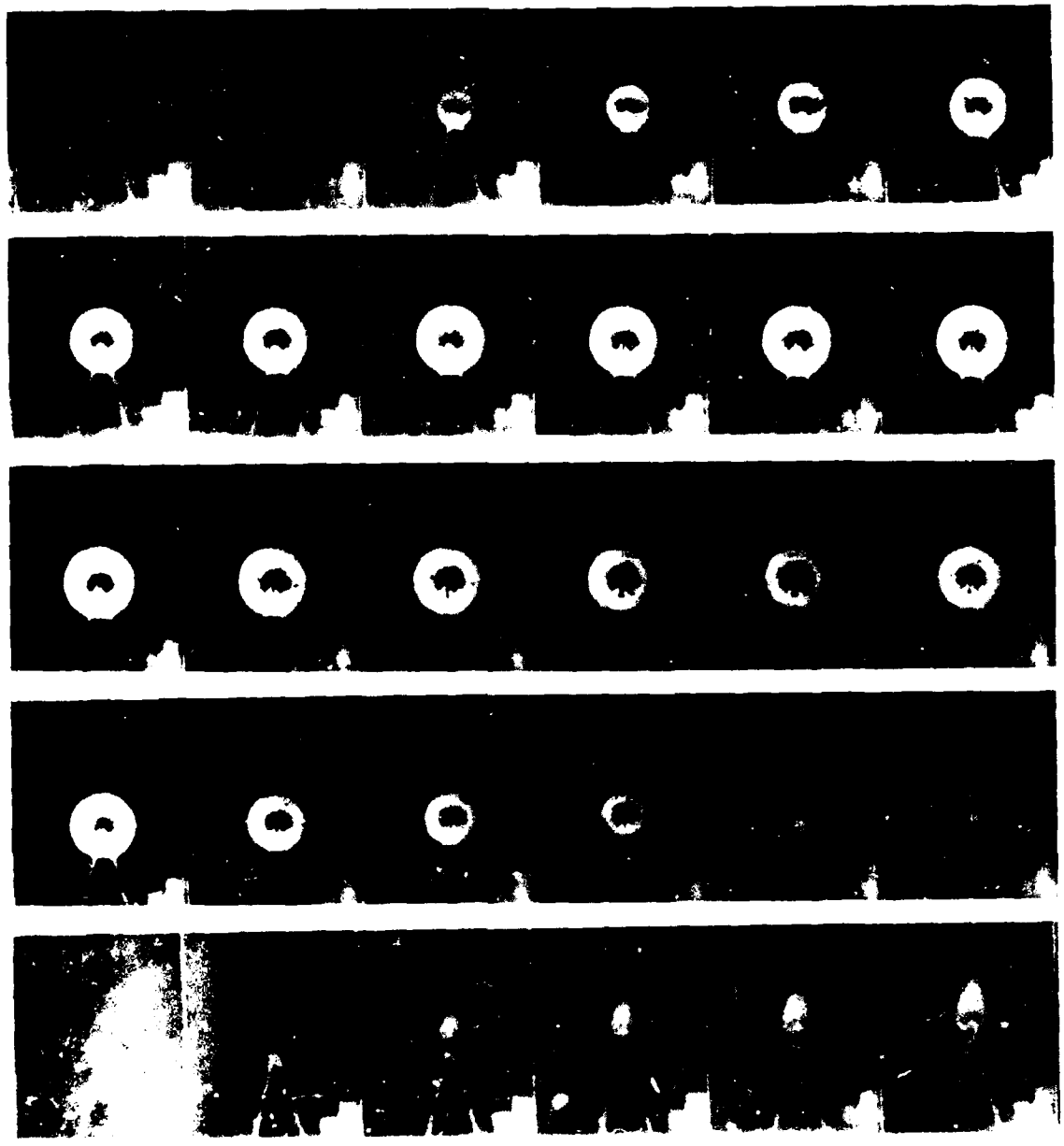

FIGURE 8.21 - GROWTH AND COLLAPSE OF A SPARK GENERATED BUBBLE INSIDE CONE. d_s = 4 inches, $\Delta P = 1.4 \times 10^4$Pa, TIME PER FRAME = 0.249 ms.

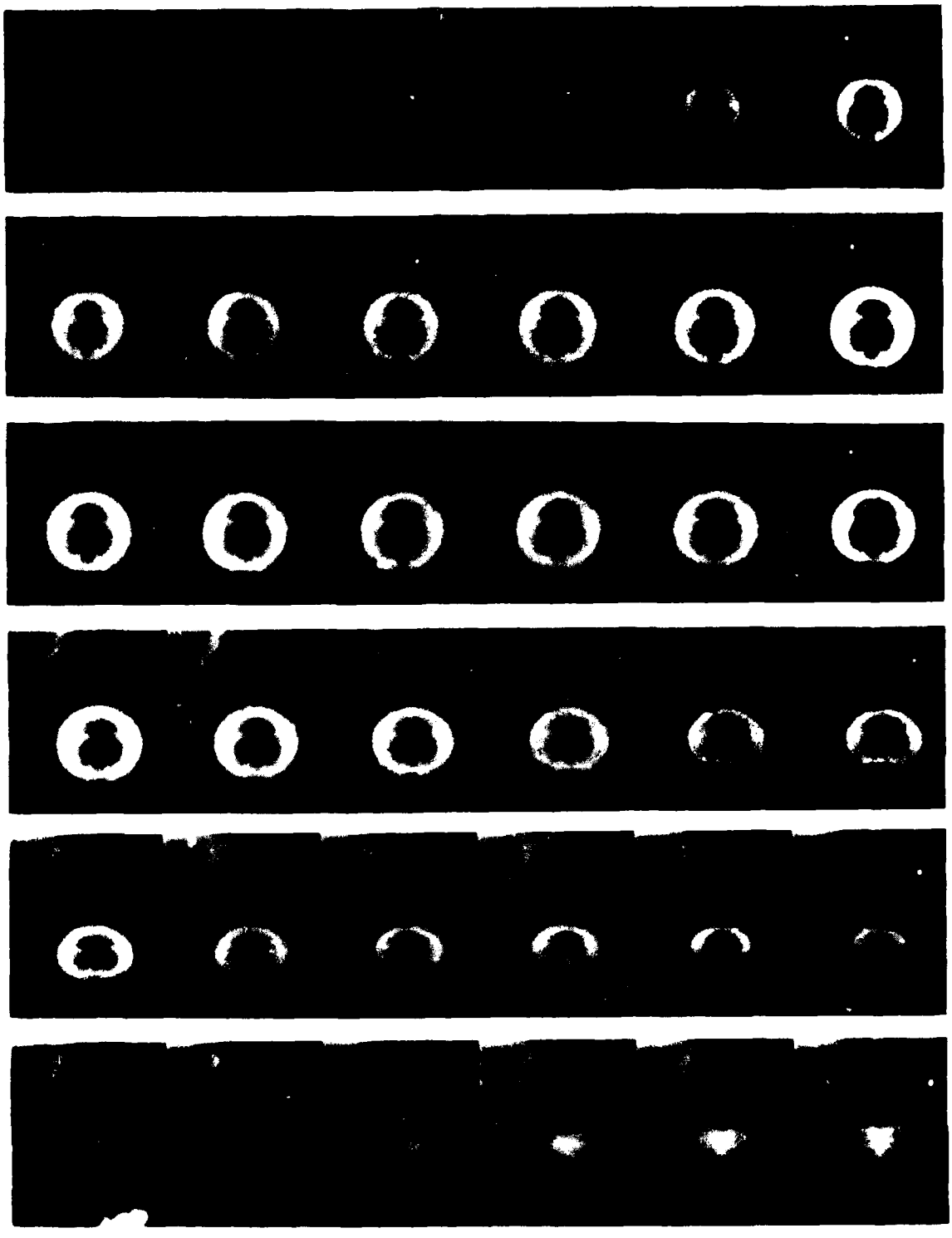

FIGURE 8.22 - GROWTH AND COLLAPSE OF SPARK GENERATED BUBBLE INSIDE CONE. d_s = 1½ inches, $\Delta P = 1.6 \times 10^4$Pa, TIME PER FRAME = 0.294 ms.

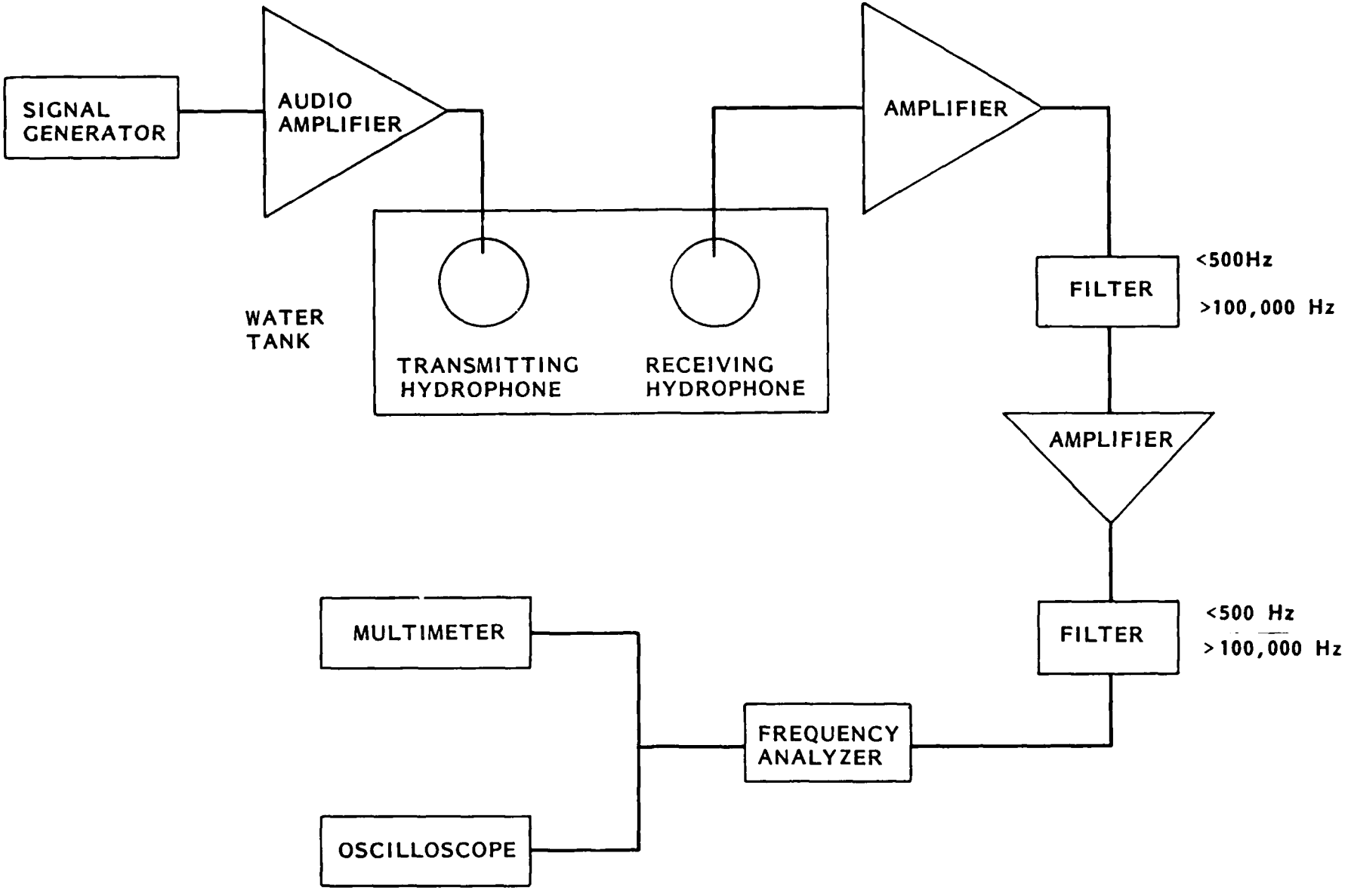

FIGURE 9.1 - DIAGRAM OF EXPERIMENTAL SET-UP

FIGURE 9.2 - PHOTOGRAPH OF WATER TANK USED FOR ACOUSTIC DAMPING TESTS SHOWING BOTH HYDROPHONES AND A BUBBLE SCREEN

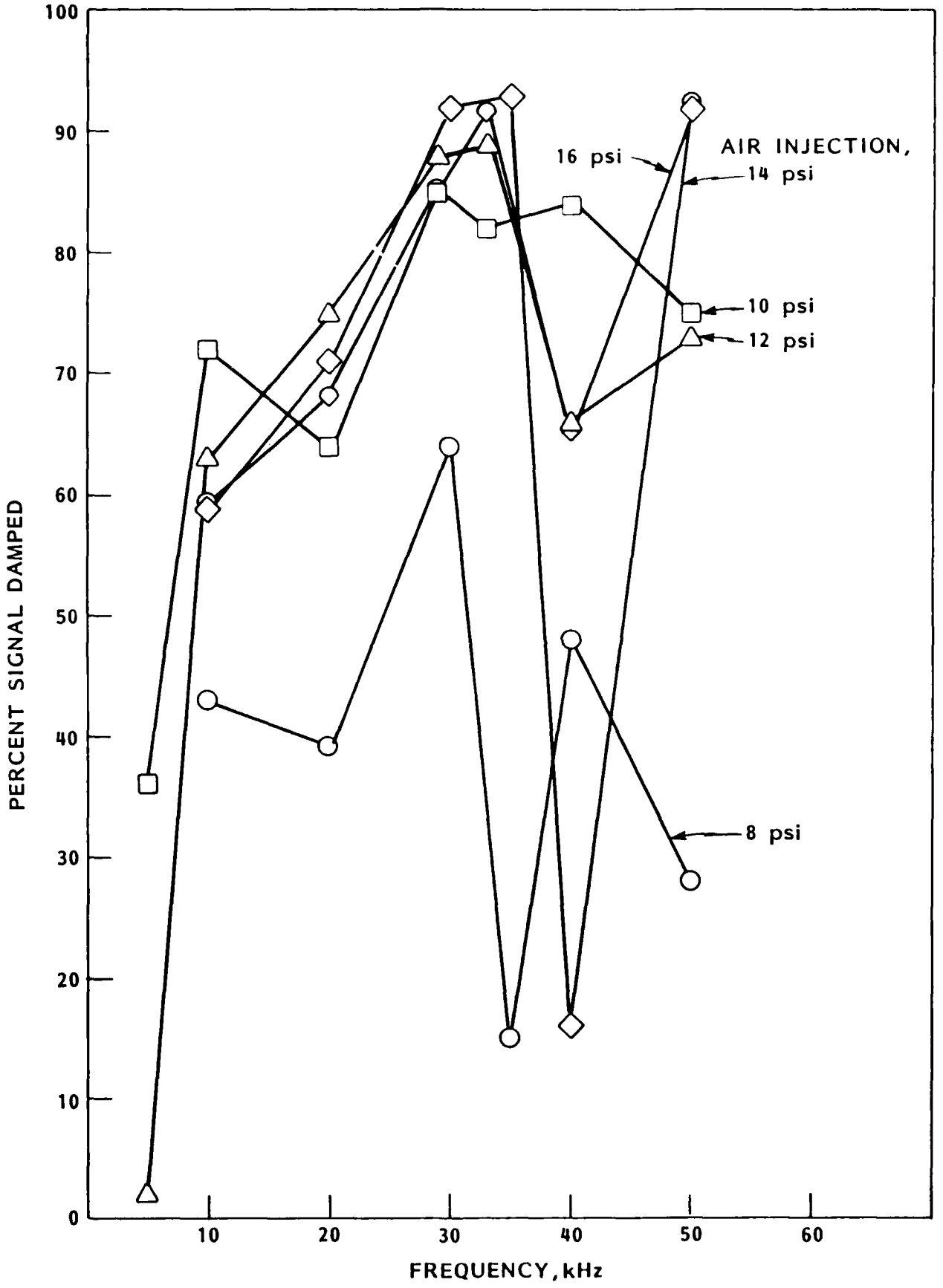

FIGURE 9.3 - DAMPING RATIO VERSUS EMISSION FREQUENCY. PRELIMINARY RESULTS WITH TWO LOW FREQUENCY RESPONSE HYDROPHONES

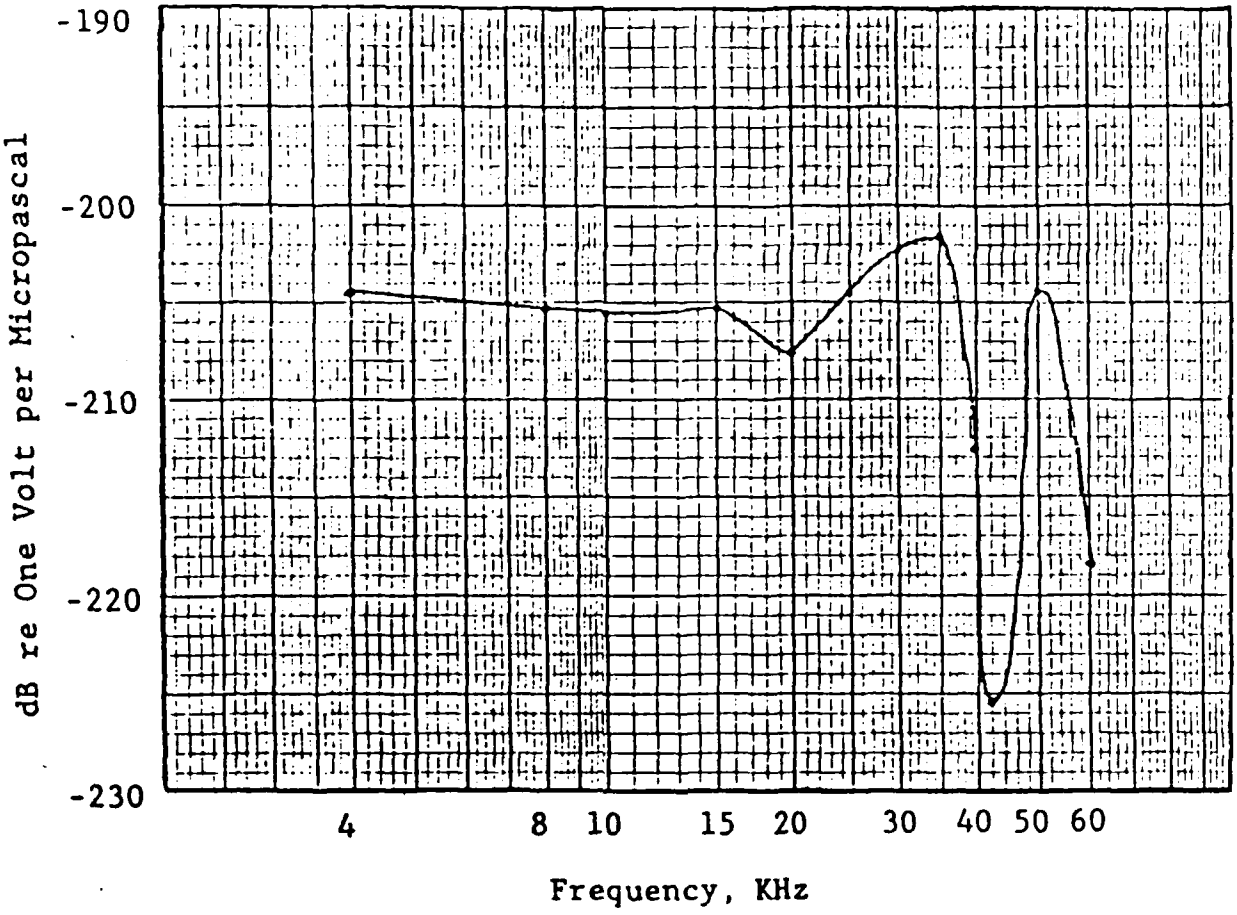

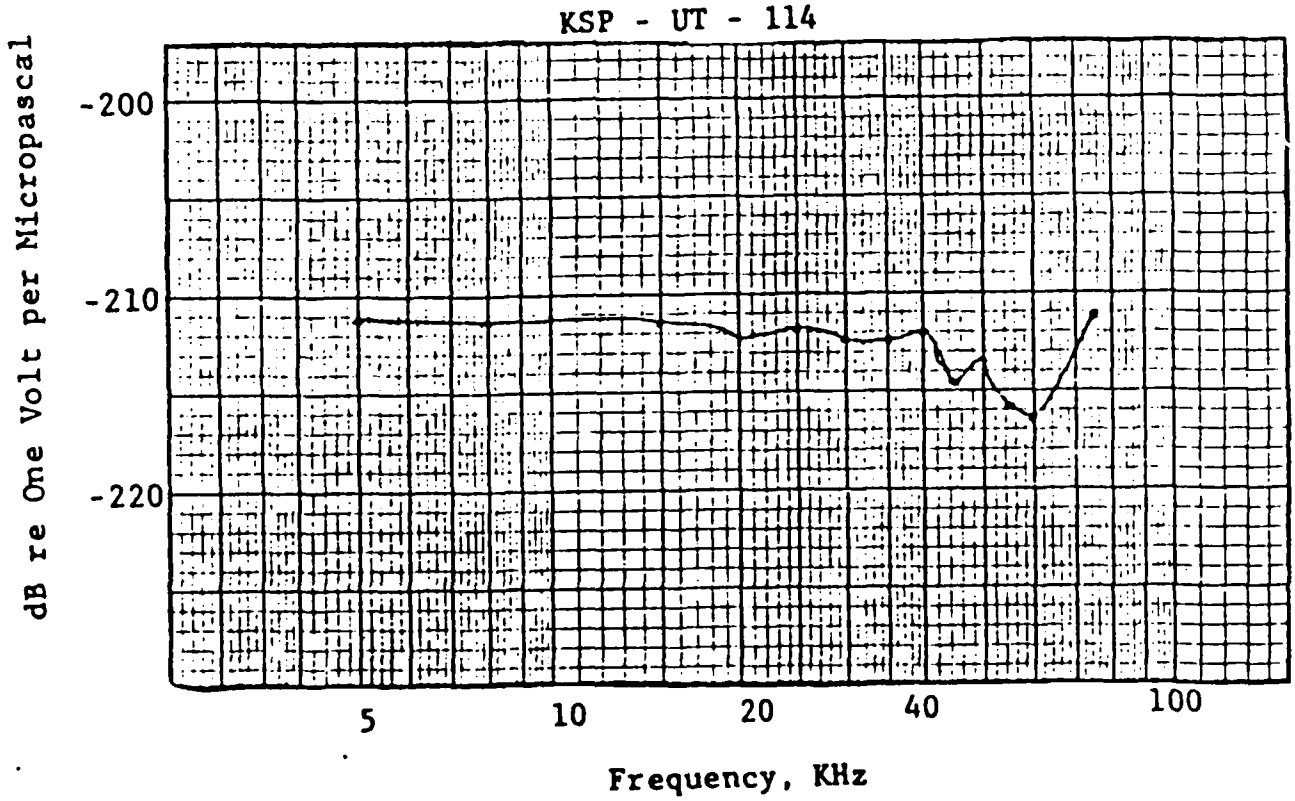

FIGURE 9.4 - CALIBRATED FREQUNCY RESPONSE OF CERAMIC CYLINDER HYDROPHONE, (TH-653) AND KSP-UT-114 HYDROPHONE

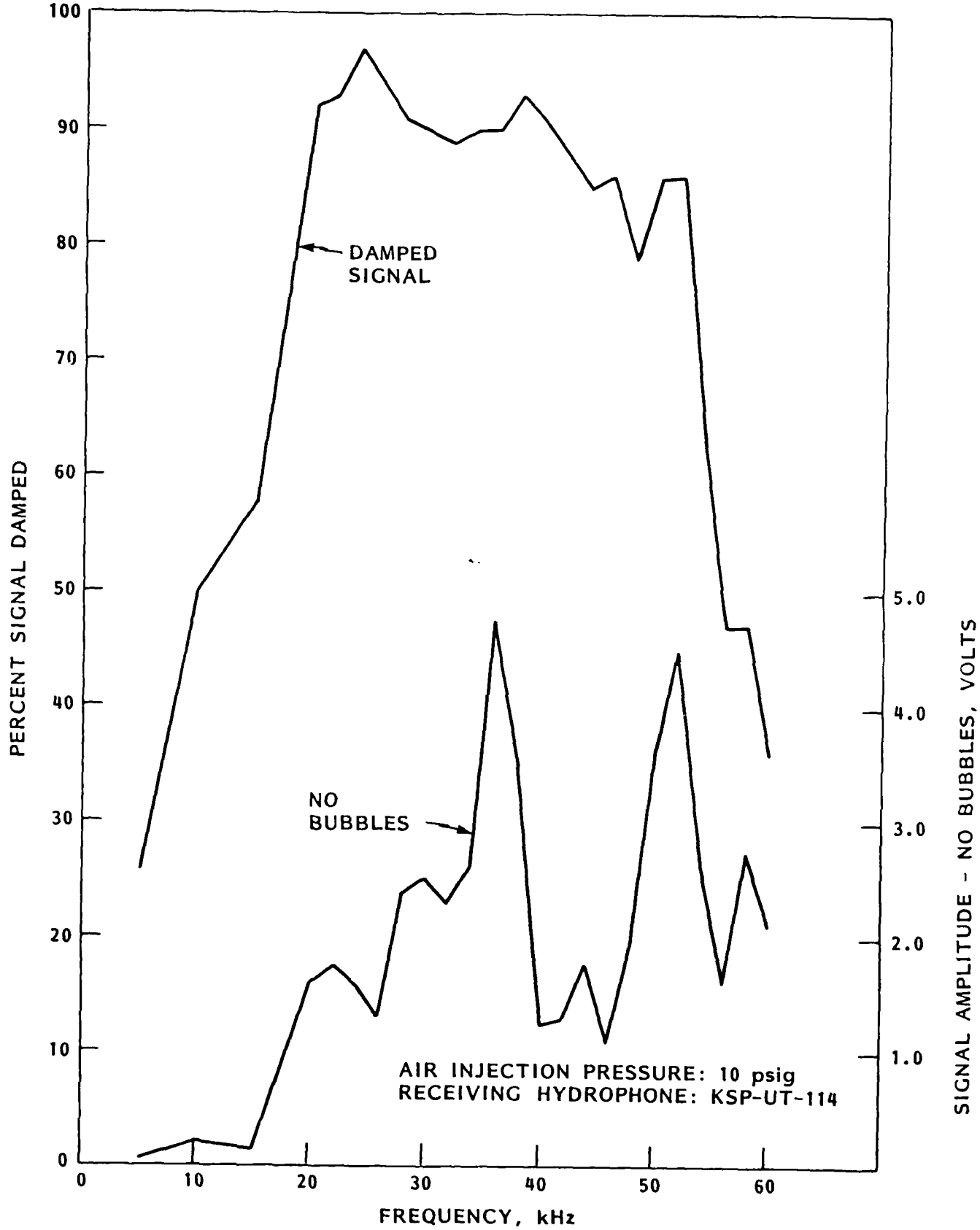

FIGURE 9.5 - DAMPING RATIO VERSUS EMISSION FREQUENCY AT CONSTANT TRANSMITTING HYDROPHONE INPUT VOLTAGE COMPARED WITH THE RECEIVED SIGNAL IN ABSENCE OF BUBBLES

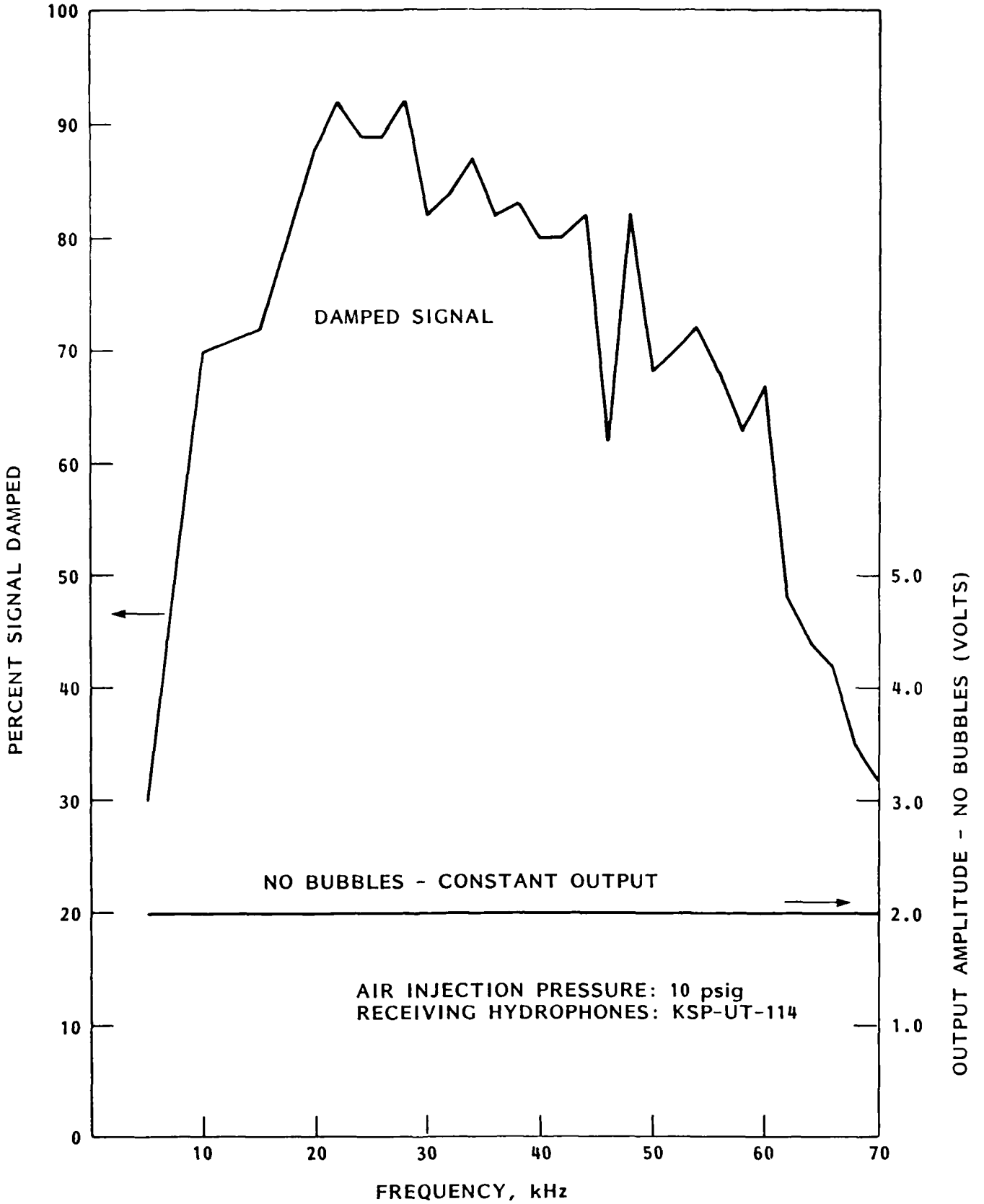

FIGURE 9.6 - DAMPING RATIO VERSUS EMISSION FREQUENCY. VARIABLE INPUT VOLTAGE

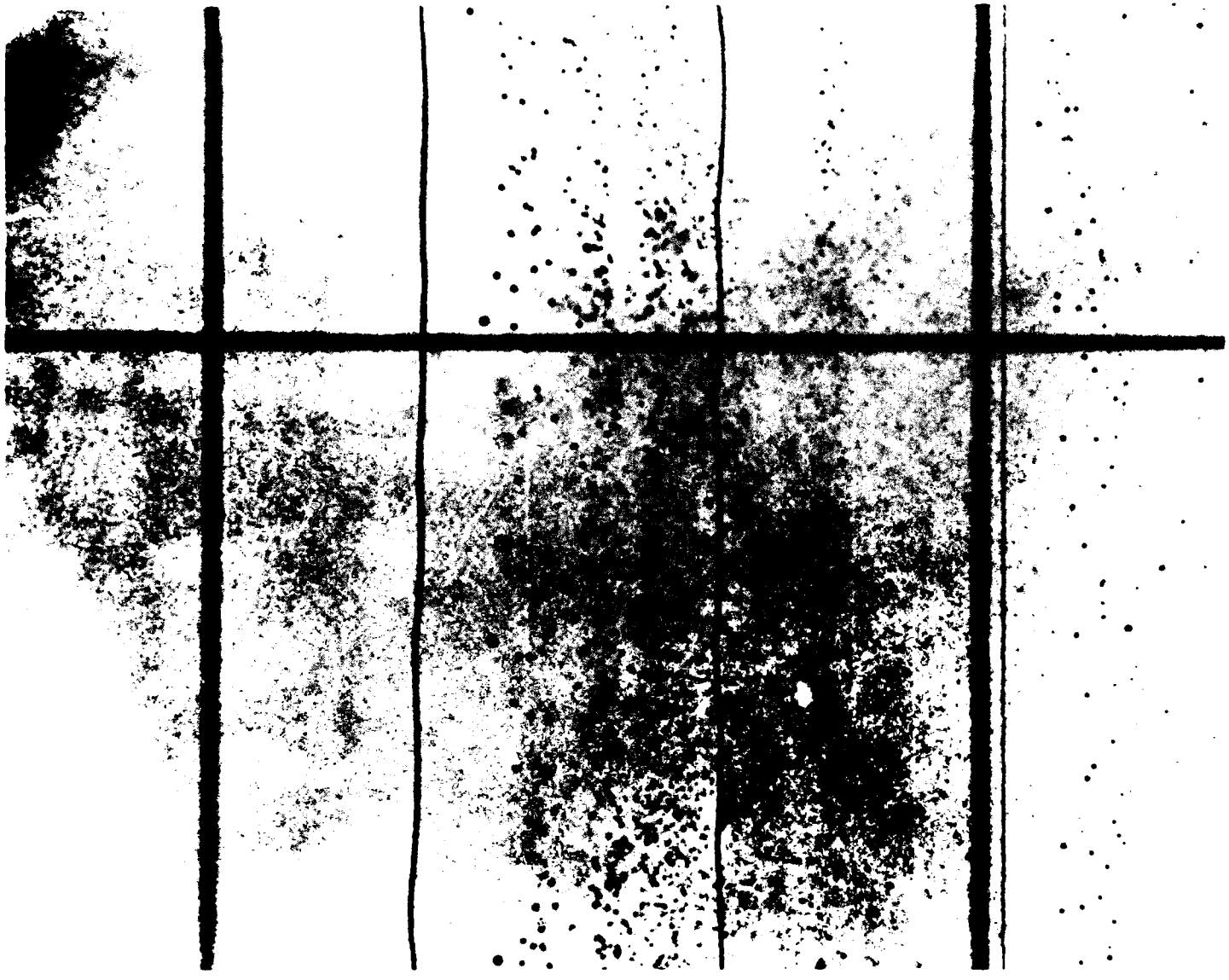

FIGURE 9.7 - PICTURE OF BUBBLE STREAM GENERATED WITH HYDROPERM TUBES. AIR INJECTION PRESSURE: 10 psig. WIRE SIZES: 5, 10, AND 15 mils.

FIGURE 9.8 - PICTURE OF BUBBLE STREAM GENERATED WITH HYDROPERM TUBES. AIR INJECTION PRESSURE: 16 psig. WIRE SIZES: 5, 10 AND 15 mils

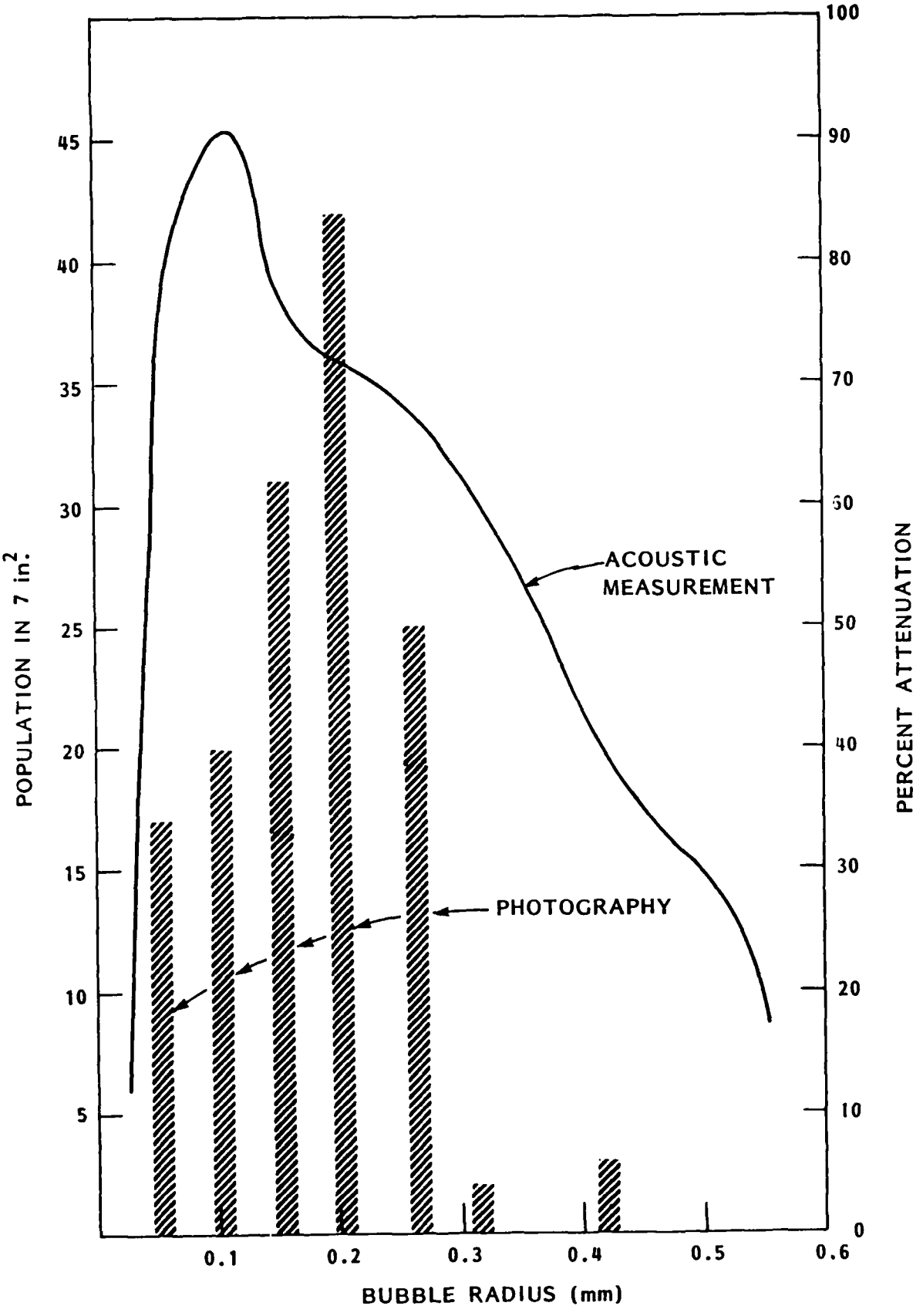

FIGURE 9.9 - BUBBLE SIZE DISTRIBUTION AS MEASURED FROM PHOTOGRAPHS AND DERIVED FROM ATTENUATION MEASUREMENTS. HYDROPERM TUBE - 10 psig

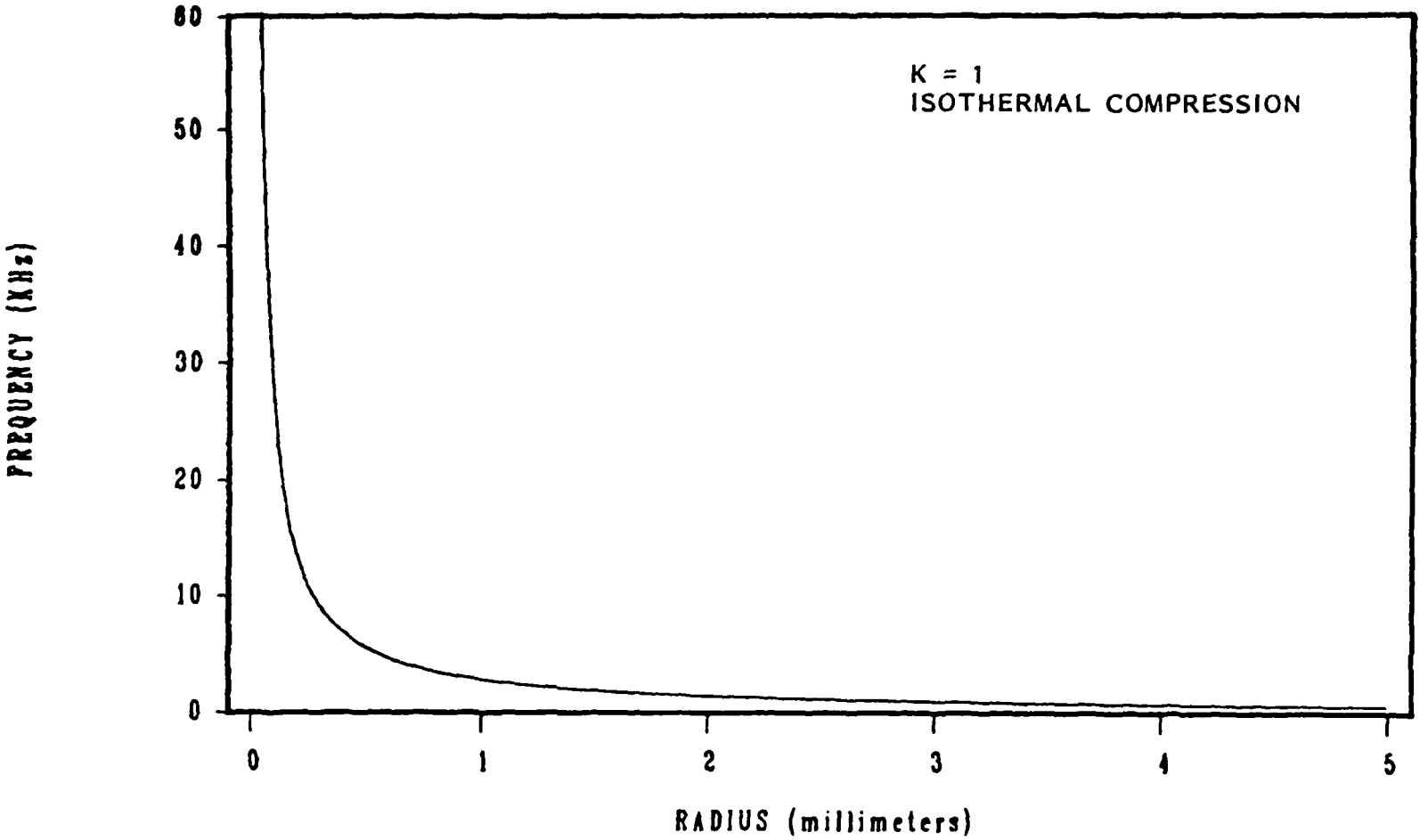

FIGURE 9.10 - RESONANCE FREQUENCY VERSUS BUBBLE RADIUS

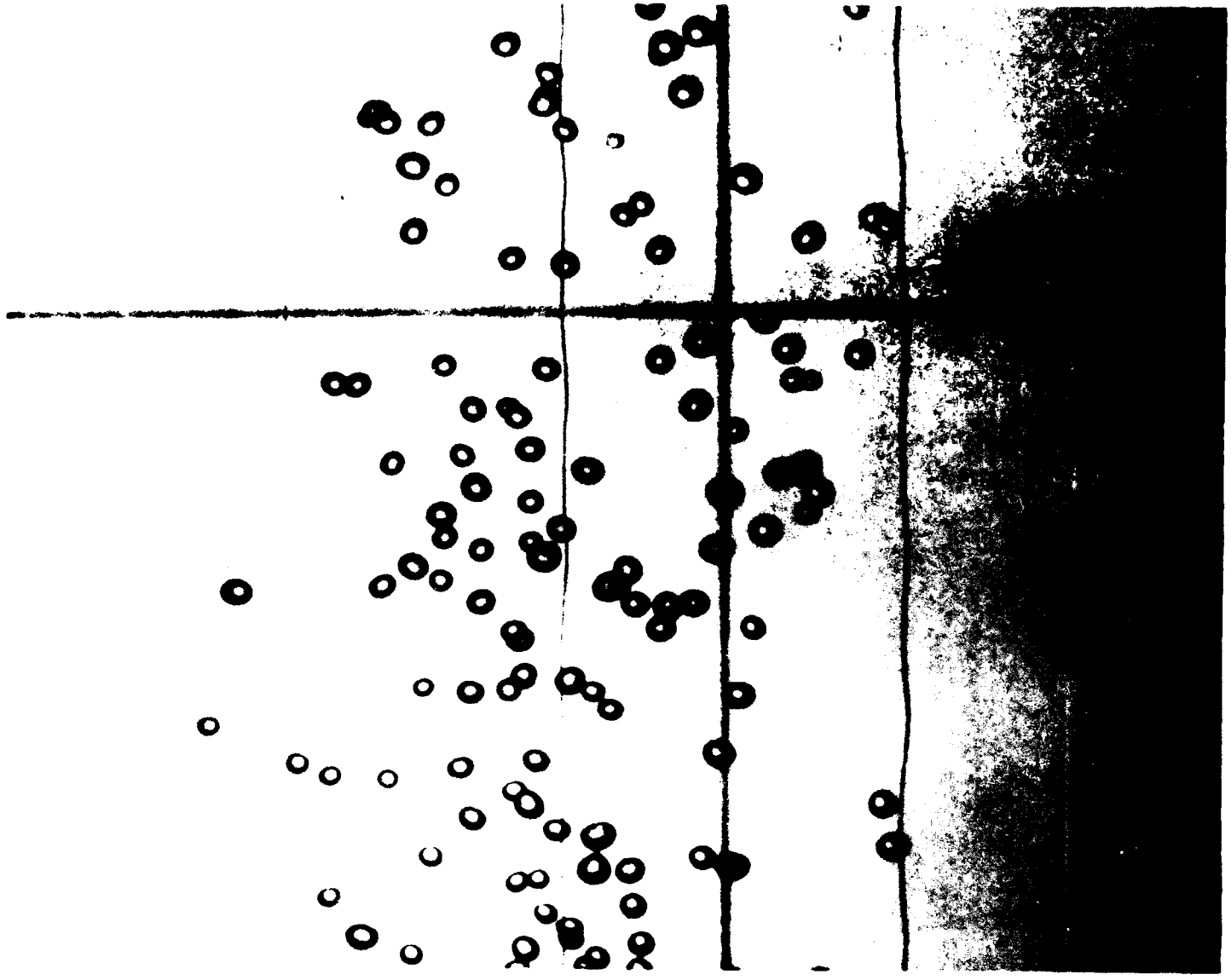

FIGURE 9.11 - PHOTOGRAPH OF BUBBLE STREAM GENERATED WITH ALUMINUM TUBE WITH DRILLED HOLES 0.006 in. DIAMETER - AIR INJECTION PRESSURE: 3 psig

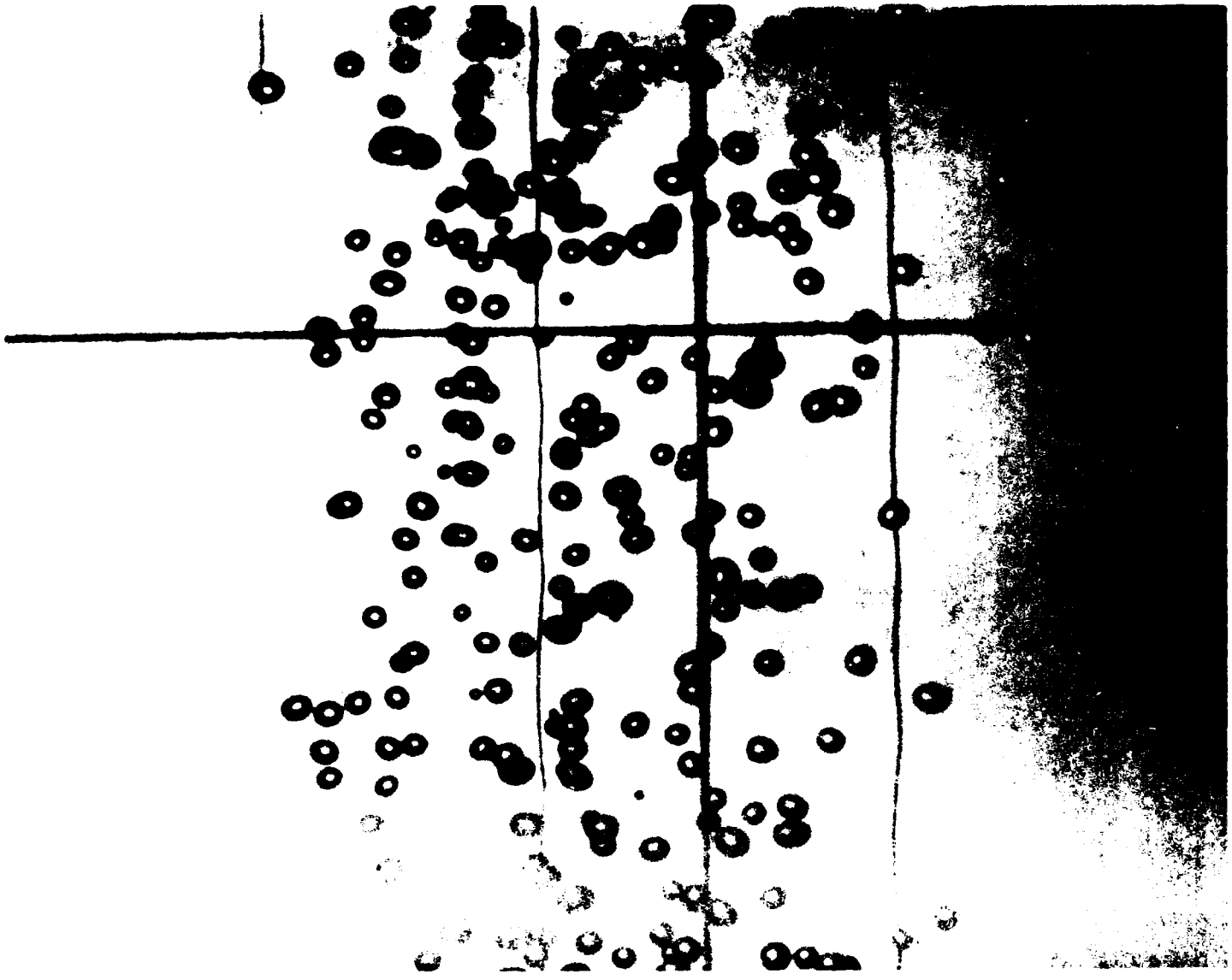

FIGURE 9.12 - PHOTOGRAPH OF BUBBLE SHOWN GENERATED WITH ALUMINUM TUBE WITH DRILLED HOLES 0.006 in. DIAMETER - AIR INJECTION PRESSURE: 7 psig

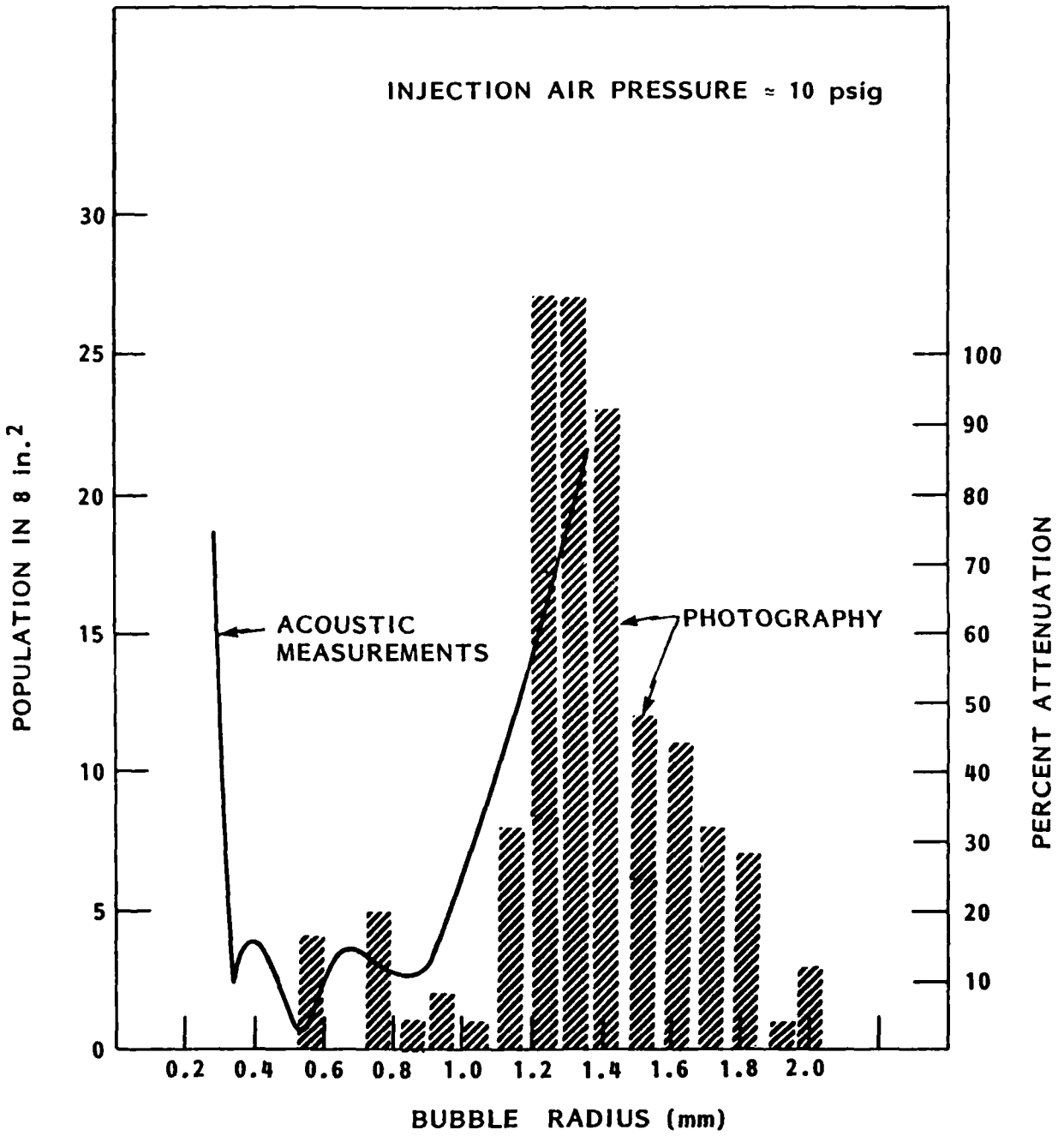

FIGURE 9.13 - BUBBLE SIZE DISTRIBUTION AS MEASURED FROM PHOTOGRAPHS AND DERIVED FROM ATTENUATION MEASUREMENTS. ALUMINUM TUBE WITH 0.06 in. DIAMETER HOLES

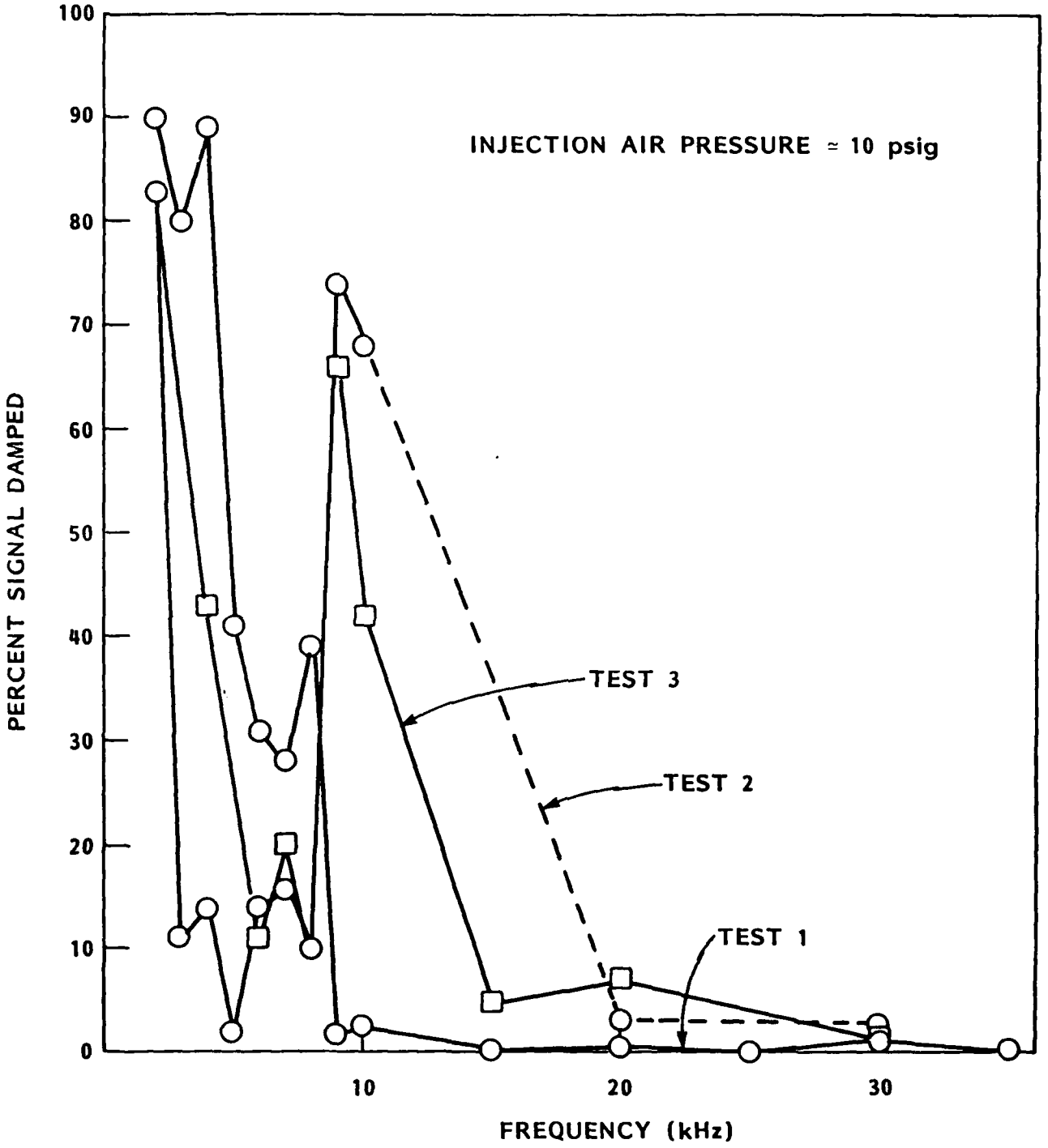

FIGURE 9.14 - DAMPING RATIO VERSUS FREQUENCY FOR THREE REPEATED TESTS

END

DTIC

9-86